# Universität Bonn

## Physikalisches Institut

# Measurement of the top-quark mass and the $t\bar{t}Z$ cross section in ATLAS: the $t\bar{t}$ dilepton way

Kaven Henry Yau Wong

A measurement of the top-quark mass and the $t\bar{t}Z$ cross section is performed using 4.6 fb$^{-1}$ and 20.3 fb$^{-1}$ of data from proton-proton collisions collected with the ATLAS detector at the LHC. The top-quark mass is measured in the $t\bar{t}$ $e\mu$ channel using the mean value of the $m_{\mathrm{T2}}$ variable with the calibration curve method to obtain the first top-quark mass measurement in the dilepton channel using the ATLAS detector: $m_{\mathrm{top}} = 175.2 \pm 1.6$ (stat.) $\pm$ 3.1 (syst.) GeV. Improvements in the computation of the systematic uncertainty, the measurement method and the inclusion of the $t\bar{t}$ $ee$ and $\mu\mu$ channels result in a significant increase in the precision of the measurement, leading to a measured top-quark mass of $m_{\mathrm{top}} = 173.7 \pm 0.8$ (stat.) $\pm$ 1.8 (syst.) GeV. The use of the $m_{\mathrm{T2perp}}$ variable is also studied, providing an additional mass measurement with similar uncertainty: $m_{\mathrm{top}} = 173.3 \pm 0.7$ (stat.) $\pm$ 1.7 (syst.) GeV. A $t\bar{t}Z$ cross-section measurement is performed in the $t\bar{t}Z \rightarrow 4\ell$ channel using a likelihood fit to five signal regions and one $ZZ$ control region used to determine the normalization of the main background from data. Seven events are selected in data and, from the result of the likelihood fit, a $t\bar{t}Z$ cross section of $\sigma_{t\bar{t}Z} = 0.32^{+0.18}_{-0.14}$ (stat.)$^{+0.12}_{-0.05}$ (syst.) pb is measured, which is compatible with the Standard Model prediction for proton-proton collisions at 8 TeV.

Physikalisches Institut der
Universität Bonn
Nussallee 12
D-53115 Bonn


BONN-IR-2015-06
May 2015
ISSN-0172-8741

# Measurement of the top-quark mass and the $t\bar{t}Z$ cross section in ATLAS: the $t\bar{t}$ dilepton way

Dissertation
zur
Erlangung des Doktorgrades (Dr. rer. nat.)
der
Mathematisch-Naturwissenschaftlichen Fakultät
der
Rheinischen Friedrich-Wilhelms-Universität Bonn

von
Kaven Henry Yau Wong
aus
Panama

Bonn, 2015

Dieser Forschungsbericht wurde als Dissertation von der Mathematisch-Naturwissenschaftlichen Fakultät der Universität Bonn angenommen und ist auf dem Hochschulschriftenserver der ULB Bonn `http://hss.ulb.uni-bonn.de/diss_online` elektronisch publiziert.

| | |
|---|---|
| 1. Gutachter: | Dr. Markus Cristinziani |
| 2. Gutachter: | Prof. Dr. Jochen Dingfelder |
| Tag der Promotion: | 22.05.2015 |
| Erscheinungsjahr: | 2015 |

# Acknowledgements

I would like to express my everlasting gratitude to Dr. Markus Cristinziani for supervising my thesis. I am much obliged for his help, insights, patience, trust, support and flexibility during all these years under his supervision. Thank you for all the long discussions that made this thesis possible. I would also like to thank Prof. Dr. Jochen Dingfelder, Prof. Dr. Herbert Dreiner and Prof. Dr. Thomas Bredow, who kindly agreed to be referees of my thesis.

Many thanks to Prof. Dr. Norbert Wermes for hosting our group and for his financial support during part of year 2013. I would also like to thank the Deutsche Forschungsgemeinschaft and its Emmy-Noether programme, as well as the European Research Council through its ERC Consolidator Grants, for their financial support of my work.

Furthermore, my utmost appreciation and gratitude to Dr. Kirika Uchida for her invaluable help and friendship during this time. I would also like to thank the other members of my group for their valuable suggestions and friendliness during these years (in alphabetical order): Dr. Tatevik Abajyan, Nello Bruscino, Sara Ghasemi, Mazuza Ghneimat, Sebastian Heer, Phan Thi Hong Ngoc, Dr. Gia Khoriauli, Dr. Vadim Kostyukhin, Agnieszka Leyko, Evan Machefer, Dr. Liza Mijović, Dr. Gizo Nanava, Ralph Schäfer and Dr. Nancy Tannoury.

To my father, my mother and my sister, thank you for all the moral, emotional and financial support offered during all my life, especially during the many years that I have been away from you.

My deepest thanks to my fiancée Elisavet Proedrou, for helping in the proofreading of this thesis, as well as for her unconditional love, support, and understanding during this time. No words will ever be expressive enough to describe my gratitude and affection.

# Contents

CHAPTER 1

# Introduction

From the four elements of the ancient greeks, to the periodic table of elements by Dmitri Mendeleev and the atomic model of Niels Bohr, coming all the way to the last century with the particle zoo, the quark model and the formulation of the Standard Model, many efforts has been made to answer questions that might be as ancient as humankind itself:

- What are the basic building blocks of matter?
- What keeps these basic building blocks together?
- How do these building blocks interact with each other?

Particle physics aims to answer these questions using the scientific method. The fruits of generations of scientific discoveries and efforts have provided better insights to what are the fundamental particles and their interactions, but also new questions and mysteries. The ultimate quest of answering these questions with a complete, elegant and correct theory is a major theoretical, experimental and technical joint effort, with theorists working towards the formulation of better models, experimentalists making more precise measurements of physics quantities and pushing the limits of the current technical constraints in order to reach domains that have never been studied before.

The work documented in this thesis measures two quantities that are of interest in particle physics: the top-quark mass and the cross section of the production of $t\bar{t}$ with an associated $Z$ boson. The top-quark mass is a fundamental parameter in the Standard Model of particle physics and a precise knowledge of its value leads to a better estimation of the strength of the electroweak radiative corrections, which are essential to constrain new physics models. A $t\bar{t}Z$ cross-section measurement, on the other hand, allows to check for the validity of the Standard Model prediction on the $tZ$ coupling, especially since many theories of physics beyond the Standard Model predict a different value.

Both analyses presented in this thesis uses data from the ATLAS detector [1], one of the experiments located at the Large Hadron Collider [2]. The measurements are performed in regions with high lepton multiplicity, with the top-quark mass measurement being measured with $t\bar{t}$ dilepton events ($t\bar{t} \to \ell^-\ell^+ b\bar{b}\nu\bar{\nu}$) and the $t\bar{t}Z$ cross-section measurement measured in the $t\bar{t}Z$ four-lepton channel (with $t\bar{t} \to \ell^-\ell^+ b\bar{b}\nu\bar{\nu}$ and $Z \to \ell^-\ell^+$), both allowing a very high-purity selection thanks to their rare signatures.

This thesis is organized as follows: In Chapter 2, the theoretical background is presented, including a small introduction to the Standard Model of particle physics, the top-quark mass and the $tZ$ coupling. In Chapter 3, the experimental setup is shown, with descriptions of the Large Hadron Collider and

the ATLAS detector. Chapter 4 discusses the simulation datasets and the data-driven methods used to model the expected results of a measurement in data, as well as the data used for each analysis. Chapter 5 is devoted to the description and definition of the physics objects used in the analyses presented in this thesis, while Chapter 6 presents an overall description of the systematic uncertainties considered in both analyses. Finally, Chapter 7 and Chapter 8 describe the top-quark mass measurement and the $t\bar{t}Z$ cross-section measurement in detail, respectively.

CHAPTER 2

# Theoretical background

## 2.1 The Standard Model of particle physics

The Standard Model of particle physics is extensively discussed in many textbooks [3–5] and it would be beyond the scope of this thesis to have a detailed explanation. Therefore, this section is only meant to be a short summary based on the sources mentioned through the text.

The Standard Model of particle physics is a theory of elementary particles and their interactions. As a theory of fundamental interactions, the Standard Model is a perturbative quantum field theory, where the interactions are understood as an exchange of mediator particles. In the Standard Model, these mediators are bosonic particles that can be separated in three groups corresponding to the three fundamental interactions considered by the Standard Model:

- the photon ($\gamma$) is the mediator for the electromagnetic interaction,
- the $W$ boson and the $Z$ boson are the mediators for the weak interaction and
- eight gluons ($g$) are the mediators for the strong interaction.

The strength of each of these interactions is characterized by its coupling constant. In this sense, the relative strength of the different interactions at the energy scale of the current high energy physics (HEP) experiments can be expressed by the ratio: $\alpha_{\text{strong}} : \alpha_{\text{electromagnetic}} : \alpha_{\text{weak}} \approx 1 : 10^{-2} : 10^{-6}$.

The electromagnetic interaction is the interaction between electrical charges. Among many other examples, this interaction keeps electrons in an atom around their atomic nucleus and it is also responsible for electron scattering (see Figure 2.1a).

The weak interaction is unique in several ways: it is the only interaction that has massive gauge bosons, the only interaction that can violate parity and also the only Standard Model interaction that affects neutrinos. It is responsible for flavor-changing decays, e.g., the decay of the top quark and the beta decay (see Figure 2.1b).

The weak and the electromagnetic interactions are unified under the electroweak theory, proposed by Glashow, Weinberg and Salam [6–8]. In the Glashow-Weinberg-Salam theory, the weak and the electromagnetic interactions are unified via the gauge group:

$$\mathrm{SU(2)_W} \times \mathrm{U(1)_Y}, \tag{2.1}$$

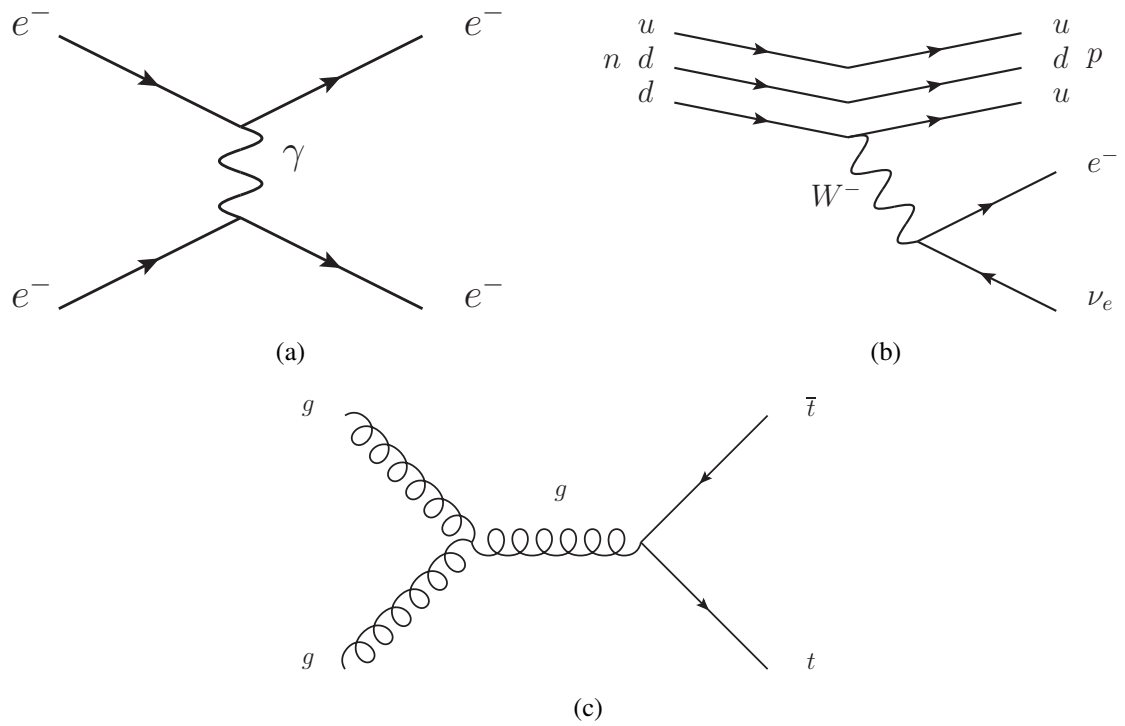


Figure 2.1: Example of interactions considered by the Standard Model of particle physics: (a) electron (Møller) scattering (electromagnetic interaction), (b) beta decay (weak interaction) and (c) gluon fusion with $t\bar{t}$ production (strong interaction).

where $SU(2)_W$ is the weak isospin symmetry and $U(1)_Y$ is the hypercharge symmetry. This symmetry is spontaneously broken to $U(1)_{EM}$, via the Brout-Englert-Higgs mechanism [9–11].

The strong interaction is related to the concept of color charge, studied by the discipline called chromodynamics. Although it is the strongest of all Standard Model interactions, the strong interaction has a very short range and only affects quarks and gluons (see Figure 2.1c). Among others, it is responsible for holding the atomic nucleus together, for the hadronization of quarks and for the confinement of quarks, i.e., that an isolated quark cannot be found in nature. In particular, it is the interaction responsible for the production of $t\bar{t}$ pairs at the LHC.

In the Standard Model, the strong interaction is represented by a $SU(3)_C$ gauge symmetry. After adding this symmetry to Equation 2.1, the Standard Model is specified by the local gauge symmetry group:

$$SU(3)_C \times SU(2)_L \times U(1)_Y. \tag{2.2}$$

Efforts to unify the electroweak and the strong interactions under a Grand Unification Theory (GUT) are ongoing [12–14]. Although several models have been proposed, no experimental evidence has been found to unequivocally support a given model.

The Higgs boson, discovered in 2012 [15, 16], is the latest boson to join the Standard Model, although it has been predicted since 1964 [10]. The existence of the Higgs boson is necessary to explain how the presence of massive $W$ and $Z$ bosons can still preserve gauge invariance in the Standard Model.

| Gauge boson | Photon ($\gamma$) | $W$ | $Z$ | Gluon ($g$) | Higgs ($H$) |
|---|---|---|---|---|---|
| Mass (GeV) | 0 | 80.385(15) | 91.1876(21) | 0 | 125.09(24) |
| Charge | 0 | ±1 | 0 | 0 | 0 |
| Role | Electromagnetic int. mediator | Weak int. mediator | Weak int. mediator | Strong int. mediator | Explains massive $W$ and $Z$ |

Table 2.1: Properties of the Standard Model bosons. The numbers in parentheses are the total uncertainty [17, 18].

Table 2.1 shows a summary of the bosons in the Standard Model. It has to be noted that the Standard Model is an incomplete theory of all known fundamental interactions, since it does not consider gravity. However, the contribution of gravity is negligible at the current energy scale used in particle physics ($10^1$ TeV), since gravity only becomes important at energies close to the Planck scale ($10^{16}$ TeV).

As a theory of elementary particles, the Standard Model states that all matter is composed of point-like fermionic particles, with spin $\frac{1}{2}$, namely the leptons and the quarks. Each of these particles has its own antiparticle which has the same mass but opposite quantum numbers.

Charged leptons are subject to the weak and electromagnetic interaction, but not the strong interaction. The neutrinos, on the other hand, are only subject to the weak interaction. Experimentally, three generations of leptons have been established, each of them containing one negatively-charged[1] particle (with charge $-1$)[2] and one almost-massless neutral particle called neutrino.

Unlike their leptonic counterparts, the quarks are affected by all the Standard Model interactions, i.e., they are also affected by the strong interaction. Like the leptons, the quarks are also divided in three generations, where each generation is formed by a positively-charged quark ($+\frac{2}{3}$) and a negatively-charged quark ($-\frac{1}{3}$). Since all quarks carry color charge and since every composite particle made of quarks is required to be colorless, not every combination is possible: only the combinations where

[1] From this point on, the term charge is to be understood as electrical charge

[2] In this thesis, the charge will be given in units of electron charge, e.g., the electron charge is $-1$

| Leptons | | First generation | Second generation | Third generation |
|---|---|---|---|---|
| Charged lepton | Name | Electron ($e$) | Muon ($\mu$) | Tau ($\tau$) |
| | Mass | 510.998928(11) keV | 105.6583715(35) MeV | 1.77682(16) GeV |
| | Charge | $-1$ | $-1$ | $-1$ |
| Neutrino | Name | Electron neutrino ($\nu_e$) | Muon neutrino ($\nu_\mu$) | Tau neutrino ($\nu_\tau$) |
| | Mass | $\approx 0$ | $\approx 0$ | $\approx 0$ |
| | Charge | 0 | 0 | 0 |
| **Quarks** | | **First generation** | **Second generation** | **Third generation** |
| Positively-charged quark | Name | Up ($u$) | Charm ($c$) | Top ($t$) |
| | Mass | $2.3^{+0.7}_{-0.5}$ MeV | 1.275(25) GeV | 173.34(76) GeV |
| | Charge | $+\frac{2}{3}$ | $+\frac{2}{3}$ | $+\frac{2}{3}$ |
| Negatively-charged quark | Name | Down ($d$) | Strange ($s$) | Bottom ($b$) |
| | Mass | $4.8^{+0.5}_{-0.3}$ MeV | 95(5) MeV | 4.18(3) GeV |
| | Charge | $-\frac{1}{3}$ | $-\frac{1}{3}$ | $-\frac{1}{3}$ |

Table 2.2: Leptons and quarks properties. The numbers in parentheses are the total uncertainty [17, 19].

the difference between the number of quarks and antiquarks is a multiple of 3 are colorless. With their peculiar fractional charge configuration and the color-charge related constraints mentioned, the quarks can combine to form integer-charged particles, namely the mesons and baryons. Mesons are particles composed of two quarks (one quark and one antiquark), while baryons are particles composed by three quarks (three quarks or three antiquarks). Particles with four or five quarks are not forbidden by chromodynamics: recent studies show possible evidence of the existence of tetraquarks [20], while experimental evidence of the existence of pentaquark particles is, at best, controversial [21]. Thereby, the existence of particles with more than three quarks is not well-established.

In Table 2.2, the main properties of leptons and quarks are summarized.

## 2.2 The top quark

The top quark has been extensively studied since its discovery by the CDF [22] and DØ [23] collaborations in 1995, and more detailed reviews can be found in the scientific literature [17, 24–29].

The top quark is the weak isospin partner of the bottom quark and, therefore, part of the third generation of quarks. The existence of this third generation was predicted by Kobayashi and Maskawa in 1973, in order to allow *CP*-violating interactions while preserving gauge invariance [30]. The existence of a weak isospin partner of the bottom quark, i.e., the requirement that quarks come in doublets, provides a natural way to suppress flavor-changing neutral currents through the GIM mechanism [31].

The top quark is the most massive elementary particle in the Standard Model, being roughly as heavy as a gold atom. Given the large value of its mass, the top quark has a very short lifetime, roughly $5 \times 10^{-25}$ s. This means that the top quark decays before it can hadronize [25] and before it can be detected directly. Therefore, the detection of the top quark is done indirectly through its decay products.

### 2.2.1 Top quark production

In hadron colliders, the production of top quarks takes place via either the strong or the weak interaction.

The strong interaction produces $t\bar{t}$ pairs by $q\bar{q}$ annihilation and gluon fusion (see Figure 2.2). At the Tevatron [32], the main process for $t\bar{t}$ production was the $q\bar{q}$ annihilation, which amounted to 85% of the produced $t\bar{t}$ pairs. At the LHC, on the other hand, the $t\bar{t}$ pair production takes place mainly through gluon fusion. Between 80% and 90% of the $t\bar{t}$ pairs at the LHC are produced from gluon fusion, depending on the center-of-mass energy, while the rest are produced from $q\bar{q}$ annihilation [17].

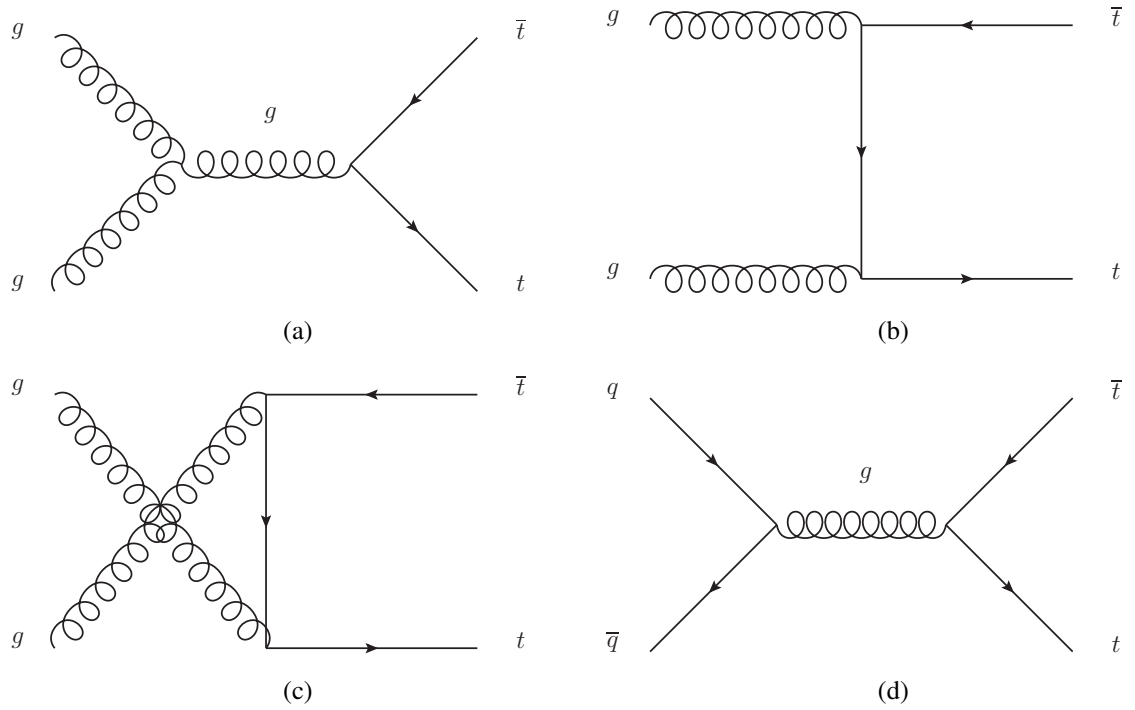


Figure 2.2: (a,b,c) $t\bar{t}$ production via gluon fusion and (d) $q\bar{q}$ annihilation.

The top quark can be also produced via the weak interaction, where only one top quark emerges. The Standard Model identifies three production processes: the $s$-channel, the $t$-channel and the $Wt$-channel [33]. The $s$-channel is the annihilation of a quark and an antiquark of different flavors into a $W$ boson that then decays into a top quark and a bottom quark (see Figure 2.3a). The $t$-channel, on the other hand, arise when a bottom quark and a light quark exchange a $W$ boson, producing a top quark and a light quark, i.e., a quark of the first or second generation (see Figure 2.3b). Lastly, a single top quark can be produced with an associated $W$ boson via the $Wt$-channel. This process takes place when a gluon splits into a $t\bar{t}$ pair, and one of the top quarks interacts with a bottom quark to produce a $W$ boson (see Figure 2.3c) or when a bottom quark absorbs a gluon and decays into a top quark and a $W$ boson (see Figure 2.3d).

The theoretical and experimental $t\bar{t}$ and single-top production cross section for different center-of-mass energies are shown in Figure 2.4. In Table 2.3, the numerical value of the expected $t\bar{t}$ cross section at the LHC are shown, where the computation is made at next-to-next-to-leading order (NNLO) in $\alpha_s$ and with next-to-next-to-leading logarithm (NNLL) soft-gluon resummation [34].

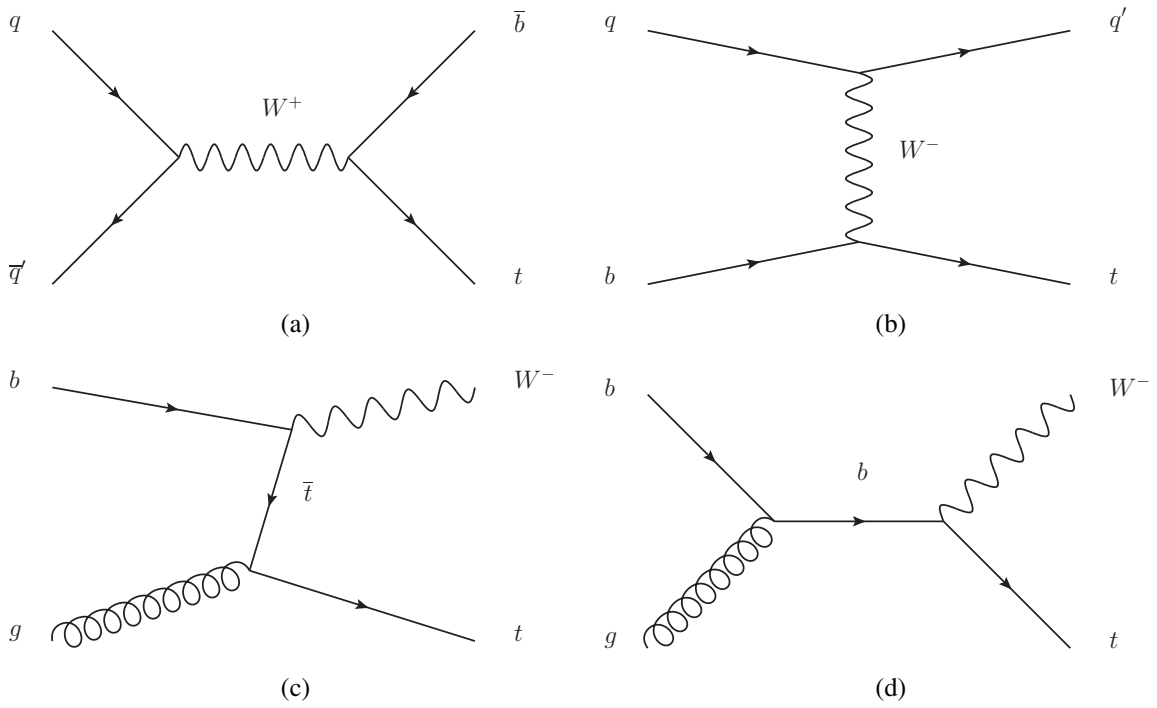


Figure 2.3: Single top quark production in the (a) *s*-channel, (b) *t*-channel, and (c,d) *Wt*-channel.

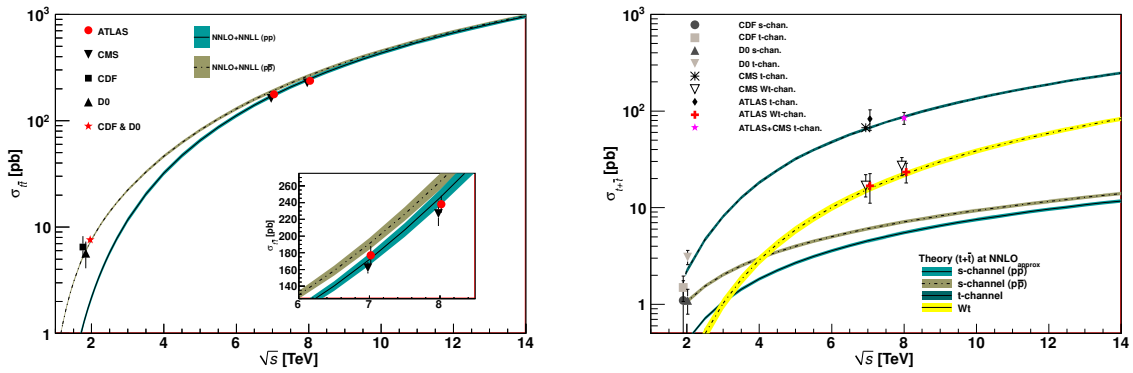


(a) (b)

Figure 2.4: Theoretical energy dependence of the production cross section for (a) $t\bar{t}$ and (b) single top [17]. Measured values corresponding to the Tevatron and LHC energies are also shown.

| Energy ( $\sqrt{s}$) | $\sigma_{t\bar{t}}$ (pb) |
|---|---|
| 7 TeV | $172.0^{+6.4}_{-7.5}$ |
| 8 TeV | $246^{+9}_{-11}$ |
| 14 TeV | $954^{+41}_{-24}$ |

Table 2.3: Theoretical $t\bar{t}$ cross section (NNLO+NNLL) for proton-proton collisions at LHC.

### 2.2.2 Top-quark decays

As mentioned previously in this section, the top quark has a very short lifetime and decays before it can hadronize. This decay takes place via the weak interaction and its strength is characterized by the values of the third row of the CKM matrix.

#### The CKM matrix

The Cabibbo-Kobayashi-Maskawa (CKM) matrix is a 3×3 unitary matrix that characterizes the strength of flavor-changing weak decays. More precisely, the square of each element in the CKM matrix gives the relative decay strength of flavor-changing weak decays between quarks:

$$V_{CKM} = \begin{pmatrix} |V_{ud}| & |V_{us}| & |V_{ub}| \\ |V_{cd}| & |V_{cs}| & |V_{cb}| \\ |V_{td}| & |V_{ts}| & |V_{tb}| \end{pmatrix}, \tag{2.3}$$

where the dimension of the CKM matrix is determined by the three generations of quarks that are known to exist.

The measured values of the elements of the CKM matrix are shown in the second column of Table 2.4. Using a global fit of all the direct measurements (assuming the unitarity of the CKM matrix), the values of the CKM matrix elements can be determined more accurately [17]. The results are shown in the third column of Table 2.4.

| Element | CKM matrix element value | |
|---|---|---|
| | Direct measurement | Global fit |
| $\|V_{ud}\|$ | 0.97425 ± 0.00022 | 0.97427 ± 0.00014 |
| $\|V_{us}\|$ | 0.2253 ± 0.0008 | 0.22536 ± 0.00061 |
| $\|V_{ub}\|$ | 0.00413 ± 0.00049 | 0.00355 ± 0.00015 |
| $\|V_{cd}\|$ | 0.225 ± 0.008 | 0.22522 ± 0.00061 |
| $\|V_{cs}\|$ | 0.986 ± 0.016 | 0.97343 ± 0.00015 |
| $\|V_{cb}\|$ | 0.0411 ± 0.0013 | 0.0414 ± 0.0012 |
| $\|V_{td}\|$ | 0.0084 ± 0.0006 | $0.00886^{+0.00033}_{-0.00032}$ |
| $\|V_{ts}\|$ | 0.0400 ± 0.0027 | $0.0405^{+0.0011}_{-0.0012}$ |
| $\|V_{tb}\|$ | 1.021 ± 0.032 | 0.99914 ± 0.00005 |

Table 2.4: Measured values of the Cabibbo-Kobayashi-Maskawa matrix elements (direct measurement and global fit). The numbers in parentheses are the total uncertainty [17].

The fitted values of the CKM matrix show that the top quark decays almost exclusively via the two-body decay $t \to Wb$ ($|V_{tb}|^2 = 99.83\%$). The decays to the lighter $s$ and $d$ quarks are highly suppressed, with a branching fraction of only 0.164% and 0.00785% respectively.

It is important to notice that, under the assumption that $|V_{tb}| \gg |V_{td}|$ and $|V_{tb}| \gg |V_{ts}|$, the cross section of the single top quark production is proportional to $|V_{tb}|^2$ [17].

### $t\bar{t}$ decay channels

As mentioned in the previous section, $t \to Wb$ is the dominant process in the decay of top quarks. The bottom quark is very likely to hadronize, while the $W$ boson can either decay hadronically 68% of the times and leptonically 32% of the times. Therefore, the $t\bar{t}$ decays can be classified according to the number and flavor of the leptons produced by the decay of the two $W$ bosons.

The tau lepton has a short lifetime and decays before it can be directly detected. It decays leptonically (i.e., to an electron or a muon, with the respective neutrinos) only 35% of the times and hadronically the rest of the times [17].

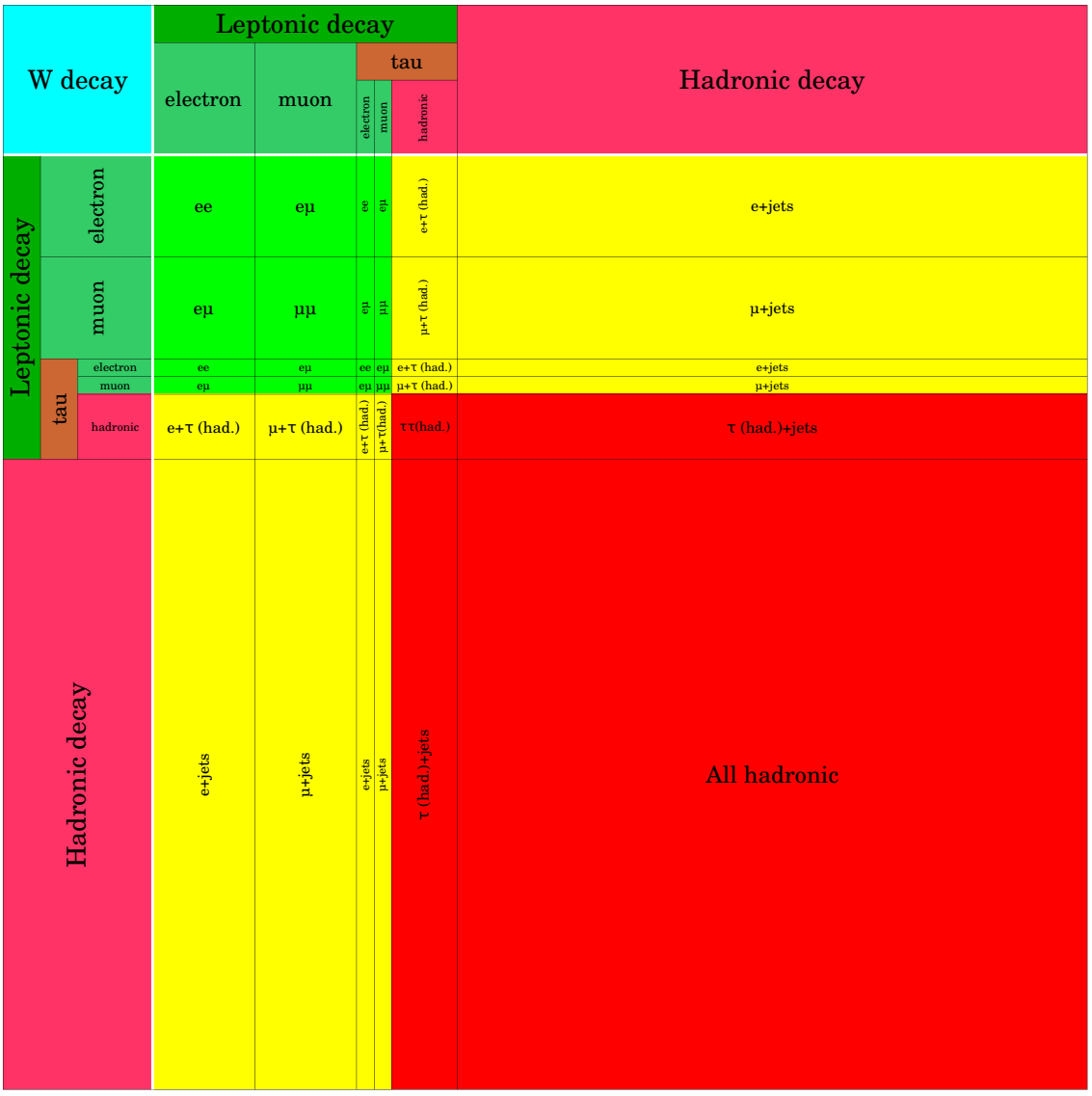


Figure 2.5: $t\bar{t}$ decay channels. Channels with no leptons (electrons or muons) in the final state are shown in red. Channels with one lepton in the final state are shown in yellow, and channels with two leptons in the final state are shown in green. The areas are proportional to the branching ratio of the channels.

With this in mind, the $t\bar{t}$ decays can be classified depending on the number of reconstructed leptons (electrons or muons) in three channels: the all hadronic channel (no reconstructed lepton), the single

lepton channel (one reconstructed lepton) and the dilepton channel (two reconstructed leptons). The detailed breakdown of the $t\bar{t}$ decay channels are shown in Figure 2.5, while the branching ratio of each $t\bar{t}$ decay channel is shown in Table 2.5.

| Channel | Number of leptons | Branching ratio | $\tau$ content |
|---|---|---|---|
| All hadronic | 0 | 0.56 | 18% |
| Single lepton | 1 | 0.38 | 24% |
| Dilepton | 2 | 0.06 | 29% |

Table 2.5: $t\bar{t}$ decay channels and their branching ratio. The $\tau$ content is the percentage of events where at least one $\tau$ was produced.

### The $t\bar{t}$ dilepton channel

The $t\bar{t}$ dilepton channel is the $t\bar{t}$ decay channel with the smallest branching ratio. As shown in Table 2.5, a $t\bar{t}$ pair decays dileptonically only 6% of the times. The Feynman diagram of the dilepton channel is shown in Figure 2.6.

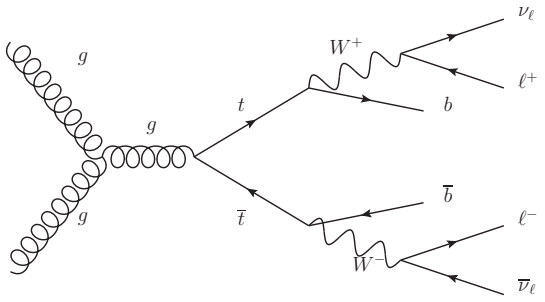


Figure 2.6: $t\bar{t}$ production by gluon fusion and decay into the dilepton channel.

In spite of the small branching ratio, the dilepton channel offers a very useful advantage compared to its statistically richer counterparts: the less common two-leptons signature allows the rejection of the $W$ + jets background and strongly suppresses the fake leptons background. Furthermore, the production of two $b$-jets and two neutrinos gives a very unique signature, which allows the suppression of the $Z$ + jets and diboson backgrounds by imposing requirements on the number of $b$-tagged jets and the missing transverse energy. All these properties allow for an extremely clean selection, giving an event purity that is unrivaled among all the $t\bar{t}$ decay channels.

From the perspective of a top-quark mass measurement, the dilepton channel presents a challenging issue: the production of two neutrinos does not allow a reliable full kinematic reconstruction of the $t\bar{t}$ decay at the current state of detector design and technology, as neutrinos escape undetected. Therefore, a direct kinematic reconstruction of the top-quark mass is out of question, and other methods are necessary to circumvent this problem. This handicap is compensated by the high purity of the dilepton channel, which greatly reduces the impact of background-related systematic uncertainties.

From the perspective of a $t\bar{t}Z$ cross-section measurement, the $t\bar{t}$ dilepton channel (with a dileptonic $Z$ decay) is a reasonable choice due to its high purity. Its downside is its limited number of events, with roughly only 20 events expected to have been produced in the LHC in the whole 2012 ATLAS run. This

disadvantage will become less significant with the increase of the LHC center-of-mass energy to 13 TeV and 14 TeV, where the $t\bar{t}Z$ cross section is expected to increase by a factor of roughly 3.7 and 4.3 of the 8 TeV value, respectively, and where more data will be collected.

### 2.2.3 The top-quark mass

The mass of the top quark is a free parameter in the Standard Model and has to be measured experimentally. Its value is very important to compute the strength of the electroweak radiative corrections, which are essential to constrain new physics models. Furthermore, the numerical value of the top-quark mass is an important parameter in the computation of the stability of the electroweak vacuum [35–37].

The value of the top-quark mass from the 2014 world average is [19]:

$$m_{\text{top}} = 173.34 \pm 0.27\ (\text{stat.}) \pm 0.71\ (\text{syst.})\ \text{GeV}, \tag{2.4}$$

which include the best measurements of the ATLAS, CMS, CDF and DØ Collaborations (see Figure 2.7).

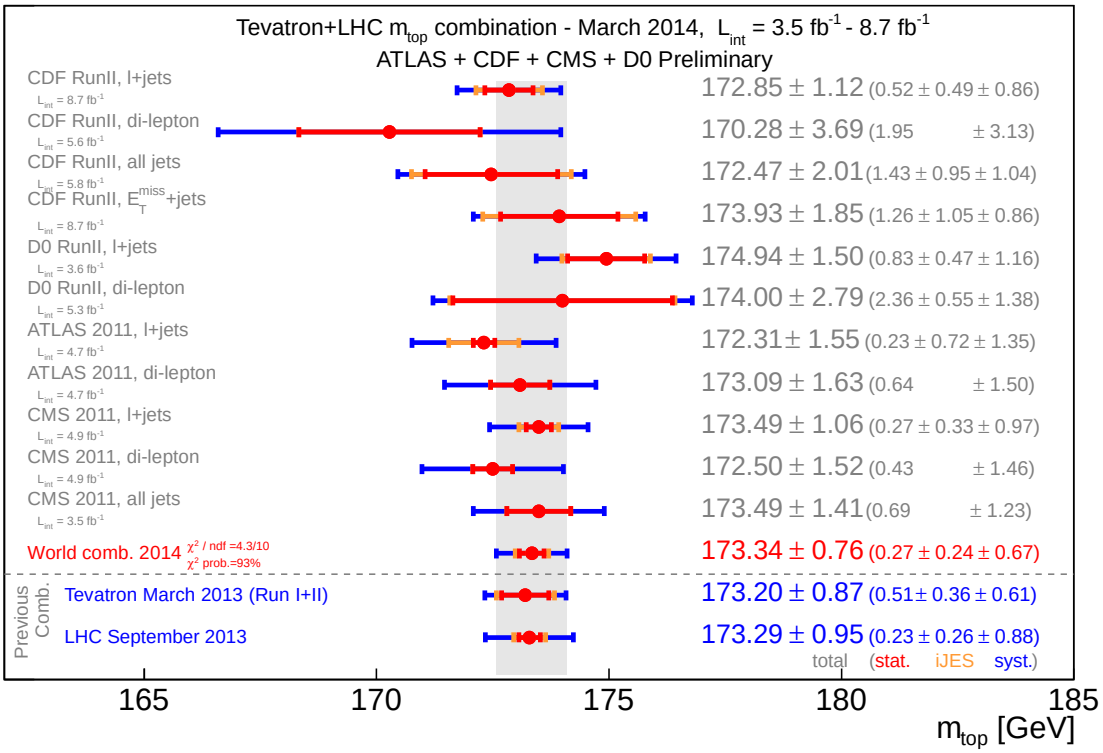


Figure 2.7: Summary of the 2014 world top-quark mass combination [19].

Since the 2014 world combination, improved measurements have been published by these collaborations. The Tevatron combination (CDF and DØ Collaborations) of Summer 2014 measures [38]:

$$m_{\text{top}} = 174.34 \pm 0.37\ (\text{stat.}) \pm 0.52\ (\text{syst.})\ \text{GeV}. \tag{2.5}$$

Furthermore, the latest ATLAS combination published in early 2015 yields [39]:

$$m_{\text{top}} = 172.99 \pm 0.48\,(\text{stat.}) \pm 0.78\,(\text{syst.})\ \text{GeV}. \tag{2.6}$$

Finally, the latest CMS combination measures [40]:

$$m_{\text{top}} = 172.38 \pm 0.10\,(\text{stat.}) \pm 0.65\,(\text{syst.})\ \text{GeV}. \tag{2.7}$$

The traditional measurements of the top-quark mass (including the one presented in this thesis) rely on the reconstruction of the decay products of the $t\bar{t}$ pair. This introduces uncertainties due to the reconstruction of leptons and jets, due to higher-level corrections and to parton showering modeling. These measured values correspond to the MC top-quark mass, a quantity that is not well-defined theoretically [41].

It seems natural to associate the reconstructed MC top-quark mass with the top-quark pole mass, since the top-quark pole mass is the renormalized top-quark mass in the on-shell scheme, i.e., $p_{\text{T}}^2 \approx m_{\text{top}}^2$. But these two values are not the same, and theoretical considerations have estimated the difference between the MC top-quark mass and the top-quark pole mass to be of the order of 1 GeV [41, 42]. The solution to this difference is still a non-trivial and open issue [43].

The top-quark pole mass suffers from the so-called infrared renormalon problem: the pole mass is sensitive to large-distance dynamics, and higher order terms in the $\alpha_s$ expansion leads to a source of divergence (renormalon) [44]. This introduces an intrinsic ambiguity of the order of the QCD momentum scale ($\Lambda_{\text{QCD}}$) [45]. Therefore, from a theoretical point of view, the top-quark pole mass is not an optimal mass scheme, and other mass schemes are preferred. Nevertheless, the ambiguity in the top-quark pole mass due to the infrared renormalon problem is of the order of 200 MeV, so its effect is not dominant at the precision of the current measurements.

The relation of the top-quark pole mass and another Lagrangian mass scheme can be expressed as [42]:

$$m_{\text{top}}^{\text{pole}} = m_{\text{top}}\,(R, \mu) + R \sum_{n=1}^{\infty} \sum_{k=0}^{\infty} a_{nk} \left[ \frac{\alpha_s\,(\mu)}{4\pi} \right]^n \ln^k \left( \frac{\mu}{R} \right), \tag{2.8}$$

where R is a scale intrinsic to the scheme, and $a_{nk}$ are numerical coefficients.

Through a suitable choice of the numerical coefficients in Equation 2.8, the so-called short-distance schemes can be defined such that they are not limited by $\Lambda_{\text{QCD}}$, e.g., the modified minimal-subtraction scheme ($\overline{\text{MS}}$ scheme) [46, 47].

The value of $m_{\text{top}}^{\overline{\text{MS}}}$ and $m_{\text{top}}^{\text{pole}}$ can be derived from the $t\bar{t}$ cross section [48]. It is usually easier to measure the top-quark pole mass from the $t\bar{t}$ cross section and compute $m_{\text{top}}^{\overline{\text{MS}}}$ from this value, since the relationship between the two masses is known to NNLO accuracy [49]. Therefore, the latest experimental measurements only extract the value of the top-quark pole mass [50, 51].

Other less dominant issues with top-quark mass measurements at hadron colliders include the reconstruction of the $t\bar{t}$ pair, effects due to the finite width of the top quark and $W$ boson, bound-state effects in $t\bar{t}$ production, higher-order corrections and non-perturbative corrections. The systematic uncertainties associated to the reconstruction of the $t\bar{t}$ pair from final state leptons and jets have an overall impact on top-quark mass measurements, while the other issues can have a significant effect on the MC modeling of the final state as well as on the shape of various kinematic distributions [43]. Finally, it is important to note that, from a theoretical point of view, the top-quark mass is simply a parameter in the QCD Lagrangian and, therefore, subject to renormalization [42].

### 2.2.4 Top quark coupling with the *Z* boson

The *Z* boson couples with all fermionic particles, including the top quark (see Figure 2.8). The *tZ* vector and axial couplings are determined without any ambiguity in the Standard Model [52]:

$$C_{\mathrm{V}}^{\mathrm{SM}} = \frac{T_{\mathrm{t}}^3 - 2q_{\mathrm{top}} \sin^2 \theta_{\mathrm{w}}}{2 \sin \theta_{\mathrm{w}} \cos \theta_{\mathrm{w}}} \approx 0.244, \tag{2.9}$$

$$C_{\mathrm{A}}^{\mathrm{SM}} = \frac{-T_{\mathrm{t}}^3}{2 \sin \theta_{\mathrm{w}} \cos \theta_{\mathrm{w}}} \approx -0.601, \tag{2.10}$$

where $T_{\mathrm{t}}^3 = 1/2$ is the weak isospin of the top quark, $\sin^2 \theta_{\mathrm{w}} \approx 0.231$ is the weak mixing angle and $q_{\mathrm{top}}$ is the charge of the top quark.

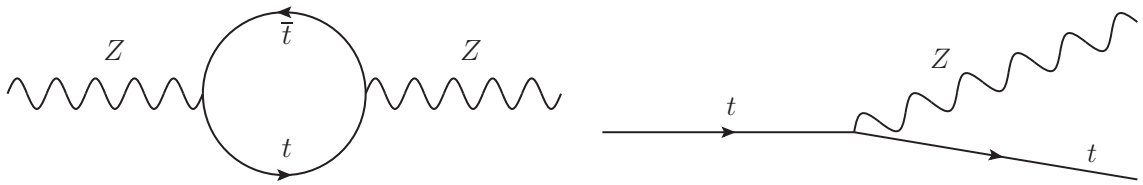


(a) *Z* boson diagram with a $t\bar{t}$ loop (b) top quark emitting a *Z* boson

Figure 2.8: Example of processes that depend on the strength of the *tZ* coupling.

An accurate measurement of the *tZ* coupling is important to check for deviations from the Standard Model prediction, since many theories of physics beyond the Standard Model (BSM), like the Little Higgs, Randall-Sundrum and related composite theories, predict a different *tZ* coupling strength [53].

One way to check the *tZ* coupling is to measure the $t\bar{t}Z$ cross section. At the LHC, the expected Standard Model $t\bar{t}Z$ cross sections at next-to-leading order (NLO) are 136.9 fb and 205.7 fb for the center-of-mass energies of 7 TeV and 8 TeV respectively [54]. Different theories of physics beyond the Standard Model predict deviations in the $t\bar{t}Z$ cross section [53], ranging from -70% to +37%. More details about these deviations are shown in Table 2.6.

A deviation of the *tZ* coupling from its Standard Model predicted value does not only modify the $t\bar{t}Z$ cross section, but can also be measured from the change in the shapes of some distributions in the $t\bar{t}Z$ channel, such as the azimuthal angle between the two leptons originating from the *Z* boson decay [52]. The data collected in the first long run of LHC is not sensitive enough to probe these changes, but it will be possible with the data collected in the second long run.

#### Little Higgs model

Theories based on the Little Higgs [55] propose a solution to the hierarchy problem by introducing diagrams to cancel the divergent contributions to the Higgs mass from loops involving the top quark, the *W* boson, the *Z* boson and the Higgs boson itself. Unlike supersymmetry, where fermion loops are canceled by boson loops (and viceversa), in the Little Higgs theory fermion loops are canceled by fermion loops and boson loops are canceled by boson loops. The problem of fine tuning is solved by explicitly breaking the SU(3) symmetry by adding two new sets of interactions to the Standard Model Lagrangian:

$$\mathcal{L}_{\mathrm{LH}} = \mathcal{L}_0 + \epsilon_1 \mathcal{L}_1 + \epsilon_2 \mathcal{L}_2, \tag{2.11}$$

| Model | Changes (%) | | |
|---|---|---|---|
| | $t_R Z$ coupling | $t_L Z$ coupling | $t\bar{t}Z$ cross section |
| Carena | 0 | -20 | -30 |
| Djouadi | -330 | 0 | 70 |
| Gherghetta | -20 | -20 | -36 |
| Grojean | 0 | 10 | 17 |
| Hosotani | 18 | -7 | -5 |
| Little Higgs | 0 | -15 | -23 |
| Pomarol | 0 | -25 | -37 |
| Wulzer 1 | 25 | 25 | 56 |
| Wulzer 2 | -10 | -10 | -20 |

Table 2.6: Expected variations in the $Z$ coupling of the left-handed and right-handed top quark, as well as the $t\bar{t}Z$ cross section for various BSM models for proton-proton collisions at a center-of-mass energy of 14 TeV [53].

where $\epsilon_1$ and $\epsilon_2$ are small spurion[3] parameters, and $\mathcal{L}_1$ and $\mathcal{L}_2$ are new sets of interactions that preserve the SU(3) symmetry independently, but break the SU(3) when summed.

The Littlest Higgs model [56] (a model based the Little Higgs theory) predict the existence of heavy quarks with masses below 1 TeV. The hypothetical existence of these heavy quarks would weaken the $tZ$ coupling, and the expected $t\bar{t}Z$ cross section at the LHC is expected to be 23% smaller [53].

### Djouadi model

The Djouadi model is a variant of the Randall-Sundrum model [57]. As such, it attempts to solve the hierarchy problem by postulating a higher-dimensional scenario, but proposing that the metric is not factorizable and is multiplied by a warp factor which is a rapidly changing function of an additional dimension:

$$ds^2 = e^{-2kr_c\phi}\eta_{\mu\nu}dx^\mu dx^\nu + r_c^2 d\phi^2, \tag{2.12}$$

where $k$ is a scale of the order of the Planck scale, $x^\mu$ are coordinates for the four dimensions, $0 < \phi < \pi$ is the coordinate for an extra finite dimension with its size set by $r_c$ [57]. The exponential in the first term, $e^{-2kr_c\phi}$, is the warp factor.

This metric creates two 4D-branes, which are separated by the fifth dimension: the Planck brane and the TeV brane. The Planck brane contains the hierarchy at the Planck scale, while the TeV brane contains the hierarchy at the TeV scale, i.e., the scale of current particle physics. The key idea in this model is that there is an exponential hierarchy that causes a suppression of the strength of the gravitational interaction in the TeV brane, solving the hierarchy problem.

The Djouadi model [58] introduces changes to the electroweak symmetry by enhancing it to a left-right $SU(2)_L \times SU(2)_R \times U(1)_X$ structure in the hyperspace[4]. In this model, the $t\bar{t}Z$ cross section is expected to be 70% larger than the Standard Model prediction [53], which is large enough to be measured at the LHC.

[3] A spurion is a fictitious, auxiliary field used in QFT.
[4] Also known as bulk.

### 2.2.5 Other properties of the top quark

#### Electric charge

In the Standard Model, the electric charge of the top quark is expected to be $+\frac{2}{3}$. Efforts to measure the top-quark charge have been made by the ATLAS, CDF, CMS and DØ collaborations [59–62], obtaining results that are compatible with the Standard Model prediction. The latest result from the ATLAS Collaboration measured a top-quark electric charge of [59]:

$$q_{\text{top}} = 0.64 \ \pm \ 0.02 \text{ (stat.)} \ \pm \ 0.08 \text{ (syst.)} \, . \tag{2.13}$$

#### *W*-boson helicity in top-quark decays

The Standard Model predicts that, due to angular conservation arguments, the top quark has a preference to decay to a zero-helicity $W$ boson. The branching ratio of such decay is given by [17]:

$$\mathcal{BR}(t \to W_0 b) \approx \frac{m_{\text{top}}^2}{m_{\text{top}}^2 + 2m_W^2} \approx 0.70. \tag{2.14}$$

The best measured value to date is [63]:

$$\mathcal{BR}(t \to W_0 b) = 0.720 \ \pm \ 0.039 \text{ (stat.)} \ \pm \ 0.037 \text{ (syst.)} \, , \tag{2.15}$$

which is consistent with the Standard Model prediction. This measurement can be used to constrain the $tWb$ anomalous couplings, setting limits to the possible contributions to this vertex from physics beyond the Standard Model.

#### Top quark Yukawa coupling

In the Standard Model, the bosonic Higgs field interacts with fermionic fields. This Yukawa interaction is known as the Yukawa coupling of the fermion. The Yukawa coupling to the top quark in the Standard Model is given by [28]:

$$y_{\text{top}} = \frac{\sqrt{2} m_{\text{top}}}{\upsilon} \approx 1, \tag{2.16}$$

where $\upsilon \approx 246$ GeV is the vacuum expectation value.

The large value of the top-quark Yukawa coupling ($y_{\text{top}}$) has lead to the formulation of models of physics beyond the Standard Model that couples preferentially to the top quark [28, 29]. With the discovery of the Higgs boson, experimental efforts are taking place to constrain the top-quark Yukawa coupling. The latest measurements from the ATLAS and CMS Collaborations are [64, 65]:

$$y_{\text{top}}^{\text{ATLAS}} = 1.35 \ \pm \ 0.30 \tag{2.17}$$

and

$$y_{\text{top}}^{\text{CMS}} = 1.67 \ \pm \ 0.30 \, . \tag{2.18}$$

#### Spin correlation in $t\bar{t}$ production

The Standard Model predicts that the spin of the quarks in a $t\bar{t}$ pair are correlated. Unlike the other quarks, the top quark decays before it is depolarized by the strong interaction [17]. Thereby, the $t\bar{t}$ spin

correlation can be measured experimentally.

The $t\bar{t}$ spin correlation depends on the mechanism used to produce the $t\bar{t}$ pair. For $q\bar{q}$ annihilation, the $t\bar{t}$ system is mainly produced in a $^3S_1$ state. This produces $t\bar{t}$ pairs with opposite helicities. For gluon fusion, in contrast, the $t\bar{t}$ system is mainly produced in a $^1S_0$ state, which leads to $t\bar{t}$ pairs with the same helicity [66].

In terms of spin correlation studies, the Tevatron and the LHC are complementary experiments: at Tevatron, the main $t\bar{t}$ production mechanism is $q\bar{q}$ annihilation, while gluon fusion is the main $t\bar{t}$ production mechanism for the LHC. All experiments have reported spin correlation measurements compatible with the Standard Model predictions [67–70].

### Forward-backward and charge asymmetry

The $t\bar{t}$ forward-backward asymmetry arises from the interference between the Born and box diagrams (see Figure 2.9) and from the interference of initial and final state radiation (see Figure 2.10), where the former gives a positive contribution to the asymmetry and the latter gives a negative contribution [71]. This asymmetry is defined as:

$$A_{FB} = \frac{N(\Delta y > 0) - N(\Delta y < 0)}{N(\Delta y > 0) + N(\Delta y < 0)} \tag{2.19}$$

where $\Delta y = y_t - y_{\bar{t}}$ is the rapidity difference between the top and the antitop quark.

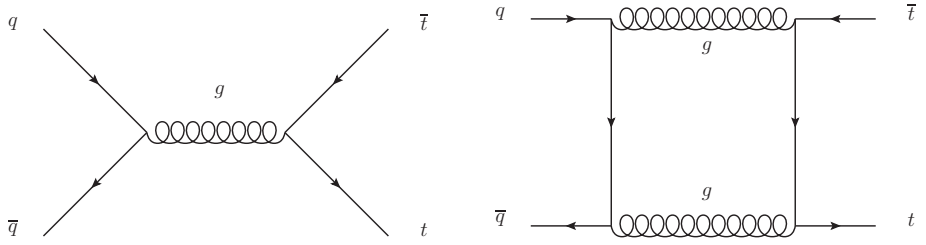


(a) Born diagram. (b) Box diagram.

Figure 2.9: Born and box diagrams in $t\bar{t}$ production. Their interference gives a positive contribution to the $t\bar{t}$ forward-backward asymmetry.

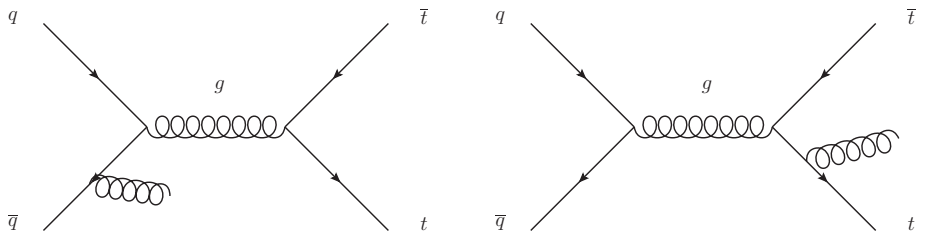


(a) Initial state radiation. (b) Final state radiation.

Figure 2.10: Diagrams of $t\bar{t}$ production with initial (a) or final state radiation (b). Their interference gives a negative contribution to the $t\bar{t}$ forward-backward asymmetry.

The value of the forward-backward asymmetry for $p\overline{p}$ collisions at Tevatron energies predicted by the

Standard Model has been computed at NNLO precision [72]:

$$A_{FB} = 0.095 \pm 0.007 \,. \tag{2.20}$$

Measurements from the CDF and DØ collaborations yields results compatible with the Standard Model: $A_{FB} = 0.164 \pm 0.047$ and $A_{FB} = 0.106 \pm 0.030$ respectively [73, 74].

Since the proton-proton collisions at LHC are symmetric, a forward and backward direction cannot be defined. Instead, the study is done via the determination of the charge asymmetry, defined as:

$$A_C = \frac{N(\Delta|y| > 0) - N(\Delta|y| < 0)}{N(\Delta|y| > 0) + N(\Delta|y| < 0)} \tag{2.21}$$

where $\Delta|y| = |y_t| - |y_{\bar{t}}|$ is the difference between the absolute value of the top-quark rapidity and the absolute value of the antitop-quark rapidity.

The Standard Model prediction for the charge asymmetry at the LHC is $A_C = 0.0123 \pm 0.0005$ [75]. The combined measurement from the ATLAS and CMS Collaborations [76] is consistent with the Standard Model prediction: $A_C = 0.005 \pm 0.007$ (stat.) $\pm$ 0.006 (syst.) .

CHAPTER 3

# The LHC and the ATLAS detector

The work presented in this thesis is based on data collected with the ATLAS detector, using proton-proton collisions at the Large Hadron Collider (LHC). A detailed description of the LHC and the ATLAS detector can be found in their respective design and technical reports [1, 2]. The information shown in this chapter is based on these reports and is only meant to be a short description.

## 3.1 The Large Hadron Collider

The Large Hadron Collider is a superconducting circular accelerator located underneath the French-Swiss border, close to the Swiss city of Geneva, at a depth ranging between 50 m and 150 m (see Figure 3.1). It is located in the tunnel of the Large Electron-Positron Collider (LEP) [77].

The LHC is a proton-proton collider. For the 2012 data [78], each proton beam had 1374 bunches (design value: up to 2808), with each bunch containing $1.6 - 1.7 \times 10^{11}$ protons (design value: $1.15 \times 10^{11}$). The spacing between bunches was 50 ns (design value: 25 ns), which translates to an interaction frequency of 20 MHz (design value: 40 MHz). The mean number of interactions per crossing ($\mu$) was 30 events/crossing, with a tail up to 40 events/crossing. The protons in each beam were accelerated to an energy of 4 TeV(design value: up to 7 TeV), providing proton-proton collisions with a center-of-mass energy of 8 TeV(design value: up to 14 TeV). The peak luminosity was 7.7 $\text{nb}^{-1}\text{s}^{-1}$ (design value: 10 $\text{nb}^{-1}\text{s}^{-1}$).

The storage ring houses 1232 cryodipole magnets which provide the magnetic field needed to keep the proton bunches in the designed trajectory. The core of the cryodipole magnets are the so-called dipole cold mass, containing all the components that are cooled using superfluid helium. The dipole cold mass works at a temperature of 1.9 K and, with a electric current up to 11850 A, can provide magnetic fields of up to 8.33 T.

The protons are accelerated in a series of steps (see Figure 3.2):

- Protons are produced by a hydrogen source and accelerated to 50 MeV using the Linear Accelerator (LINAC).
- These protons are then sent to the Synchrotron Booster (BOOSTER), where they are further accelerated to 1.4 GeV.
- The next stage takes place in the Proton Synchrotron (PS), where the protons acquire an energy of 25 GeV.

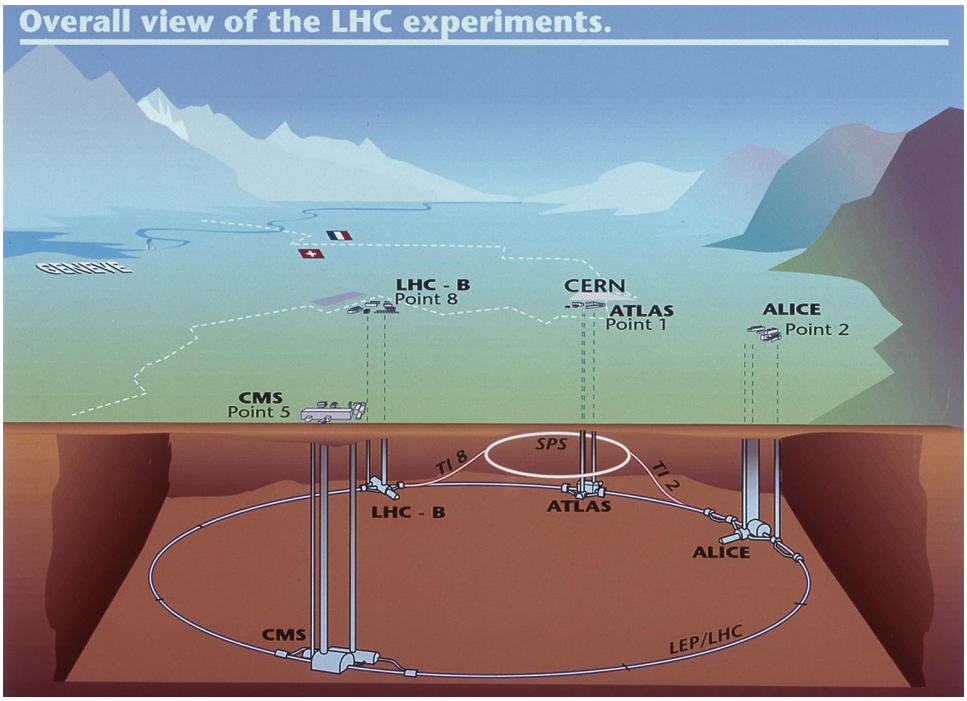


Figure 3.1: Location of the LHC and general layout (© 2014 CERN).

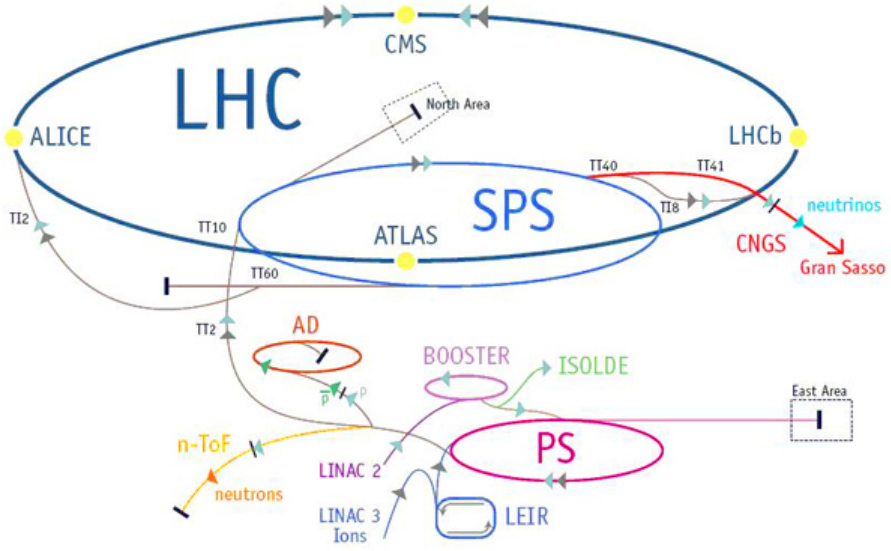


Figure 3.2: Schematic view of the accelerator complex of CERN (© 2013 CERN).

- In the next step, the protons are accelerated in the Super Proton Synchrotron (SPS) up to 450 GeV.
- Finally, the protons are sent to the LHC ring, where they are accelerated to up to 7 GeV using radio frequency (RF) cavities.

The LHC delivered 47 $pb^{-1}$ and 5.5 $fb^{-1}$ of proton-proton collisions at a center-of-mass energy of 7 TeV in 2010 and 2011, respectively [79]. In 2012, the center-of-mass energy of the proton-proton collisions was increased to 8 TeV, delivering a total of roughly 23 $fb^{-1}$ of data. The LHC is expected to run at a center-of-mass energy of 13 TeV in 2015. Current estimations expect that the LHC will reach the 200 $fb^{-1}$ mark by the end of 2017, right before the second long shutdown [80].

The LHC storage ring has a circumference of 26.7 km that roughly encloses an area of 56.5 $km^2$ (see Figure 3.2). This ring is slightly tilted, since the LEP tunnel has a slope of 1.4% in order to ensure that all the underground caverns and the main tunnel are located in solid rock [77]. It services four major experiments, each of them located at one of the four collision points in LHC: ATLAS [81] and CMS [82] are general-purpose detectors, while ALICE [83] and LHCb [84] are devoted to the study of heavy ions and the precision measurement of the CP violation and rare B-hadron decays, respectively. Three smaller experiments are also hosted by the LHC storage ring: the LHCf experiment [85], which measures neutral particles in the very forward region of LHC collisions, the TOTEM experiment [86], committed to the measurement of the total proton-proton cross section and the study of elastic and diffractive scattering in the LHC, and the MoEDAL experiment [87], which searches for magnetic monopoles and other highly-ionizing particles.

## 3.2 The ATLAS detector

ATLAS is the acronym for *A Toroidal LHC AparatuS*, a general-purpose detector located in the LHC and designed to accommodate a wide range of studies. It has a cylindrical shape, with a length of 44 m and a diameter of 25 m, as shown in Figure 3.3.

The detector can be separated in five main components:

- the superconducting magnet system,
- the inner detector,
- the electromagnetic calorimeter,
- the hadron calorimeter and
- the muon spectrometer.

These five components are used together to reconstruct an event (see Figure 3.4). Without getting into many details, the superconducting magnet system provides the magnetic fields needed for the operation of the inner detector and muon spectrometer, the inner detector contains the tracking system used to measure the momentum and sign of charged particles. The electromagnetic calorimeter is designed in such a way that most hard-process electrons and photons will deposit all their energy in its cells. This allows the identification of these particles in collaboration with the inner detector. The hadron calorimeter is located after the electromagnetic calorimeter. As its name indicates, this calorimeter aims to collect all the energy of hadronic particles in its cells, which is then used to identify and measure jets. In this design, ideally only muons and neutrinos are able to exit the hadron calorimeter. The muon spectrometer is located after the hadron calorimeter and is used to identify muons and measure

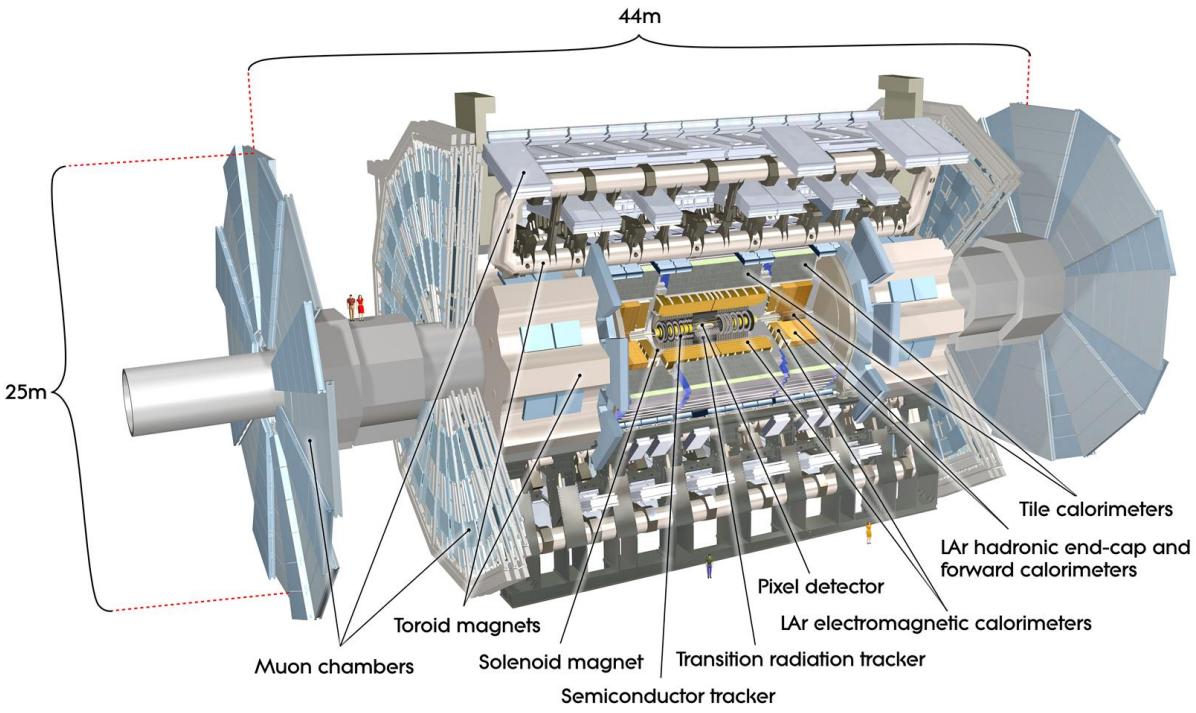


Figure 3.3: Overview of the ATLAS detector (ATLAS Experiment © 2014 CERN).

their charge and momentum. Finally, neutrinos escape undetected and their kinematic information is associated with the missing transverse momentum of each event. A more detailed discussion of each component will be given later in this chapter.

### 3.2.1 The ATLAS coordinate system

Before discussing the ATLAS subsystems, it is useful to define a coordinate system. The coordinate system used in the ATLAS detector is defined as follows:

- the origin of the coordinate system is located at the expected point of interaction.
- The z axis is parallel to the direction of the beam. Notice that the positive direction has not been defined yet.
- The positive x axis points towards the center of the LHC storage ring.
- The y axis is parallel to the vectorial product of the x and z axis. The direction pointing away from the Earth's core is taken as the positive direction.
- With the x and y directions now fully defined, the positive direction of the z axis is defined such that the result is a right-handed coordinate system.

Once the coordinate system is defined, some other useful quantities can be defined. These quantities are frequently used throughout this thesis.

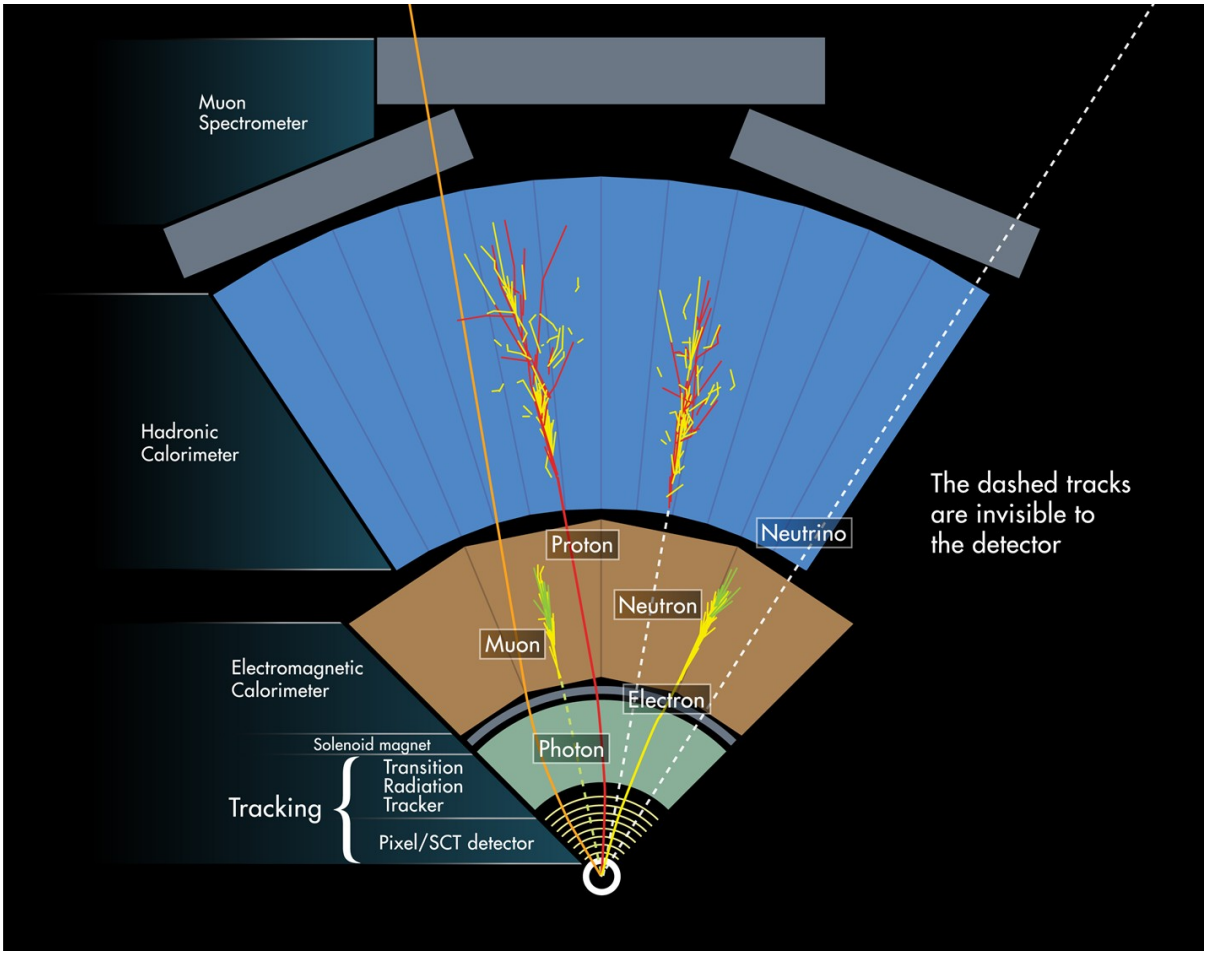


Figure 3.4: Event reconstruction with the ATLAS detector (ATLAS Experiment © 2014 CERN).

- The transverse plane is the plane that contains the x and y axis.
- Given an arbitrary direction, the azimuthal angle ($\phi$) is defined as the angle between the x axis and the projection of the arbitrary direction on the transverse plane.
- Given an arbitrary direction, the polar angle ($\theta$) is defined as the angle with respect to the z axis. By itself, the polar angle is not a very useful quantity. Instead, a more useful quantity called pseudorapidity ($\eta$) can be defined in terms of the polar angle:

$$\eta \equiv -\ln\left(\tan\frac{\theta}{2}\right). \tag{3.1}$$

  The pseudorapidity has the advantage that the difference between two pseudorapidities is a Lorentz invariant.
- Once $\phi$ and $\eta$ are defined, an angular separation quantity ($\Delta R$) can be defined using:

$$(\Delta R)^2 \equiv (\Delta\phi)^2 + (\Delta\eta)^2 . \tag{3.2}$$

  This quantity is a Lorentz invariant with respect to boosts in the z axis.

### 3.2.2 The superconducting magnet system

The superconducting magnet system (SMS) provides the magnetic fields needed to bend charged particles in the inner detector and muon spectrometer. The general overlay of the SMS is shown in Figure 3.5.

The central solenoid provides the 2 T magnetic field used by the inner detector and is located between the inner detector and the electromagnetic calorimeter, and it is made of aluminium, copper and niobium-titanium. It has an axial length of 5.3 m and a diameter of roughly 2.5 m with a total of 1173 coil turns and an operating current of 7.6 kA.

Three large air-core toroids generate the magnetic field used in the muon spectrometer: a barrel toroid and two end-cap toroids. They are also made of aluminium, copper and niobium-titanium, but have a higher aluminium composition than the central solenoid. The peak magnetic field on the barrel toroid is 3.9 T, while in the end-cap toroids it goes up to 4.1 T. The end-cap toroid coil system is rotated by 22.5 degrees with respect to the barrel toroid to provide radial overlap and optimize the bending power in the region between both coil systems. The barrel toroid and the end-cap toroids are composed of eight coils (with 120 and 116 turns each, respectively) which are placed radially and symmetrically around the z axis. Each coil in the barrel toroid and the end-cap toroids operates at a current of 20.5 kA and 20.0 kA respectively. The barrel toroid has an axial length of 25.3 m, an inner radius of 9.4 m and an outer radius of 20.1 m, while each end-cap toroid has an axial length of 5 m, an inner radius of 1.65 m and an outer radius of 10.7 m.

All the magnets in the SMS are cooled by forced flow using liquid helium at 4.5 K, using a vacuum flask (Dewar flask) coupled to the central refrigerator. In addition to the vacuum flask, the barrel toroid and the end-cap toroids feature cold helium pumps to guarantee an appropiate cooling of these elements.

### 3.2.3 The inner detector

The inner detector collects information that allows to measure the charge and momentum of charged particles. It is located inside the central solenoid, which provides a 2 T magnetic field used to bend the trajectory of charged particles.

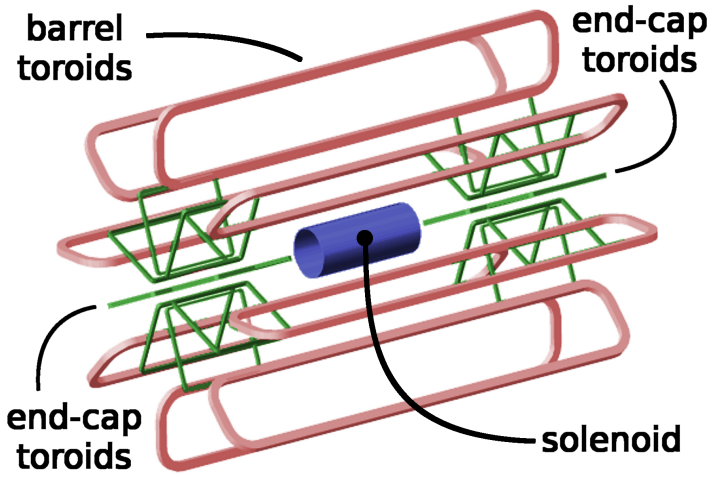


Figure 3.5: Superconducting magnet system in ATLAS [88].

In order to achieve the high resolution needed for precision measurements, fine-granularity detectors are needed. The best granularity is offered by pixel detectors, but due to their high costs in terms of research, development and production, only a limited number of pixel detectors are installed. Instead, a combination of high-resolution pixel detectors, silicon microstrips and straw detectors is used (see Figure 3.6). This setup reduces the construction costs and the amount of material introduced into the system without sacrificing too much precision.

The innermost layers are formed by three layers of pixel detectors located at a distance between 50.5 mm and 122.5 mm from the interaction point. The first layer of pixel detectors, the closest layer to the interaction point, is the removable barrel layer (b-layer). Unlike the next two layers of pixel detectors, the removable barrel layer covers the entire pseudorapidity $|\eta| < 2.5$ region with only one barrel and $16 \times 10^6$ channels. The last two pixel detector layers are divided in two parts: the two barrels, covering the pseudorapidity $|\eta| < 1.7$ range, and five end-caps on each side, covering the pseudorapidity $1.7 < |\eta| < 2.5$ range. As a whole, the pixel system in the inner detector is formed by a total of approximately 1500 barrel modules and 700 disk modules, where all the pixel modules are identical. Each pixel module is 64.2 mm long and 21.4 mm wide and contains 61 440 pixel elements read out by 16 chips, where each chip is in charge of an array of $24 \times 160$ pixels.

The semiconductor tracker system (SCT) is located after the pixel detectors, at a distance of 299 mm to 514 mm from the interaction point. It is formed by four pairs of silicon microstrip detectors layers, which provides eight measurements per charged track.

Each silicon detector is 64.0 mm long and 63.6 mm wide, containing 768 readout strips. The SCT system contains 61 $m^2$ covered by silicon detectors, with $6.2 \times 10^6$ readout channels. Due to its spatial resolution, tracks can be distinguished if they are separated by a distance of more than 200 μm. Like the outer layers of the pixel detector, the SCT is separated in barrel modules and end-cap modules. The barrel layers provide coverage for the $|\eta| < 1.4$ region, while the end-caps cover the $1.4 < |\eta| < 2.5$ region.

The SCT and the pixel system need to be in a very high dimensional and thermal stability environment. A carefully designed cooling system is used to remove the heat generated from the electronics and detector leakage current in order to keep the equipment within working temperature parameters. Furthermore, materials with low thermal expansion coefficients are used to achieve the degree of dimensional stability required by the two systems.

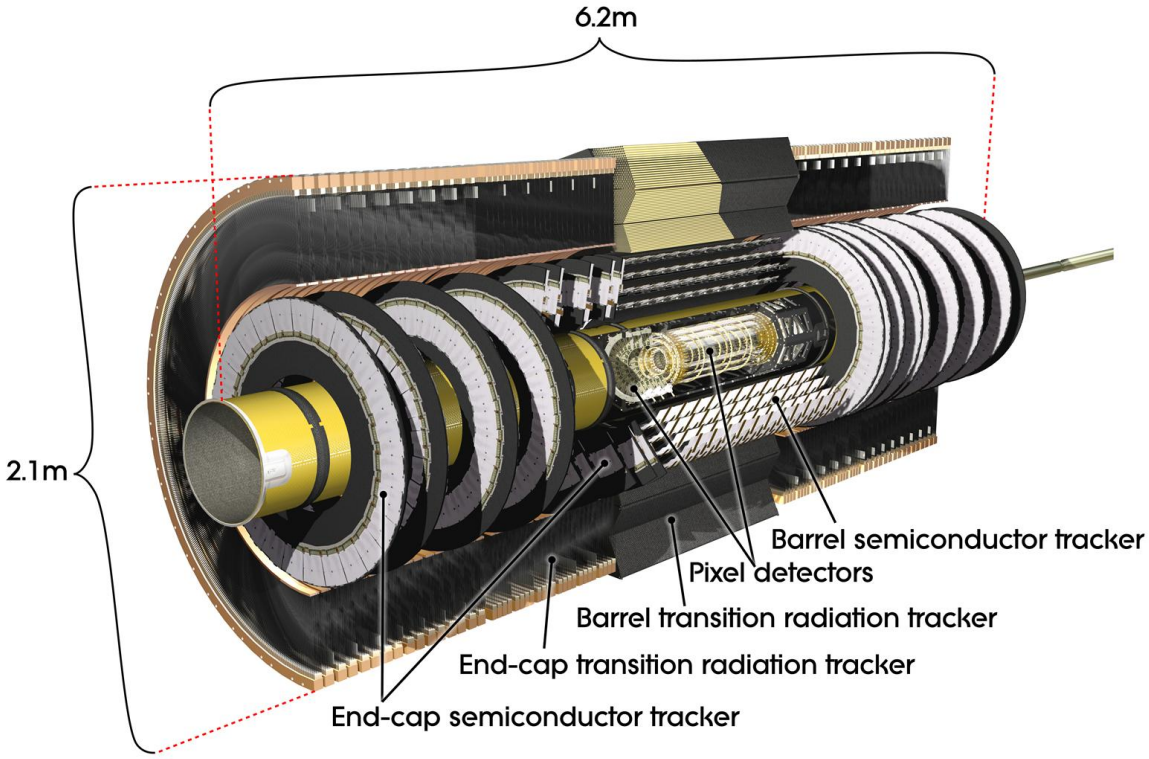


Figure 3.6: ATLAS inner detector layout (ATLAS Experiment © 2014 CERN).

The transition radiation tracker (TRT) is the outermost layer of the inner detector, located at a distance of 554 mm to 1082 mm from the interaction point. It uses straw detectors, which are able to withstand the demanding hit rates expected from the LHC collisions. In addition to providing further tracking capabilities, it is able to identify electrons thanks to the use of xenon gas, allowing for a better discrimination between hadrons and electrons. The barrel module covers the $|\eta| < 0.7$ region and is composed of individual modules containing between 329 and 793 axial straws each. Each straw has a diameter of 4 mm and a length of up to 1440 mm. Each of the two end-caps is formed by 18 wheels and covers the pseudorapidity $0.7 < |\eta| < 2.5$ region.

In the absence of pile-up effects, the inner detector can provide the location of the primary vertex with a resolution of 41 μm along the z axis and 18 μm in the transverse plane for $t\bar{t}$ events [89]. Secondary vertices can be provided with a radial resolution of down to 0.7 mm, depending on the $\eta$ region. The resolution of the inverse transverse momentum in the barrel region, measured using muons with high transverse momentum, is expected to be 0.34 $\text{TeV}^{-1}$. In the barrel region, the muon identification efficiency is above 98% for muons with $p_{\text{T}} > 1$ GeV. Electrons and pions with tracks around 5 GeV can be reconstructed with efficiencies between 70% and 95%.

### 3.2.4 Calorimeters

The ATLAS calorimeters play the main role in the measurement of the energy of the particles produced by the LHC collisions. Calorimetric methods are based on the absorption of the energy of particles as they travel through the material. The energy deposited in the material can then be measured to determine the energy of the particles. In ATLAS, two calorimetry systems are used, namely, the electromagnetic calorimeter and the hadron calorimeter (see Figure 3.7).

#### Electromagnetic calorimeter

At high energies ($E > 100$ MeV), electrons lose their energy almost exclusively by bremsstrahlung radiation, i.e., the production of photons. Subsequently, photons lose their energy in electron-positron pair production. The combination of these two processes produces electron-photon cascades, which are the fundamental processes that take place in electromagnetic calorimeters. The length scale of a shower is set by the radiation length, a quantity that depends on the absorbing material of the calorimeter. Therefore, the energy of an electron or a photon can be determined by measuring the electron-photon cascade produced. This measurement is done by placing active material between layers of absorbing material. When the electrons and photons in the cascade go through the active material, the material gets ionized. This ionization can then be measured by the collection of the charged particles on electrodes.

The ATLAS electromagnetic calorimeter is a lead/liquid argon detector with accordion geometry. The lead plates act as the absorber, while the liquid argon acts as the active medium. The electrodes are made of Kapton. Like most components in ATLAS, the electromagnetic calorimeter is divided into a barrel module and two end-caps modules. The barrel covers the pseudorapidity $|\eta| < 1.475$ region, while the end-caps cover the region corresponding to $1.375 < |\eta| < 3.2$. The barrel is formed by two identical half-barrels, separated by a 6 mm gap. Each end-cap region contains two coaxial wheels. Each wheel covers the region given by $1.375 < |\eta| < 2.5$ and $2.5 < |\eta| < 3.2$, respectively.

In the ($|\eta| < 2.5$) region, which is devoted to precision measurements, the electromagnetic calorimeter is divided in three sections: the strip section, the middle section and the back section. The strip section has a constant thickness of roughly six radiation lengths and a very fine granularity in $\eta$, with a granularity ($\Delta\eta \times \Delta\phi$) of $0.003 \times 0.1$, providing a precise measurement of this quantity and improving particle identification. The middle section is segmented in squares with granularity $0.025 \times 0.025$ and a

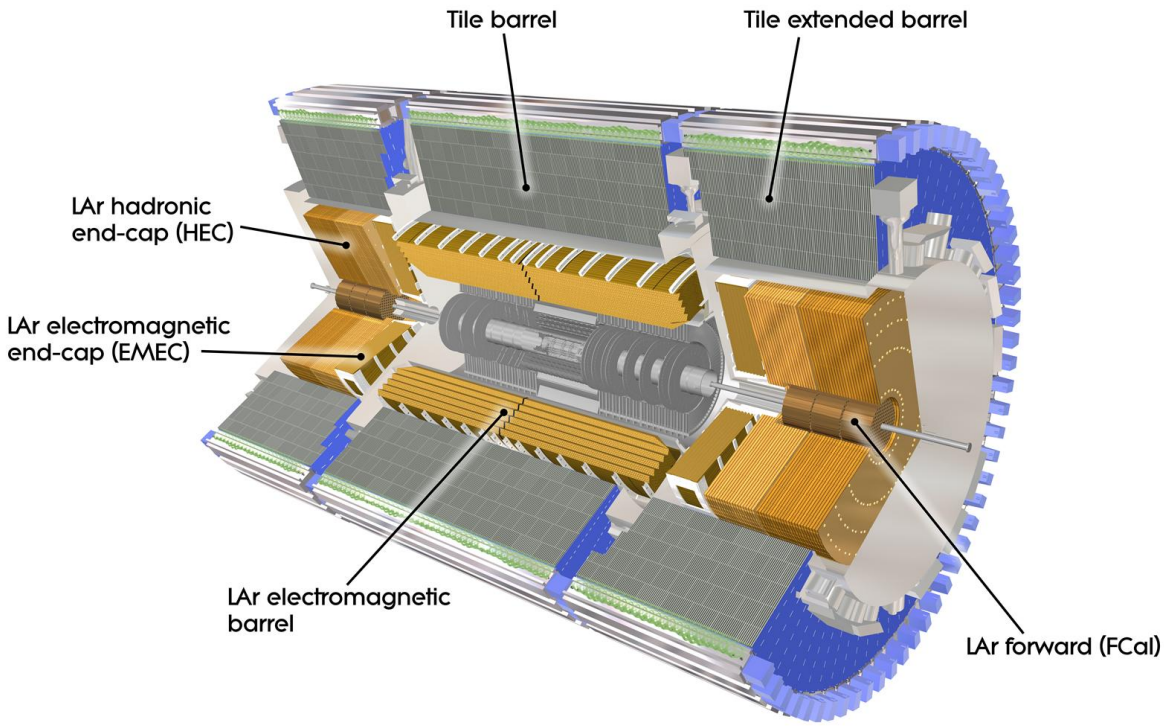


Figure 3.7: ATLAS calorimeter layout (ATLAS Experiment © 2014 CERN).

thickness roughly three times larger than the strip section. Finally, the back section has a granularity of $0.05 \times 0.025$ and a thickness varying between two and twelve times the radiation length.

In the ($|\eta| > 2.5$) region, the calorimeter is segmented in two sections and has a worse granularity by design. This lower resolution is sufficient to provide the measurements needed in the reconstruction of jets and the measuring of the missing transverse momentum.

#### Hadron calorimeter

A hadron calorimeter works on the same principle as the electromagnetic calorimeters, but the longitudinal development is determined by the average nuclear interaction length. The average nuclear interaction length is much larger than the average radiation length, which means that hadron calorimeters need to be much larger than their electromagnetic counterparts. Additionally, the thickness of a hadron calorimeter is a very important parameter, since it has to provide a good containment of hadronic showers and avoid punch-throughs into the next detector system.

The ATLAS hadron calorimeter covers a large pseudorapidity range ($|\eta| < 4.9$). It can be split in three components: the tile calorimeter, the end-cap calorimeters and the forward calorimeter.

The tile calorimeter, which covers the pseudorapidity $|\eta| < 1.7$ region, is a sampling calorimeter with a periodic structure in the z axis. The iron plates that act as absorbers have a thickness of 14 mm per period, while the scintillating tiles that act as active material have a thickness of 3 mm per period. This calorimeter is composed of one main barrel and two extended barrels. The main barrel covers the $|\eta| < 1.0$ region, while the extended barrels cover the $0.8 < |\eta| < 1.7$ region. All barrels are segmented in three layers. They are divided in sixty four modules in the azimuthal direction. In the pseudorapidity space, the readout cells are arranged such that the resulting granularity is $0.1 \times 0.1$ for the first two layers and $0.2 \times 0.1$ for the last layer.

Each end-cap calorimeter consists of two independent wheels covering the $1.5 < |\eta| < 3.2$ region. In this calorimeter, copper plates are used as absorbers while liquid argon is used as active material. Each wheel is built out of 32 identical modules, with a 2 mm gap between each module. The first wheel, the one closest to the interaction point, covers the pseudorapidity range $1.5 < |\eta| < 2.5$. It uses 25 mm copper plates and has a granularity of $0.1 \times 0.1$. The second wheel, which covers the $2.5 < |\eta| < 3.2$ region, uses 50 mm copper plates and has a granularity of $0.2 \times 0.2$.

The forward calorimeter covers the forward region, specifically in the pseudorapidity range $3.1 < |\eta| < 4.9$. Its design is particularly challenging due to the high levels of radiation that it must be able to withstand. The calorimeter is composed of three sections. The first one is made out of copper and the other two are made out of tungsten. In both cases, the active material is liquid argon and the granularity is roughly $0.2 \times 0.2$.

### 3.2.5 Muon spectrometer

Muons do not deposit too much energy in either calorimeter, so they can pass through them without too much energy loss. Therefore, it is useful to place a system that detects and measures muons after both calorimeters. Located after the hadron calorimeter, the muon spectrometer is the largest and outermost component of the ATLAS detector, contributing more than 80% of the volume of the whole detector (see Figure 3.8).

Its operation is based on the deflection of muons using a magnetic field. The information obtained by the muon spectrometer is combined with the tracker information in order to reconstruct the trajectory of muons through the detector. The charge and momentum can be determined using the curvature of the reconstructed trajectory inside the spectrometer.

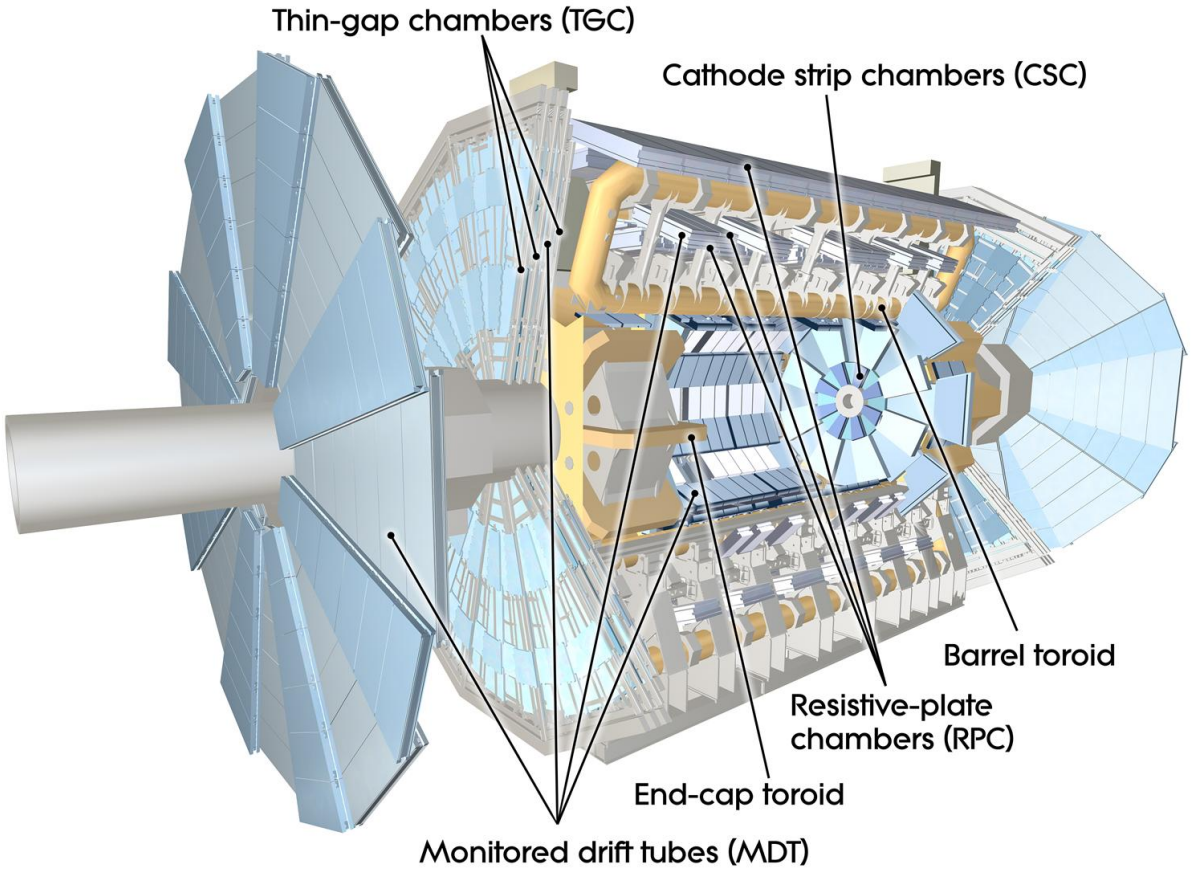


Figure 3.8: Components of the ATLAS muon spectrometer (ATLAS Experiment © 2014 CERN).

In the barrel region ($|\eta| < 1.0$), the magnetic field is provided by the superconducting air barrel toroid, while two end-cap magnets provide the magnetic field for the end-cap region ($1.4 < |\eta| < 2.7$). The magnetic field is located in the transition region ($1.0 < |\eta| < 1.4$) and is given by the combined fields of the large barrel toroid and the end-cap magnets.

The muon chamber uses four different technologies in its structure: monitored drift tube chambers, cathode strip chambers, resistive plate chambers and thin gap chambers. The monitored drift tube chambers provide a precise measurement of the coordinates of the tracks over most of the $\eta$ range. The first layer of the areas close to the interaction point and close to the beamline ($2.0 < |\eta| < 2.7$) is made of cathode strip chambers, which have higher-granularity, in order to withstand the demanding rate and background conditions. Resistive plate chambers are used in the barrel, while thin gap chambers are placed in the transition and end-cap regions (see Figure 3.9). These two last components are used in the trigger system, which covers the $|\eta| < 2.4$ range.

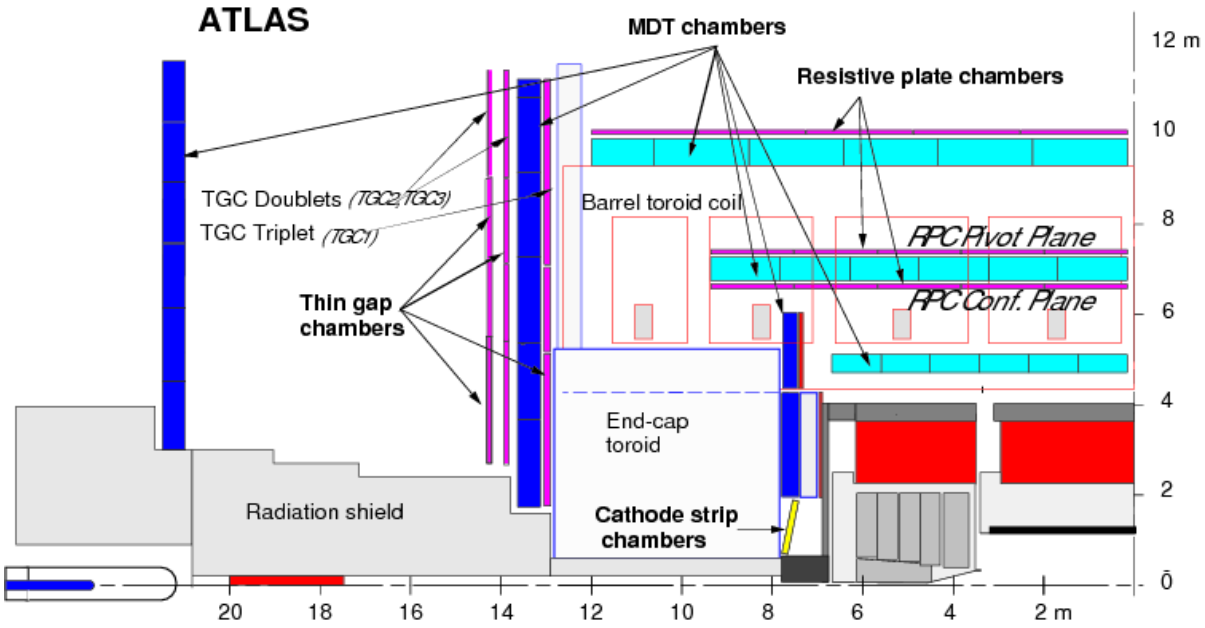


Figure 3.9: Muon chamber projection in the YZ plane [90].

### 3.2.6 Trigger and data acquisition system

The raw event production rate in ATLAS is several orders of magnitude higher than the ability of the detector to permanently store the event-related data. Furthermore, most events taking place in the collisions are not of interest. Therefore, a trigger system is necessary to quickly identify and select the events that are of interest, so that only such data are stored permanently.

The ATLAS trigger system is based on three levels of online selection, where each successive level refines the selection made by the previous level (see Figure 3.10).

The level 1 trigger reduces the number of events from an interaction rate of roughly 1 GHz to less than 50 kHz, using only the information provided by a subset of detectors. The muon spectrometer trigger searches for muons with high transverse momenta, which are identified using the trigger system of the muon spectrometer. The calorimeter trigger looks for high-momentum electrons and photons, tau hadronic decays, a large amount of missing transverse energy or a large scalar sum of jet transverse

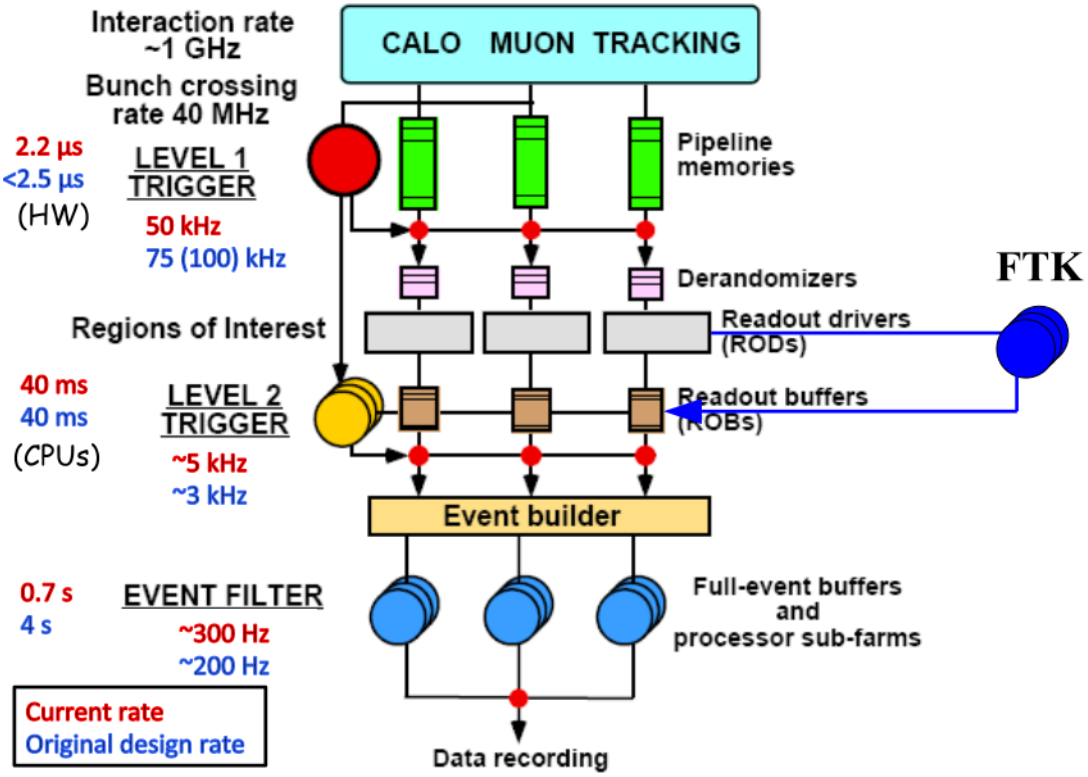


Figure 3.10: ATLAS trigger scheme [91].

energies using reduced-granularity information provided by both calorimeters. All the level 1 trigger processes are done in 2.2 µs, roughly 2000 times slower than the interaction rate.

The level 2 trigger uses the information provided by the level 1 trigger, which includes the position and transverse momentum of candidate objects and energy sums. Using this data, the level 2 trigger selectively accesses data from readout buffers in order to make a decision. In theory, this trigger is allowed to access the event data with full precision and granularity, but in practice only a small percentage of the full data is needed for a decision to be made, reducing the event rate to roughly 5 kHz.

The level 3 trigger is performed by the event filter and decides whether the data of an event will be written to the permanent mass storage. It employs offline algorithms and methods adapted to the online environment to confirm the decision of the level 2 trigger using more refined algorithms, the full set of data and, when necessary, tighter transverse momentum thresholds. This trigger reduces the event rate down to an event rate of roughly 300 Hz.

CHAPTER 4

# Data, simulation samples and data-driven methods

## 4.1 Data

The analyses presented in this thesis use two sets of data events, both taken from proton-proton collisions at the LHC with the ATLAS detector. The first set was taken in 2011 at a center-of-mass energy of 7 TeV and amounts to an integrated luminosity of 4.6 $fb^{-1}$ (uncertainty:1.8%) [92], while the second set was taken in 2012 at a higher center-of-mass energy (8 TeV) and the data collected correspond to an integrated luminosity of 20.3 $fb^{-1}$ (uncertainty:2.8%) [93]. The time evolution of the total integrated luminosity collected in ATLAS between 2011 and 2012 is shown in Figure 4.1 [94]. The 2011 and 2012 data are used in the top-quark mass and the $t\bar{t}Z$ cross-section measurement respectively.

Each year is split in periods in order to organize and separate different running conditions, such as trigger configurations, firmware versions or detector repairs. The 2011 data are composed of twelve periods taken between March 13$^{th}$ and October 30$^{th}$ [95] (see Table 4.1), while the 2012 data are separated in eleven periods taken between April 4$^{th}$ and December 16$^{th}$ [96] (see Table 4.2).

All events in data are required to have triggered the single electron or the single muon trigger. For the 2011 data, the electron trigger depends on the period, as follows:

- before period K: EF_e20_medium,
- period K: EF_e22_medium,
- periods L and M: EF_e22vh_medium1 or EF_e45_medium1.

Likewise, the muon trigger is period-dependent for 2011 data:

- before period J: EF_mu18,
- starting from period J: EF_mu18_medium.

For 2012 data, the same lepton triggers are used for all periods:

- Electron trigger: EF_e24vhi_medium1 or EF_e60_medium1.
- Muon trigger: EF_mu24i_tight or EF_mu36_tight.

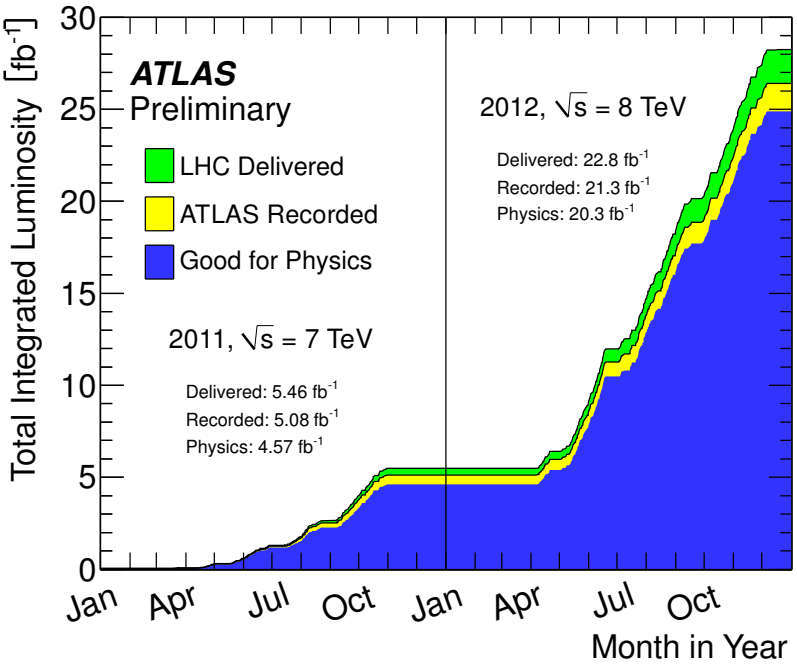


Figure 4.1: Time evolution of the total integrated luminosity collected in 2011 and 2012 [92–94].

| Data period | Date | Run number | Delivered luminosity ($pb^{-1}$) |
|---|---|---|---|
| A | March 13$^{th}$ to March 21$^{st}$ | 177531 - 177965 | 8.98 |
| B | March 21$^{st}$ to March 24$^{th}$ | 177986 - 178109 | 18 |
| D | April 14$^{th}$ to April 29$^{th}$ | 179710 - 180481 | 186 |
| E | April 30$^{th}$ to May 3$^{rd}$ | 180614 - 180776 | 52.7 |
| F | May 15$^{th}$ to May 25$^{th}$ | 182013 - 182519 | 160 |
| G | May 27$^{th}$ to June 14$^{th}$ | 182726 - 183462 | 572 |
| H | June 16$^{th}$ to June 28$^{th}$ | 183544 - 184169 | 287 |
| I | July 13$^{th}$ to July 29$^{th}$ | 185353 - 186493 | 416 |
| J | July 30$^{th}$ to August 4$^{th}$ | 186516 - 186755 | 240 |
| K | August 4$^{th}$ to August 22$^{nd}$ | 186873 - 187815 | 685 |
| L | September 7$^{th}$ to October 5$^{th}$ | 188902 - 190343 | 1625 |
| M | October 6$^{th}$ to October 30$^{th}$ | 190503 - 191933 | 1184 |

Table 4.1: Summary of the 2011 data periods [95].

The data are further filtered through one of the so-called Good Run Lists (GRL). The GRLs are created using information provided by the data quality flags, which are used to mark possible performance issues in the detectors, the combined performance objects or the trigger [97]. The events passing the GRL filter, shown in blue in Figure 4.1, are considered "good for physics" and used in ATLAS analyses.

## 4.2 Simulation

The data taken with the ATLAS detector must be compared with theoretical models in order to obtain new physics knowledge. To predict and compare a given physics theory with the measurements, Monte-Carlo (MC) simulations are used to model the backgrounds and the signal prediction under a given theory. Due to the probabilistic nature of particle physics processes, the MC simulations generate hypothetical events based on theoretical probability distributions in order to predict the expected statistical behavior of the events recorded by the detector.

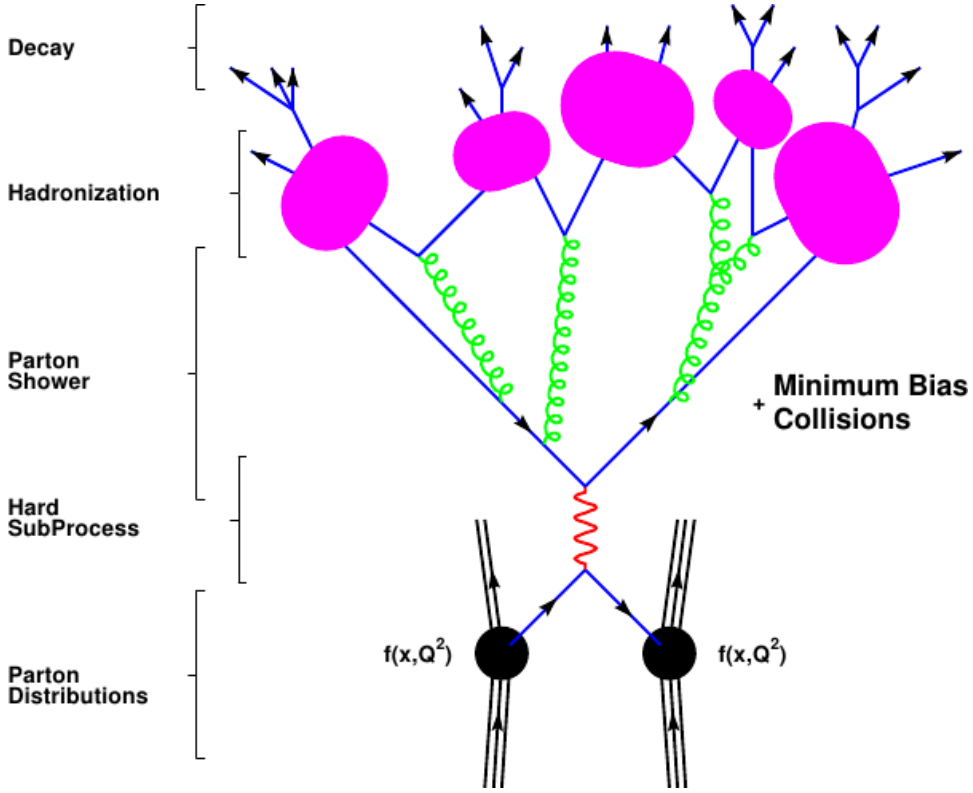


Figure 4.2: Scheme showing the parts of a MC simulation for hadron colliders [98].

Figure 4.2 shows a schematic view of the different components of a MC simulation for hadron colliders [98]: the parton distribution, the hard process (called hard subprocess in Figure 4.2), the parton shower and the hadronization.

In order to simulate a proton-proton collision, its parton distribution must be modeled, i.e., a parton must be resolved at scale $Q$ and momentum fraction $x$ for each proton. The phenomenology of the parton resolution is modeled by a set of parton distribution functions (PDF). All the MC simulations in this thesis use one of the following PDF sets: CT10 [99], CTEQ6.6 [100], CTEQ6L1 [101] or MSTW2008LO [102].

The hard process involves the tree-level processes taking place during the inelastic proton-proton collision. The so-called parton-level generators (also known as event generators) are used to simulate specific final states to the lowest order of perturbation theory. In other words, the event generators produce events associated with a given set of leading-order diagrams (e.g., $t\bar{t} \to 2\ell$, $Z \to 2\ell$, $t\bar{t}Z \to 4\ell$ and so on). A large number of parton-level generators is available, which can be separated in two groups: process-specific generators and arbitrary-process generators. Process-specific generators are only able to generate a limited list of processes, but are usually optimized to simulate these. In contrast, arbitrary-process generators are able to generate any tree-level Standard Model process, but the lack of optimization leads to higher computation times when compared to their process-specific counterparts. This can limit the degree of complexity and accuracy that the generated events can achieve due to pragmatic considerations. The process-specific generators used in the analyses presented in this thesis are ALPGEN [103] and ACERMC [104]. ALPGEN specializes in processes with high jet multiplicity in the final state, while ACERMC is dedicated to the Standard Model background processes taking place in proton-proton collisions in the LHC. In addition to these generators, the following arbitrary-process generators are used in this thesis: MADGRAPH [105], MC@NLO [106], POWHEG [107] and SHERPA [108].

The parton shower and the hadronization are provided by programs called showering and hadronization generators (SHG). The parton shower provides higher-order QCD effects, generating high-multiplicity partonic states called parton showers. These parton showers are composed of a number of particles, including many isolated color-carrying partons. Since isolated colored partons are not allowed due to color confinement, the hadronization process takes place, i.e., the colored partons are grouped to form color-neutral hadrons. In order to simulate a reasonable hadronization process using their limited models, SHG programs contain several non-physical parameters that need to be calibrated using experimental data. Each set of these calibration parameters is called a "tune". The SHGs (and their tunes) used in the analyses covered in this thesis are:

- HERWIG [109], using the tune AUET1 [110]. HERWIG is often interfaced with JIMMY [111] routines to generate multiple parton scattering processes.
- PYTHIA6 [112], tuned with either AUET2B [113] or PERUGIA P2011C [114].
- PYTHIA8 [115], using the tune AU2 [116].

Finally, it is important to notice that SHERPA has its own SHG and, therefore, does not need to be interfaced with one.

In order to simulate the detector response to each of the generated events, a GEANT4 [117, 118] simulation of the ATLAS detector is used on all the generated events. This process is performed either as a full simulation or as a fast simulation [119]. In a full simulation, any small structure that could affect traversing particles is simulated, independent of the origin of the structure. This approach gives the most accurate description of the process, but is computationally intensive. In contrast, a fast simulation uses parametrizations or a simplified approach to model the detector material and the response of the active detector components. This simplification leads to less accurate simulations, but lowers the requirements on computational power. Therefore, a fast simulation is usually used when a large number of generated events is required, since the processing time needed for a full simulation could be prohibitive.

In the rest of this section, all the processes are assumed to be modeled as a full simulation and all $t\bar{t}$ datasets mentioned are filtered to have at least one prompt lepton[1], unless explicitly stated otherwise.

[1] Prompt leptons are leptons originating from the hard process.

### 4.2.1 MC simulation datasets used for the top-quark mass measurement

The nominal $t\bar{t}$ signal sample is generated using the MC@NLO event generator using the PDF set CTEQ6.6, interfaced with HERWIG using the tune AUET1. In order to measure the top-quark mass, ten fast simulation samples are generated by the same combination of generators, each using a different input top-quark mass, ranging from 150 GeV to 200 GeV.

To estimate the systematic uncertainty associated with the event generator and the SHG, three additional $t\bar{t}$ fast simulation datasets are generated: MC@NLO interfaced with HERWIG, POWHEG interfaced with HERWIG and POWHEG interfaced with PYTHIA6. Another eight fast simulation datasets are generated with ACERMC as event generator and PYTHIA6 as SHG. They are used to estimate the systematic uncertainty due to the modeling of the initial and final state radiation (ISR/FSR), color reconnection (CR) and underlying events (UE). Table 4.3 shows all the $t\bar{t}$ datasets used in the top-quark mass measurement. A detailed description of the estimation of the systematic uncertainty will be given in a later chapter.

The $t\bar{t}$ dilepton channel signal used in the analysis has a signature of exactly two leptons. Therefore, Standard Model background processes that produce two prompt leptons are considered (see Figure 4.3), namely, $Z$ + jets events, $Wt$-channel of the single-top production and diboson events. The generation of diboson events ($WW$, $WZ$, $ZZ$) used ALPGEN with the PDF set CTEQ6L1 and hadronized with HERWIG (see Table 4.4). The Drell-Yan processes are modeled using ALPGEN with the PDF set CTEQ6L1 and hadronized with HERWIG, produced in the phase spaces corresponding to 10 GeV $< m_{\ell\ell} <$ 40 GeV (see Table 4.5) and 40 GeV $< m_{\ell\ell} <$ 2000 GeV (see Table 4.6) separately. The single top $Wt$-channel is modeled with MC@NLO interfaced with HERWIG (see Table 4.4).

Processes with less than two prompt leptons are not modeled with MC simulations, since their modeling of fake leptons[2] is not considered reliable. Instead, the contribution of this process is estimated using the data driven methods described at the end of this chapter. Processes with more than two leptons are not considered (except for diboson events), since their contribution is negligible.

### 4.2.2 MC simulation datasets used for the $t\bar{t}Z$ cross section measurement

As stated in the introduction, the $t\bar{t}Z$ cross section measurement is done in the $t\bar{t}Z \to 4\ell$ channel (see Figure 4.4). The signal $t\bar{t}Z$ process is modeled using a fast simulation sample generated with MADGRAPH (with CTEQ6L1 as PDF) and interfaced to PYTHIA6 tuned with AUET2B. A filter is applied to only allow events with at least one lepton.

Analogously to the top-quark mass measurement datasets, only the MC background processes that produce four prompt leptons are considered: $ZZ$, $t\bar{t}H$, $H \to ZZ$, $t\bar{t}t\bar{t}$, $t\bar{t}WW$, tribosons and $WtZ$ (see Figure 4.5).

The diboson $ZZ \to 4\ell$ process is modeled with SHERPA using the PDF set CT10 and considering massive $c$ and $b$ quarks, where the detector response is simulated with a fast simulation. The $t\bar{t}H$ background modeling used POWHEG with the PDF set CT10, interfaced to PYTHIA8 tuned with AU2. The $H \to ZZ$ background is modeled by POWHEG using the PDF set CTEQ6L1, with PYTHIA8 used as its SHG (tuned using AU2). The simulation of the $t\bar{t}t\bar{t}$ background is performed by MADGRAPH interfaced to the PDF set MSTW2008LO, where the hadronization and parton showering are simulated using PYTHIA8 with the AU2 tune. The $WtZ$, $t\bar{t}WW$ and tribosons backgrounds are modeled using MADGRAPH as event generator, CTEQ6L1 as PDF and PYTHIA6 (tuned with AUET2B) as SHG. Table 4.7 summarizes all the MC datasets used in the $t\bar{t}Z$ cross section measurement presented in this thesis.

[2] Fake leptons are objects misidentified as prompt leptons by the reconstruction algorithm.

| Data period | Date | Run number | Delivered luminosity ($pb^{-1}$) |
|---|---|---|---|
| A | April 4$^{th}$ to April 20$^{th}$ | 200804 - 201556 | 910 |
| B | May 1$^{st}$ to June 18$^{th}$ | 202660 - 205113 | 5594 |
| C | July 1$^{st}$ to July 24$^{th}$ | 206248 - 207397 | 1643 |
| D | July 24$^{th}$ to August 23$^{rd}$ | 207447 - 209025 | 3598 |
| E | August 23$^{rd}$ to September 17$^{th}$ | 209074 - 210308 | 2863 |
| G | September 26$^{th}$ to October 8$^{th}$ | 211522 - 212272 | 1404 |
| H | October 13$^{th}$ to October 26$^{th}$ | 212619 - 213359 | 1655 |
| I | October 26$^{th}$ to November 2$^{nd}$ | 213431 - 213819 | 1149 |
| J | November 2$^{nd}$ to November 26$^{th}$ | 213900 - 215091 | 2941 |
| L | November 30$^{th}$ to December 6$^{th}$ | 215414 - 215643 | 983 |
| M | December 15$^{th}$ to December 16$^{th}$ | 216399 - 216432 | 13.8 |

Table 4.2: Summary of the 2012 data periods [96].

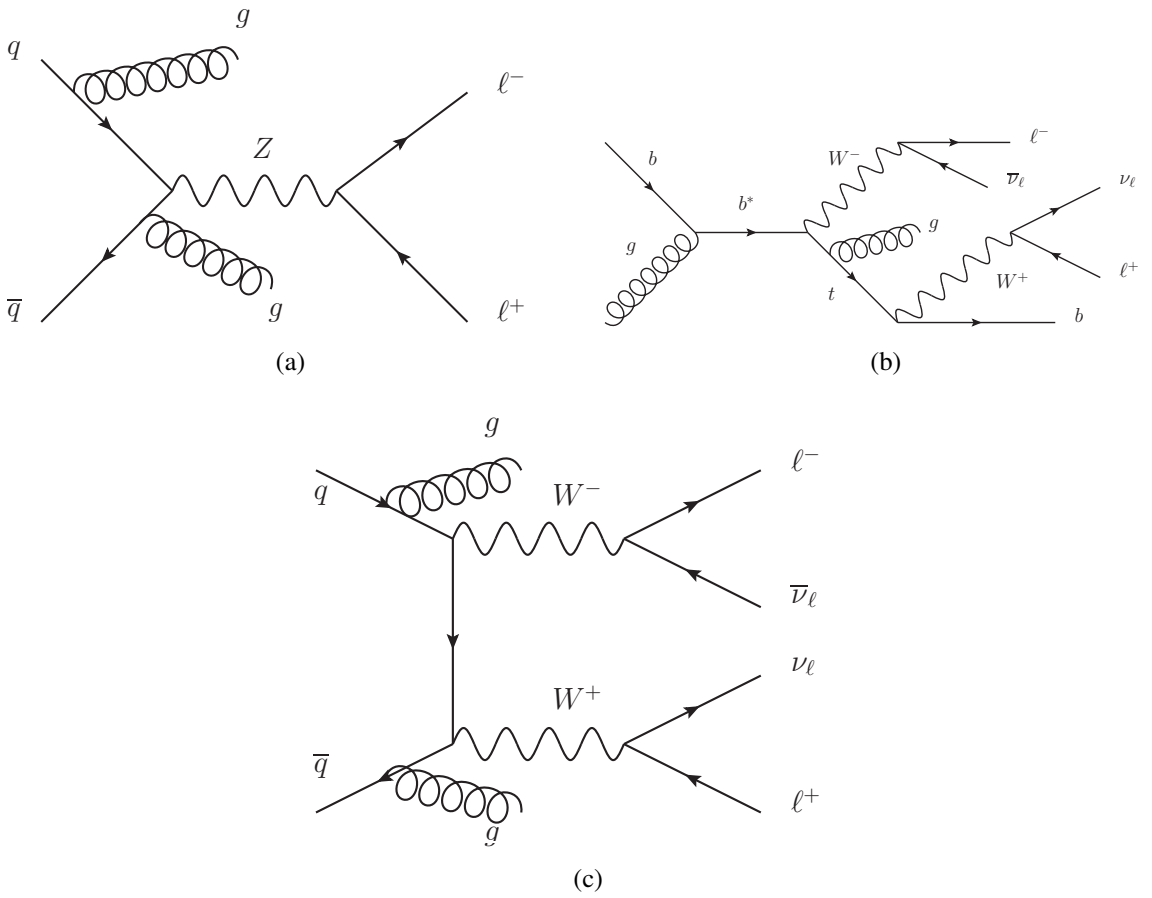


Figure 4.3: Main backgrounds for the $t\bar{t}$ dilepton channel: (a) $Z$+jets, (b) $Wt$-channel of the single-top production, and (c) Diboson ($WW$ channel is shown).

| Dataset number | Description | Event generator+SHG | $\sigma_{\text{NLO}}$ (pb) | Events $\mathcal{L}$ (fb$^{-1}$) | Sim. type |
|---|---|---|---|---|---|
| 105200 | Nominal sample | MC@NLO+Herwig | 89.7 | 127.9 | full |
| 105200 | Generator syst. variation | MC@NLO+Herwig | 89.7 | 127.9 | fast |
| 105860 | Generator syst. variation | Powheg+Herwig | 89.4 | 16.5 | fast |
| 105861 | Generator syst. variation | Powheg+Pythia6 | 89.4 | 110.3 | fast |
| 117209 | ISR/FSR syst. variation | AcerMC+Pythia6 | 90.5 | 110.4 | fast |
| 117210 | ISR/FSR syst. variation | AcerMC+Pythia6 | 90.6 | 110.2 | fast |
| 117240 | CR syst. variation | AcerMC+Pythia6 | 89.2 | 110.3 | fast |
| 117241 | CR syst. variation | AcerMC+Pythia6 | 89.3 | 110.4 | fast |
| 117242 | CR syst. variation | AcerMC+Pythia6 | 89.3 | 110.4 | fast |
| 117243 | CR syst. variation | AcerMC+Pythia6 | 89.3 | 110.4 | fast |
| 117403 | UE syst. variation | AcerMC+Pythia6 | 90.6 | 110.3 | fast |
| 117404 | UE syst. variation | AcerMC+Pythia6 | 90.7 | 109.8 | fast |
| 117208 | $m_{\text{top}}^{MC} = 150.0$ GeV | MC@NLO+Herwig | 185.4 | 41.9 | fast |
| 106203 | $m_{\text{top}}^{MC} = 160.0$ GeV | MC@NLO+Herwig | 133.5 | 29.2 | fast |
| 106208 | $m_{\text{top}}^{MC} = 165.0$ GeV | MC@NLO+Herwig | 114.0 | 34.2 | fast |
| 106205 | $m_{\text{top}}^{MC} = 167.5$ GeV | MC@NLO+Herwig | 105.5 | 74.1 | fast |
| 106201 | $m_{\text{top}}^{MC} = 170.0$ GeV | MC@NLO+Herwig | 97.7 | 40.1 | fast |
| 106206 | $m_{\text{top}}^{MC} = 175.0$ GeV | MC@NLO+Herwig | 84.0 | 46.4 | fast |
| 106207 | $m_{\text{top}}^{MC} = 177.5$ GeV | MC@NLO+Herwig | 78.0 | 100.4 | fast |
| 106202 | $m_{\text{top}}^{MC} = 180.0$ GeV | MC@NLO+Herwig | 72.5 | 53.1 | fast |
| 106204 | $m_{\text{top}}^{MC} = 190.0$ GeV | MC@NLO+Herwig | 54.6 | 71.8 | fast |
| 117205 | $m_{\text{top}}^{MC} = 200.0$ GeV | MC@NLO+Herwig | 41.5 | 183.2 | fast |

Table 4.3: $t\bar{t}$ datasets used in the top-quark mass measurement.

| Dataset number | Description | Event generator+SHG | $\sigma_{\text{NLO}}$ (pb) | Events $\mathcal{L}$ (fb$^{-1}$) | Sim. type |
|---|---|---|---|---|---|
| 105985 | $WW$ | Alpgen+Herwig | 17.0 | 146.2 | full |
| 105986 | $ZZ$ | Alpgen+Herwig | 1.3 | 197.8 | full |
| 105987 | $WZ$ | Alpgen+Herwig | 5.5 | 180.4 | full |
| 108346 | $Wt$ | MC@NLO+Herwig | 50.6 | 16.0 | full |

Table 4.4: Diboson and single top datasets used in the top-quark mass measurement.

| Dataset number | Description | Event generator+SHG | $\sigma_{\text{NLO}}$ (pb) | Events $\mathcal{L}$ (fb$^{-1}$) | Sim. type |
|---|---|---|---|---|---|
| 116250 | $Z \to ee$ + 0 partons | ALPGEN+HERWIG | 3819.0 | 0.3 | full |
| 116251 | $Z \to ee$ + 1 parton | ALPGEN+HERWIG | 106.1 | 2.8 | full |
| 116252 | $Z \to ee$ + 2 partons | ALPGEN+HERWIG | 51.8 | 19.3 | full |
| 116253 | $Z \to ee$ + 3 partons | ALPGEN+HERWIG | 10.5 | 14.3 | full |
| 116254 | $Z \to ee$ + 4 partons | ALPGEN+HERWIG | 2.4 | 17.3 | full |
| 116255 | $Z \to ee$ + 5 partons | ALPGEN+HERWIG | 0.6 | 17.4 | full |
| 116260 | $Z \to \mu\mu$ + 0 partons | ALPGEN+HERWIG | 3818.6 | 0.3 | full |
| 116261 | $Z \to \mu\mu$ + 1 parton | ALPGEN+HERWIG | 106.1 | 2.8 | full |
| 116262 | $Z \to \mu\mu$ + 2 partons | ALPGEN+HERWIG | 51.9 | 19.3 | full |
| 116263 | $Z \to \mu\mu$ + 3 partons | ALPGEN+HERWIG | 10.5 | 14.3 | full |
| 116264 | $Z \to \mu\mu$ + 4 partons | ALPGEN+HERWIG | 2.4 | 17.3 | full |
| 116265 | $Z \to \mu\mu$ + 5 partons | ALPGEN+HERWIG | 0.6 | 17.4 | full |
| 116270 | $Z \to \tau\tau$ + 0 partons | ALPGEN+HERWIG | 3818.9 | 0.3 | full |
| 116271 | $Z \to \tau\tau$ + 1 parton | ALPGEN+HERWIG | 106.1 | 2.8 | full |
| 116272 | $Z \to \tau\tau$ + 2 partons | ALPGEN+HERWIG | 51.9 | 9.6 | full |
| 116273 | $Z \to \tau\tau$ + 3 partons | ALPGEN+HERWIG | 10.5 | 14.4 | full |
| 116274 | $Z \to \tau\tau$ + 4 partons | ALPGEN+HERWIG | 2.4 | 17.3 | full |
| 116275 | $Z \to \tau\tau$ + 5 partons | ALPGEN+HERWIG | 0.6 | 17.4 | full |

Table 4.5: Drell-Yan datasets (10 GeV $< m_{\ell\ell} <$ 40 GeV) used in the top-quark mass measurement.

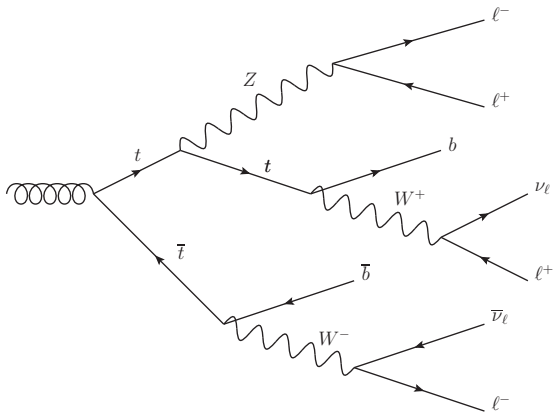


Figure 4.4: $t\bar{t}Z \to 4\ell$ channel.

| Dataset number | Description | Event generator+SHG | $\sigma_{\text{NLO}}$ (pb) | Events $\mathcal{L}$ (fb$^{-1}$) | Sim. type |
|---|---|---|---|---|---|
| 107650 | $Z \to ee$ + 0 partons | Alpgen+Herwig | 835.4 | 7.9 | full |
| 107651 | $Z \to ee$ + 1 parton | Alpgen+Herwig | 168.0 | 8.0 | full |
| 107652 | $Z \to ee$ + 2 partons | Alpgen+Herwig | 50.6 | 16.0 | full |
| 107653 | $Z \to ee$ + 3 partons | Alpgen+Herwig | 14.0 | 15.8 | full |
| 107654 | $Z \to ee$ + 4 partons | Alpgen+Herwig | 3.6 | 16.7 | full |
| 107655 | $Z \to ee$ + 5 partons | Alpgen+Herwig | 1.0 | 19.3 | full |
| 107660 | $Z \to \mu\mu$ + 0 partons | Alpgen+Herwig | 835.9 | 7.9 | full |
| 107661 | $Z \to \mu\mu$ + 1 parton | Alpgen+Herwig | 167.6 | 8.0 | full |
| 107662 | $Z \to \mu\mu$ + 2 partons | Alpgen+Herwig | 50.4 | 8.0 | full |
| 107663 | $Z \to \mu\mu$ + 3 partons | Alpgen+Herwig | 14.0 | 7.9 | full |
| 107664 | $Z \to \mu\mu$ + 4 partons | Alpgen+Herwig | 3.5 | 8.7 | full |
| 107665 | $Z \to \mu\mu$ + 5 partons | Alpgen+Herwig | 1.0 | 10.4 | full |
| 107670 | $Z \to \tau\tau$ + 0 partons | Alpgen+Herwig | 835.5 | 12.7 | full |
| 107671 | $Z \to \tau\tau$ + 1 parton | Alpgen+Herwig | 168.5 | 19.8 | full |
| 107672 | $Z \to \tau\tau$ + 2 partons | Alpgen+Herwig | 50.5 | 19.9 | full |
| 107673 | $Z \to \tau\tau$ + 3 partons | Alpgen+Herwig | 14.1 | 36.3 | full |
| 107674 | $Z \to \tau\tau$ + 4 partons | Alpgen+Herwig | 3.5 | 41.6 | full |
| 107675 | $Z \to \tau\tau$ + 5 partons | Alpgen+Herwig | 1.0 | 46.8 | full |

Table 4.6: Drell-Yan datasets (40 GeV $< m_{\ell\ell} <$ 2 TeV) used in the top-quark mass measurement.

| Dataset number | Description | Event generator+SHG | $\sigma_{\text{NLO}}$ (fb) | Events $\mathcal{L}$ (ab$^{-1}$) | Sim. type |
|---|---|---|---|---|---|
| 117489 | $t\bar{t}Z$+0 partons | MadGraph+Pythia6 | 67.5 | 44.5 | fast |
| 117490 | $t\bar{t}Z$+1 partons(incl.) | MadGraph+Pythia6 | 17.6 | 33.8 | fast |
| 189608 | $ZZ \to 4\ell$ | Sherpa | 8650 | 2.3 | fast |
| 167007 | tribosons($ZWW$) | MadGraph+Pythia6 | 1.56 | 32.2 | full |
| 167008 | tribosons($ZZZ$) | MadGraph+Pythia6 | 0.33 | 150.4 | full |
| 160155 | $H \to ZZ$ | Powheg+Pythia8 | 5.39 | 37.1 | full |
| 158344 | $t\bar{t}t\bar{t}$ | MadGraph+Pythia8 | 0.68 | 291.9 | full |
| 169889 | $t\bar{t}H$ | Powheg+Pythia8 | 13.6 | 73.7 | full |
| 119583 | $t\bar{t}WW$ | MadGraph+Pythia6 | 1.90 | 5.3 | full |
| 179991 | $WtZ$ | MadGraph+Pythia6 | 4.13 | 24.2 | full |

Table 4.7: MC datasets used in the $t\bar{t}Z$ cross section measurement.

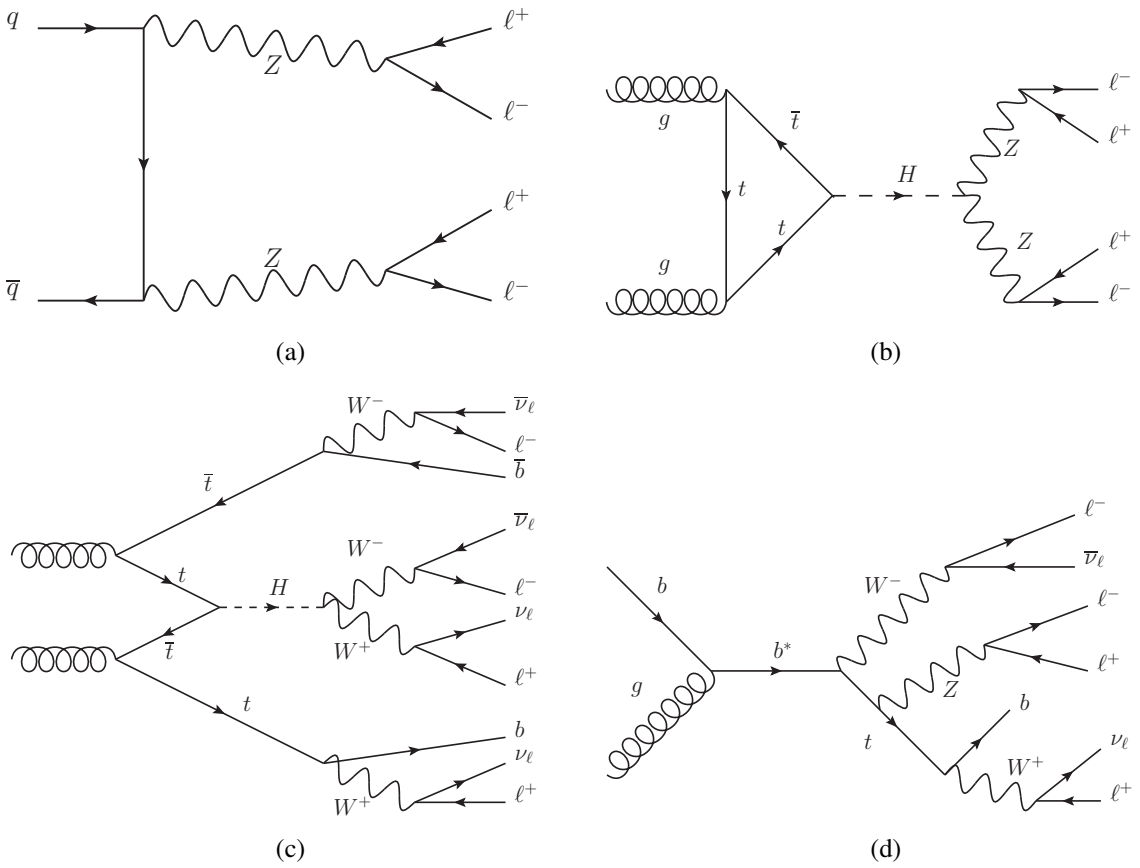


Figure 4.5: Main backgrounds for the $t\bar{t}Z \to 4\ell$ channel:(a) $ZZ \to 4\ell$, (b) $H \to ZZ \to 4\ell$, (c) $t\bar{t}H \to 4\ell + 4\nu + b\bar{b}$, and (d) $WtZ$ $4\ell$ channel.

## 4.3 Background estimation using data-driven methods

### 4.3.1 Events with fake leptons and the need for data-driven methods

A fake lepton is an object that is misidentified as a prompt lepton. In the case of fake electrons, they can arise from different sources such as the semileptonic decays of the bottom or the charm quark, photon conversion, jets with a large electromagnetic energy component and the misidentification of photons or pions as electrons. In the case of fake muons, they originate mainly from the semileptonic decays of the bottom or the charm quark, and the decay of charged hadrons or particles from highly energetic hadronic showers that manage to pass through the hadronic calorimeter into the muon chambers.

Events with at least one fake lepton (called fake lepton events) can be a significant source of background. Therefore, an accurate description of this process is needed. Unfortunately, the MC simulations introduced in the previous section are unable to produce a precise estimation of the behavior of fake lepton events due to either technical or pragmatic reasons and, therefore, data-driven methods are used instead. These data-driven methods derive their results from data events, usually making assumptions about the behavior of the fake leptons and are sometimes assisted with results from MC simulations.

In the top-quark mass and the $t\bar{t}Z$ cross section analyses, the matrix method [120] and the ABCD method are the two data-driven methods used to estimate the fake lepton events contribution respectively.

### 4.3.2 The matrix method

The matrix method is discussed in detail in Ref. [120]. For the sake of clarity, the matrix method will be discussed for a single-lepton selection. Then, the discussion will be extended to a dilepton selection.

The basic idea behind the matrix method is to build two definitions of each lepton type, named loose definition (L) and tight definition (T). The tight definition is chosen to be the same one as the lepton definition used in the analysis, while the loose definition is defined in such a way that it encompasses the tight definition, i.e., any lepton passing the tight definition will also pass the loose definition.

For the sake of argumentation, a selection that requires exactly one lepton is assumed. Then, the following quantities can be defined:

- $N^{\mathrm{L}}$: number of "loose events", defined as the number of events selected using the loose lepton definition that would not pass the tight lepton definition.
- $N^{\mathrm{T}}$: number of "tight events", defined as the number of events selected using the tight lepton definition.
- $N^{\mathrm{A}}$: number of "all" (loose plus tight) events, i.e., number of events selected using the loose or tight lepton definition.
- $N_{\mathrm{R}}^{\mathrm{L}}$: number of loose events, where the selected lepton is a real lepton[3].
- $N_{\mathrm{R}}^{\mathrm{T}}$: number of tight events, where the selected lepton is a real lepton.
- $N_{\mathrm{R}}^{\mathrm{A}}$: number of all events, where the selected lepton is a real lepton.
- $N_{\mathrm{F}}^{\mathrm{L}}$: number of loose events, where the selected lepton is a fake lepton.
- $N_{\mathrm{F}}^{\mathrm{T}}$: number of tight events, where the selected lepton is a fake lepton.

[3] The term *real lepton* is used to identify a prompt lepton, as opposed of a *fake lepton*.

- $N_{\mathrm{F}}^{\mathrm{A}}$: number of all events, where the selected lepton is a fake lepton.

Since, by definition, a selected event can be either loose or tight, the following statement is always true:

$$N^{\mathrm{T}} = N_{\mathrm{R}}^{\mathrm{T}} + N_{\mathrm{F}}^{\mathrm{T}} = \frac{N_{\mathrm{R}}^{\mathrm{T}}}{N_{\mathrm{R}}^{\mathrm{A}}} N_{\mathrm{R}}^{\mathrm{A}} + \frac{N_{\mathrm{F}}^{\mathrm{T}}}{N_{\mathrm{F}}^{\mathrm{A}}} N_{\mathrm{F}}^{\mathrm{A}} = r N_{\mathrm{R}}^{\mathrm{A}} + f N_{\mathrm{F}}^{\mathrm{A}}, \tag{4.1}$$

where $r$ and $f$ are defined as the rates:

$$\begin{aligned} r &\equiv \frac{N_{\mathrm{R}}^{\mathrm{T}}}{N_{\mathrm{R}}^{\mathrm{A}}}, \\ f &\equiv \frac{N_{\mathrm{F}}^{\mathrm{T}}}{N_{\mathrm{F}}^{\mathrm{A}}}. \end{aligned} \tag{4.2}$$

A second equation can be written for $N^{\mathrm{L}}$:

$$N^{\mathrm{L}} = N_{\mathrm{R}}^{\mathrm{L}} + N_{\mathrm{F}}^{\mathrm{L}} = (N_{\mathrm{R}}^{\mathrm{A}} - N_{\mathrm{R}}^{\mathrm{T}}) + (N_{\mathrm{F}}^{\mathrm{A}} - N_{\mathrm{F}}^{\mathrm{T}}) = (1 - r)\, N_{\mathrm{R}}^{\mathrm{A}} + (1 - f)\, N_{\mathrm{F}}^{\mathrm{A}}. \tag{4.3}$$

Equation 4.1 and Equation 4.3 can be represented by the matrix equation:

$$\begin{pmatrix} N^{\mathrm{T}} \\ N^{\mathrm{L}} \end{pmatrix} = \begin{pmatrix} r & f \\ 1 - r & 1 - f \end{pmatrix} \begin{pmatrix} N_{\mathrm{R}}^{\mathrm{A}} \\ N_{\mathrm{F}}^{\mathrm{A}} \end{pmatrix}. \tag{4.4}$$

Inverting the $2 \times 2$ matrix solves the system of equations:

$$\begin{pmatrix} N_{\mathrm{R}}^{\mathrm{A}} \\ N_{\mathrm{F}}^{\mathrm{A}} \end{pmatrix} = \frac{1}{r - f} \begin{pmatrix} 1 - f & -f \\ r - 1 & r \end{pmatrix} \begin{pmatrix} N^{\mathrm{T}} \\ N^{\mathrm{L}} \end{pmatrix}. \tag{4.5}$$

In particular, the solution for $N_{\mathrm{F}}^{\mathrm{A}}$ is of interest:

$$N_{\mathrm{F}}^{\mathrm{A}} = \frac{1}{r - f} \left[ (r - 1)\, N^{\mathrm{T}} + r N^{\mathrm{L}} \right] = \frac{r - 1}{r - f} N^{\mathrm{T}} + \frac{r}{r - f} N^{\mathrm{L}}, \tag{4.6}$$

which can be combined with Equation 4.2 to give:

$$N_{\mathrm{F}}^{\mathrm{T}} = f N_{\mathrm{F}}^{\mathrm{A}} = f \frac{r - 1}{r - f} N^{\mathrm{T}} + f \frac{r}{r - f} N^{\mathrm{L}}. \tag{4.7}$$

Equation 4.7 can be used to provide an estimate for the number of fake lepton events using the tight lepton selection in a given single lepton selection. This is accomplished by measuring the values of $N^{\mathrm{T}}$ and $N^{\mathrm{L}}$ in data, provided that the quantities $f$ and $r$ are known.

The estimation of $f$ and $r$ is performed in control regions dominated by fake and real lepton events respectively. In a region dominated by fake lepton events, $f$ can be estimated using (the process is analogous for $r$):

$$f = \frac{N_{\mathrm{F}}^{\mathrm{T}}}{N_{\mathrm{F}}^{\mathrm{A}}} \approx \frac{N^{\mathrm{T}}}{N^{\mathrm{A}}}. \tag{4.8}$$

For a selection with exactly two leptons, where the leptons have been ordered by their transverse

momentum, Equation 4.4 is expanded into:

$$\begin{pmatrix} N^{\mathrm{TT}} \\ N^{\mathrm{TL}} \\ N^{\mathrm{LT}} \\ N^{\mathrm{LL}} \end{pmatrix} = \begin{pmatrix} r_1 r_2 & r_1 f_2 & f_1 r_2 & f_1 f_2 \\ r_1 (1-r_2) & r_1 (1-f_2) & f_1 (1-r_2) & f_1 (1-f_2) \\ (1-r_1) r_2 & (1-r_1) f_2 & (1-f_1) r_2 & (1-f_1) f_2 \\ (1-r_1)(1-r_2) & (1-r_1)(1-f_2) & (1-f_1)(1-r_2) & (1-f_1)(1-f_2) \end{pmatrix} \begin{pmatrix} N^{\mathrm{AA}}_{\mathrm{RR}} \\ N^{\mathrm{AA}}_{\mathrm{RF}} \\ N^{\mathrm{AA}}_{\mathrm{FR}} \\ N^{\mathrm{AA}}_{\mathrm{FF}} \end{pmatrix}, \tag{4.9}$$

where $N$ has two superscripts and two subscripts. The first superscript-subscript set refers to the first lepton, while the second superscript-subscript set refers to the second lepton. In the same way, $r_1$ and $f_1$ refer to the first lepton, while $r_2$ and $f_2$ refer to the second lepton.

Inverting the matrix in Equation 4.9 gives:

$$\begin{pmatrix} N^{\mathrm{AA}}_{\mathrm{RR}} \\ N^{\mathrm{AA}}_{\mathrm{RF}} \\ N^{\mathrm{AA}}_{\mathrm{FR}} \\ N^{\mathrm{AA}}_{\mathrm{FF}} \end{pmatrix} = \alpha \begin{pmatrix} (1-f_1)(1-f_2) & (f_1-1) f_2 & f_1 (f_2-1) & f_1 f_2 \\ (f_1-1)(1-r_2) & (1-f_1) r_2 & f_1 (1-r_2) & -f_1 r_2 \\ (r_1-1)(1-f_2) & (1-r_1) f_2 & r_1 (1-f_2) & -r_1 f_2 \\ (1-r_1)(1-r_2) & (r_1-1) r_2 & r_1 (r_2-1) & r_1 r_2 \end{pmatrix} \begin{pmatrix} N^{\mathrm{TT}} \\ N^{\mathrm{TL}} \\ N^{\mathrm{LT}} \\ N^{\mathrm{LL}} \end{pmatrix}, \tag{4.10}$$

where:

$$\alpha = \frac{1}{(r_1 - f_1)(r_2 - f_2)} \tag{4.11}$$

Using the two-leptons equation equivalent of Equation 4.2, the estimate of the number of fake lepton events using the tight selection is:

$$\begin{aligned} N^{\mathrm{TT}}_{\mathrm{F}} =& r_1 f_2 N^{\mathrm{AA}}_{\mathrm{RF}} + f_1 r_2 N^{\mathrm{AA}}_{\mathrm{FR}} + f_1 f_2 N^{\mathrm{AA}}_{\mathrm{FF}} \\ =& \alpha r_1 f_2 \left[ (f_1 - 1)(1 - r_2) N^{\mathrm{TT}} + (1 - f_1) r_2 N^{\mathrm{TL}} + f_1 (1 - r_2) N^{\mathrm{LT}} - f_1 r_2 N^{\mathrm{LL}} \right] \\ &+ \alpha f_1 r_2 \left[ (r_1 - 1)(1 - f_2) N^{\mathrm{TT}} + (1 - r_1) f_2 N^{\mathrm{TL}} + r_1 (1 - f_2) N^{\mathrm{LT}} - r_1 f_2 N^{\mathrm{LL}} \right] \\ &+ \alpha f_1 f_2 \left[ (1 - r_1)(1 - r_2) N^{\mathrm{TT}} + (r_1 - 1) r_2 N^{\mathrm{TL}} + r_1 (r_2 - 1) N^{\mathrm{LT}} + r_1 r_2 N^{\mathrm{LL}} \right]. \end{aligned} \tag{4.12}$$

The determination of the electron and muon real and fake efficiencies for 2011 data is documented in Ref. [121]. The main results that are of interest for the use of the matrix method in the $t\bar{t}$ dilepton channel are presented in the following paragraphs, where it is assumed that $r_1 = r_2$ and $f_1 = f_2$. The loose and tight lepton definitions used are presented in Section 5.1.2 and Section 5.2.2.

The electron real efficiency is measured in the $Z \to ee$ channel using a tag and probe method for different regions of the electron $\eta$ and $p_{\mathrm{T}}$ space (see Figure 4.6). The electron fake efficiency is measured in a region with exactly one loose electron, at least one jet and $E_{\mathrm{T}}^{\mathrm{miss}} < 20$ GeV. To account for the contamination from real electrons, the number of loose and tight events in data are corrected using the estimates obtained from MC simulations of $t\bar{t}$, single top, $Z$ + jets, $W$ + jets and diboson processes. The final efficiencies are shown in Figure 4.7 for different $\eta$ and $p_{\mathrm{T}}$ regions.

The measurement of the muon real efficiency is analogous to its electron counterpart, using the $Z \to \mu\mu$ channel and a tag and probe method. The muon fake efficiency is determined in a $\mu$+jets region with $m_{\mathrm{T}}(W) < 20$ GeV and the inverted triangular cut defined by $E_{\mathrm{T}}^{\mathrm{miss}} + m_{\mathrm{T}}(W) < 60$ GeV. The resulting muon real and fake efficiencies are shown in Figure 4.8 as a function of the muon $\eta$.

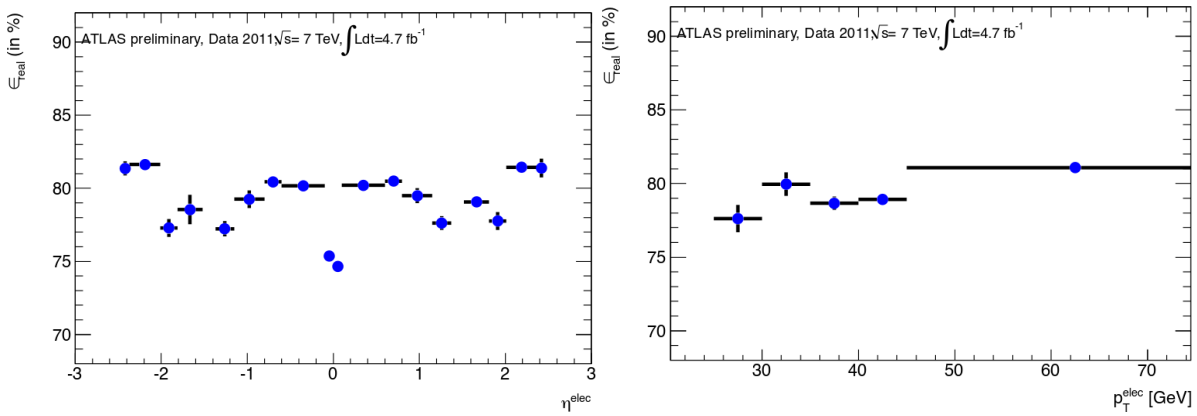


Figure 4.6: Electron real efficiency dependence on $\eta$ and $p_{\mathrm{T}}$ [121].

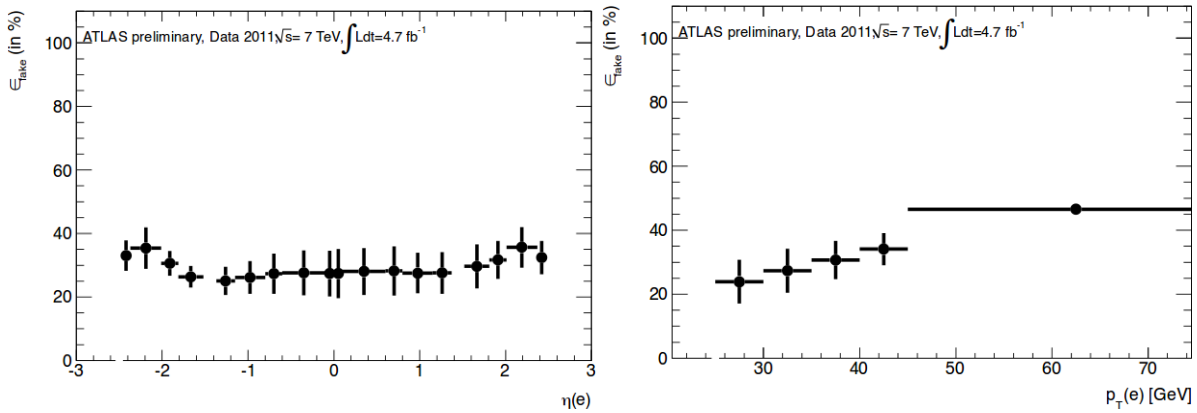


Figure 4.7: Electron fake efficiency dependence on $\eta$ and $p_{\mathrm{T}}$ [121].

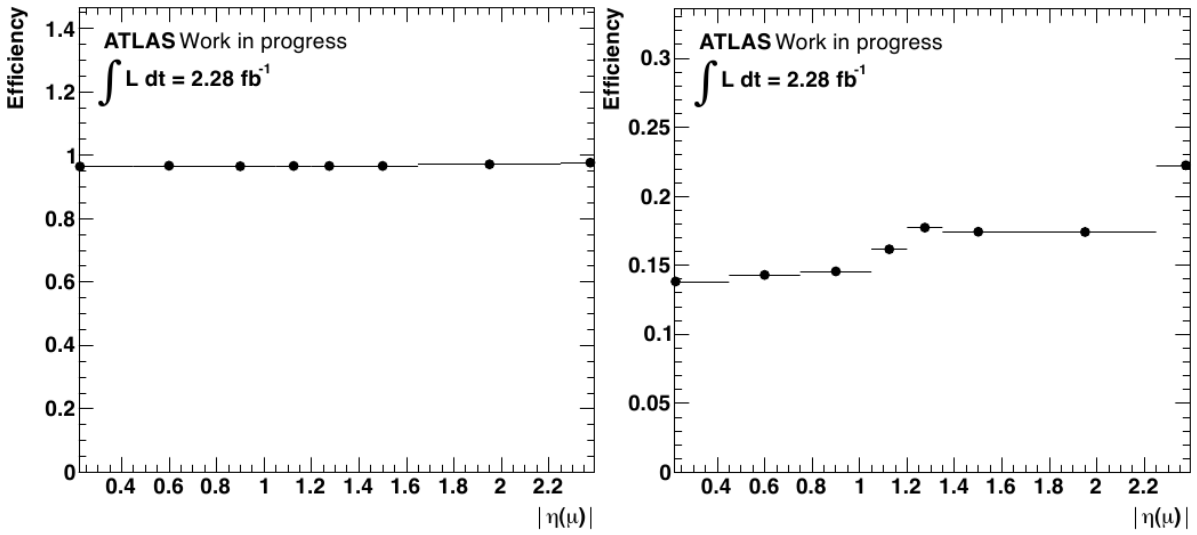


(a) (b)

Figure 4.8: $\eta$ dependency on the muon (a) real and (b) fake efficiencies measured in periods B to K [121].

### 4.3.3 ABCD method

The ABCD method uses two sets of two mutually exclusive selections to create four mutually exclusive regions.

For the sake of argumentation, let $x$ and $y$ be two quantities that can be measured in each event. Let $h$ be a given preselection and let $f_1^x$ and $f_2^x$ be selections based only on $x$, such that no event can pass both selections, i.e., $f_1^x$ and $f_2^x$ are mutually exclusive. Furthermore, let $g_1^y$ and $g_2^y$ represent mutually exclusive selections based only on $y$. Then, four regions can be defined based on these selections, as shown in Table 4.8.

| Selections | $f_1^x$ | $f_2^x$ |
|---|---|---|
| $g_1^y$ | Region A: $f_1^x \wedge g_1^y \wedge h$ | Region B: $f_2^x \wedge g_1^y \wedge h$ |
| $g_2^y$ | Region C: $f_1^x \wedge g_2^y \wedge h$ | Region D: $f_2^x \wedge g_2^y \wedge h$ |

Table 4.8: Generic definition of the regions in the ABCD method. $h$ is the preselection applied to all regions.

Assuming that $x$ and $y$ are independent, the following relationship can be assumed:

$$\frac{N_{\mathrm{F}}^{\mathrm{A}}}{N_{\mathrm{F}}^{\mathrm{B}}} = \frac{N_{\mathrm{F}}^{\mathrm{C}}}{N_{\mathrm{F}}^{\mathrm{D}}}, \tag{4.13}$$

where $N_{\mathrm{F}}^{\mathrm{X}}$ is the number of fake lepton events[4] in the region X ($\mathrm{X} \in \{\mathrm{A}, \mathrm{B}, \mathrm{C}, \mathrm{D}\}$).

Let the definition of region D be equivalent to the region of interest, i.e., the region where an estimate of the number of fake lepton events is needed. Then, from Equation 4.13:

$$N_{\mathrm{F}}^{\mathrm{D}} = \frac{N_{\mathrm{F}}^{\mathrm{B}}}{N_{\mathrm{F}}^{\mathrm{A}}} N_{\mathrm{F}}^{\mathrm{C}}. \tag{4.14}$$

In order to use Equation 4.14, regions A, B and C are assumed to be completely dominated by fake events. This can be sometimes achieved by a careful choice of the definitions of $f_1^x$ and $g_1^y$, such that $N_{\mathrm{F}}^{\mathrm{A}} \approx N_{\mathrm{Data}}^{\mathrm{A}}$, $N_{\mathrm{F}}^{\mathrm{B}} \approx N_{\mathrm{Data}}^{\mathrm{B}}$ and $N_{\mathrm{F}}^{\mathrm{C}} \approx N_{\mathrm{Data}}^{\mathrm{C}}$. In practice, however, it is often more convenient and accurate to use:

$$N_{\mathrm{F}}^{\mathrm{X}} = N_{\mathrm{Data}}^{\mathrm{X}} - N_{\mathrm{R}}^{\mathrm{X}}, \tag{4.15}$$

where $\mathrm{X} \in \{\mathrm{A}, \mathrm{B}, \mathrm{C}\}$ and $N_{\mathrm{R}}^{\mathrm{X}}$ is the expected number of events with only real leptons selected in the region X, as estimated by MC simulations.

Using Equation 4.15 in Equation 4.14, the final form of the estimate using the ABCD method is:

$$N_{\mathrm{F}}^{\mathrm{D}} = \frac{N_{\mathrm{Data}}^{\mathrm{B}} - N_{\mathrm{R}}^{\mathrm{B}}}{N_{\mathrm{Data}}^{\mathrm{A}} - N_{\mathrm{R}}^{\mathrm{A}}} \left( N_{\mathrm{Data}}^{\mathrm{C}} - N_{\mathrm{R}}^{\mathrm{C}} \right). \tag{4.16}$$

Although the use of Equation 4.16 relaxes the requirements on the regions A, B and C (they do not need to be completely dominated by fake lepton events), it is still very important to have predominantly fake lepton events in the regions A, B and C in order to obtain good estimates, since the relative statistical

[4] The ABCD method can also be applied to other kinds of processes.

uncertainty on $N_{\mathrm{F}}^{\mathrm{X}}$ is given by:

$$\epsilon = \sqrt{\frac{1}{N_{\mathrm{Data}}^{\mathrm{X}}}} \cdot \sqrt{\frac{1+\rho}{(1-\rho)^2}} \tag{4.17}$$

where $\rho = \frac{N_{\mathrm{R}}^{\mathrm{X}}}{N_{\mathrm{Data}}^{\mathrm{X}}}$ is the fraction of expected events in data where only real leptons are selected. Notice that, for a fixed value of $N_{\mathrm{R}}^{\mathrm{X}}$, the value of $\epsilon$ increases with $\rho$. Furthermore, a higher value of $\rho$ magnifies the effect of the systematic uncertainties associated with the estimation of $N_{\mathrm{R}}^{\mathrm{X}}$.

CHAPTER 5

# Physics objects definition, reconstruction and identification

Physics objects are the final product of the ATLAS reconstruction software and have a well-defined physics meaning. They are designed to be closely related to particles from the hard process. Several algorithms are used to reconstruct accurate physics objects from the detector response. These algorithms are usually developed using MC simulations of the detector response and calibrated with data. The physics objects used in the analyses presented in this thesis are: electrons, muons, jets and missing transverse momentum.

## 5.1 Electrons

### 5.1.1 Reconstruction

Three different algorithms are used to reconstruct an electron: egammaBuilder, softeBuilder and egammaForwardBuilder.

**Standard electron algorithm (egammaBuilder):** the egammaBuilder is a cluster-based algorithm devoted to the reconstruction of isolated electrons with high transverse momentum. It uses the sliding window algorithm [122], which consists of three steps: tower building, precluster finding and electron cluster formation.

During tower building, the $\eta - \phi$ space is divided into a grid of $N_\phi \times N_\eta$ elements, each element with a size of $0.025 \times 0.025$, and the energies of all longitudinal[1] cells inside each element are summed into the so-called tower energy. During the precluster finding, the tower energies are scanned using a $5 \times 5$ elements window. If a local maximum is found and the window transverse energy[2] is larger than the energy threshold (3 GeV), a precluster is formed. The position of the precluster is computed from the energy-weighted $\eta$ and $\phi$ barycenters of the 9 central elements[3] in the window. If two preclusters can be contained within an $\eta - \phi$ space of size $0.05 \times 0.05$, the precluster with less transverse energy is considered a duplicate and removed from the preclusters list.

[1] The longitudinal direction is defined as the radial direction.
[2] Defined as the sum of all the tower energies of the towers inside a window.
[3] The 9 central elements form a $3 \times 3$ grid concentric with the $5 \times 5$ window.

In the next step (electron cluster formation), the energy of each electromagnetic calorimeter layer is assigned to electron clusters. For each layer, all cells within a rectangle of size $3 \times 7$ (barrel region) or $5 \times 5$ (end-cap region) are assigned to the cluster. The center of the rectangle is determined by the so-called seed position. The seed position for the middle layer is given by the position of each precluster. Once the cells in the middle layer are determined, their energy-weighted $\eta$ and $\phi$ barycenters are used to create a new seed position, which is used by the strips layer and the back layer. Once the cells in the strips layer are assigned to the cluster, their energy-weighted $\eta$ and $\phi$ barycenters are used to determine the seed position used for the presampler layer.

Once these clusters are defined, a cluster-track matching reconstructs and identifies the electron candidates. If the position of the cluster and the direction of a valid track are within 0.2 in $\eta$ and 0.1 in $\phi$, the track is considered a possible match to the cluster.

The path of a charged particle through the inner detector is known as a track. A track candidate is considered valid if it is associated with at least one hit in the pixel detector and it has at least 7 precision hits, where the number of precision hits is defined as the number of hits in the pixel detector and the SCT.

If more than one track are possible matches to a cluster, the track giving the best match to the position of the layers of the cluster is taken. This is determined by extrapolating each track and summing the angular distances between the extrapolated track and each calorimeter layer in the cluster, where the track with the smallest sum of angular distances is chosen as the best match.

The total energy of the reconstructed lepton are computed from the electron cluster energy determined from the algorithm, while its direction is obtained from the associated track in the inner detector. The $E_{\mathrm{T}}$ and the $p_{\mathrm{T}}$ of the electron is then computed using the usual four-vector projections.

**Soft-electron reconstruction algorithm (softeBuilder):** the softeBuilder is a track-based algorithm dedicated to reconstruct electrons with low transverse momentum [123]. The algorithm is optimized to fit the tracks of low-energy electrons, considering the effects of bremsstrahlung, and provides significant improvements for the reconstruction of electrons with $p_{\mathrm{T}} < 25$ GeV [89].

**Forward electron algorithm (egammaForwardBuilder):** the egammaForwardBuilder algorithm specializes in the reconstruction and identification of electrons in the forward region ($2.5 < |\eta| < 4.9$) of the ATLAS detector. This algorithm relies only on the information provided by the electromagnetic calorimeter, since tracking is not available in the forward region. Forward electrons are not used in the analyses presented in this thesis.

### 5.1.2 Electron definitions, identification and isolation for the 2011 data

Many of the electron clusters identified using the algorithms described earlier in this section are not related to hard-process electrons. Therefore, additional requirements are imposed on reconstructed electron candidates in order to separate energy clusters originating from jets and those originating from electrons.

Three sets of identification settings are used as standards in ATLAS: loose++, medium++ and tight++.

**loose++:** the loose++ setting is expected to have an efficiency of roughly 95% and a jet rejection rate of approximately 500. This setting provides the highest electron identification efficiency at the expense of a modest jet rejection rate. It only considers electrons detected in the central region ($|\eta| < 2.47$) and requires low hadronic leakage, i.e., the ratio of the transverse energy in the

first hadronic calorimeter layer to the transverse energy in the electromagnetic calorimeter must be small. Additionally, it requires a loose track-cluster matching in $\eta$ ($\Delta\eta < 0.015$) and imposes restrictions on the shower shapes and the minimum quality of the tracks in the inner detector [124, 125].

**medium++:** the medium++ setting is expected to have an efficiency of around 85% and a jet rejection rate of roughly 4400. In addition to the loose++ setting, a small impact parameter is required ($d_0 < 5$ mm), the track-cluster matching criterion is changed to $\Delta\eta < 0.005$ and the shower-shape requirements are tightened for the $|\eta| > 2.01$ region. Furthermore, the quality-of-tracks requirements are also increased, requiring at least one hit in the b-layer and at least an additional hit in the pixel detector for the $|\eta| < 2.01$ region, and at least two pixel detector hits for the $|\eta| > 2.01$ region.

**tight++:** the tight++ setting is expected to have an efficiency of approximately 78% and a jet rejection rate of roughly 43000. It includes all the requirements of the medium++ setting, but requires even higher track quality, requiring at least one hit in the b-layer for all regions. Finally, the impact-parameter requirement is tightened to $d_0 < 1$ mm.

Isolation requirements are applied separately from the identification process, since different analyses may need different isolation criteria. Two main variables are used to determine the isolation of a physics object: $E_{\mathrm{T}}^{\mathrm{ConeX}}$ and $p_{\mathrm{T}}^{\mathrm{ConeX}}$.

The $E_{\mathrm{T}}^{\mathrm{ConeX}}$ of an electron candidate is defined as the reconstructed energy in a cone of half-opening angle $X$ around the direction of the electron candidate, where the energy assigned to the electron is excluded [124]. Analogous to the $E_{\mathrm{T}}^{\mathrm{ConeX}}$ definition, the $p_{\mathrm{T}}^{\mathrm{ConeX}}$ of an electron candidate is the scalar sum of the transverse momenta of the tracks inside a cone of half-opening angle $X$ around the direction of the electron candidate, excluding the track associated to the electron candidate.

Only tracks of a reasonable quality are considered in the computation of $p_{\mathrm{T}}^{\mathrm{ConeX}}$, i.e., they should have $p_{\mathrm{T}} > 1$ GeV, a hit in the innermost pixel-detector layer, at least 7 hits in the silicon detectors, $z_0 < 1$ mm[4] and $d_0 < 1$ mm.

For the top-quark mass measurement, two electron definitions are used:

- Loose definition, used to estimate the contribution of backgrounds with fake leptons using the matrix method, defined as:
  - Identified with the medium++ setting.
  - Electron candidates matched to photon conversions are rejected.
  - $E_{\mathrm{T}}^{\mathrm{Cone20}} < 6$ GeV.
  - $p_{\mathrm{T}}^{\mathrm{Cone30}} < 6$ GeV.
  - $p_{\mathrm{T}} > 25$ GeV.
  - $0 < |\eta| < 1.37$ or $1.52 < |\eta| < 2.47$. The excluded region, $1.37 < |\eta| < 1.52$, corresponds to the calorimeter crack region.
- Tight definition, used in the rest of the analysis as the standard selection. It is defined as follows [126]:
  - It should meet all the requirements of the loose definition.
  - Identified with the tight++ setting.

[4] $z_0$ is the transverse impact parameter

- The electron reconstruction is done using only the egammaBuilder algorithm (el_author=1). Alternatively, if the egammaBuilder is used but also the softeBuilder, the electron is also accepted (el_author=3) [123].
- The longitudinal impact parameter must be less than 2 mm from the primary vertex.
- A $p_{\mathrm{T}}$-independent isolation in $E_{\mathrm{T}}^{\mathrm{Cone20}}$ at 90% efficiency and in $p_{\mathrm{T}}^{\mathrm{Cone30}}$ at 90% efficiency is required.
- The electron must pass the object-quality flag. This flag alerts the analyzer of the presence of a dead front-end board or the presence of dead high-voltage regions in the cluster where the electron is defined [127].

### 5.1.3 Electron definitions, identification and isolation for the 2012 data

For the 2012 data ($t\bar{t}Z$ cross-section measurement), a different approach is used to define electrons, namely, the so-called likelihood electrons [128]. The process to define likelihood electrons is based on the information provided by 18 variables, divided in 7 regions based on the $|\eta|$ binning:

$$[0.00, 0.80, 1.35, 1.50, 1.80, 2.00, 2.35, 2.47]\,.$$

The 18 variables include information from the inner detector, electromagnetic and hadronic calorimeter, energy, momentum, isolation, angular distances and longitudinal impact parameter. The complete list of variables is described in Ref. [128]. Not all variables are used in all regions. In particular, for some regions, only the most discriminating variables are considered.

For each variable, the normalized signal (hard-process electrons) and background distribution (fake electrons) can be used to assign the probability of a given electron candidate to be a signal electron ($P_i^{\mathrm{signal}}$) or a background electron ($P_i^{\mathrm{background}}$). To combine the information from all the variables ($i$), the following logarithmic likelihood ratio is built:

$$\ln L = \sum_i \left( \ln P_i^{\mathrm{signal}} - \ln P_i^{\mathrm{background}} \right). \tag{5.1}$$

The value of $\ln L$ can be computed for each electron candidate for both signal and background electron candidates, as shown in Figure 5.1. Using this information, electron candidates can be defined with different efficiency and jet rejection rate by applying cuts on different values of $\ln L$.

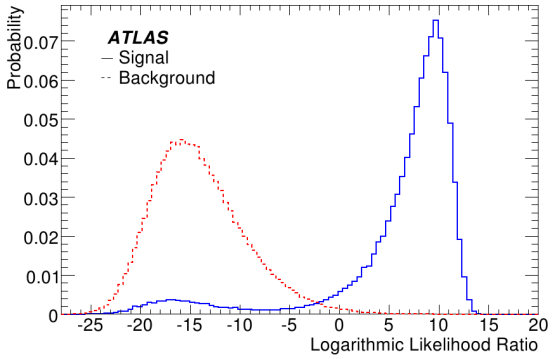


Figure 5.1: Distribution of $\ln L$ for signal and background reconstructed electrons in the region $|\eta| < 0.8$ [128].

Six standard working points have been defined: very loose, loose relaxed, loose, medium, tight and very tight. Loose is a subset of, both, very loose and loose relaxed. The other working points are not

subsets of the looser ones, but the level of non-overlap between a tighter setting and a looser one is less than 0.1%.

The working points chosen for the $t\bar{t}Z$ cross-section measurement are the very loose and the medium working points. The very loose working point is chosen such that it has a background rejection comparable to the loose++ setting used for 2011 data, but it offers higher selection efficiency. On the other hand, the medium working point is chosen such that its selection efficiency is similar to the medium++ setting used for 2011 data, but it has a higher background-rejection rate [129].

Two electron definitions are used, both requiring that the transverse momentum of the electron candidate is larger than 7 GeV:

- Loose electron definition, used to estimate the contribution of backgrounds with fake leptons using the ABCD method, requiring that the lepton candidate is a very loose likelihood electron.
- Tight electron definition, used as the standard selection. The electron candidate must be a medium-likelihood electron and further isolation is imposed using the cut

$$\frac{p_{\mathrm{T}}^{\mathrm{Cone30}}}{p_{\mathrm{T}}} < 0.18. \tag{5.2}$$

### 5.1.4 Energy scale and energy resolution

In order to calibrate the energy scale, a generic energy scale can be defined as [130]:

$$E_{\mathrm{measured}} = (1 + \alpha)\, E_{\mathrm{true}}, \tag{5.3}$$

where $E_{\mathrm{measured}}$ is the measured electron energy, $E_{\mathrm{true}}$ is the true electron energy and $\alpha$ is an energy scale that depends on the angular position of the electron. The value of this scale can be obtained from $Z \to ee$ and $J/\psi \to ee$ decays. The main technique used to calibrate the electron energy scale is the in-situ calibration.

The in-situ calibration exploits the well-known mass resonances of the $Z$ boson and the $J/\psi$ meson. Neglecting second-order terms and assuming that the angle between electrons is perfectly known, the effect of the miscalibration in the invariant mass is [130]:

$$m_{ij}^{\mathrm{measured}} = m_{ij}^{true}\left(1 + \frac{\alpha_i + \alpha_j}{2}\right), \tag{5.4}$$

where $m_{ij}^{\mathrm{measured}}$ is the invariant mass obtained from the measured energy of the electrons and $m_{ij}^{\mathrm{true}}$ is the invariant mass computed from the true energy of the electrons.

Equation 5.4 provides a model to perform a likelihood fit of events in data to obtain the values of $\alpha_i$ and $\alpha_j$ by maximizing the unbinned likelihood [130]:

$$\ln L_{\mathrm{total}} = \sum_{i}^{N_{\mathrm{events}}} \ln L\left[\frac{m_{ij}^{measured}}{\left(1 + \frac{\alpha_i + \alpha_j}{2}\right)}\right], \tag{5.5}$$

where $L(m)$ is the probability density function of the true invariant mass and can be obtained from MC simulations.

This fit allows the determination of the energy scale $\alpha$. With enough data events, the value of $\alpha$ can be determined for different regions of the detector, e.g., different $|\eta|$ ranges. Once these correction factors are measured, they can be applied to either the data or the MC simulations. The effect of the

uncertainties on the determination of the correction factors is usually estimated by variations in the MC simulation events. Figure 5.2 shows the dependence of the energy-scale correction factors as a function of the pseudorapidity, as derived from $Z \to ee$ decays in the 2011 data.

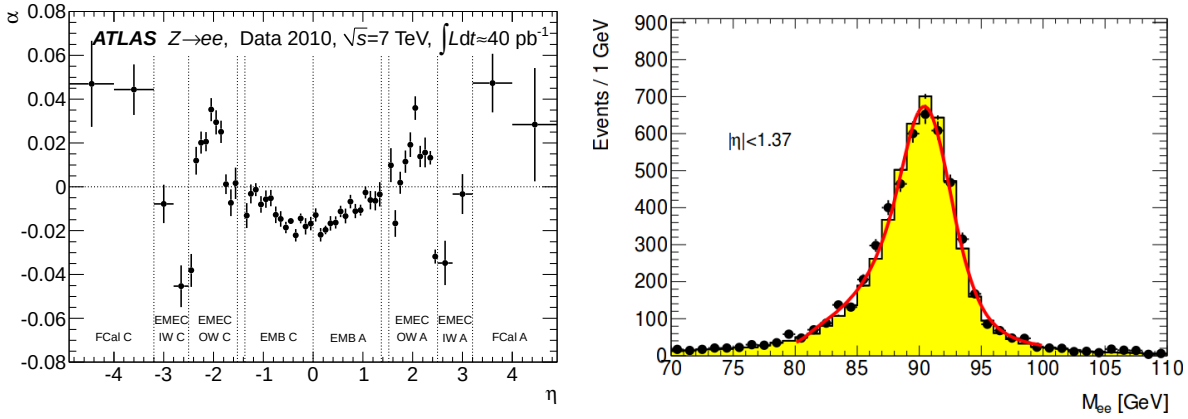


Figure 5.2: Left: electron energy-scale correction factor as a function of the electron pseudorapidity derived from $Z \to ee$ decays. The boundaries of the detector parts are indicated with dotted lines [131]. Right: comparison of the invariant-mass distribution of the $Z \to ee$ decay in data and MC simulations. The fit is a Breit-Wigner distribution convoluted with a Crystal ball function, which is used to determine the electron energy resolution [130].

The energy-resolution function can be expressed as:

$$\frac{\sigma_E}{E} = \frac{a}{\sqrt{E}} \oplus \frac{b}{E} \oplus c, \tag{5.6}$$

where $a$ and $c$ have to be determined. The value of $a$ is related to statistics-related fluctuations in the calorimeter. The value of $b$ is the noise term and is negligible, only having significant contributions at low energies. The value of $c$ represents the detector non-uniformity, calibration uncertainties and uncertainties due to radiation damage.

The energy-resolution function is determined by comparing the invariant-mass distribution of the $Z \to ee$ decay in data and MC simulations (see Figure 5.2). These are fitted using a Breit-Wigner distribution convoluted with a Crystal Ball function in the mass range 80-100 GeV for central events and in the mass range 75-105 GeV for forward events. The width of the Breit-Wigner distribution is given by the $Z$ boson width. The energy resolution is then determined from the fitted parameter values of the Crystal Ball function [130].

The corrections of the electron energy scale and the electron energy resolution are based on calibrations provided by the ATLAS top working group: the top-quark mass measurement uses the calibrations provided in the package ATLAS-GEO-18-01-03 while the $t\bar{t}Z$ cross-section measurement uses those provided in the package ATLAS-GEO-20-00-01.

### 5.1.5 Efficiency scale factors

The different requirements on electron reconstruction, trigger, identification and isolation can have a different effect in MC simulations and in data. In order to recover data-MC agreement after applying these requirements, several scale factors are used [132, 133].

The electron reconstruction and trigger efficiency scale factors are measured using $Z \to ee$ decays. Using a tag-and-probe method, the ratio of the efficiencies in data and MC are determined in differ-

ent $\eta$ and $E_{\mathrm{T}}$ regions [134]. Analogously, the scale factors of the electron identification efficiency are determined from combined measurements in the $Z \to ee$ and $W \to e\nu$ channels. The scale factors of the electron isolation efficiency are also determined from $Z \to ee$ decays, where the effect of pile up in the isolation efficiency is evaluated by comparing the scale factors as a function of the number of reconstructed vertices [135].

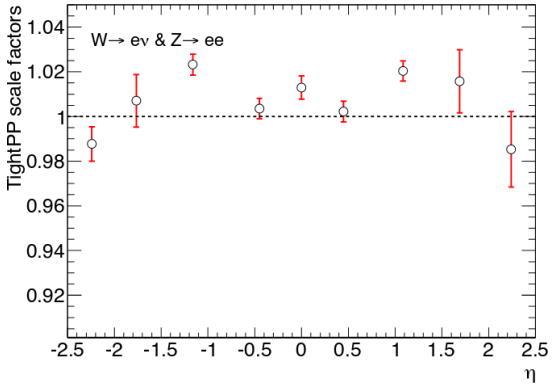


Figure 5.3: Electron-reconstruction scale factor for the tight++ setting [135].

As an example, the electron-reconstruction scale factor for the 7 TeV analyses is shown in Figure 5.3. All these scale factors are integrated in the TopElectronSFUtils-00-00-18 package for the 2011 data [132] and in the TopElectronSFUtils-00-00-29 package for the 2012 data [133].

## 5.2 Muons

### 5.2.1 Reconstruction and identification

The ATLAS detector has excellent muon reconstruction and identification capabilities thanks to its inner detector and its muon spectrometer. These two subsystems provide two independent measurements used to reconstruct and identify muons.

The reconstruction and identification of muons are based on four algorithms which produce four definitions of muon candidates [136]: standalone muons, combined muons, segment-tagged muons and calorimeter-tagged muons.

**Standalone muons:** the trajectory of standalone muons is reconstructed using only the muon spectrometer. The direction of flight and impact parameter of the muon can be obtained by extrapolating the spectrometer's track back to the beamline, while the muon momentum is measured using the muon spectrometer and corrected with information provided by the calorimeters.

**Combined muons:** a combined muon is an improvement to standalone muons. The momentum measurement of a standalone muon is improved by combining it with the momentum measurement from the inner detector. Likewise, the measurement of the impact parameter with respect to the primary vertex is also improved using information from the inner detector. In case that a momentum measurement from the inner detector is not available, a combined muon cannot be defined.

**Segment-tagged muons:** a segment-tagged muon is identified when a trajectory in the inner detector extrapolated to the muon spectrometer can be associated to a track reconstructed in the muon chambers.

**Calorimeter-tagged muons:** a calorimeter-tagged muon is reconstructed using the information from the calorimeter information. This is done by identifying energy depositions in the calorimeters that are compatible with the low energy depositions expected from a muon.

The analyses presented in this thesis only use combined muons, as recommended by the ATLAS top working group. This choice of identification setting is tighter than the default tight identification setting from the Muid muon reconstruction chain [126, 137, 138].

### 5.2.2 Muon definitions and isolation

Applying an isolation requirement is useful to remove muons that are produced from hadronic decays inside jets, which is an important source of fake muons. Muon isolation requirements use the same observables as the electrons: $p_{\mathrm{T}}^{\mathrm{ConeX}}$ and $E_{\mathrm{T}}^{\mathrm{ConeX}}$.

Analogous to the electron definitions, two muon definitions are used for the 2011 data: loose and tight, defined for the same reason as their electron counterparts. The loose definition is defined by the following requirements [126]:

- The muon candidate must have been reconstructed as a combined muon.
- The transverse momentum of the muon candidate must be larger than 20 GeV.
- The muon must be in the central region ($|\eta| < 2.5$).
- Additional requirements in the number of hits in the inner detector must be met:
  - At least one hit in the b-layer.
  - At least two pixel hits.
  - At least six SCT hits.
  - The sum of holes in the pixel and the SCT hits must be less than three. A hole is defined as follows: if the interpolation or extrapolation of a track passes through a layer of the detector that is uninstrumented or dead, this layer is assumed to have registered a hit and adds towards the hit-requirement count. Each hit registered in this fashion is considered a hole [139].
  - For the region with $|\eta| < 1.9$, at least six hits in the TRT are required and the number of outliers[5] must not exceed 90%.
  - If $|\eta| > 1.9$ and at least six hits in the TRT are registered, the number of outliers must not exceed 90%.
- The longitudinal impact parameter with respect to the primary vertex must be less than 2 mm.

The tight definition adds the following isolation requirements to the loose definition [126]:

- $p_{\mathrm{T}}^{\mathrm{Cone30}} < 2.5$ GeV.
- $E_{\mathrm{T}}^{\mathrm{Cone20}} < 4.0$ GeV.
- If any jet in the event has a transverse momentum larger than 25 GeV and its jet vertex fraction (JVF)[6] is larger than 0.75, the angular separation between the muon and this jet must satisfy $\Delta R > 0.4$.

[5] An outlier is defined as a straw tube with a signal that is not crossed by a nearby track or a set of TRT measurements in the extrapolation of a track that fails to form a smooth trajectory with the measurements from the pixel detector and the SCT.

[6] The jet vertex fraction measures the probability that a jet has originated from a particular vertex [140].

Similar definitions are given for the loose and tight muons for the 2012 data. Here, the loose definition is defined by the following requirements [137]:

- The muon candidates must have been reconstructed as combined muons.
- The transverse momentum of the muon candidate must be larger than 7 GeV.
- The muon must be in the central region ($|\eta| < 2.5$).
- Additional requirements in the number of hits in the inner detector must be met:
  - At least one pixel hit.
  - At least five SCT hits.
  - The sum of holes in the pixel and the SCT hits must be less than three.
  - If $|\eta| < 1.9$, at least five hits in the TRT are required and the number of outliers should not exceed 90%.
- The longitudinal impact parameter with respect to the primary vertex must be less than 2 mm.

The tight definition adds the following isolation requirement:

$$\frac{p_{\mathrm{T}}^{\mathrm{Cone30}}}{p_{\mathrm{T}}} < 0.18. \tag{5.7}$$

### 5.2.3 Energy scale and energy resolution

The process used to determine the muon energy scale and energy resolution is analogous to the one used for electrons, using the $Z \to \mu\mu$, $\Upsilon \to \mu\mu$ and $J/\psi \to \mu\mu$ decays. Since the inner detector and the muon spectrometer can measure the muon momentum, an energy scale calibration is made for each of them [132].

The effect of the energy-scale correction in the dimuon invariant-mass distribution is shown in Figure 5.4, along with the correction to the muon energy resolution [141]. The energy-scale correction is applied to the energy of the muons in events from MC simulations using a multiplicative scale factor. On the other hand, the muon energy is smeared in order to apply the energy-resolution correction, i.e., a random scale factor distributed according to a Gaussian function centered at one and with a standard deviation that depends on the value of the the energy-resolution correction is multiplied to the muon energy [126, 137].

The energy scale and energy resolution used by the analyses in this thesis follow the recommendations of the ATLAS top working group. The values are provided centrally by the ATLAS Collaboration via the packages MuonMomentumCorrections-00-05-03 [132] for 2011 data and MuonEfficiencyCorrections-02-01-20 [133] for 2012 data.

### 5.2.4 Efficiency scale factors

Similar to the case of electrons, the requirements on muon reconstruction, identification and trigger can have a different effect in MC simulations and in data. In order to recover data-MC agreement after applying these requirements, several correction factors are needed [132, 133, 135].

The measurement of the reconstruction and identification efficiencies [142] are analogous to the electron case. In Figure 5.5 (left), the reconstruction efficiency for the combined muons are shown as a

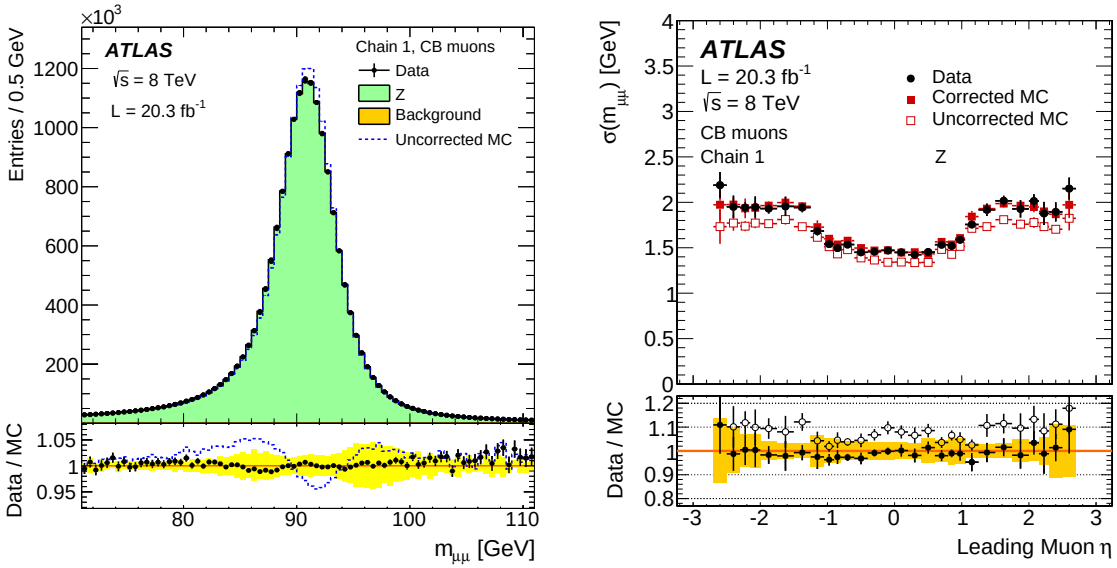


Figure 5.4: Dimuon invariant mass distribution (left) used to calibrate the muon energy scale and muon energy resolution with respect to the leading-muon pseudorapidity (uncorrected and corrected muon energy resolution) (right). The yellow bands in the ratio plots represent the systematic uncertainty [141].

function of the transverse momentum of the muon candidate (2012 data). The muon trigger efficiency is measured by comparing data with MC simulations in the $Z \to \mu\mu$ decay channel using a tag-and-probe method [135]. The trigger scale factors are computed for different values of $\eta$ and $\phi$, as shown in the example in Figure 5.5 (right) for 2011 data.

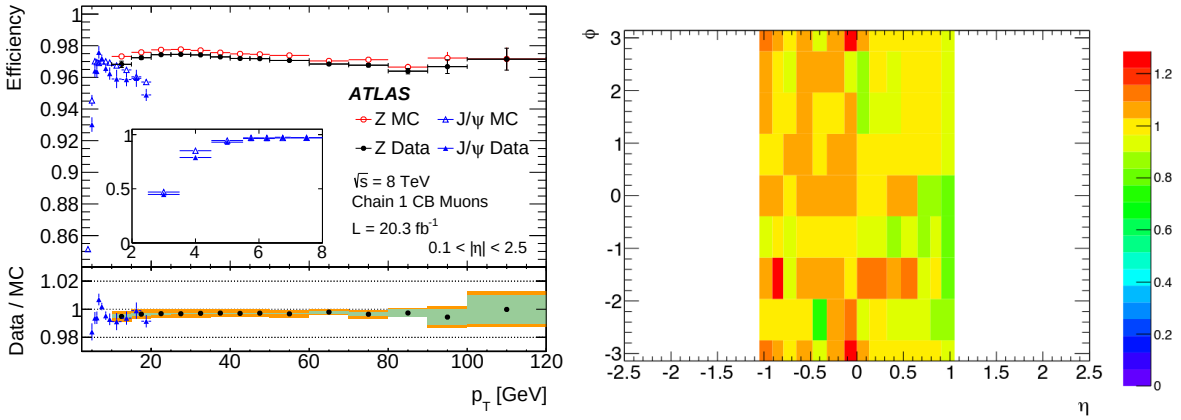


Figure 5.5: Left: muon reconstruction efficiency for combined muons (CB muons) in the $Z \to \mu\mu$ channel. The green area is the statistical uncertainty while the orange areas also include the systematic uncertainty [141]. Right: muon trigger scale factors in the barrel region for the mu18 trigger in periods B-I of 2011 data [135].

All these scale factors are integrated in the MuonEfficiencyCorrections-01-01-00 package for the 2011 data [132] and in the MuonEfficiencyCorrections-02-01-20 package for the 2012 data [133].

## 5.3 Jets

### 5.3.1 Reconstruction

When quarks or gluons are produced, they may hadronize and form a collimated group of particles. Motivated by this concept, jets are physics objects defined with the purpose of reconstructing the kinematic properties of the parent quark or gluon before the hadronization takes place. In practice, jets do not exist as a standalone entity (in spite of being related to partons) and are characterized by the algorithm used to define them.

In order to obtain algorithms that define jets that are meaningful for physics analyses, a jet algorithm should meet the following requirements that are also summarized in Ref. [143]:

- the algorithm should be able to define observables that are sensitive to the short-distance physics in a collision event and robust against effects that are not part of the hard process, e.g., the effect of hadronization must be small and controllable.
- The algorithm must be able to handle high-multiplicity events without breaking down or becoming too computationally intensive.
- The algorithm must be collinear safe and must be detector independent.
- The algorithm must be robust against noise and pile up.
- The algorithm must be robust against the collinear splitting of the input objects.
- The algorithm must be robust to the addition of arbitrarily-soft particles.

All jets can be considered a combined entity formed by simpler entities (e.g., particles) that can be represented by four-vectors. The jet reconstruction algorithm used in ATLAS is the anti-$k_t$ algorithm [144]. The anti-$k_t$ algorithm is a cluster algorithm, i.e., the algorithm defines a distance measure between particles and a termination condition that ends the clustering. The distance between two entities $i$ and $j$ is given by [144]:

$$d_{ij} = \min\left(k_{T_i}^{-2}, k_{T_j}^{-2}\right) \frac{\Delta_{ij}^2}{R^2}, \tag{5.8}$$

where $\Delta_{ij}^2 = \left(y_i - y_j\right)^2 + \left(\phi_i - \phi_j\right)^2$, $R$ is a radius parameter, $k_{Ti}$, $y_i$ and $\phi_i$, are the transverse momentum, the rapidity and the azimuth angle of the $i$-th entity, respectively.

Additionally, the distance between an entity and the beam is defined as:

$$d_{iB} = k_{T_i}^{-2}. \tag{5.9}$$

Once these distances are defined, the clustering algorithm is recursive:

- Compute all distances for all pairs of entities (both $d_{ij}$ and $d_{iB}$).
- Find the smallest value of all the computed distances.
- Conditional:
  - If the smallest value is the value of the distance from an entity to the beam ($d_{iB}$), label this entity as a jet, and remove it from the list of available entities.

  - If the smallest value is the value of the distance between two entities ($d_{ij}$), merge entity $i$ and entity $j$ into a new entity by summing their four-momenta.

- Repeat until no entity remains.

The behavior of the anti-$k_t$ algorithm can be tuned using different values of the radius parameter $R$. The ATLAS standard value for R is 0.4, which is the same value used for the analyses presented in this thesis.

The entities needed by the anti-$k_t$ are the so-called topological clusters [89, 122, 145]. Topological clusters are calorimeter clusters that are strongly correlated with the number of stable particles produced in an event. Their use reduce the impact of calorimeter noise in the jet reconstruction process by grouping cells that have an energy significantly above the noise level.

#### Algorithm to create topological clusters

The algorithm used to create topological clusters consists of various steps [122]. In a given region of interest (usually, the whole calorimeter), all the cells with an energy level at least four times above the noise level are identified (seed cells) and a "protocluster" is associated to each seed cell. The list of all the seed cells are sorted in descending order of signal-to-noise ratio and the following iterative process follows:

- For each cell in the seed list, consider the adjacent cells around it that are not associated to a protocluster:
  - If the energy of the cell is at least two times larger than the noise level:
    * Add the cell to the "neighbor cell" seed list.
    * Add the cell to the protocluster of the seed cell. If the cell can be associated to more than one protocluster, the protoclusters are merged.
  - If the energy of the cell is larger than zero but less than two times larger than the noise level:
    * Add the cell to the protocluster of the first seed cell that considers it.

- Repeat the procedure with the neighbor cell seed list as the new seed list until the seed list is empty.

The final list of protoclusters is defined as the list of topological clusters in the region.

### 5.3.2 Energy scale

For 2011 data, the jet energy scale (JES) is calibrated using the electromagnetic scale (EM+JES scheme) [135]. The EM+JES scheme consists of four steps [146]:

- pile-up correction,
- vertex correction,
- jet energy correction and
- jet pseudorapidity correction.

The pile-up correction compensates for the contributions to the jet energy originated from additional proton-proton collisions within the same bunch crossing (pile up). This correction factor term is subtracted from the uncorrected jet energy and depends on the number of reconstructed primary vertices ($N_{PV}$), the jet pseudorapidity and the bunch spacing.

The vertex correction addresses the effect of a simplification used during the reconstruction of calorimeter jets: the geometrical center of the detector is used as reference to calculate the direction of the jet, instead of the actual location of the primary vertex. The vertex correction recalculates the kinematic variables of the topological clusters. These corrected topological clusters are then used to recompute the direction and transverse momentum of the jet.

The jet energy correction aims to scale the reconstructed jet energy to the true jet energy. This correction is derived using MC simulations at reconstruction level and comparing the reconstructed jets to the truth level values. This correction is parametrized as a function of the uncorrected energy and the pseudorapidity of the jets.

An additional correction to the jet pseudorapidity is applied after the first three corrections. This corrects the bias introduced by poorly-instrumented regions in the calorimeter, which causes the pseudorapidity of jets to be biased towards the better-instrumented regions. This correction is only significant in the transition regions and is parametrized as a function of the jet energy and the uncorrected pseudorapidity. The jet energy scale calibration and its uncertainty for the 2011 data as a function of the jet $p_T$ are shown in Figure 5.6.

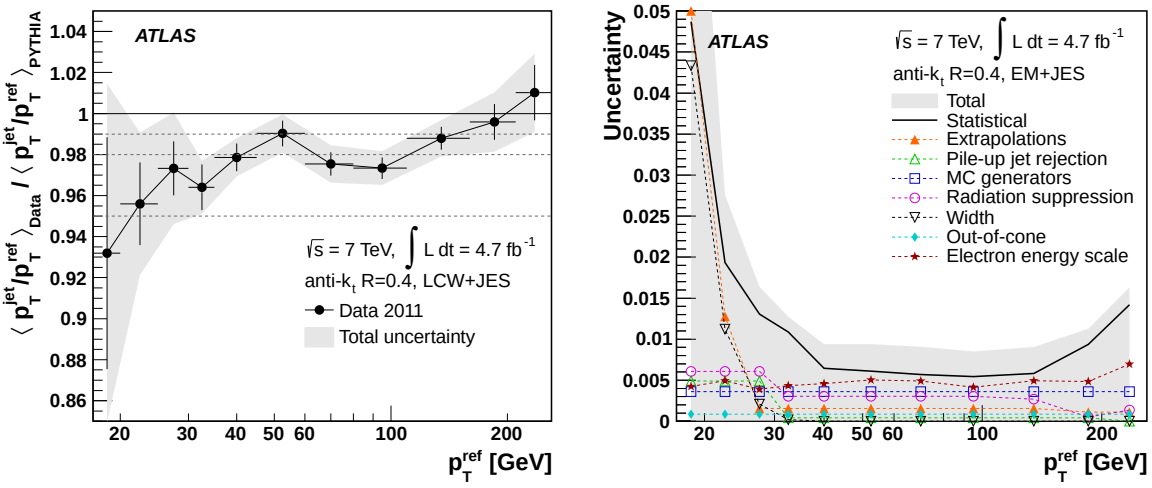


Figure 5.6: Calibration of the jet energy scale and its uncertainty for the 2011 data as a function of the jet $p_T$ [147].

For the 2012 data, the topological clusters are calibrated using the local-cluster-weighting (LCW) method [148, 149]. The LCW algorithm calibrates calorimeter clusters based on cluster properties related to shower development in an attempt to correct the response and reduce fluctuations due to the non-compensating nature of the ATLAS calorimeters. The jet energy scale is based on three components: the clustering-independent pile-up correction, clustering-dependent residual correction and an additional jet energy correction.

The pile-up correction for 2012 data uses two new observables [150]: the jet area ($A_{jet}$) and the median $p_T$ density ($\rho$). The concept of jet area is intuitive and is related to the total number of particles in the jet, but the formal definition is more involved (full details in Ref. [151]). The median $p_T$ density, on the

other hand, is simply defined as:

$$\rho = \text{Median}\left(\frac{{p_{\text{T}}}^{i}}{A^{i}_{\text{jet}}}\right), \tag{5.10}$$

where the index $i$ enumerates each jet found by the jet-clustering algorithm.

The use of $\rho$ provides an event-based description of pile-up activity, in contrast to the variables used in the 2011 calibration. This leads to improvements in the resolution and the rejection of pile-up jets. Furthermore, the method is less sensitive to mismodelings of the pile-up activity. The use of the jet area allows the same correction to be used to any jet regardless of the clustering mechanism, except for a small residual correction factor (see Figure 5.7).

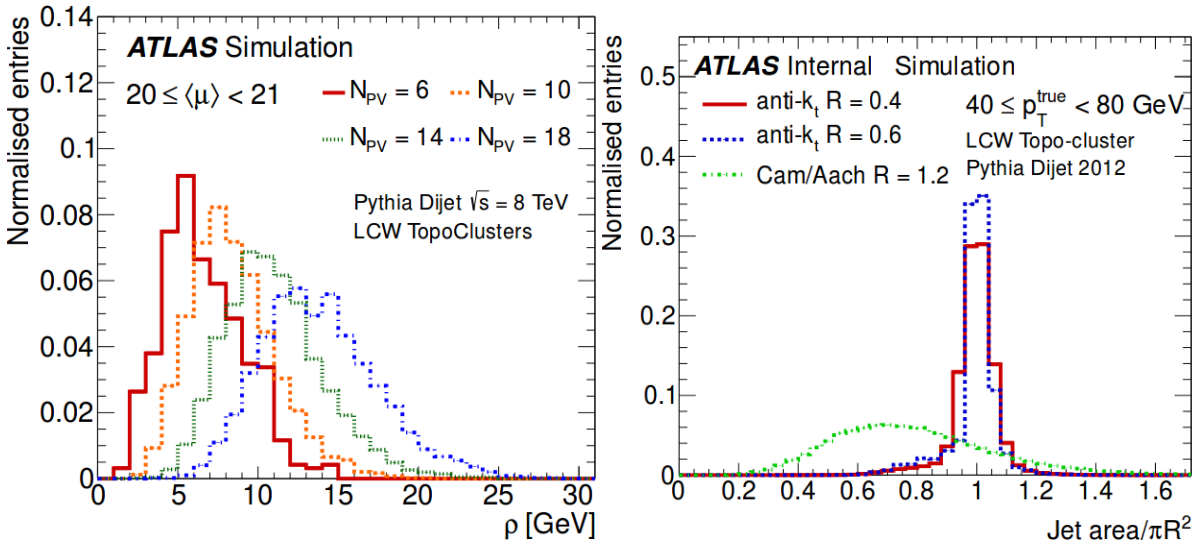


Figure 5.7: Distributions of $\rho$ (left) for an average number of interactions between 20 and 21 [150] and the jet-area (right) for different jet-clustering algorithms [150].

The clustering-independent pile-up correction is given by:

$$p_{\text{T}}^{\text{jet,corrected}} = p_{\text{T}}^{\text{jet,uncorrected}} - \rho A_{\text{j}}. \tag{5.11}$$

The clustering-dependent residual correction is obtained by comparing reconstructed MC dijet events to their truth values. This residual correction is very small in the central region.

The additional jet energy correction is based on comparisons between data and MC using in-situ balance techniques [148].

### 5.3.3 Jet definitions

Jet candidates for the top-quark mass measurement are defined as follows [126]:

- Jets must be reconstructed using the anti-$k_t$ algorithm with $R = 0.4$, and using the EM+JES calibration.
- For all events, if there are reconstructed jets close to an electron within $\Delta R < 0.2$, the jet that is the closest to the electron is removed.

In order to ensure jet quality in the events used for the analysis, events that fulfil one of the following conditions are rejected:

- Events with identified bad jets [152], i.e., jets that are not associated with real energy deposits in the calorimeters.

- Events with jets with JVF < 0.75.

For the $t\bar{t}Z$ cross-section measurement, the JVF requirement is relaxed: only events with central low-energy jets ($p_{\mathrm{T}} < 50$ GeV and $|\eta| < 2.4$) with JVF < 0.5 are removed.

### 5.3.4 Energy resolution

The jet energy resolution (JER) is measured in situ using the dijet balance method. The dijet balance method relies on the approximate balance of the transverse momentum of the jets in a dijet event. For each event, the degree of asymmetry between the transverse momenta of the jets can be characterized by [153]:

$$A = \frac{p_{T,1} - p_{T,2}}{p_{T,1} + p_{T,2}}, \tag{5.12}$$

where $p_{T,1}$ and $p_{T,2}$ are the transverse momenta of the jets in the dijet event (ordered randomly).

The distribution of $A$ is expected to be Gaussian, where the value of the standard deviation can be associated with the individual jet energy resolutions by:

$$\sigma(A) \approx \frac{1}{\sqrt{2}} \frac{\sigma(p_{\mathrm{T}})}{p_{\mathrm{T}}}. \tag{5.13}$$

Figure 5.8 shows an example of the distribution of $A$ in data and MC simulation. The JER in data and MC simulation agrees within the uncertainties for 2011 data, and also agree in the 2012 data except for a few regions of the $p_{\mathrm{T}} - \eta$ space [153]. Therefore, the ATLAS top working group recommendation is to not apply any jet energy resolution correction, but to consider this effect in the estimation of the JER systematic uncertainty [135, 148].

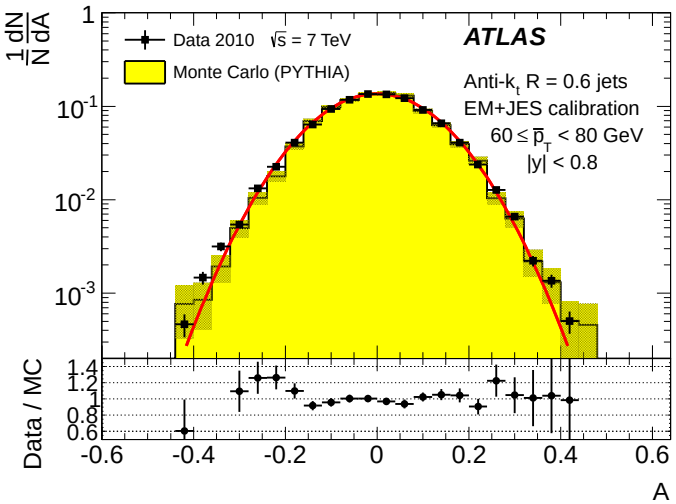


Figure 5.8: Distribution of the dijet $p_{\mathrm{T}}$ asymmetry in data and MC simulation. The data is fitted with a Gaussian function. The hashed areas show the statistical uncertainty. [153].

### 5.3.5 Reconstruction efficiency

The jet reconstruction efficiency (JRE) is measured using a tag-and-probe method [154]. The technique determines the efficiency to match calorimeter jets to track jets[7] in dijet back-to-back events.

The track jet with the highest transverse momentum is defined as the tag object, whereas a second track jet balancing the first track jet in $\phi$ is considered the probe object and must satisfy $\Delta\phi > 2.8$ with respect to the first track jet. Only events with exactly one track jet satisfying $\Delta\phi > 2.8$ are used.

The efficiency is measured by matching calorimeter jets to the probe jet. A calorimeter jet is considered matched to the probe jet if they are within $\Delta R < 0.4$. The observed difference in data and MC simulation is used to correct the MC events (see Figure 5.9). This is done by randomly discarding jets in the MC-generated events based on the magnitude of the data-MC difference [135, 148].

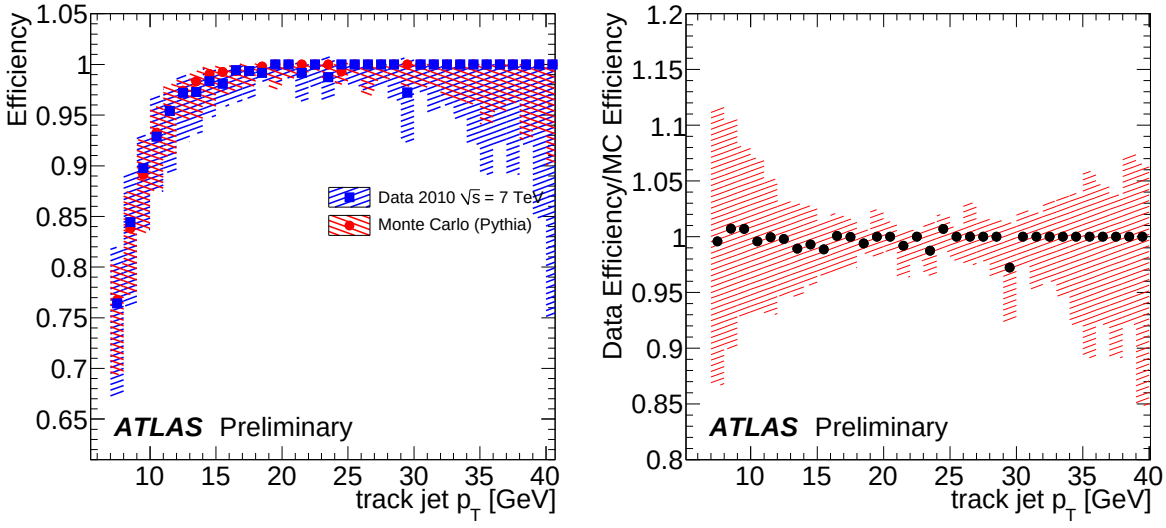


Figure 5.9: Left: calorimeter jet reconstruction efficiency (JRE) with respect to track jets. Right: difference in JRE between data and MC simulation. The hashed areas show the total uncertainty [154].

## 5.4 *b*-tagging

The process of identifying a jet as a $b$-jet, i.e., a jet that originates from a hard-process bottom quark, is called $b$-tagging. Since the top quark decays almost exclusively via $t \to Wb$ and many background processes do not produce $b$-jets, the ability to identify $b$-jets is an excellent tool to reject these backgrounds.

The process of $b$-tagging relies on the ability to identify properties of $b$-jets that separate them from $c$-jets or light jets (i.e., $u$-jets, $d$-jets, $s$-jets and jets from gluons and $\tau$). The main property used by $b$-tagging algorithms is the fact that bottom quarks form $b$-hadrons, which have a relatively long lifetime, of the order of $10^{-12}$ s. $b$-hadrons travel an average distance of roughly 2 mm (assuming $p_{\mathrm{T}} = 25$ GeV) in the detector before decaying, producing a displaced secondary vertex and the corresponding displaced tracks.

In this thesis, the so-called MV1 algorithm is used [155], using the calibration points giving a $b$-jet tagging efficiency of 70% and 85%. MV1 is a neutral-network algorithm that uses the outputs of the

[7] Jets reconstructed using the inner detector.

IP3D, SV1 and JetFitter $b$-tagging algorithms. Figure 5.10 shows the light jet rejection rate as a function of the $b$-tagging efficiency, while a short description of each algorithm is given in the following paragraphs.

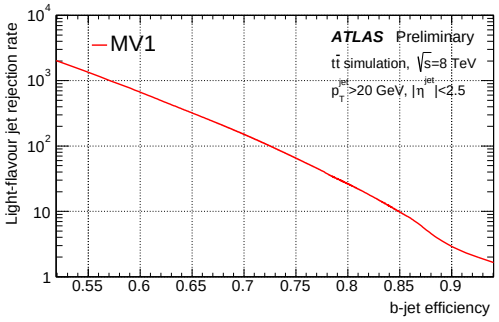


Figure 5.10: Performance of the MV1 algorithm [155].

The IP3D algorithm [156] combines the information on the impact-parameter significance of all the tracks associated to a jet, where the tracks are required to have $p_{\mathrm{T}} > 1$ GeV and at least 7 quality hits (pixel or SCT hits). At least one of these hits should be in the b-layer and another one should be from the pixel detector. From MC simulations, the two-dimensional distribution of the transverse and longitudinal impact-parameter significance can be built for the $b$-jet and light-jet hypotheses. This distribution is smoothed and normalized to be used in a likelihood ratio: the inputs from each jet are compared to this distribution in order to obtain a weight, which is a discriminant on how likely the jet is a $b$-jet and how incompatible it is with a light jet.

SV1 [156] is a secondary-vertex-based algorithm and tries to reconstruct the secondary vertex of the $b$-hadron involved in the production of the $b$-jet. It uses a loose track-quality requirement (at least 7 quality hits, at least one hit in the pixel detector and $p_{\mathrm{T}} > 0.4$ GeV) in order to improve the reconstruction and remove long-lived particles[8], photon conversions or hadronic interactions. The algorithm is able to determine the decay length in three dimensions, which is used to define a signed decay-length significance using the uncertainty of the decay-length estimation and comparing the direction of the decay length and the direction of the reconstructed jet.

In order to improve the discriminating power, three additional vertex properties are used in the SV1 algorithm: the invariant mass of all the (loose) tracks associated with the vertex, the ratio between the sum of all the energies of the tracks in the vertex divided by the sum of all the energy of the tracks in the jet, and the number of two-tracks vertices. A likelihood is built based on the two-dimensional distribution of the first two observables and the one-dimensional distribution of the third observable. Finally, in order to further increase the discriminating power, the $\Delta R$ of the vector characterizing the position of the secondary vertex and the vector characterizing the jet axis is added to the likelihood computation.

The JetFitter algorithm [156, 157] uses the information on the topology of weak $b$-flavored hadrons and $c$-flavored hadrons decays inside the jet. It uses a Kalman filter [158] to reconstruct vertices and estimate the flight path of the parent $b$-hadron.

The $b$-tagging efficiency calibration can be performed using muon-based methods. Muon-based methods, such as the $p_{\mathrm{T}}^{\mathrm{rel}}$ method, select jets that contain a muon, exploiting the semileptonic decay of $b$-hadrons to obtain a $b$-jet-enriched selection [159]. For example, the $p_{\mathrm{T}}^{\mathrm{rel}}$ method uses the momentum of the muon transverse to the combined muon plus jet axis (called $p_{\mathrm{T}}^{\mathrm{rel}}$). Muons from $b$-hadron decays

[8] Examples:$K_s$ and $\Lambda$.

have a harder $p_{\mathrm{T}}^{\mathrm{rel}}$ distribution than their $c$-jet and light-jet counterparts. The fraction of $b$-jets, $c$-jets and light jets in data for a given selection can be determined using the MC-based templates for the $p_{\mathrm{T}}^{\mathrm{rel}}$ distribution of $b$-jets, $c$-jets and light jets and applying a template fit to data.

The $b$-tagging efficiency calibration can also be done in the $t\bar{t}$ single-lepton or dilepton channels, since these channels contain two $b$-jets, where both channels are expected to give similar results. The calibration using the $t\bar{t}$ dilepton channel is straightforward. A standard dilepton selection can be applied, but any cut that has $b$-tagging requirements is removed to avoid the introduction of a bias. The calibration in the $t\bar{t}$ single-lepton channel is more elaborate and will be discussed later in this chapter.

### 5.4.1 *b*-tagging efficiency calibration using the tag-counting method

The use of the different $b$-tagging algorithms to select events with $b$-tagged jets can alter the agreement between the results of data and MC simulations, due to deficiencies in the MC modeling. Therefore, correction factors must be applied to the MC events to fix this effect.

One of the methods to determine these corrections is the tag-counting method [160]. For an arbitrary selection of jets, the fraction of $b$-tagged jets (using a given $b$-tagging algorithm) in data is given by:

$$f_{b\text{-tagged}} = \epsilon_b f_{b\text{-jets}} + \epsilon_c f_{c\text{-jets}} + \epsilon_{\mathrm{l}} f_{\mathrm{l}\text{-jets}} + \epsilon_{\mathrm{QCD}} f_{\mathrm{QCD}\text{-jets}}, \tag{5.14}$$

where $\epsilon_X$ is the probability of jets of type $X$ to be tagged and $f_{X\text{-jets}}$ is the true fraction of jets originating from the source $X$ in the selection. Light jets are identified by the subscript l, while the label "QCD" refers to the QCD multijet background.

The fraction of $b$-tagged jets selected in data can be determined directly from data:

$$f_{b\text{-tagged}} = \frac{N_{\text{tagged}}^{\text{data}}}{N_{\text{all jets}}^{\text{data}}}, \tag{5.15}$$

where $N_{\text{tagged}}^{\text{data}}$ is the number of $b$-tagged jets in data, and $N_{\text{all jets}}^{\text{data}}$ is the total number of jets selected in data.

The values of the jet fractions $f_{b\text{-jets}}$, $f_{c\text{-jets}}$ and $f_{\mathrm{l}\text{-jets}}$ are measured from MC simulations, while the value of $f_{\mathrm{QCD}\text{-jets}}$ is measured using the matrix method (see Section 4.3.2). The estimate of the expected number of jets selected in data is given by:

$$N_{\text{total}}^{\text{est.}} = N_{b\text{-jets}} + N_{c\text{-jets}} + N_{\mathrm{l}\text{-jets}} + N_{\mathrm{QCD}\text{-jets}}, \tag{5.16}$$

where $N_{b\text{-jets}}$, $N_{c\text{-jets}}$ and $N_{\mathrm{l}\text{-jets}}$ are the expected number of $b$-jets, $c$-jets and light jets as predicted by MC simulations, and $N_{\mathrm{QCD}\text{-jets}}$ is the number of jets selected from QCD multijet events, as estimated by the matrix method. Therefore, all the fractions can be computed using:

$$f_{X\text{-jets}} = \frac{N_{X\text{-jets}}}{N_{\text{total}}^{\text{est.}}}. \tag{5.17}$$

The value of the tagging efficiencies $\epsilon_c$ and $\epsilon_{\mathrm{l}}$ are also computed from MC simulations using:

$$\epsilon_X = \frac{N_{\text{tagged}}^{\text{truth-}X}}{N_{\text{all}}^{\text{truth-}X}}, \tag{5.18}$$

where $N_{\text{all}}^{\text{truth-}X}$ is the total number of jets that originate from the source $X$ (obtained from MC truth[9] information), and $N_{\text{tagged}}^{\text{truth-}X}$ is the number of these jets that are $b$-tagged.

The tagging efficiency of QCD multijet events ($\epsilon_{\text{QCD}}$) is estimated by:

$$\epsilon_{\text{QCD}} = \frac{N_{\text{tagged}}^{\text{QCD}}}{N_{\text{all}}^{\text{QCD}}}, \tag{5.19}$$

where $N_{\text{all}}^{\text{QCD}}$ are all the selected jets in QCD multijet events and $N_{\text{tagged}}^{\text{QCD}}$ is the number of these jets that are $b$-tagged.

The method to compute the value of almost all the components in Equation 5.14 has been defined in the previous paragraph. The only missing component is the $b$-jet tagging efficiency ($\epsilon_b$), which can be then measured from data using:

$$\epsilon_b^{\text{data}} = \frac{f_{b\text{-tagged}} - \epsilon_c f_{c\text{-jets}} - \epsilon_{\text{l}} f_{\text{l-jets}} - \epsilon_{\text{QCD}} f_{\text{QCD-jets}}}{f_{b\text{-jets}}}. \tag{5.20}$$

Another estimate of $\epsilon_b$ can be computed using Equation 5.18 with simulation datasets, which provides a MC-based $b$-jet tagging efficiency ($\epsilon_b^{\text{MC}}$).

These two efficiencies are used to define the correction factor:

$$\alpha_{\text{corr.}} = \frac{\epsilon_b^{\text{data}}}{\epsilon_b^{\text{MC}}}, \tag{5.21}$$

where $\epsilon_b^{\text{data}}$ and $\epsilon_b^{\text{MC}}$ are the $b$-jet tagging efficiency estimated from data and simulation, respectively. The computed value ($\alpha_{\text{corr.}}$) is the scale factor needed to correct the MC simulations.

### 5.4.2 *b*-tagging calibration in the $t\bar{t}$ single-lepton channel

In order to select $t\bar{t}$ single-lepton events for the $b$-tagging calibration, the following single-lepton selection is applied:

- Data events must pass the good run list filter, as explained in Section 4.1.
- At least one of the lepton triggers has fired (see Section 4.1). These lepton triggers require the trigger lepton to have $p_{\text{T}} > 25$ GeV.
- The trigger object must match a reconstructed lepton within $\Delta R < 0.15$.
- The event must contain at least one good primary vertex with at least five associated tracks with $p_{\text{T}} > 400$ MeV.
- Events with cosmic muons are rejected [137]. An event is considered to have cosmic muons if it contains a pair of muons with large azimuthal separation ($\Delta\phi > 3.1$) and large opposite-signed impact parameters ($d_0^{\mu_1} \times d_0^{\mu_2} < 0$, $|d_0^{\mu_1}| > 0.5$ and $|d_0^{\mu_2}| > 0.5$).
- Exactly one reconstructed lepton with $p_{\text{T}} > 25$ GeV.

[9] MC truth information is provided by the MC generator. It can identify the hard-process particle associated to a given MC-generated physics object.

- The events must not have bad jets, i.e., there is a LooseBadMinus jet in the AntiKt4TopoEMJets collection with $p_{\mathrm{T}} > 20$ GeV and $E > 0$ [161].
- The event is rejected if an electron and a muon share an inner detector track.
- At least 4 jets with $p_{\mathrm{T}} > 20$ GeV.
- At least 1 $b$-tagged jet using the MV1 algorithm at 70% efficiency (MV1@70%).

In addition to the requirements presented above, one of the following orthogonal sets is used in order to create a QCD-enriched or a QCD-depleted event selection:

- Selection used to supressed QCD multijet background events:
  - For the electron channel, $E_{\mathrm{T}}^{\mathrm{miss}} > 30$ GeV and $m_{\mathrm{T}} > 30$ GeV, where $m_{\mathrm{T}}$ is the transverse mass of the leptonic $W$ boson, defined as: $m_{\mathrm{T}} = \sqrt{\left(E_{\mathrm{T}}^{\ell} + E_{\mathrm{T}}^{\mathrm{miss}}\right)^2 - \left(\vec{p}_{\mathrm{T}}^{\,\ell} + \vec{p}_{\mathrm{T}}^{\,\mathrm{miss}}\right)^2}$.
  - For the muon channel, $E_{\mathrm{T}}^{\mathrm{miss}} > 20$ GeV and $\left(m_{\mathrm{T}} + E_{\mathrm{T}}^{\mathrm{miss}}\right) > 60$ GeV.
- Selection used to select QCD multijet events:
  - For the electron channel, 5 GeV $< E_{\mathrm{T}}^{\mathrm{miss}} < 30$ GeV and $m_{\mathrm{T}} < 30$ GeV.
  - For the muon channel, 5 GeV $< E_{\mathrm{T}}^{\mathrm{miss}} < 15$ GeV or $\left(m_{\mathrm{T}} + E_{\mathrm{T}}^{\mathrm{miss}}\right) < 60$ GeV.

In contrast to the dilepton case, $b$-tagging requirements are needed in the single-lepton channel to provide a selection with reasonable purity. But the introduction of these requirements could bias the selection of the jets used in the calibration. This bias can be avoided by using events where the leading-$p_{\mathrm{T}}$ jet is $b$-tagged, and only selecting the second, third and fourth jets (ordered according to their $p_{\mathrm{T}}$) in the event for the calibration (L234 region). However, this strategy reduces considerably the amount of selected high-$p_{\mathrm{T}}$ jets, which reduces the quality of the calibration for jets with large energy. In order to increase the amount of high-$p_{\mathrm{T}}$ jets used in the calibration, the leading-$p_{\mathrm{T}}$ jet is also selected in events where the subleading-$p_{\mathrm{T}}$ jet is $b$-tagged (L1 region).

In summary, the selection of jets (in events passing the event selection) used in the calibration, where the jets are ordered according to their transverse momentum, is:

- The first jet is included if the second jet is tagged by the default $b$-tagging algorithm (L1).
- The second, third and fourth jets are included if the first jet is tagged by the default $b$-tagging algorithm (L234).

The selected jets are then separated in different $p_{\mathrm{T}}$ ranges ([25, 30, 40, 50, 60, 75, 90, 110, 140, 200, 300]), different $b$-tagging algorithms and different efficiency benchmarks [162] in order to provide the correction factors for different $b$-tagging algorithms, efficiency benchmarks and $p_{\mathrm{T}}$ regions.

The distributions of the $p_{\mathrm{T}}$ of the four leading jets for the electron and muon channels for 2012 data are shown in Figure 5.11.

The preliminary 2012 measurement of the $b$-tagging efficiency ($\epsilon_b^{\mathrm{data}}$) and the correction scale factors ($\alpha_{\mathrm{corr.}}$) for the MV1 algorithm at the 70% working point are shown in Figure 5.12. As an example, the values and uncertainties taking part in the computation of the scale factor in the bin 75 GeV $< p_{\mathrm{T}} <$ 90 GeV for MV1@70% are shown in Table 5.1. These results were part of a larger effort that ultimately provided the $b$-tagging calibration for 2012 data. The final values of $\alpha_{\mathrm{corr.}}$ and the tools to apply the $b$-tagging efficiency correction are provided by the ATLAS Flavour Tagging Working Group [163] for 2011 [160] and 2012 data [164, 165].

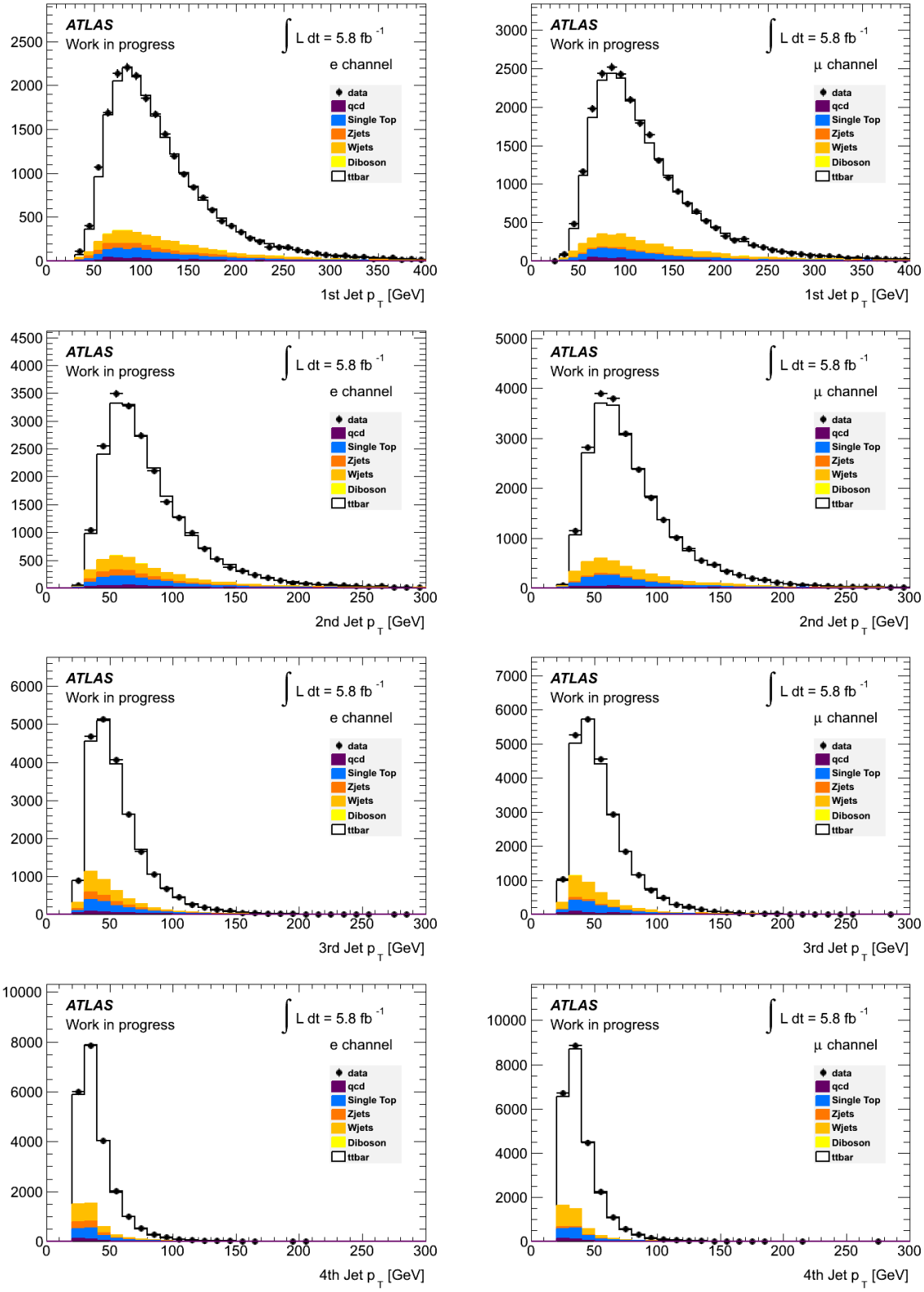


Figure 5.11: $p_{\mathrm{T}}$ distributions of the four leading jets for the $t\bar{t}$ single electron (left) and single muon (right) channels.

| Description | Value | Stat.(%) | Syst-(%) | Syst+(%) |
|---|---|---|---|---|
| $f_{\text{l-jets}}$ | 0.56 | 0.2 | -3.9 | 3.6 |
| $f_{c\text{-jets}}$ | 0.11 | 0.7 | -5.8 | 8.2 |
| $f_{b\text{-jets}}$ | 0.33 | 0.4 | -5.8 | 6 |
| $f_{\text{QCD-jets}}$ | 0.01 | 3.1 | -100 | 100 |
| $\epsilon_{\text{l}}$ | 0.01 | 3.6 | -3.3 | 4.9 |
| $\epsilon_c$ | 0.24 | 1.4 | -7.5 | 6.9 |
| $\epsilon_b^{\text{MC}}$ | 0.75 | 0.2 | -1.4 | 1.6 |
| $\epsilon_{\text{QCD}}$ | 0.18 | 20.8 | -100 | 0 |
| $f_{b\text{-tagged}}$ | 0.3 | 1.7 | -0 | 0 |
| $\epsilon_b^{\text{data}}$ | 0.8 | 1.9 | -6.2 | 6.1 |
| $\alpha_{\text{corr.}}$ | 1.07 | 1.9 | -6.8 | 6.8 |

Table 5.1: Computation of the scale factor for the $p_{\text{T}}$ range 75.0 GeV $< p_{\text{T}} <$ 90.0 GeV for the MV1 algorithm at the 70% working point. The largest contributions to the total systematic uncertainty are from the background normalization, the flavor composition and systematic uncertainties associated with the MC generators.

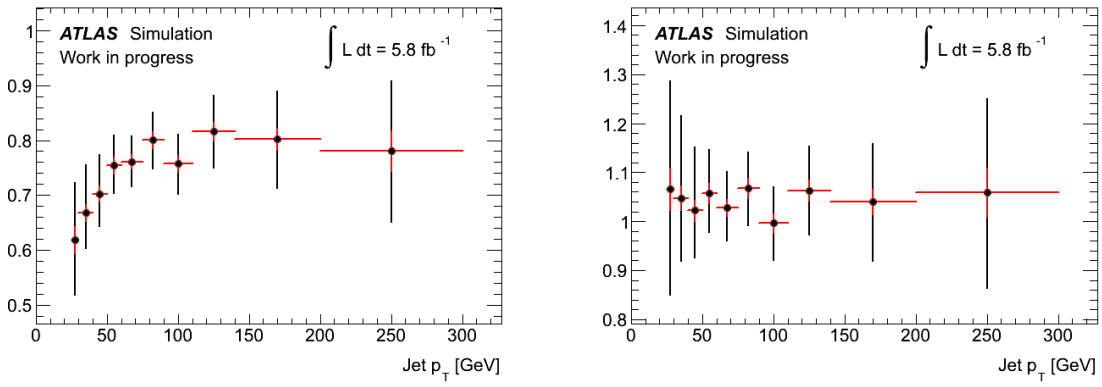


Figure 5.12: Measured $b$-tagging efficiency and $b$-tagging correction scale factor for MV1@70%. The red bars represent the statistical uncertainty, while the black bars represent the systematic uncertainty.

## 5.5 Missing transverse momentum

Unlike the other physics objects presented in this chapter, the missing transverse momentum ($E_{\mathrm{T}}^{\mathrm{miss}}$) is not related to a hard-process particle, but to a whole group of hard-process particles. The missing transverse momentum is a measure of the sum of the momenta of all the invisible particles, i.e., hard-process particles that cannot be detected by the ATLAS detector. Neutrinos escape detection in ATLAS and are the main source of missing transverse momenta in the Standard Model.

For both analyses presented in this thesis, it is very important to have a precise measurement of the missing transverse momentum, since the $t\bar{t}$ dilepton channel produces two neutrinos.

The definition of missing transverse momentum derives from the conservation of momentum in a hard process:

$$\vec{p}_{\mathrm{T}}^{\,\text{initial state}} = \sum_{i}^{\text{all particles}} \vec{p}_{\mathrm{T}}^{\,i} = \sum_{i}^{\text{visible}} \vec{p}_{\mathrm{T}}^{\,i} + \sum_{i}^{\text{invisible}} \vec{p}_{\mathrm{T}}^{\,i}. \tag{5.22}$$

If the initial state of the hard process is at rest in the transverse plane, then the following equation is valid:

$$\vec{p}_{\mathrm{T}}^{\,\mathrm{miss}} \equiv \sum_{i}^{\text{invisible}} \vec{p}_{\mathrm{T}}^{\,i} = -\sum_{i}^{\text{visible}} \vec{p}_{\mathrm{T}}^{\,i}. \tag{5.23}$$

A full definition of the missing momentum is unsuited for ATLAS, since the longitudinal component of the momentum of the initial state cannot be estimated reliably on an event-by-event basis. On the other hand, assuming that the initial state is at rest in the transverse plane is reasonable.

### 5.5.1 Cell-based missing transverse momentum

The missing transverse momentum is computed as the sum of three components [89]:

$$\vec{p}_{\mathrm{T}}^{\,\mathrm{miss}} = \vec{p}_{\mathrm{T}}^{\,\mathrm{miss}}\,(\mathrm{Calo}) + \vec{p}_{\mathrm{T}}^{\,\mathrm{miss}}\,(\mathrm{Muon}) + \vec{p}_{\mathrm{T}}^{\,\mathrm{miss}}\,(\mathrm{Cryo})\,, \tag{5.24}$$

where $\vec{p}_{\mathrm{T}}^{\,\mathrm{miss}}$ (Calo), $\vec{p}_{\mathrm{T}}^{\,\mathrm{miss}}$ (Muon) and $\vec{p}_{\mathrm{T}}^{\,\mathrm{miss}}$ (Cryo) are the calorimeter component, the muon-spectrometer component and corrections for energy loss in the cryostat, respectively.

The calorimeter component is computed from the vectorial sum of all the calorimeters topological clusters of a given event. This vectorial sum can be interpreted as the sum of the momentum of all visible particles, except for the muons. Formally, $\vec{p}_{\mathrm{T}}^{\,\mathrm{miss}}$ (Calo) can be defined as:

$$\vec{p}_{\mathrm{T}}^{\,\mathrm{miss}}\,(\mathrm{Calo}) = -\sum_{\text{all TC}} \vec{p}_{\mathrm{T}}, \tag{5.25}$$

where "TC" stands for "topological clusters". The result from Equation 5.25 is roughly 30% shifted from the true $\vec{p}_{\mathrm{T}}^{\,\mathrm{miss}}$ (Calo) value. To correct this behavior, the contribution of topological clusters that are associated with a high-energy physics object are replaced by the energy of these reconstructed objects (since they are better calibrated) [89].

The muon-spectrometer component is computed from the transverse momenta of the reconstructed muons:

$$\vec{p}_{\mathrm{T}}^{\,\mathrm{miss}}\,(\mathrm{Muon}) = -\sum_{\text{all muons}} \vec{p}_{\mathrm{T}}. \tag{5.26}$$

The muons used in Equation 5.26 are reconstructed in the pseudorapidity range $|\eta| < 2.7$, without applying any $p_{\mathrm{T}}$ threshold. In order to avoid contamination from fake muons, only track-matched

muons (i.e., combined muons, defined in Section 5.2.1) are used for the region with $|\eta| < 2.5$. For $2.5 < |\eta| < 2.7$, where no information from the inner detector is possible, only the muon spectrometer is used (i.e., standalone muons). In both cases, the muon momentum measured in the muon spectrometer is used, since the energy lost in the calorimeters is already included in the calorimeter term.

The cryostat term arises from the loss of energy that takes place when particles transverse the cryostat [1], which is located between the electromagnetic and the hadronic calorimeter. This energy loss can be computed from the energies measured in the third (last) layer of the electromagnetic calorimeter and the first layer of the hadronic calorimeter (layers ordered from the center of the detector):

$$\vec{p}_{\mathrm{T}}^{\,\mathrm{miss}}\,(\mathrm{Cryo}) = -\sum_{\text{all jets}} E^{\text{jet Cryo}}\,\hat{p_{\mathrm{T}}}, \tag{5.27}$$

where, for each jet, $\hat{p_{\mathrm{T}}}$ is the direction of the transverse momentum of the jet and $E^{\text{jet Cryo}}$ is computed as:

$$E^{\text{jet Cryo}} = w^{\mathrm{Cryo}}\sqrt{E_{\mathrm{ECal3}} \cdot E_{\mathrm{HCal1}}}, \tag{5.28}$$

with $w^{\mathrm{Cryo}}$ being a calibration weight, $E_{\mathrm{ECal3}}$ being the jet energy measured in the third layer of the electromagnetic calorimeter and $E_{\mathrm{HCal1}}$ being the jet energy measured in the first layer of the hadronic calorimeter. The cryostat term is particularly important for high-$p_{\mathrm{T}}$ jets, with a contribution of roughly 5% for jets above 500 GeV [89].

### 5.5.2 Performance and resolution of the $E_{\mathrm{T}}^{\mathrm{miss}}$ reconstruction

In order to determine the performance of the $E_{\mathrm{T}}^{\mathrm{miss}}$ reconstruction, the $E_{\mathrm{T}}^{\mathrm{miss}}$ and $\phi^{\mathrm{miss}}$ (azimuthal angle of $\vec{p}_{\mathrm{T}}^{\,\mathrm{miss}}$) distributions of the minimum bias, dijet and $Z \to \ell\ell$ events in data and simulation are compared, as documented in Ref. [166]. These channels allow the study of the $E_{\mathrm{T}}^{\mathrm{miss}}$ without having to rely on the MC detector simulations.

For the minimum bias events[10], there are some disagreements in some distributions (see Figure 5.13). In contrast, a reasonable agreement is found for all basic distributions for dijet events. These disagreements in the minimum bias events are attributed to the modeling of soft particles in simulation.

The $Z \to \ell\ell$ channel is also useful to evaluate the performance of the $E_{\mathrm{T}}^{\mathrm{miss}}$ reconstruction due to its clean signature, large cross section and the fact that $E_{\mathrm{T}}^{\mathrm{miss}} = 0$ in the hard process. Figure 5.14 shows a reasonable agreement between the $E_{\mathrm{T}}^{\mathrm{miss}}$ and $\phi^{\mathrm{miss}}$ distributions in data and simulation of $Z \to ee$ and $Z \to \mu\mu$ events [166].

The $E_{\mathrm{T}}^{\mathrm{miss}}$ resolution can be measured in minimum bias, dijet and $Z \to \ell\ell$ events, exploiting the fact that $E_{\mathrm{T}}^{\mathrm{miss}} = 0$ is expected. The resolution of the $E_{\mathrm{T}}^{\mathrm{miss}}$ components ($E_x^{\mathrm{miss}}$ and $E_y^{\mathrm{miss}}$) can be determined assuming that their true value is zero and fitting the combined distributions with a Gaussian. The resolution for different $\sum E_{\mathrm{T}}$ regions can be determined, where $\sum E_{\mathrm{T}}$ is the total transverse energy in the calorimeters, as shown in Figure 5.15. These results allow to parametrize the resolution as a function of $\sum E_{\mathrm{T}}$:

$$\sigma = k\sqrt{\sum E_{\mathrm{T}}}, \tag{5.29}$$

where the value of $k$ ranges between 0.42 $\mathrm{GeV}^{\frac{1}{2}}$ for $Z \to \ell\ell$ events to 0.51 $\mathrm{GeV}^{\frac{1}{2}}$ for dijet events [166].

[10] Selection using the minimum requirements necessary to ensure that an inelastic collision ocurred.

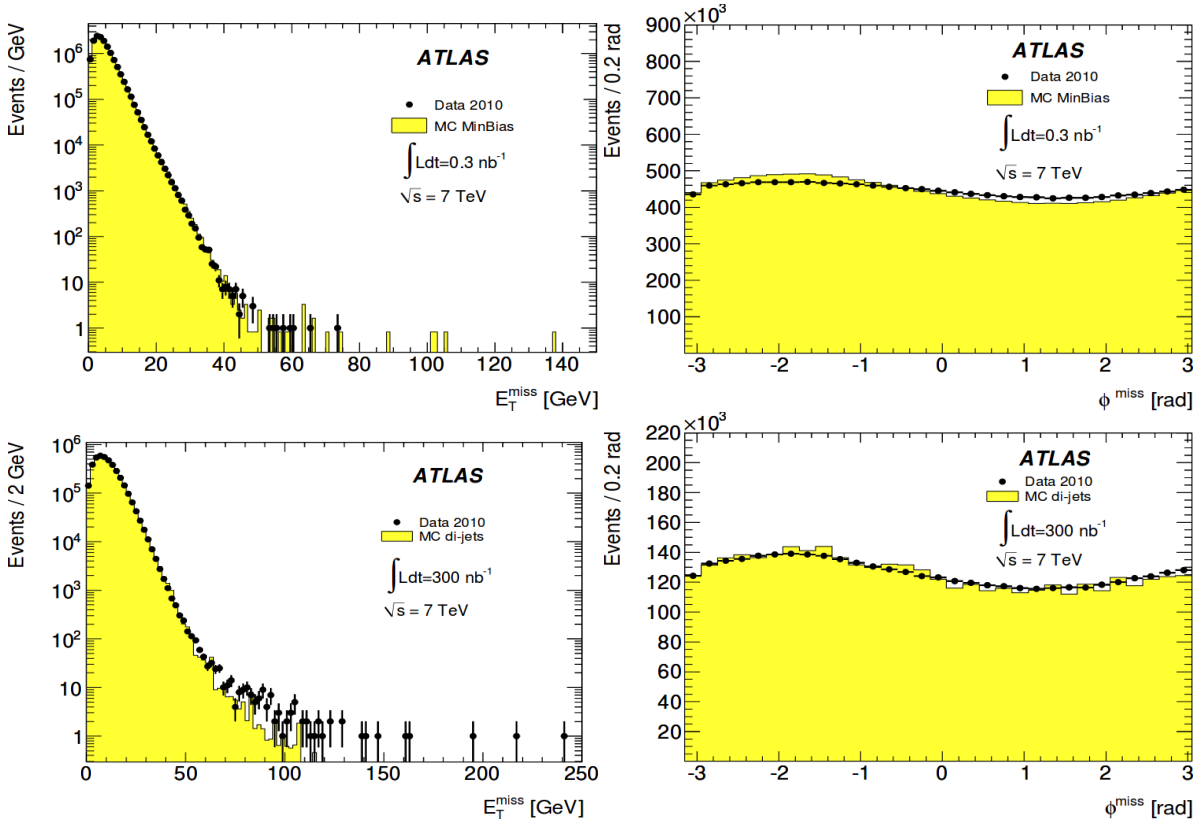


Figure 5.13: Comparison of the $E_{\mathrm{T}}^{\mathrm{miss}}$ and $\phi^{\mathrm{miss}}$ distributions between data and simulation for (top) minimum bias and (down) dijet events [166].

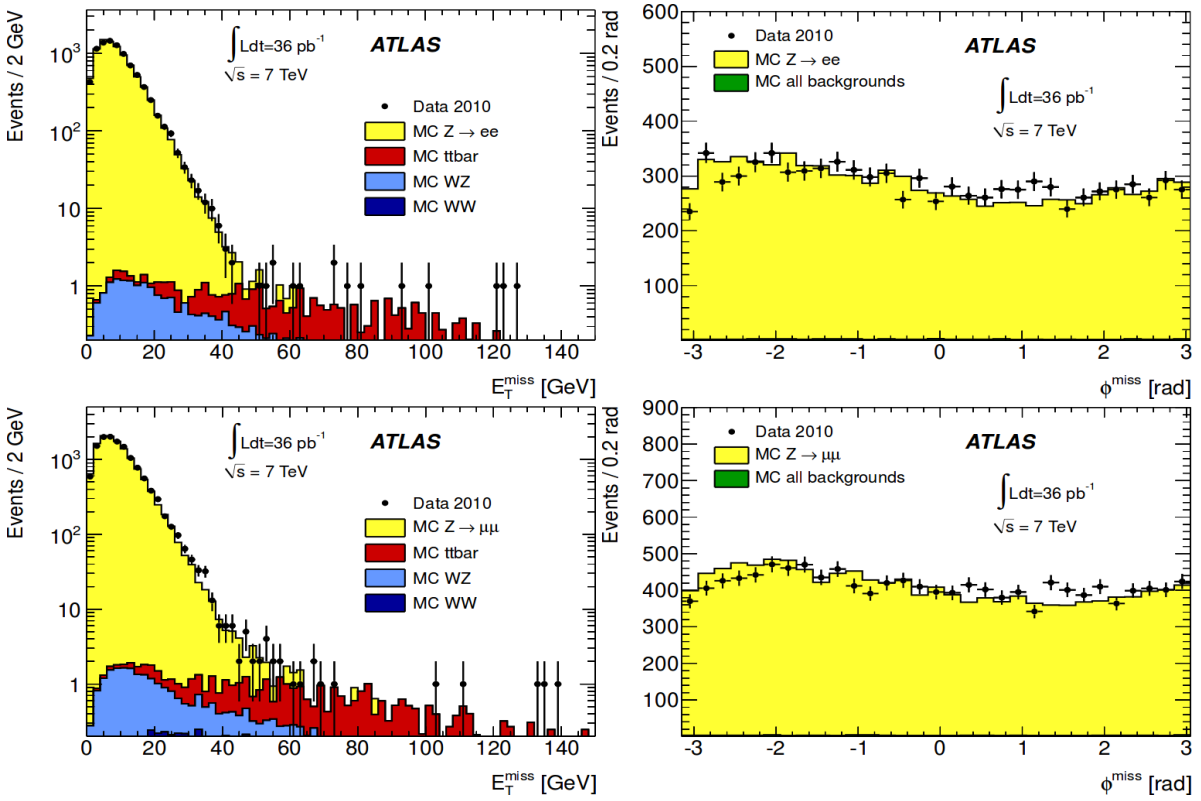


Figure 5.14: Comparison of the $E_{\mathrm{T}}^{\mathrm{miss}}$ and $\phi^{\mathrm{miss}}$ distributions between data and simulation for (top) $Z \rightarrow ee$ and (down) $Z \rightarrow \mu\mu$ events [166].

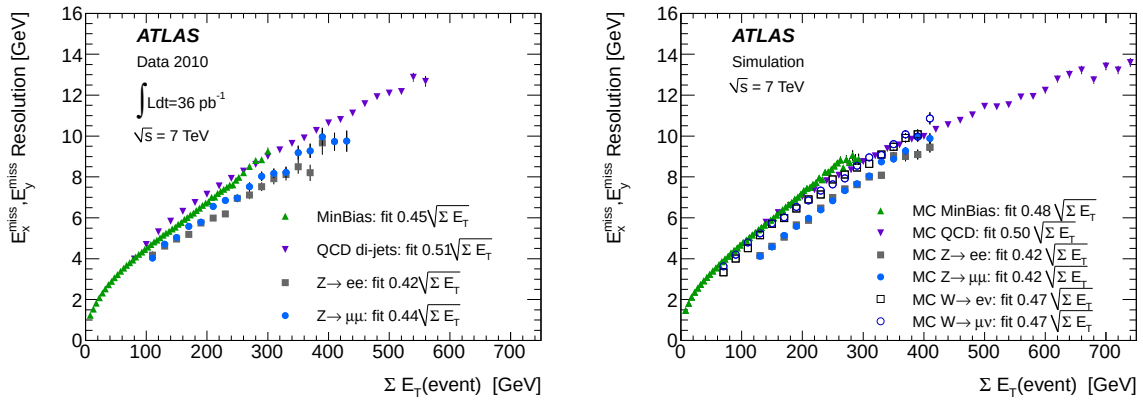


Figure 5.15: $E_{\mathrm{T}}^{\mathrm{miss}}$ resolution as a function of $\sum E_{\mathrm{T}}$ in (left) data and (right) simulation [166].

### 5.5.3 $E_{\mathrm{T}}^{\mathrm{miss}}$ linearity

The $W \to \ell\nu$ channel has a large cross section and an intrinsic source of $E_{\mathrm{T}}^{\mathrm{miss}}$, i.e., the neutrino, and offers the opportunity to check the linearity of the $E_{\mathrm{T}}^{\mathrm{miss}}$ calculation using simulation events. A measurement of the linearity is defined as follows [166]:

$$\lambda = \frac{E_{\mathrm{T}}^{\mathrm{miss}}\,(\mathrm{reco}) - E_{\mathrm{T}}^{\mathrm{miss}}\,(\mathrm{true})}{E_{\mathrm{T}}^{\mathrm{miss}}\,(\mathrm{true})}, \tag{5.30}$$

where $E_{\mathrm{T}}^{\mathrm{miss}}\,(\mathrm{reco})$ is the computed $E_{\mathrm{T}}^{\mathrm{miss}}$, while $E_{\mathrm{T}}^{\mathrm{miss}}\,(\mathrm{true})$ is the transverse momentum of the hard-process neutrino, as provided by the event generator.

The results of this study are shown in Figure 5.16 for different regions of $E_{\mathrm{T}}^{\mathrm{miss}}\,(\mathrm{true})$. This plot shows a deviation from zero of roughly 5% in the $E_{\mathrm{T}}^{\mathrm{miss}}\,(\mathrm{true}) < 40$ GeV region which is attributed to the impact of the finite resolution of the $E_{\mathrm{T}}^{\mathrm{miss}}$ calculation. Furthermore, the bias is consistently larger in the $W \to \mu\nu$ channel than the $W \to e\nu$ channel in most bins. This is attributed to an underestimation of the muon energy deposited in the calorimeters, where too few calorimeter cells are associated to the reconstructed muon [166].

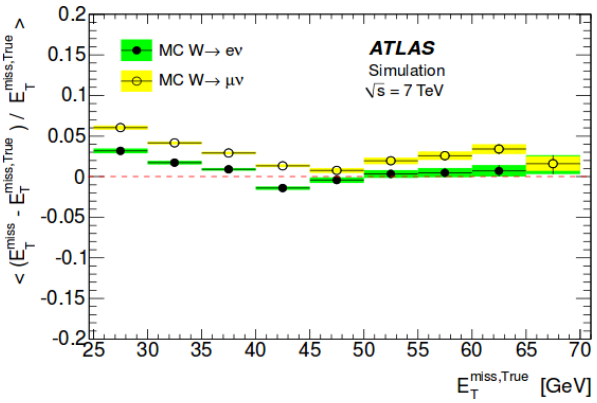


Figure 5.16: Linearity check for different regions of $E_{\mathrm{T}}^{\mathrm{miss}}\,(\mathrm{true})$ performed in MC simulation [166].

CHAPTER 6

# Systematic uncertainties

Systematic uncertainties are uncertainties that are not caused by statistical chance, but rather related to the instruments, techniques, assumptions and calibrations used to make a given measurement.

In the analyses presented in this thesis, the systematic uncertainties arise from several sources: objects calibrations, defective detector parts, accuracy of the simulations, methods and algorithms used, simplifications, and so on.

In Section 6.1 and Section 6.2, the systematic uncertainties associated with physics objects and the normalization-related uncertainties are presented. These uncertainties are common to both analyses. The systematic uncertainties specific to each analysis are presented in the sections dedicated to the respective analysis.

## 6.1 Systematic uncertainties associated with physics objects

As detailed in Chapter 5, the physics objects used in the analyses need to be calibrated. These calibrations are not perfect and have associated uncertainties. These uncertainties are usually propagated to the analyses as follows:

- Perform the analysis with the nominal calibration and obtain the result.
- Repeat the analysis shifting the calibration up by one standard deviation and obtain a modified result.
- Repeat the analysis shifting the calibration down by one standard deviation and obtain a modified result.
- Compare these results and quote the differences as the systematic uncertainty.

The physics-objects-associated systematic uncertainties used in the analyses are listed below:

- electrons:
  - trigger efficiency,
  - reconstruction efficiency,
  - identification efficiency,

  - isolation efficiency and
  - energy scale and resolution.
- Muons:
  - trigger efficiency,
  - isolation efficiency,
  - reconstruction efficiency,
  - momentum scale and
  - momentum resolution.
- Jets:
  - energy scale and $b$-jet energy scale,
  - energy resolution,
  - reconstruction efficiency and
  - $b$-tagging efficiency.
- Missing transverse momentum:
  - pile-up and
  - momentum of soft jets and remaining calorimeter energy.

The effects of all these uncertainties are assumed to be uncorrelated from each other and summed in quadrature to obtain the final uncertainty. Unless explicitly stated otherwise, the full differences between the two shifted results and the nominal result are taken as the uncertainty for each source of systematic uncertainty. Ideally, these differences have opposite signs and the positive and negative uncertainty are defined accordingly. If, for the sake of argumentation, both differences are negative, the difference with the largest absolute value is used as the negative uncertainty, while the positive uncertainty is assumed to be zero. Analogously, if both differences are positive, the largest difference is used as the positive uncertainty, while the negative uncertainty is assumed to be zero.

In the rest of this section, the term symmetrize will refer to the process of assigning the given quantity $x$ as the positive and the negative uncertainty, i.e., $\pm x$.

### 6.1.1 Electron trigger, reconstruction, identification and isolation efficiencies

The calibrations of the electron trigger, reconstruction, identification and isolation efficiencies are measured from $Z \to ee$ and $W \to e\nu$ decays (see Section 5.1.5). These values depend on the $\eta$ and the combined transverse energy ($E_{\mathrm{T}}^{\mathrm{comb.}} = E_{\mathrm{cluster}}/\cosh\eta_{\mathrm{track}}$) of each electron. The calibrations are implemented and applied using the TopElectronSFUtils-00-00-18 tool [167] for the 2011 datasets and the TElectronEfficiencyCorrectionTool package [168] for the 2012 datasets.

### 6.1.2 Electron energy scale and energy resolution

The calibrations of the electron energy scale and the electron energy resolution are based on data-MC comparisons performed in the $Z \to ee$ and $J/\psi \to ee$ decays, as described in Section 5.1.4. The calibration values depend on the direction of the reconstructed electron ($\phi$ and $\eta$) and are applied to the analysis using the EnergyRescaler tool [169], available in the egammaAnalysisUtils-00-02-81 package [170] for

the 2011 datasets and the egammaAnalysisUtils-00-04-58 package [171] for the 2012 datasets. The EnergyRescaler tool also provides the uncertainties of the calibration values, which are used to estimate the associated systematic uncertainties.

### 6.1.3 Muon trigger efficiency

The muon-trigger-efficiency calibration is measured using a tag-and-probe method in the $Z \to \mu\mu$ decay (see Section 5.2.4). The calibration of the 2011 datasets depends on the angular information of the muon candidate direction, both $\phi$ and $\eta$, and the trigger definition used (identified by the data period). This calibration is applied using the MuonSF tool available in the TopMuonSFUtils-00-00-14 package [172].

The 2012 calibration uses parameters similar to its 2011 counterpart [173]. In addition to the angular information of the candidate muons, it also requires the muon reconstruction classification (see Section 5.2.1). The interface to apply this calibration is provided by the LeptonTriggerSF Tool available in the TrigMuonEfficiency-00-02-42 package [174], while the values of the scale factors are provided by the TopMuonSFUtils-00-00-20 package [175].

### 6.1.4 Muon isolation efficiency

The isolation requirements on muons are useful to remove fake muons originating from jets (see Section 5.2.2). For the 2011 datasets, the calibration depends on the data period. The scale factors for each period are stored in the TopMuonSFUtils-00-00-14 package [172], along with the uncertainty in the estimation of these scale factors [132]. For the 2012 data, no scaling is applied, but an uncertainty of $\pm 0.5\%$ per selected muon is applied to account for the small data-MC disagreement observed in $Z \to \mu\mu$ events [133].

### 6.1.5 Muon reconstruction efficiency

The muon-reconstruction-efficiency calibration is performed in the $Z \to \mu\mu$ channel using a tag-and-probe method [142] analogous to the electron case. The calibration values are provided according to the value of the $p_{\mathrm{T}}$, $\phi$ and $\eta$ of the muon candidates by the MuonEfficiencyCorrections-01-01-00 package [176] for the 2011 data. For the 2012 datasets, the calibration also depends on the data period and the muon charge. The calibration values and their uncertainties for the 2012 datasets are provided by the MuonEfficiencyCorrections-02-01-20 package [177].

### 6.1.6 Muon momentum scale and resolution

The muon momentum scale and resolution are measured from $Z \to \mu\mu$, $\Upsilon \to \mu\mu$ and $J/\psi \to \mu\mu$ decays, as presented in Section 5.2.3. There are two calibration components for the muon momentum scale: one associated with the inner detector and one associated with the muon spectrometer. These two components are smeared individually to account for the momentum resolution calibration before the reconstruction of a combined muon.

The systematic uncertainty associated with the muon momentum scale is estimated as the half-difference between the analysis result using the nominal calibration and the analysis result without applying the muon momentum scale [132, 133].

Four different calibration values shifts are used to estimate the systematic uncertainty associated with the muon momentum resolution:

- momentum resolution of the inner detector shifted up by one standard deviation,
- momentum resolution of the inner detector shifted down by one standard deviation,
- momentum resolution of the muon spectrometer shifted up by one standard deviation and
- momentum resolution of the muon spectrometer shifted down by one standard deviation.

The uncertainties associated with the momentum resolution of these subsystems are correlated and are not summed in quadrature. Instead, the overall muon-momentum-resolution uncertainty is estimated as half the maximum difference among the results of all individual shifts and symmetrized [132, 133].

### 6.1.7 Jet energy scale

The calibration of the jet energy scale is discussed in Section 5.3.2. The jet energy scale and its uncertainty are parametrized as a function of the energy, transverse momentum, pseudorapidity, azimuth angle and mass of the jets, as well as the number of reconstructed primary vertices and the degree of pile up present in the event.

For the 2011 datasets, the jet energy scale is corrected in the analysis using the ApplyJetCalibration-00-02-07 package [178], which also provides the uncertainty values and tools to shift the jet energy scale up or down by one standard deviation. The jet energy scale has uncertainties below 1% for jets in the central region of the calorimeter ($|\eta| < 1.2$) with high transverse momentum (55 GeV $< p_{\mathrm{T}} <$ 500 GeV). For jets in the central region with lower transverse momentum, the uncertainty is around 3%.

The jet-energy-scale uncertainty is split in 60 components [179] related to the in-situ analyses used to measure the calibration, to the pseudorapidity intercalibration, to the effect of pile up, to the treatment of jets with high transverse momentum and to MC non closure, i.e., the fact that the MC-simulation datasets used for the calibration are different from the MC-simulation datasets used in the analysis.

In addition to these 60 components, three extra components are added due to flavor and topology uncertainties related to:

- the flavor composition uncertainty of the samples used in the calibration,
- the flavor response uncertainty of the samples and
- the flavor composition and response uncertainty of $b$-jets, also known as $b$-jet-energy-scale uncertainty.

In the top-quark mass measurement, a category-preserving simplified version of 17 components is used instead. This simplified version contains:

- 3 statistical in-situ components,
- 2 detector in-situ components,
- 4 modeling in-situ components,
- 2 mixed components, related to the detector and modeling,
- 2 pseudorapidity-intercalibration components,
- 2 components to account for the effect of pile up,
- 1 component related to MC non closure and

- 1 component to treat jets with high transverse momentum.

The three flavor-and-topology-related uncertainties are added to these 17 components to provide a total of 20 systematic uncertainties components which are added in quadrature to estimate the total uncertainty associated with the jet energy scale.

The JetUncertainties-00-08-07 package [180] provides the tools and calibration values needed to estimate the jet-energy-scale uncertainty for the 2012 datasets [181], split in 56 components similar to its 2011 counterpart. The three flavour-and-topology-related uncertainties described previously in this section are added to these 56 components to estimate the total uncertainty associated with the jet energy scale.

Like the top-quark mass measurement, the $t\bar{t}Z$ cross-section measurement uses a category-preserving simplified version containing 19 components [181]:

- 3 statistical in-situ components,
- 3 detector in-situ components,
- 4 modeling in-situ components,
- 2 mixed components, related to the detector and modeling,
- 2 pseudorapidity-intercalibration components,
- 4 components to account for the effect of pile up,
- 1 component to treat jets with high transverse momentum.

Like in the previous configurations, the three flavor-and-topology-related uncertainties are added to these 19 components to compute the total uncertainty associated with the jet energy scale.

### 6.1.8 Jet energy resolution

The measurement and calibration of the jet energy resolution exploits the approximate balance of the transverse momentum of the jets in dijet events (see Section 5.3.4). Since the data and simulations agree within the uncertainty of the measurements, a jet energy resolution correction is not applied. However, the uncertainties need to be propagated to each analysis as a systematic uncertainty.

The jet energy is smeared according to its transverse momentum and pseudorapidity in order to estimate the jet-energy-resolution uncertainty. The full difference between the analysis result with nominal and smeared jet energy is symmetrized and taken as the uncertainty associated with the jet energy resolution. Notice that there is only one variation, in contrast to the more general setup with two variations.

The ApplyJetCalibration-00-02-07 package is used to compute the jet-energy-resolution uncertainty for the 2011 datasets, while the JetResolution-02-00-03 [182] and ApplyJetResolutionSmearing-00-01-03 [183] packages are used together to estimate the jet-energy-resolution uncertainty for the 2012 datasets. The first package provides the numerical values used for the smearing, while the second package provides the tools used to apply the smearing.

### 6.1.9 Jet reconstruction efficiency

The jet-reconstruction-efficiency calibration is performed using a tag-and-probe method on dijet events, as described in Section 5.3.5. The jet reconstruction is expected to be 100% efficient for jets with $p_{\mathrm{T}} > 30$ GeV and around 99.8% for jets with 20 GeV $< p_{\mathrm{T}} < 30$ GeV in the region with $|\eta| < 2.5$ [184]. Similar

to the jet-energy-resolution calibration, the jet-reconstruction-efficiency calibration is not applied in the nominal analysis, but the results of the calibration studies provide the numerical values used to estimate the uncertainty associated with the jet reconstruction efficiency [185, 186].

In order to estimate the uncertainty associated with the jet reconstruction efficiency, the results of the analyses are recomputed using a modified jet reconstruction efficiency. This is achieved by randomly removing reconstructed jets from the events according to the uncertainties provided by the calibration studies. The probability of a jet to be removed depends on the transverse momentum and pseudorapidity of the calorimeter jets, i.e., jets reconstructed from calorimeter topological clusters [184]. The full difference between the nominal analysis result and analysis with modified jet reconstruction efficiency is symmetrized and assigned as the systematic uncertainty.

The JetEffiProvider-00-00-04 package [187] and the JetEffiProvider-00-00-05 package [188] provide the tools used to estimate the jet-reconstruction-efficiency uncertainty for the 2011 and 2012 datasets, respectively.

### 6.1.10 Jet vertex fraction

The systematic uncertainty associated with the introduction of the JFV requirements on the jet definitions described in Section 5.3.3 needs to be quantified. In order to estimate the JFV uncertainty, the analysis is repeated with a different cut value on the JFV.

For the 2011 calibration, the TopJetUtils-00-00-07 package [189] provides the upwards and downwards variation sets to the JVF cut. These sets correspond to the hard-scatter jet selection efficiency and inefficiency, and the pile-up jets rejection efficiency and inefficiency [190]. The variation of the JVF cuts depends on the transverse momentum of the jets and is less than 0.5% for the hard-scatter jet selection efficiency, up to 10% for the hard-scatter jet selection inefficiency, roughly 1% for the pile-up jets rejection efficiency and roughly 1% for the pile-up jets rejection inefficiency.

For the 2012 calibration, the JVF cut is shifted upwards or downwards by a flat 6% using the JVFUncertaintyTool-00-00-04 package [191].

### 6.1.11 *b*-tagging

In Section 5.4, the *b*-tagging calibration was discussed in some detail. The results of those calibrations and their uncertainties are provided for different ranges of the transverse momentum of jets. In the case of light jets, the calibration also depends on the pseudorapidity [192].

In order to estimate the systematic uncertainty associated with the use of *b*-tagging, six sets of scale factors are needed:

- *b*-jet tagging efficiency,
- *c*-jet tagging efficiency,
- light-jet tagging efficiency,
- *b*-jet tagging inefficiency,
- *c*-jet tagging inefficiency and
- light-jet tagging inefficiency.

The efficiency and inefficiency scale factors for each jet flavor are anticorrelated and the variation of the scale factors must take this anticorrelation into account. Therefore, when an efficiency is shifted up, its corresponding inefficiency must be shifted down at the same time.

This approach, called envelope approach, is relatively simple but does not implement the correct correlation between kinematic bins. As a result, the systematic uncertainty is overestimated.

An improvement to the envelope approach is achieved using the so-called Eigenvector method [192]. The Eigenvector method takes into account the effect of each source of uncertainty on the scale-factor calibration in each bin of the calibration. In order to reduce the number of variations, the covariance matrix corresponding to each source of systematic variation is computed, with the sum of all these covariance matrices forming the total covariance matrix. This can be considered an eigenvector problem and the vectors resulting from its solution provide a set of independent set of variation "directions" which are then used to assess the total uncertainty associated with the use of $b$-tagging in the analyses. Due to the improved treatment of correlations, the Eigenvector method provides smaller uncertainty values than the envelope approach.

The envelope method is used for the top-quark mass measurement, since the impact of the $b$-tagging calibration uncertainty on the measurement is small. Its implementation, scale factor values and uncertainties are provided by the CalibrationDataInterface-00-01-02 package [193] ($t\bar{t}$-based calibration). The Eigenvector method is used for the $t\bar{t}Z$ cross-section measurement. The implementation is provided by the CalibrationDataInterface-00-03-06 package [194] interfaced with the $t\bar{t}$-based calibration provided in the TopD3PDCorrections-12-01-74 package [195].

### 6.1.12 Missing transverse momentum

The momentum of soft jets (i.e., jets with small transverse momentum: 7 GeV $< p_{\mathrm{T}} <$ 20 GeV) and the remaining calorimeter energy (i.e., the energy in the calorimeter that is not associated with any reconstructed physics object) are part of the computation of the missing transverse momentum. The uncertainties on the calibration of these two contributions need to be propagated to the computation of the missing transverse momentum and to the analyses themselves [196]. Since the two quantities are 100% correlated, both calibration scales are simultaneously varied upwards or downwards by one standard deviation, and the missing transverse momentum of each event is recomputed using these shifted values. This uncertainty is known as the CellOut+SoftJet uncertainty of the missing transverse momentum.

For the 2011 datasets, a second uncertainty is considered. This uncertainty is related to the effect of pile up in the computation of the missing transverse momentum [196] and is introduced to account for the differences in the computation of the missing transverse momentum in data and simulations under different pile-up conditions. The associated uncertainty is a flat increase or decrease on the magnitude of the missing transverse momentum of 6.6%.

For the 2012 datasets, the uncertainty on the calibration of the momentum resolution of soft jets is propagated to the analysis by smearing the soft jets (depending on their $p_{\mathrm{T}}$, $\eta$ and $\phi$) and recomputing the missing transverse momentum.

For the 2011 datasets, both systematic uncertainties are computed using the tools and scale factors provided by the MissingETUtility-01-00-09 package [197]. For the 2012 datasets, the MissingETUtility-01-01-03 package [198] is used in combination with the calibration values provided by TopD3PDCorrections-12-01-20 package [199].

## 6.2 Normalization-related systematic uncertainties

### 6.2.1 Uncertainty on the integrated luminosity

In order to rescale the MC-simulated events to match the expected number of events in data, a luminosity weight is applied based on the cross section of the process, the number of events generated and the integrated luminosity of the data:

$$w_{\text{luminosity}} = \frac{N_{\text{data}}}{N_{\text{MC}}} = \frac{A \cdot \epsilon \cdot \sigma \cdot \mathcal{L}_{\text{int}}}{N_{\text{MC}}}, \tag{6.1}$$

where $N_{\text{data}}$ is the number of events expected in data, $N_{\text{MC}}$ is the number of events generated for the MC dataset, $A$ is the acceptance of the detector, $\epsilon$ is the selection efficiency, $\sigma$ is the cross section of the simulated process and $\mathcal{L}_{\text{int}}$ is the integrated luminosity of the data.

A source of systematic uncertainty is the precision on the measurement of the integrated luminosity. This value directly affects the estimation of the expected number of events based on MC simulations, which is important for analyses that depend on this value, such as the cut-and-count method used to measure the $t\bar{t}Z$ cross section presented in this thesis.

On the other hand, the top-quark mass measurement does not depend on the overall normalization, since it is an analysis based on shape comparisons. Therefore, the integrated luminosity uncertainty does not affect this analysis.

For the 2012 data, the uncertainty in the measurement of the integrated luminosity is estimated to be 2.8% [94].

### 6.2.2 MC-normalization uncertainty

As mentioned in Section 6.2.1, a luminosity weight is needed to rescale the MC-simulated events to the number of expected events in data. This weight is computed for each MC process using Equation 6.1, where the value of $\sigma$ is taken from theoretical calculations which have a limited precision (e.g., NNLO+NNLL for $t\bar{t}$). This introduces systematic uncertainties to analyses that use a luminosity weight as defined by Equation 6.1, since changes in $\sigma$ for different processes change the total number of events and the overall shape of kinematic distributions. This effect is estimated by the MC-normalization uncertainty.

Different processes have different MC-normalization uncertainties. These uncertainties are summarized in Table 6.1.

| Physics process | MC-normalization uncertainty | Analysis |
|---|---|---|
| $t\bar{t}$ | 10% | top-quark mass measurement |
| single top | 8% | top-quark mass measurement |
| $WtZ$ | 10% | $t\bar{t}Z$ cross-section measurement |

Table 6.1: MC-normalization uncertainty for the analyses presented in this thesis [185, 200].

The effect of the MC-normalization uncertainty is expected to have little impact on the top-quark mass measurement and the $t\bar{t}Z$ cross-section measurement, since the selections for both analyses have a high purity.

CHAPTER 7

# Top-quark mass measurement

## 7.1 The calibration curve method

The top-quark mass measurement is performed using the calibration curve method. It consists of the following steps:

- choose an observable that depends on the top-quark mass (calibration observable).
- Use simulation datasets with different assumed values of the top-quark mass (mass variation datasets) to obtain the dependence of the chosen observable on the top-quark mass.
- Fit this dependence to create a calibration curve.
- Measure the observable in data and determine the top-quark mass using the calibration curve.

The top-quark mass measurement presented in this thesis uses observables derived from the kinematic distribution of the $m_{\mathrm{T2}}$ variable. It is important to choose an observable that is sensitive to the top-quark mass and with small dependency on systematic uncertainties.

## 7.2 The $m_{\mathrm{T2}}$ variable

The $m_{\mathrm{T2}}$ variable [201] (also known as stransverse mass) is a kinematic variable used in pair-production events where each parent particle decays into visible particles (i.e., reconstructed in the detector) and one invisible particle (i.e., escapes detector reconstruction), such as the $t\bar{t}$ dilepton channel.

The motivation to use the $m_{\mathrm{T2}}$ variable to measure the top quark mass is the fact that $m_{\mathrm{T2}}$ depends on the mass of the parent particle. As a matter of fact, it represents a lower boundary to the mass of the parent particle [201, 202].

Formally, the $m_{\mathrm{T2}}$ variable is defined as:

$$m_{\mathrm{T2}}\left(m_{\mathrm{inv}}\right) = \min_{\vec{p}_{\mathrm{T}}^{(1)},\vec{p}_{\mathrm{T}}^{(2)}} \left\{ \max\left[ m_{\mathrm{T}}\left(m_{\mathrm{inv}}, \vec{p}_{\mathrm{T}}^{(1)}\right), m_{\mathrm{T}}\left(m_{\mathrm{inv}}, \vec{p}_{\mathrm{T}}^{(2)}\right)\right]\right\}, \tag{7.1}$$

with

$$\vec{p}_{\mathrm{T}}^{(1)} + \vec{p}_{\mathrm{T}}^{(2)} = \vec{p}_{\mathrm{T}}^{\mathrm{miss}}, \tag{7.2}$$

where $\vec{p}_{\mathrm{T}}^{\,\mathrm{miss}}$ is the missing transverse momentum of the event, $\vec{p}_{\mathrm{T}}^{\,(n)}$ is the assumed transverse momentum of the invisible particle in the $n$th branch.

The transverse mass $m_{\mathrm{T}}\left(m_{\mathrm{inv}}, \vec{p}_{\mathrm{T}}^{\,(n)}\right)$ is defined as follows:

$$m_{\mathrm{T}}\left(m_{\mathrm{inv}}, \vec{p}_{\mathrm{T}}^{\,(n)}\right) = \sqrt{m_{\mathrm{vis}}^2 + m_{\mathrm{inv}}^2 + 2\left(E_{\mathrm{T}}^{\mathrm{vis}} E_{\mathrm{T}}^{\mathrm{inv}} - \vec{p}_{\mathrm{T}}^{\,\mathrm{vis}} \cdot \vec{p}_{\mathrm{T}}^{\,(n)}\right)}, \tag{7.3}$$

where $m_{\mathrm{vis}}$ is the invariant mass of the visible particles, $m_{\mathrm{inv}}$ is the invariant mass of the invisible particle, $E_{\mathrm{T}}^{\mathrm{vis}}$ is the transverse energy of the visible particles, $E_{\mathrm{T}}^{\mathrm{inv}}$ is the transverse energy of the invisible particles and $\vec{p}_{\mathrm{T}}^{\,\mathrm{vis}}$ is the transverse momentum of the visible particles. It is important to note that the value of $m_{\mathrm{T}}\left(m_{\mathrm{inv}}, \vec{p}_{\mathrm{T}}^{\,(n)}\right)$ is defined for each of the two decay branches. Therefore, the computation of $m_{\mathrm{vis}}$, $m_{\mathrm{inv}}$, $E_{\mathrm{T}}^{\mathrm{vis}}$, $E_{\mathrm{T}}^{\mathrm{inv}}$ and $\vec{p}_{\mathrm{T}}^{\,\mathrm{vis}}$ only involve the particles that are part of the given decay branch.

In order to understand the meaning of $m_{\mathrm{T2}}$, it is useful to "derive" its definition. For the sake of argumentation, consider a $t\bar{t}$ event. For the top quark decay branch ($t \to b\ell^+\nu$), the transverse mass is defined as:

$$m_{\mathrm{T}}(t) = \sqrt{m_{b\ell^+}^2 + m_{\nu}^2 + 2\left(E_{\mathrm{T}}^{b\ell^+} E_{\mathrm{T}}^{\nu} - \vec{p}_{\mathrm{T}}^{\,b\ell^+} \cdot \vec{p}_{\mathrm{T}}^{\,\nu}\right)}, \tag{7.4}$$

where $m$, $p_{\mathrm{T}}$ and $E_{\mathrm{T}}$ are, respectively, the invariant mass, the transverse momentum and transverse energy of the corresponding four-momentum, with $\mathbf{P}^{\nu}$ being the four-momentum of the neutrino and where the four-momentum for the visible particles ($b\ell^+$) is defined as:

$$\mathbf{P}^{b\ell^+} = \mathbf{P}^{b} + \mathbf{P}^{\ell^+}, \tag{7.5}$$

where $\mathbf{P}^{b}$ and $\mathbf{P}^{\ell^+}$ are the four-momenta of the bottom quark and the antilepton, respectively.

Analogously, for the antitop quark decay branch ($\bar{t} \to \bar{b}\ell^-\bar{\nu}$), the transverse mass is defined as:

$$m_{\mathrm{T}}\left(\bar{t}\right) = \sqrt{m_{\bar{b}\ell^-}^2 + m_{\bar{\nu}}^2 + 2\left(E_{\mathrm{T}}^{\bar{b}\ell^-} E_{\mathrm{T}}^{\bar{\nu}} - \vec{p}_{\mathrm{T}}^{\,\bar{b}\ell^-} \cdot \vec{p}_{\mathrm{T}}^{\,\bar{\nu}}\right)}. \tag{7.6}$$

Since the transverse mass is a lower boundary of the mass of the parent particle, both Equation 7.4 and Equation 7.6 represent a lower boundary of the top-quark mass. Taking the most restrictive boundary to the top-quark mass from Equation 7.4 and Equation 7.6:

$$m_{\mathrm{T}}\,(\mathrm{max}) \equiv \max\left[m_{\mathrm{T}}(t), m_{\mathrm{T}}(\bar{t})\right] \leq m_{\mathrm{top}}. \tag{7.7}$$

The computation of $m_{\mathrm{T}}\,(\mathrm{max})$ assumes that the values of $\vec{p}_{\mathrm{T}}^{\,\nu}$ and $\vec{p}_{\mathrm{T}}^{\,\bar{\nu}}$ are known. In practice, however, the transverse momentum of each individual neutrino cannot be measured in ATLAS. Instead, the missing transverse momentum is associated to the sum of all the transverse momenta of the neutrinos in an event using:

$$\vec{p}_{\mathrm{T}}^{\,\mathrm{miss}} = \vec{p}_{\mathrm{T}}^{\,\nu} + \vec{p}_{\mathrm{T}}^{\,\bar{\nu}}. \tag{7.8}$$

Since $\vec{p}_{\mathrm{T}}^{\,\nu}$ and $\vec{p}_{\mathrm{T}}^{\,\bar{\nu}}$ cannot be determined separately, the value of $m_{\mathrm{T}}\,(\mathrm{max})$ depends on the value of four parameters ($p_x^{\nu}$, $p_y^{\nu}$, $p_x^{\bar{\nu}}$ and $p_y^{\bar{\nu}}$) subject to the constraints imposed by Equation 7.8. These constraints reduce the number of degrees of freedom to two independent parameters (e.g., $p_x^{\nu}$, $p_y^{\nu}$).

If no further information is given, any combination of these two independent parameters defines a value for $m_{\mathrm{T}}\,(\mathrm{max})$. Since only one combination of these two parameters is correct, only the least

constraining requirement on the mass of the parent particle is ensured to be valid:

$$X \equiv \min_{\vec{p}_T^{\nu}, \vec{p}_T^{\bar{\nu}}} \left[ m_T\,(\text{max}) \left( \vec{p}_T^{\nu}, \vec{p}_T^{\bar{\nu}} \right) \right] \leq m_T\,(\text{max})^{\text{truth}} \leq m_{\text{top}}, \tag{7.9}$$

where $X$ is the constraint to the mass of the parent particle (in this discussion, the top-quark mass), $m_T\,(\text{max}) \left( \vec{p}_T^{\nu}, \vec{p}_T^{\bar{\nu}} \right)$ is the computed value of $m_T\,(\text{max})$ for a given value of $\vec{p}_T^{\nu}$ and $\vec{p}_T^{\bar{\nu}}$ subject to the constraint given by Equation 7.8 and $m_T\,(\text{max})^{\text{truth}}$ is the value of $m_T\,(\text{max})$ using the real values of $\vec{p}_T^{\nu}$ and $\vec{p}_T^{\bar{\nu}}$.

Replacing Equation 7.7 into Equation 7.9:

$$X \equiv \min_{\vec{p}_T^{\nu}, \vec{p}_T^{\bar{\nu}}} \left\{ \max \left[ m_T(t), m_T(\bar{t}) \right] \right\} \leq m_{\text{top}}. \tag{7.10}$$

The definition of $X$ given by Equation 7.10 is the same as the $m_{T2}$ definition provided in Equation 7.1.

A graphical illustration of the $m_{T2}$ variable is shown in Figure 7.1. The colored and the black-and-white distributions are the two $m_T$ distributions. For each point of $p_x^{\nu}$ and $p_y^{\nu}$, the largest value of the two distributions is taken to create the "maximum surface". The minimum point in this "maximum surface" is the value of the $m_{T2}$variable.

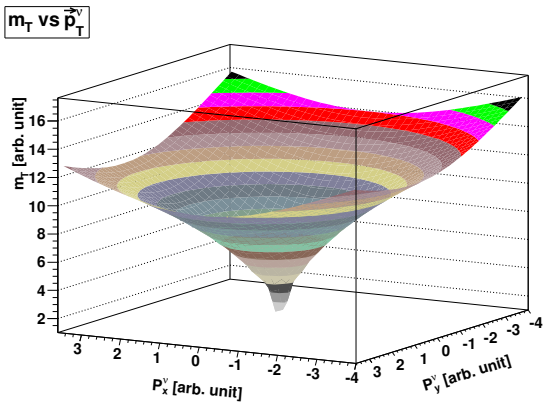


(a) $m_T$ dependence on $\vec{p}_T^{\nu}$.

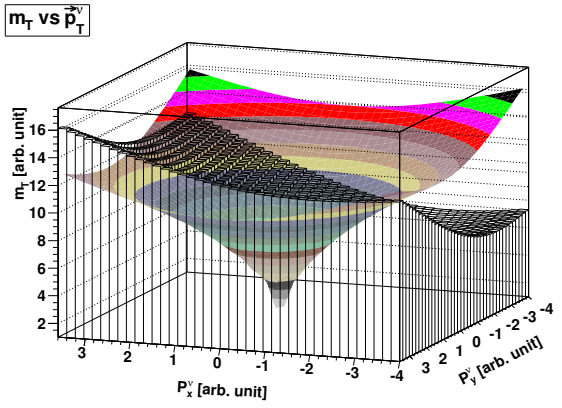


(b) Overlap of the two $m_T$ distributions as a function of $\vec{p}_T^{\nu}$.

Figure 7.1: Graphical illustration of the $m_{T2}$ variable. In this example, the value of $m_{T2}$ is the minimum value of the intersection of the two surfaces shown in the right plot.

The computation of the $m_{T2}$ variable is performed using the bisect algorithm provided by Cheng and Han [203]. The algorithm is based on the fact that $m_{T2}$ is the boundary of the mass region consistent with the minimal constraints. These constraints provide those valid values of $\vec{p}_T^{(1)}$ and $\vec{p}_T^{(2)}$ consistent with a given value of $m_{T2}$, which lie on an elliptical surface in the $p_x^{(1)} p_y^{(1)}$ and $p_x^{(2)} p_y^{(2)}$ planes. Using Equation 7.2, both ellipses can be placed in the same plane (see Figure 7.2). The value of $m_{T2}$ where the two ellipses are tangent to each other is the solution to the minimization problem in Equation 7.1.

Since the lepton-jet pairing in a $t\bar{t}$ event is not known a priory at reconstruction level, all suitable lepton-jet combinations are tried and the combination giving the smallest value of $m_{T2}$ is used as the correct combination. In the analysis, the two $b$-tagged jets with the largest $p_T$ are assumed to have originated from the $t\bar{t}$ decay.

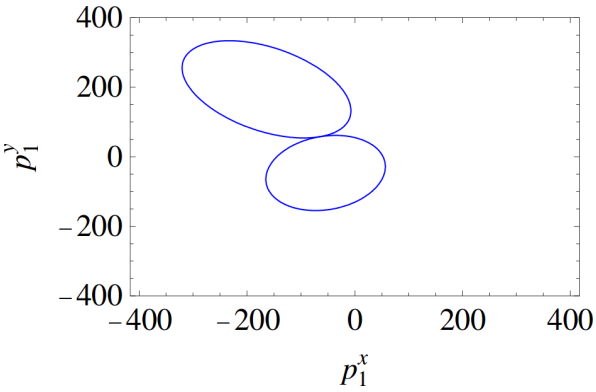


Figure 7.2: Graphical solution of the $m_{T2}$ computation using the bisect algorithm. The solution is located at the intersection of the two ellipses (adapted from [203]).

Figure 7.3 shows the $m_{T2}$ distribution at truth level for simulation datasets with different input top-quark masses. As discussed earlier in this section, the distribution depends on the assumed top-quark mass and is bounded from above by it.

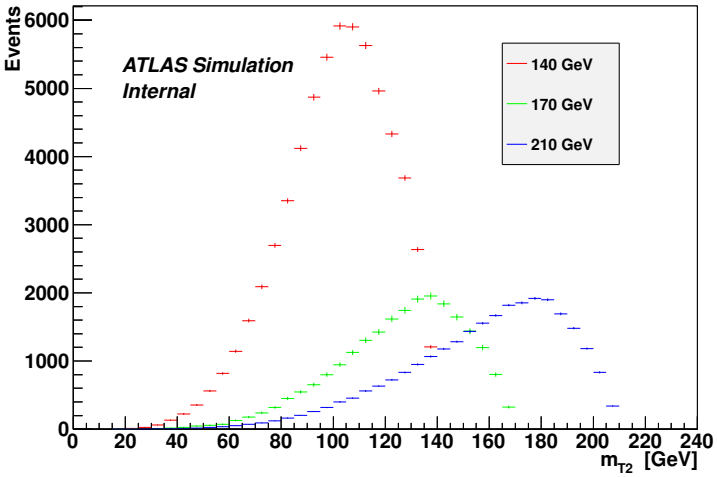


Figure 7.3: $m_{T2}$ distribution at truth level for simulation datasets with different input top-quark masses. It can be seen that the input top-quark mass is the upper boundary of the $m_{T2}$ distribution.

## 7.3 Mass measurement

The mean value of the $m_{T2}$ distribution ($\overline{m}_{T2}$) in the $t\bar{t}$ dilepton channel is used as the calibration observable in the calibration curve method described earlier in this chapter.

The standard ATLAS $t\bar{t}$ dilepton selection (e.g., see Ref. [204]) is combined with a rectangular multivariate analysis in order to obtain an event selection that provides the smallest value of the total uncertainty on the top-quark mass measurement. The use of this rectangular multivariate optimization reduces the total systematic uncertainty considerably and will be discussed in detail in Section 7.3.2. This analysis is the first top-quark mass measurement in the dilepton channel in ATLAS and was pub-

lished as a preliminary result in Ref. [205].

### 7.3.1 Event selection

As mentioned in Section 2.2.2, a $t\bar{t}$ dilepton event has a very distinctive signature that allows event selections with high signal purity. The signature of the $t\bar{t}$ dilepton channel is (see Figure 7.4):

- two leptons.
- Two $b$-jets.
- Missing transverse momentum, due to the two neutrinos.

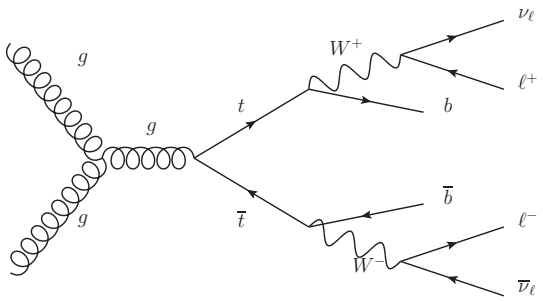


Figure 7.4: $t\bar{t}$ production by gluon fusion and decay into the dilepton channel.

The main sources of background events with two prompt leptons are the $Z$ + jets, the single-top and diboson backgrounds:

- The $Z$ + jets background produces two leptons from a $Z$ boson leptonic decay and is one of the most important backgrounds of the $t\bar{t}$ dilepton channel due to its large cross section. This background can be suppressed with a combination of cuts requiring large $E_{\mathrm{T}}^{\mathrm{miss}}$, large number of jets, existence of $b$-tagged jets and a large value of $|m_{\ell\ell} - m_Z|$. A special case is the dileptonic $Z \to \tau\tau$ background. The signature of this decay include the production of four neutrinos and a pair of leptons with an invariant mass below the mass of the $Z$ boson, making the use of a $|m_{\ell\ell} - m_Z|$ requirement ineffective. Instead, the scalar sum of all the leptons and jets selected in the event ($H_{\mathrm{T}}$) is used to suppress this $Z$ + jets decay channel, along with requirements on the number of jets and $b$-jets.
- The signature of single-top background ($Wt$-channel, dilepton decay) is almost the same as the $t\bar{t}$ dilepton signature, except for the number of $b$-jets (one less). Therefore, a good separation between single-top events and $t\bar{t}$ dilepton events is difficult to achieve. This background is suppressed by requiring at least two jets and is better suppressed by requiring at least two $b$-tagged jets. Fortunately, the cross section for this process is fairly small, being roughly 14 times smaller than the $t\bar{t}$ dilepton cross section.
- The diboson backgrounds are composed of three different components: $WW$, $WZ$, $ZZ$ and $Z\gamma$. The signature of the $WW$ background is similar to the one from $t\bar{t}$ dilepton events, but produces no jets at tree-level. Therefore, a good suppression is achieved by requiring at least two jets or requiring the presence of $b$-tagged jets in the selected events. The $WZ$ and $ZZ$ backgrounds produce two leptons from a $Z$ boson leptonic decay and two jets (for $W$ and $Z$) or two neutrinos (only $Z$) from

the remaining boson. A good suppression can be achieved requiring a large value of $|m_{\ell\ell} - m_Z|$ and the presence of $b$-tagged jets. The $Z\gamma$ background produces two prompt leptons when the $Z$ boson decays dileptonically. This background is suppressed using the same requirements as the $Z$ + jets background.

The tree-level signature of each background and the variables used to suppress each background are shown in Table 7.1.

| Name | Tree-level signature | Discrimination from $t\bar{t}$ dilepton |
|---|---|---|
| $t\bar{t}$ dilepton | 2 leptons<br>2 $b$-jets<br>2 neutrinos (large $E_{\mathrm{T}}^{\mathrm{miss}}$) | SIGNAL |
| $Z \to ee, Z \to \mu\mu$ | 2 leptons from $Z$<br>No jets<br>no neutrinos (small $E_{\mathrm{T}}^{\mathrm{miss}}$) | $\lvert m_{\ell\ell} - m_Z \rvert$<br>$N_{\mathrm{jets}}$ and $N_{b\mathrm{tag}}$<br>$E_{\mathrm{T}}^{\mathrm{miss}}$ |
| $Z \to \tau\tau \to \ell\ell$ | No jets<br>4 neutrinos (large $E_{\mathrm{T}}^{\mathrm{miss}}$)<br>2 leptons | $N_{\mathrm{jets}}$ and $N_{b\mathrm{tag}}$<br>$H_{\mathrm{T}}$ |
| Single top ($Wt$) | 1 $b$-jet<br>2 neutrinos (large $E_{\mathrm{T}}^{\mathrm{miss}}$)<br>2 leptons | $N_{\mathrm{jets}}$ and $N_{b\mathrm{tag}}$ |
| Diboson ($WW$) | No jets<br>2 leptons<br>2 neutrinos (large $E_{\mathrm{T}}^{\mathrm{miss}}$) | $N_{\mathrm{jets}}$ and $N_{b\mathrm{tag}}$ |
| Diboson ($WZ$) | 2 leptons from $Z$<br>2 light jets<br>no neutrinos (small $E_{\mathrm{T}}^{\mathrm{miss}}$) | $\lvert m_{\ell\ell} - m_Z \rvert$<br>$N_{b\mathrm{tag}}$<br>$E_{\mathrm{T}}^{\mathrm{miss}}$ |
| Diboson ($ZZ$) | 2 leptons from $Z$<br>2 jets (mostly light jets) or 2 neutrinos | $\lvert m_{\ell\ell} - m_Z \rvert$<br>$N_{b\mathrm{tag}}$ |

Table 7.1: Sources of events with two prompt leptons and their tree-level signature. The variables used to suppress the given background are shown in the right-most column.

In order to select $t\bar{t}$ dilepton events and reject background events, signal event candidates must meet the following requirements:

- to ensure the quality of data events, all events selected in data must pass the GRL filter (see Section 4.1). Simulation events are required to be true dilepton events (i.e., they have exactly two leptons at generator level), where $\tau$ leptons only add towards the lepton count if they decay leptonically.
- At least one of the lepton triggers has fired (see Section 4.1). The electron trigger requires at least

one reconstructed electron with $p_T > 20$ GeV (before period K) or with $p_T > 22$ GeV (after period K). The muon trigger requires at least one reconstructed muon with $p_T > 18$ GeV (all periods).

- Events with cosmic muons are rejected.
- The trigger object must match a reconstructed lepton within $\Delta R < 0.15$.
- The event must not have noise bursts in the liquid argon calorimeter.
- All jets with $p_T > 10$ GeV (before calibration) must satisfy the jet-reconstruction-quality criteria [206].
- The event must contain at least one good primary vertex with at least five associated tracks.
- Exactly one reconstructed electron and one reconstructed muon ($e\mu$ channel). Electron candidates are required to have $E_T > 25$ GeV while muon candidates are required to have $p_T > 25$ GeV.
- The charge of the reconstructed leptons must have opposite signs (OS).
- The event is rejected if an electron and a muon candidate share the same track.
- $H_T > 130$ GeV.
- $E_T^{miss} > 45$ GeV.
- The event must have at least two $b$-tagged jets (MV1 at 85% efficiency) with $p_T > 45$ GeV.
- The azimuthal separation between the two $b$-tagged jets with the largest transverse momenta($\Delta\phi_{b_1 b_2}$) must be larger than 2.2. This requirement is used to reduce the systematic uncertainty associated with the jet energy scale, ISR/FSR and color reconnection, as explained later in this section.
- Events with $m_{T2} > 220$ GeV are removed in order to remove $t\bar{t}$ events with at least one misidentified $b$-jet (see Figure 7.5).

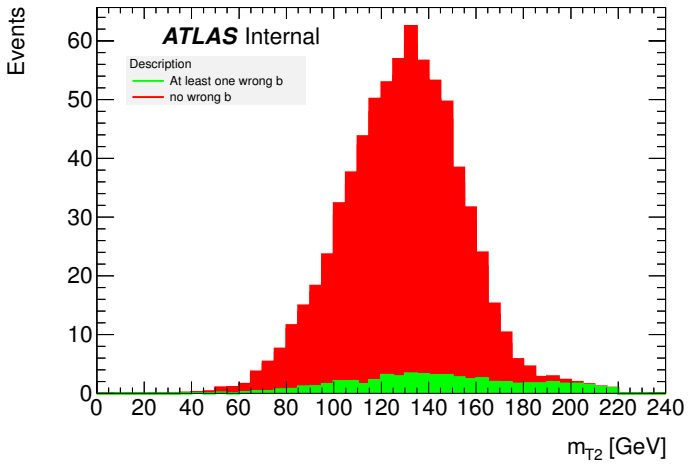


Figure 7.5: $m_{T2}$ distribution of events where all $b$-tagged jets are correctly assigned (red) and events where at least one $b$-tagged jet is not correctly assigned to the $t\bar{t}$ decay branches (green).

The chosen cuts are a combination of the standard dilepton cuts used widely in the ATLAS top working group, and the addition of extra requirements on the lepton $p_{\mathrm{T}}$, $b$-tagged jets $p_{\mathrm{T}}$, $\Delta\phi_{b_1 b_2}$, $E_{\mathrm{T}}^{\mathrm{miss}}$ and $m_{\mathrm{T2}}$. The values of the latter cuts (except for $m_{\mathrm{T2}}$) are chosen using a rectangular multivariate analysis. The $m_{\mathrm{T2}}$ cut is chosen such that it removes events that are obviously misreconstructed. This cut significantly increases the robustness of the measurement to fluctuations in the tail of the distribution.

### 7.3.2 Choosing the analysis specific cuts

The event cuts are chosen using a simple rectangular multivariate analysis based on the following variables: jet $\eta$, lepton $p_{\mathrm{T}}$, $\Delta\phi_{b_1 b_2}$, $E_{\mathrm{T}}^{\mathrm{miss}}$, leading $b$-tagged jet $p_{\mathrm{T}}$ and subleading $b$-tagged jet $p_{\mathrm{T}}$. To avoid biases, the analysis is performed in simulation events with two electrons ($ee$ channel) or events with two muons ($\mu\mu$ channel) satisfying the selection criteria of the $e\mu$ channel, except for the requirement on the lepton flavor. Instead of having exactly one electron and one muon, the events are required to have exactly two electrons or exactly two muons.

Varying each of these 6 variables in evenly-spaced steps creates a 6-dimensional rectangular grid. The total uncertainty ($\sigma_{\mathrm{total}} = \sqrt{\sigma_{\mathrm{stat.}}^2 + \sigma_{\mathrm{syst.}}^2}$) in each of the vertices of this 6-dimensional grid is computed. The results are ordered to find the cuts that minimize the total uncertainty. In order to avoid obtaining results due to statistical fluctuations in the simulation events, the vertex in the 6-dimensional grid giving the smallest value is not necessarily taken as the solution. Instead, regions with similar cuts producing similar total uncertainties are identified and the region with the lowest uncertainty is chosen.

To further ensure that the chosen cuts are not chosen due to a statistical fluctuation, the total uncertainty distribution is determined for each of the variables while keeping the other five variables at their solution value. These six distributions are shown in Figure 7.6. The minimum lepton $p_{\mathrm{T}}$ and minimum $|\eta|$ of jets dependencies show that the best value for those cuts are the loosest value. For the $E_{\mathrm{T}}^{\mathrm{miss}}$ and the $\Delta\phi_{b_1 b_2}$ cut, Figure 7.6 shows that the chosen cuts are sitting at the minima, but concerns about the validity of the minima can be raised. Nevertheless, the same distributions show that the optimal values are not far from the chosen values. Overtraining is not an issue here, since the analysis is performed using the $ee$ and $\mu\mu$ control region. The distribution of the $p_{\mathrm{T}}$ of the leading $b$-tagged jet shows that the best cut is $p_{\mathrm{T}} > 45$ GeV, where the flat slope for the region $p_{\mathrm{T}} < 45$ GeV is due to the $p_{\mathrm{T}}$ requirement for the subleading $b$-tagged jet ($p_{\mathrm{T}} > 45$ GeV). Finally, the $p_{\mathrm{T}}$ cut of the subleading $b$-tagged jet is roughly optimal.

One variable that deserves special attention is $\Delta\phi_{b_1 b_2}$, since it strongly reduces the total uncertainty of the top-quark mass measurement. The dependencies of the dominant uncertainties with respect to the value of the $\Delta\phi_{b_1 b_2}$ cut are shown in Figure 7.7. It can be seen that the jet energy scale (JES), jet energy resolution (JER), color reconnection (CR) decrease with a tighter $\Delta\phi_{b_1 b_2}$ cut, while the generator (mcGenerator) and statistical uncertainties increase. Figure 7.7 shows that the choice of the $\Delta\phi_{b_1 b_2}$ cut is a compromise between two competing effects: the reduction of the systematic uncertainty due to mainly a reduction in JES and CR, and an increase in the statistical uncertainty due to fewer selected events.

### 7.3.3 Event yields and background estimation

Applying the cuts defined in the last section to the different luminosity-weighted (see Section 6.2.1) MC-simulation datasets and estimating the fakes contribution using the matrix method introduced in Section 4.3.2, the expected number of events for the signal and each background can be computed. The expected number of events is shown in Table 7.2, along with the measured number of events in data.

The event purity of the expected number of events is almost 95%, with the events with fake leptons being the dominant background. The number of events measured in data is compatible with the expected

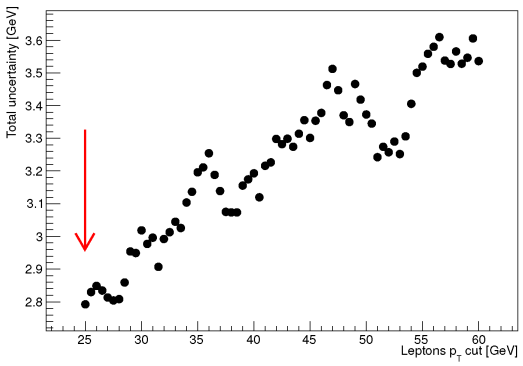


(a) Minimum lepton $p_{\mathrm{T}}$

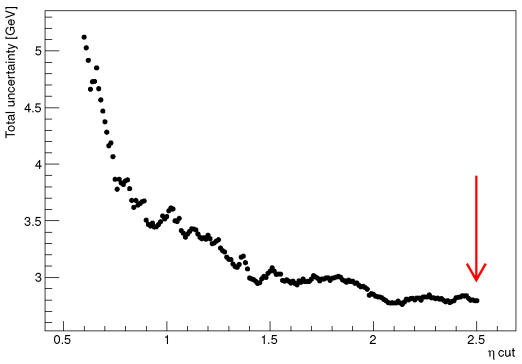


(b) Maximum $|\eta|$ *o*f jets

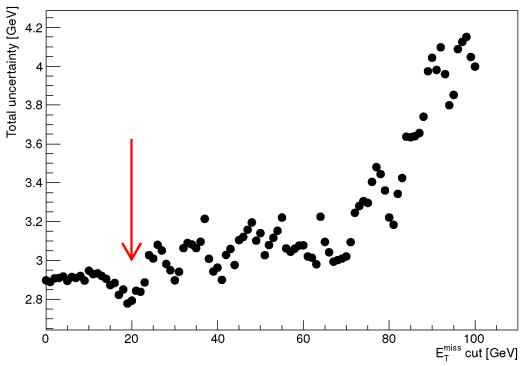


(c) Minimum $E_{\mathrm{T}}^{\mathrm{miss}}$

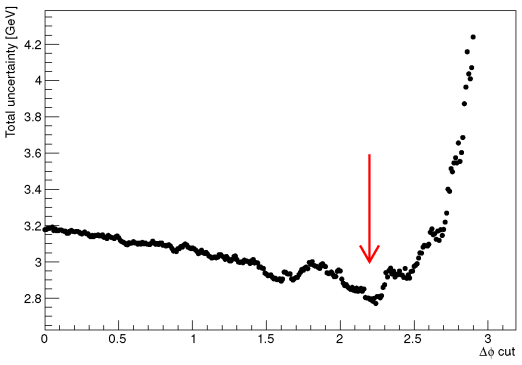


(d) Minimum $\Delta\phi_{b_1 b_2}$

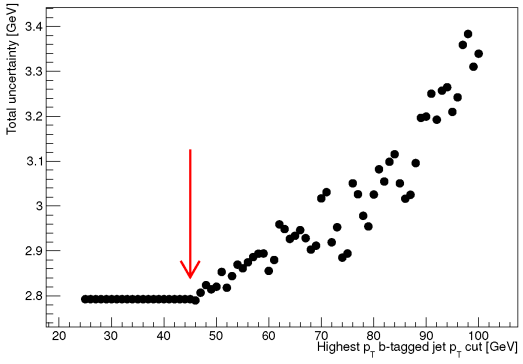


(e) Minimum $p_{\mathrm{T}}$ of leading $b$-tagged jet

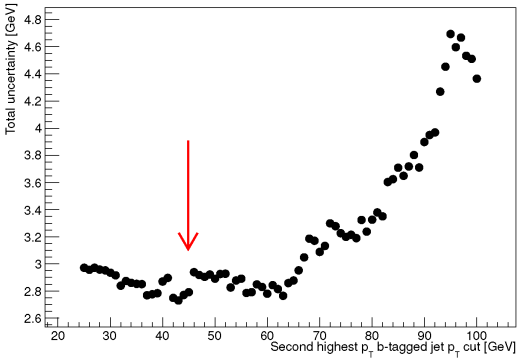


(f) Minimum $p_{\mathrm{T}}$ of subleading $b$-tagged jet

Figure 7.6: Total uncertainty dependence on each optimization variable while keeping all other optimization variables at the optimized value. The red arrow indicates the position of the cut.

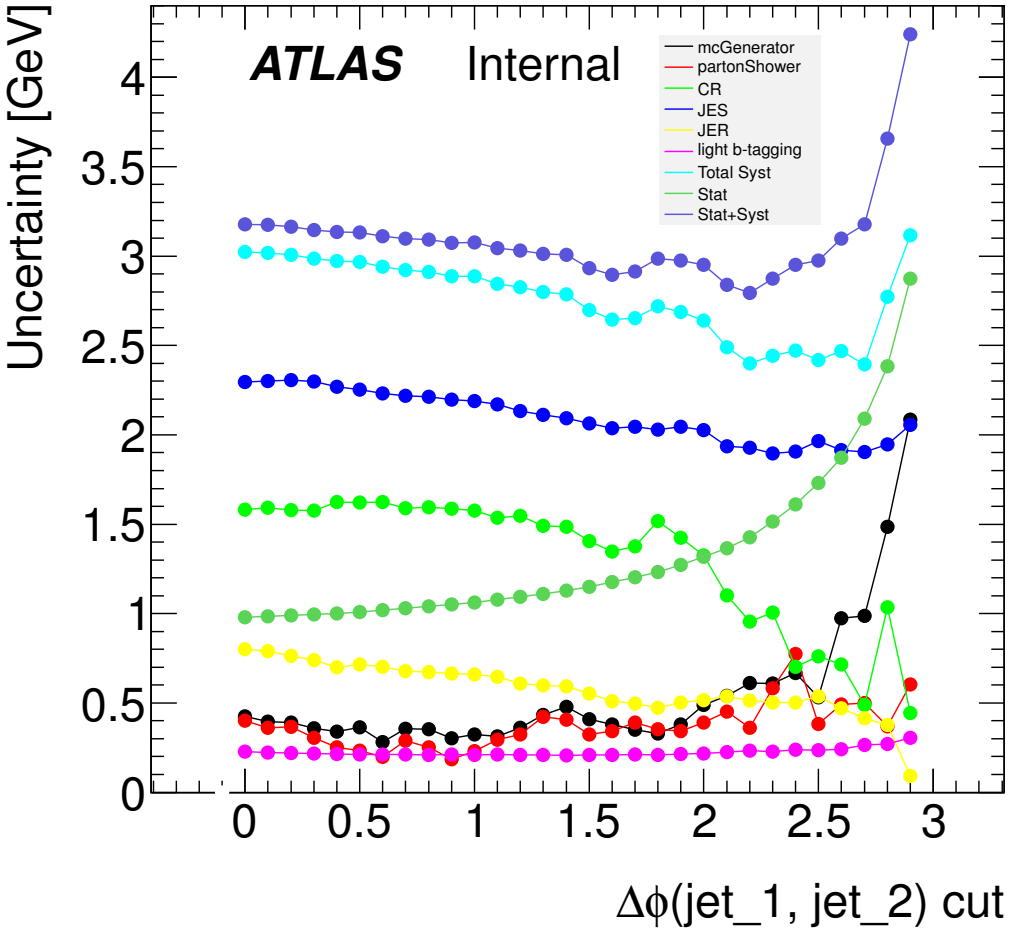


Figure 7.7: Behavior of the dominant uncertainties with respect to the $\Delta\phi_{b_1 b_2}$ cut.

| Sample | Events | Stat. | Syst. |
|---|---|---|---|
| $t\bar{t}$ signal | 720 | ± 5 | $^{+190}_{-200}$ |
| Single top | 9.2 | ± 0.8 | $^{+1.6}_{-1.3}$ |
| Drell-Yan | 0.84 | ± 0.38 | $^{+0.12}_{-0.11}$ |
| Dibosons | 0.14 | ± 0.07 | $^{+0.05}_{-0.04}$ |
| Fake electrons | 24.7 | ± 1.0 | ± 9.9 |
| Fake muons | 2.7 | ± 0.7 | ± 1.1 |
| Total expected | 760 | ± 5 | $^{+190}_{-200}$ |
| Total observed | 731 | - | - |

Table 7.2: Event yields after applying all cuts described Section 7.3.1, including the statistical and systematic uncertainty. No $Z$ + jets background events were selected.

number of events within the expected uncertainty. The agreement between data and simulation is shown in Figure 7.8, Figure 7.9 and Figure 7.10.

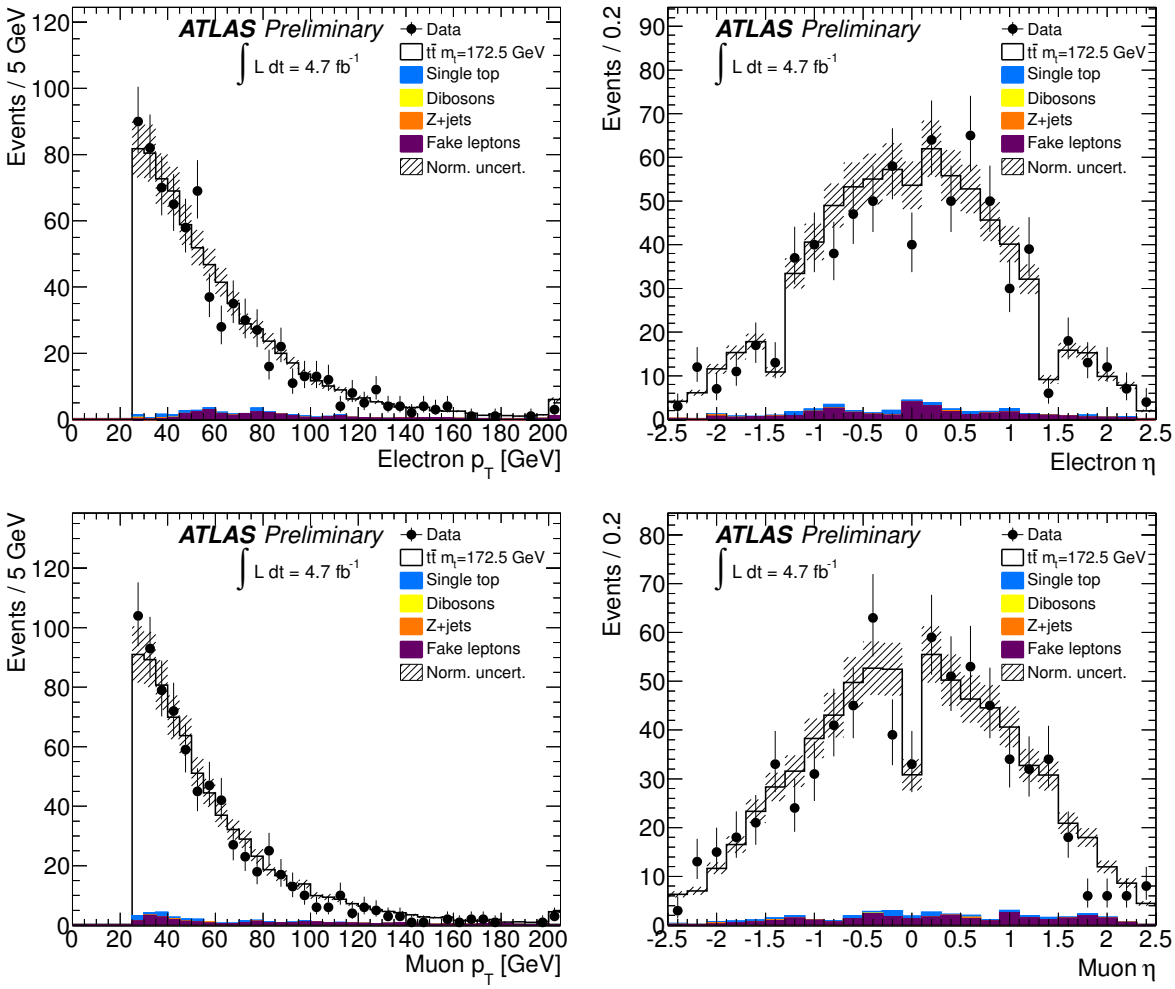


Figure 7.8: Agreement between data and simulation after all the selection cuts for electron and muon $p_{\mathrm{T}}$ and $\eta$.

### 7.3.4 Calibration curve

The calibration curve can be built computing $\overline{m}_{\mathrm{T2}}$ from the expected $m_{\mathrm{T2}}$ distributions (expected signal and background) with $t\bar{t}$ datasets with different input top-quark masses (see Figure 7.12). A linear fit is applied to the points in the calibration curve to obtain the mass dependence of the observable. As shown in Figure 7.11, the linear fit adequately describes the behavior of the calibration points. A fit with a second degree polynomial, such as the one used in Ref. [207], results in a quadratic term coefficient that is compatible with zero within the uncertainties.

From Figure 7.11, it is clear that a linear fit seems adequate to describe the mass dependence of $\overline{m}_{\mathrm{T2}}$. Therefore, the top-quark mass can be obtained using:

$$m_{\mathrm{top}} = \frac{\overline{m}_{\mathrm{T2}} - a}{b}, \tag{7.11}$$

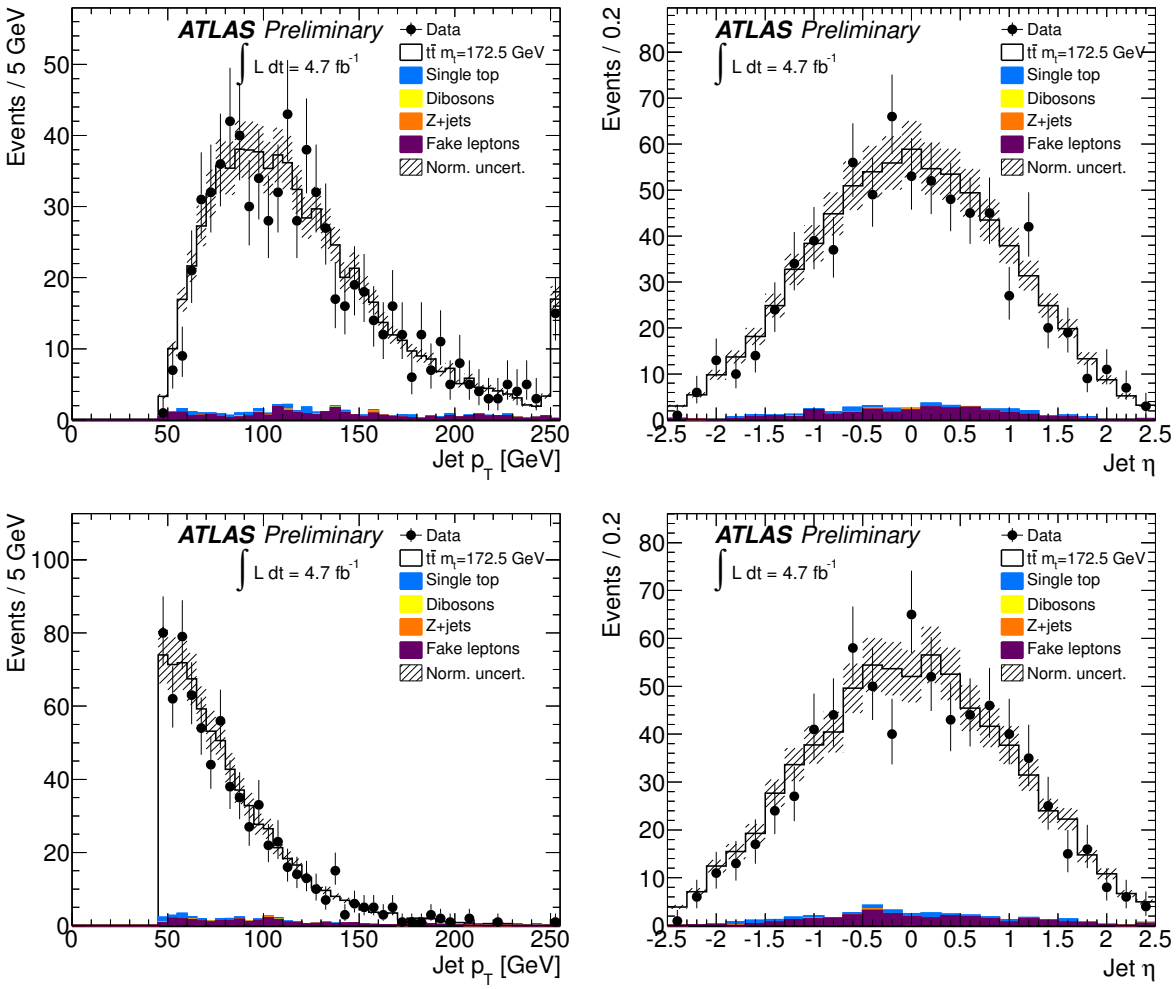


Figure 7.9: Agreement between data and simulation after all the selection cuts for the leading and subleading *b*-tagged jets.

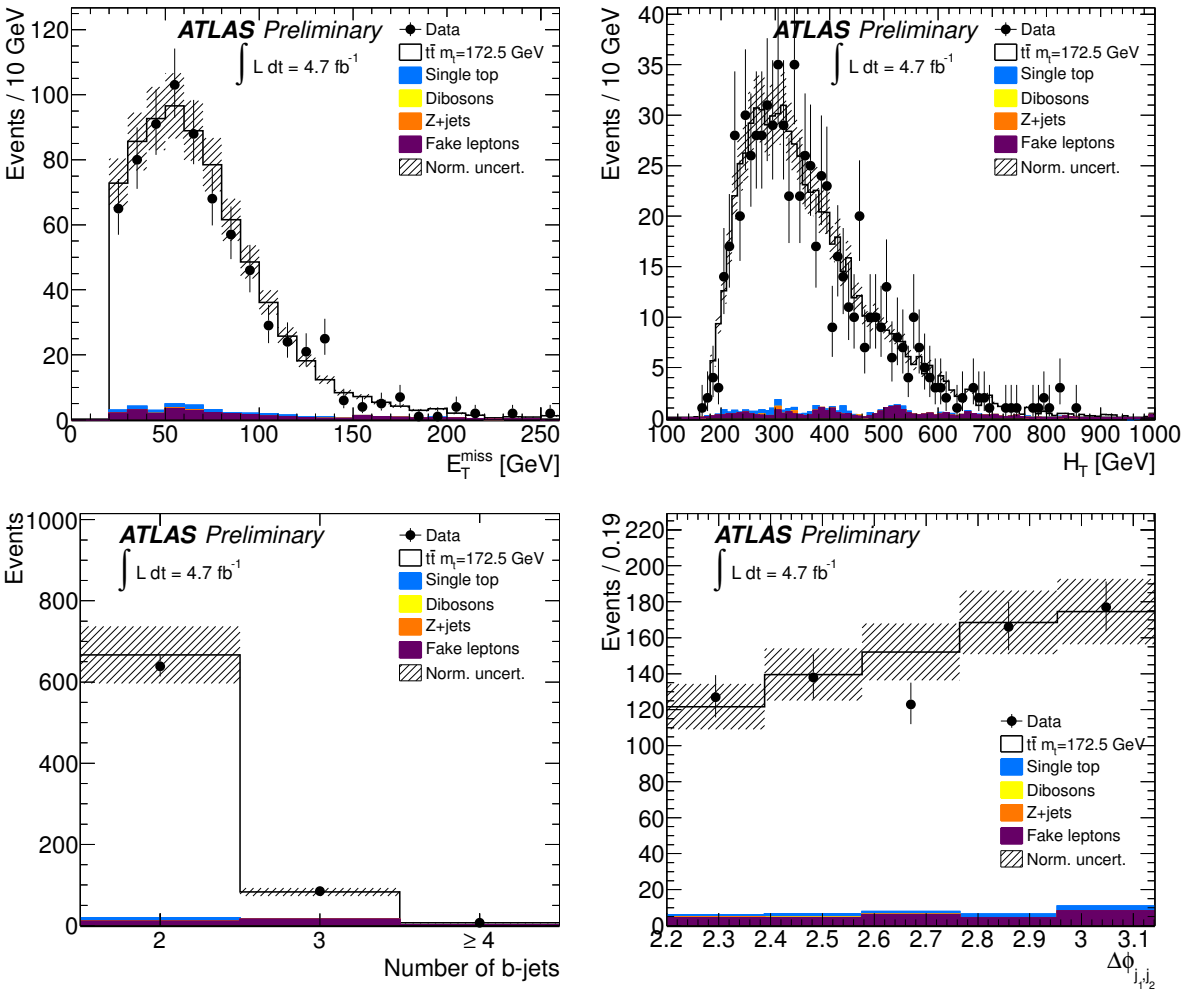


Figure 7.10: Agreement between data and simulation after all the selection cuts for $E_{\mathrm{T}}^{\mathrm{miss}}$, $H_{\mathrm{T}}$, $N_{b\mathrm{tag}}$ and $\Delta\phi_{b_1 b_2}$.

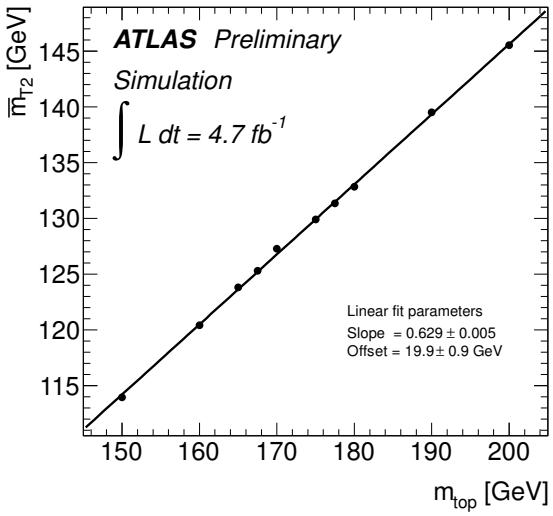


Figure 7.11: Calibration curve used in the top-quark mass measurement. The statistical uncertainty in each point is slightly smaller than the marker size.

where $a = 19.9 \pm 0.9$ GeV is the fitted offset and $b = 0.629 \pm 0.005$ is the fitted slope.

### 7.3.5 Fast simulation bias in the calibration curve

The calibration curve is constructed using datasets generated using fast simulation $t\bar{t}$ datasets (see Section 4.2), while the rest of the analysis is performed using full simulation $t\bar{t}$ datasets. In order to correct for a possible bias introduced by the use of fast simulation $t\bar{t}$ datasets, the value of $\overline{m}_{\mathrm{T2}}$ is computed using the expected $m_{\mathrm{T2}}$ distribution using the full simulation $t\bar{t}$ dataset, obtaining:

$$\overline{m}_{\mathrm{T2}}^{\mathrm{fullsim}} = 129.13 \pm 0.16 \text{ GeV}. \tag{7.12}$$

Replacing the value of $\overline{m}_{\mathrm{T2}}^{\mathrm{fullsim}}$ in Equation 7.11 gives:

$$m_{\mathrm{top}}^{\mathrm{fullsim}} = 173.66 \pm 0.26 \text{ GeV}, \tag{7.13}$$

whereas the input top-quark mass for the full simulation $t\bar{t}$ dataset is 172.5 GeV. Therefore, the calibration curve constructed with fast simulation datasets has a bias of $+1.16 \pm 0.26$ GeV. This bias is corrected changing Equation 7.11 to:

$$m_{\mathrm{top}} = \frac{\overline{m}_{\mathrm{T2}} - a}{b} - 1.16 \text{ GeV}, \tag{7.14}$$

where $a = 19.9 \pm 0.9$ and $b = 0.629 \pm 0.005$ as before and the -1.16 GeV term is the bias correction. The uncertainty in the bias correction is assigned as an additional systematic uncertainty associated to the use of fast simulation datasets.

### 7.3.6 Data measurement

As mentioned earlier in this section, 731 data events are selected in data. In Figure 7.13, the $m_{\mathrm{T2}}$ distribution in data is compared to the expected distribution using the nominal $t\bar{t}$ full simulation dataset

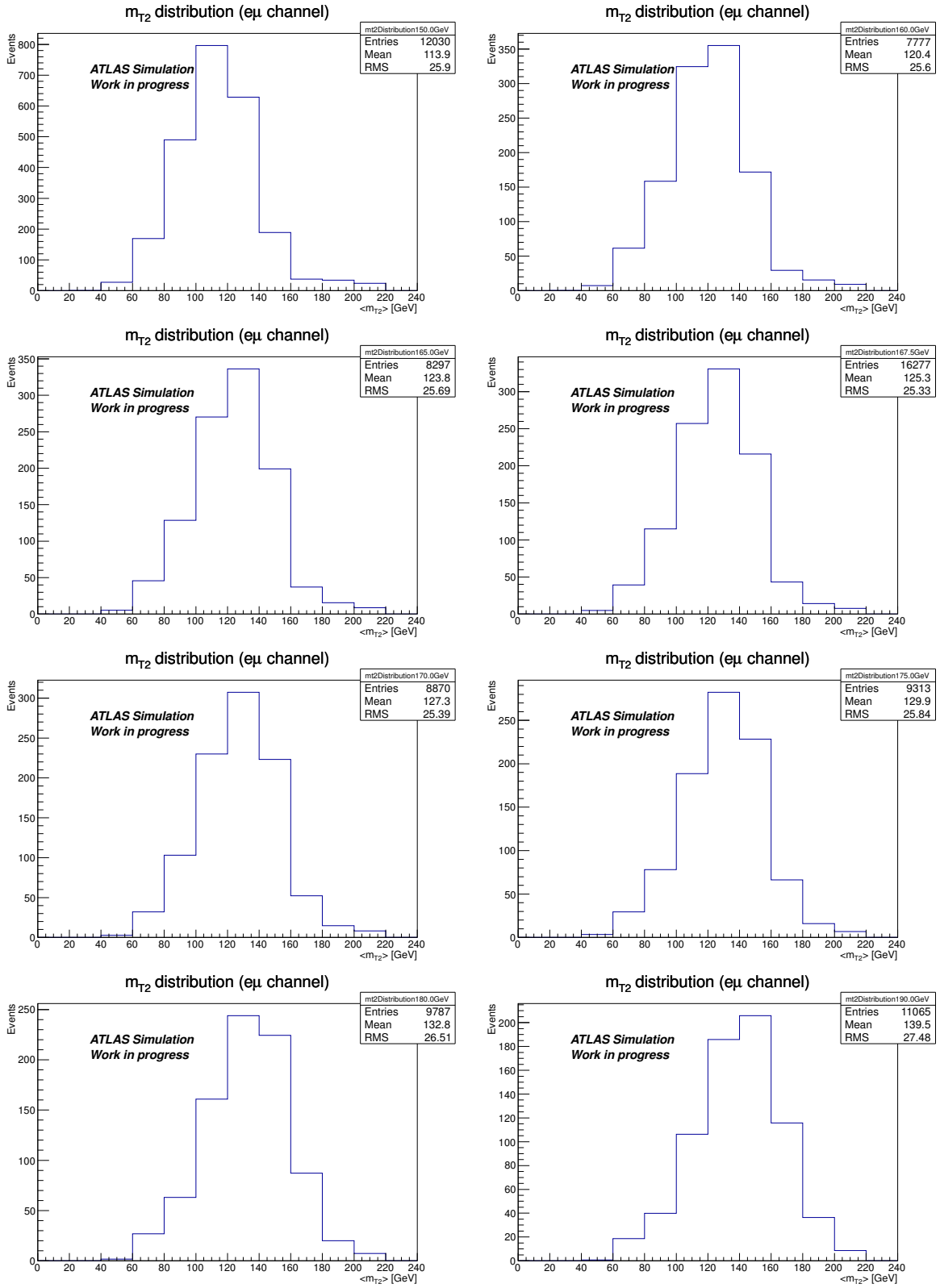


Figure 7.12: $m_{T2}$ distribution for different input top-quark masses.

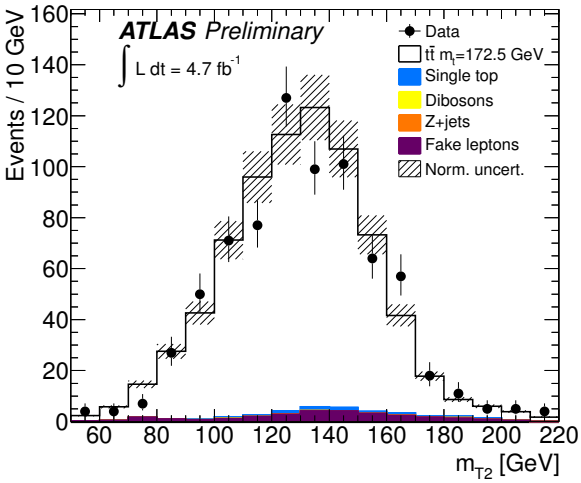


Figure 7.13: $m_{T2}$ distribution in data and simulation (input: $m_{top}$ = 172.5 GeV).

with a input top-quark mass of 172.5 GeV. The value of $\overline{m}_{T2}$ is found to be:

$$\overline{m}_{T2}^{data} = 130.8 \pm 1.0 \text{ GeV}. \tag{7.15}$$

Replacing $\overline{m}_{T2}^{data}$ in Equation 7.14, the measured top-quark mass is:

$$m_{top}^{data} = 175.2 \pm 1.6 \text{ GeV}, \tag{7.16}$$

where the quoted uncertainty is the statistical uncertainty associated with $\overline{m}_{T2}^{data}$, which is estimated using error propagation in Equation 7.14.

### 7.3.7 Systematic uncertainty

The general systematic uncertainties affecting ATLAS analyses have been already discussed in Chapter 6. However, additional systematic uncertainties related to the modeling of $t\bar{t}$ may affect the result of the measurement. Furthermore, a few systematic uncertainties are unique to this analysis and also deserve additional discussion. The impact of the systematic uncertainties affecting the measured value of $m_{top}$ is given in Table 7.3.

Table 7.3 shows the complete list of uncertainties, but many of them have negligible effect, such as the lepton uncertainties. The dominant systematic uncertainties are (largest contribution first):

- jet energy scale,
- $b$-jet energy scale,
- MC generator,
- color reconnection and
- parton shower.

The effect of the improved selection is shown in Table 7.4, where the total uncertainty is decreased by roughly 0.3 GeV.

| Source of systematic uncertainty | $\Delta m_{\text{top}}$ [GeV] |
|---|---|
| MC generator | ± 1.2 |
| Fast simulation bias | ± 0.3 |
| Parton shower | ± 0.9 |
| Color reconnection | ± 1.2 |
| PDF | ± 0.1 |
| ISR/FSR | ± 0.5 |
| Underlying events | ± 0.4 |
| Uncertainty from fit | ± 0.1 |
| Signal normalization | ± 0.0 |
| Single-top normalization | ± 0.0 |
| Fake lepton events normalization | ± 0.2 |
| Fake electron events shape | $^{+0.2}_{-0.1}$ |
| Fake muon events shape | ± 0.0 |
| Jet energy scale | $^{+1.6}_{-1.4}$ |
| $b$-jet energy scale | $^{+1.5}_{-1.2}$ |
| Jet energy resolution | ± 0.5 |
| Jet reconstruction | ± 0.0 |
| Jet vertex fraction | ± 0.0 |
| $E_{\text{T}}^{\text{miss}}$ CellOut+SoftJet | $^{+0.1}_{-0.0}$ |
| $E_{\text{T}}^{\text{miss}}$ pile up | ± 0.0 |
| Electron trigger | ± 0.0 |
| Electron reconstruction | ± 0.0 |
| Electron energy scale | $^{+0.2}_{-0.1}$ |
| Electron resolution | ± 0.0 |
| Muon trigger | ± 0.0 |
| Muon reconstruction | ± 0.0 |
| Muon energy scale and resolution | ± 0.0 |
| $b$-tagging efficiency | ± 0.3 |
| $c$-jet-tagging efficiency | ± 0.1 |
| $b$-tagging fake rate | ± 0.2 |
| Total systematic uncertainty | $^{+3.1}_{-2.9}$ |
| Statistical uncertainty | ± 1.6 |
| Total uncertainty | $^{+3.4}_{-3.2}$ |

Table 7.3: Full list of systematic uncertainties considered in the top-quark mass measurement.

| Description | $\sigma_{\text{std}}$ [GeV] | $\sigma_{\text{this}}$ [GeV] | $\sigma^2_{\text{this}} - \sigma^2_{\text{std}}$[GeV$^2$] |
|---|---|---|---|
| Jet energy scale | $^{+1.7}_{-1.6}$ | $^{+1.6}_{-1.4}$ | -0.6 |
| $b$-jet energy scale | $^{+2.0}_{-1.8}$ | $^{+1.5}_{-1.2}$ | -1.8 |
| MC generator | ± 0.5 | ± 1.2 | +1.2 |
| Color reconnection | ± 1.5 | ± 1.2 | -0.8 |
| Parton shower | ± 0.8 | ± 0.9 | +0.2 |
| Total | $^{+3.2}_{-3.0}$ | $^{+2.9}_{-2.7}$ | -1.7 |

Table 7.4: Comparison of the dominant uncertainties using the standard dilepton cuts ($\sigma_{\text{std}}$) and the cuts used in this analysis ($\sigma_{\text{this}}$). The last column, $\sigma^2 - \sigma^2_{\text{SM}}$, describes the impact on the total uncertainty. The overall effect is a reduction of the total uncertainty by roughly 0.3 GeV.

### 7.3.8 Modeling of $t\bar{t}$

Since the analysis relies heavily on the shape of $t\bar{t}$ kinematic distributions obtained from simulation, it is important to properly estimate the systematic uncertainties associated with the use of these simulations. The systematic uncertainties considered are related to:

- the choice of the event generator,
- parton shower and fragmentation,
- initial and final state radiation,
- parton density functions,
- color reconnection and underlying events.

#### Event generator

The event generators (see Section 4.2) used to model the $t\bar{t}$ dilepton events need to make different assumptions on the physics processes. The impact of these different assumptions on the result is quantified by replacing the event generator for another one, while keeping the rest of the parameters in the analysis unchanged.

The nominal events generator is MC@NLO. The systematic uncertainty is obtained by symmetrizing the full difference between the results of the analysis performed with MC@NLO and a second generator, POWHEG.

#### Showering and hadronization generator

Following the same principle as for the events generator, the use of a given showering and hadronization generator (SHG) also introduces a systematic uncertainty in the measurement.

Two SHGs are used: HERWIG and PYTHIA, where the first one is used as the nominal SHG. A set of $t\bar{t}$ events generated with POWHEG are separately interfaced with these two SHG to produce two datasets (see Table 4.3). These two datasets are then used to estimate the systematic uncertainty associated with the usage of HERWIG. Like in the events generator case, the full difference between the results is symmetrized and taken as the systematic uncertainty.

### Initial and final state radiation

The amount of initial state radiation (ISR) and the final state radiation (FSR) of the generated $t\bar{t}$ events (see Figure 7.14) affect the kinematic distributions of the $t\bar{t}$ events.

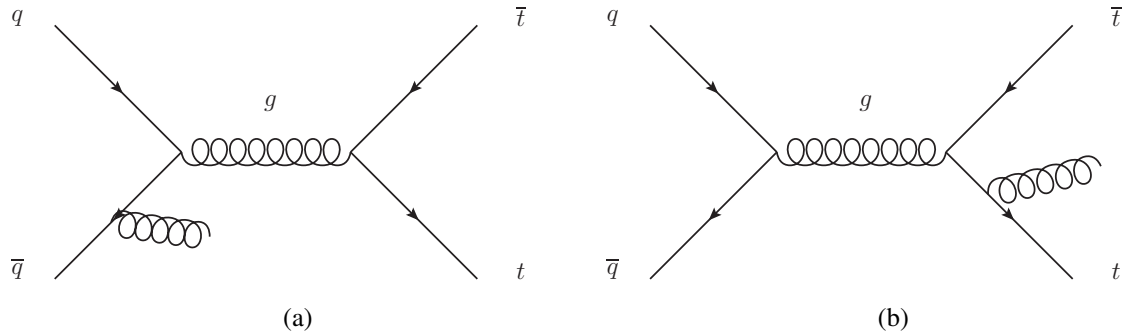


Figure 7.14: Example diagrams of (a) initial and (b) final state radiation.

More specifically, an increase in the rate of ISR or FSR increases the number of jets that are not interesting for the top-quark mass measurement, while decreasing the overall energy of the objects that are of interest in the analysis.

All the $t\bar{t}$ datasets in the nominal analysis assume a given amount of ISR and FSR. In order to quantify the effect of this assumption, one set of events is generated with AcerMC using LHAPDF [208] as PDF set. This set of events is then interfaced with Pythia6 tuned with two different assumptions on the amount of ISR and FSR to create two different datasets (see Table 4.3). The analysis is repeated replacing the $t\bar{t}$ dataset for one of these two datasets, and the half difference between the two results is symmetrized and quoted as the systematic uncertainty associated with the ISR and FSR [209].

The initial comparison of the datasets with more and less ISR/FSR gives a difference of only 0.1 GeV. But the $m_{\mathrm{T2}}$ distribution (see Figure 7.15) shows that there are two canceling effects in the distribution that affect the value of $\overline{m}_{\mathrm{T2}}$: a shift in the bulk of the distribution and a decrease in the right tail. This cancellation might be accidental and, therefore, the two effects are taken into account separately. Since the shift takes places around $m_{\mathrm{T2}} = 180$ GeV, the ISR/FSR uncertainty is computed twice, once for the region $m_{\mathrm{T2}} < 180$ GeV (bulk) and one for the region $m_{\mathrm{T2}} > 180$ GeV (tail). The difference in the bulk region is computed to be 0.3 GeV, while the effect of the tail region is found to be 0.4 GeV. Summing these two quantities in quadrature, the combined uncertainty of both effects is 0.5 GeV.

### Parton density functions

As described in Section 4.2, the simulation of $t\bar{t}$ events needs parton distribution function sets (PDF set) to model the incoming partons of a hard scattering process. Each PDF set uses assumptions that have an impact in the final result of the analysis. Therefore, the usage of a given PDF set introduces a systematic uncertainty that needs to be quantified and propagated to the result of the measurement.

To evaluate the systematic uncertainty associated with the usage of the nominal PDF set, the analysis is repeated using three different PDF sets:

- CT10, using its best fit,
- MSTW2008LO, using its best fit (68% CL) and
- NNPDF2.0 [210], using the mean of 100 parameter variations.

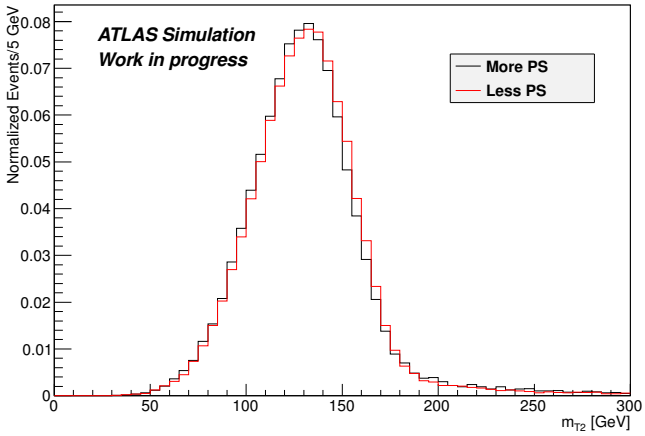


Figure 7.15: $m_{T2}$ distributions for $t\bar{t}$ simulation datasets with more or less ISR/FSR.

The largest half-difference among these three sets is symmetrized and assigned as the PDF systematic uncertainty [185].

### Color reconnection and underlying events

In the proton-proton collisions at the LHC, color string formation between the final partons from independent hard scatterings can take place [211], a process known as color reconnection (CR). Furthermore, during the production of the hard-scattering processes, additional particles such as beam-beam remnants and particles originating from multiple-parton interactions are also present. These particles are known as the underlying event (UE) [212].

The assumptions made on CR and UE introduce a systematic uncertainty that is quantified using a set of events generated with AcerMC and interfaced with Pythia6 as SHG (see Table 4.3) using different tunes [209].

In order to estimate the systematic uncertainty associated with CR, four different Pythia tunes are used, grouped in two sets:

- Perugia set [114]:
  - Perugia 11 and
  - Perugia 11 without CR.
- Professor set [213]:
  - A-Pro and
  - ACR-Pro.

First, the analysis is recomputed using the four different tunes. Then, the full difference in the results of the tunes in the Perugia set is computed. Likewise, the full difference in the results of the tunes in the Professor is also computed. Finally, the maximum value of these two differences is assigned as the systematic uncertainty associated with CR [185].

In order to estimate the systematic uncertainty associated with UE, two Pythia tunes are used: Perugia 11 and Perugia mpiHi [114, 209]. The Perugia mpiHi tune assumes a higher amount of UE activity than

Perugia 11. These two datasets (see Table 4.3) are used to recompute the result of the analysis and the full difference in the result is taken as the systematic uncertainty associated with UE [185].

### 7.3.9 Calibration curve

The calibration curve method assumes a linear relationship between the chosen observable and the value of the top-quark mass [205].

The systematic uncertainty introduced by this assumption is estimated by propagating the uncertainties on the fit parameters into the mass measurement, taking into account the correlation between the slope and the offset parameters, using the error propagation formula:

$$\sigma_y^2 = \sum_{i,j} \left[\frac{\partial y}{\partial \theta_i}\right] \left[\frac{\partial y}{\partial \theta_j}\right] V_{ij}, \tag{7.17}$$

where $y$ is a function of the parameters $\theta$ and $V$ is the covariance matrix of the parameters $\theta$.

### 7.3.10 Pile up

In order to estimate the effect of different pile-up conditions in data, the value of $\overline{m}_{\mathrm{T2}}$ is measured in data events with low and high pile-up conditions. The data events are splitted evenly according to the median of the average number of interactions ($\overline{N}_{\mathrm{int}}$):

- events with $\overline{N}_{\mathrm{int}} < 8.14$ are considered to have low pile-up conditions and
- events with $\overline{N}_{\mathrm{int}} > 8.14$ are considered to have high pile-up conditions.

The value of $\overline{m}_{\mathrm{T2}}$ is found to be 131.3 ± 1.4 GeV for the low pile-up region and 130.2 ± 1.4 GeV for the high pile-up region. Computing the difference between the two values yields: 1.1 ± 1.9 GeV, which is compatible with zero within the statistical uncertainty. Therefore, no extra uncertainty is assigned.

#### Stability of $\overline{m}_{\mathrm{T2}}$

The top-quark mass measurement using $\overline{m}_{\mathrm{T2}}$ as the calibration curve observable may introduce robustness issues. In order to check the stability of the measurement, the $m_{\mathrm{T2}}$ cut is modified from 180 GeV up to 240 GeV in steps of 5 GeV. The whole top-quark mass measurement is repeated for data and simulation for each modification. All measurements are compatible with each other within statistical uncertainties, as shown in Table 7.5.

## 7.4 Improvements to the measurement

Based on the experience acquired in the top-quark mass measurement described in the last section, a number of improvements to this measurement has been tested to reduce the total uncertainty. These improvements can be classified in three categories:

- improvements in the baseline systematic uncertainties,
- redefinition of the event selection,
- improvements to the calibration observables and
- alternative to the $m_{\mathrm{T2}}$ observable.

| $m_{T2}$ cut | Mass measurement (without bias correction) | |
|---|---|---|
| | Data [GeV] | Simulation [GeV] |
| $m_{T2} < 180$ GeV | 175.4 ± 1.6 | 173.73 ± 0.27 |
| $m_{T2} < 185$ GeV | 175.6 ± 1.6 | 173.66 ± 0.26 |
| $m_{T2} < 190$ GeV | 175.7 ± 1.5 | 173.58 ± 0.25 |
| $m_{T2} < 195$ GeV | 175.6 ± 1.5 | 173.64 ± 0.25 |
| $m_{T2} < 200$ GeV | 175.6 ± 1.5 | 173.65 ± 0.25 |
| $m_{T2} < 205$ GeV | 175.2 ± 1.5 | 173.75 ± 0.26 |
| $m_{T2} < 210$ GeV | 175.9 ± 1.5 | 173.71 ± 0.26 |
| $m_{T2} < 215$ GeV | 176.4 ± 1.6 | 173.60 ± 0.26 |
| $m_{T2} < 220$ GeV | 176.2 ± 1.6 | 173.56 ± 0.26 |
| $m_{T2} < 225$ GeV | 176.3 ± 1.6 | 173.50 ± 0.26 |
| $m_{T2} < 230$ GeV | 176.5 ± 1.6 | 173.54 ± 0.27 |
| $m_{T2} < 235$ GeV | 176.6 ± 1.6 | 173.58 ± 0.27 |
| $m_{T2} < 240$ GeV | 176.2 ± 1.6 | 173.66 ± 0.28 |
| Minimum | 175.2 ± 1.5 | 173.50 ± 0.26 |
| Maximum | 176.6 ± 1.6 | 173.75 ± 0.26 |
| Maximum difference | 1.4 | 0.19 |
| Statistical uncertainty | 1.6 | 0.26 |

Table 7.5: Top-quark mass measurement for different values of the $m_{T2}$ cut to assess the stability of the measurement. All measurements in data and simulation are compatible within their respective statistical uncertainties. The fast simulation bias correction is not included since it does not affect the final conclusion.

### 7.4.1 Improvements in the baseline systematic uncertainties

The analysis presented in the last section uses the ATLAS calibrations that were available in 2012. A significant reduction of the systematic uncertainties is possible thanks to the new calibrations and prescriptions produced in 2013, as shown in Table 7.6.

The most significant change for the top-quark mass measurement is the introduction of an improved prescription for the evaluation of the jet-energy-scale and $b$-jet-energy-scale uncertainty [179]. The new calibrations reduce the uncertainty on the jet energy scale by 33%, and the uncertainty on the $b$-jet energy scale by 71% in the top-quark mass measurement. The evaluation of the systematic uncertainties associated with the modeling of $t\bar{t}$ is also improved. These new prescriptions reduce the systematic uncertainty related to the modeling of $t\bar{t}$ by roughly 15%, with the strongest improvements taking place in the parton shower and color reconnection uncertainties. The overall reduction of the dominant systematic uncertainties is of the order of 30%.

| Description | 2012 prescriptions [GeV] | 2013 prescriptions [GeV] |
|---|---|---|
| Jet energy scale | ± 1.5 | ± 1.0 |
| $b$-jet energy scale | ± 1.4 | ± 0.4 |
| MC generator | ± 1.2 | ± 1.5 |
| Color reconnection | ± 1.2 | ± 0.6 |
| Parton shower | ± 0.9 | ± 0.3 |
| Sum | ± 2.8 | ± 2.0 |

Table 7.6: Changes in the dominant systematic uncertainties due to the new systematic uncertainty prescriptions.

Another change in the analysis is the change of the MC generator used to simulate $t\bar{t}$ events to POWHEG+PYTHIA6 using the PERUGIA P2011C tune. Full simulation datasets are produced for the nominal ($m_{\text{top}}$=172.5 GeV) and mass variation datasets corresponding to input top-quark masses in the range 165 − 180 GeV in steps of 2.5 GeV, as well as the corresponding systematic variation datasets (in fast simulation). The list of all the $t\bar{t}$ datasets is shown in Table 7.7 and the calibration curves built with the old and new mass variation datasets are compared in Figure 7.16, where it can be seen that the full simulation datasets have a larger value of $m_{\text{T2}}$ than their fast simulation counterparts.

### 7.4.2 Redefinition of the event selection

The reduction in the magnitude of the systematic uncertainties implies that the statistical uncertainty has a more important role in the top-quark mass measurement. Furthermore, the top-quark mass measurement presented in the last section is tuned to give a smaller total uncertainty based on the systematic uncertainty prescriptions available in 2012. Therefore, the event selection is changed to better fit the new conditions. In particular, the $t\bar{t}$ $ee$ channel and $\mu\mu$ channel are included in the analysis.

The new event selection is almost identical to the standard dilepton selection of the ATLAS top working group, except for the removal of the $H_{\text{T}}$ requirement in the $e\mu$ channel and that at least two $b$-tagged jets are required instead of at least one.

The most important change in the event selection is the inclusion of the $ee$ channel and the $\mu\mu$ channel, i.e., the event must have exactly two reconstructed leptons (electrons, muons or both). Furthermore, the electron trigger for all data events before period K has been changed from EF_e20_medium to EF_e22_medium, effectively raising the trigger electron $p_{\text{T}}$ threshold to 22 GeV. The $E_{\text{T}}$ requirement on

| Dataset number | Description | Event generator+SHG | $\sigma_{\text{NLO}}$ (pb) | Events $\mathcal{L}$ (fb$^{-1}$) | Sim. type |
|---|---|---|---|---|---|
| 117050 | Nominal sample | POWHEG+PYTHIA6 | 96.2 | 103.9 | full |
| 105200 | Generator syst. variation | MC@NLO+HERWIG | 96.3 | 155.7 | fast |
| 105860 | Generator syst. variation | POWHEG+HERWIG | 96.3 | 103.9 | fast |
| 117050 | Generator syst. variation | POWHEG+PYTHIA6 | 96.2 | 103.9 | fast |
| 117862 | ISR/FSR syst. variation | ACERMC+PYTHIA6 | 96.3 | 311.4 | fast |
| 117863 | ISR/FSR syst. variation | ACERMC+PYTHIA6 | 96.3 | 311.4 | fast |
| 117428 | CR and UE syst. variation (nominal) | POWHEG+PYTHIA6 | 96.2 | 103.9 | fast |
| 117429 | UE syst. variation | POWHEG+PYTHIA6 | 96.2 | 103.9 | fast |
| 117430 | CR syst. variation | POWHEG+PYTHIA6 | 96.2 | 103.9 | fast |
| 117836 | $m_{\text{top}}^{MC} = 165.0$ GeV | POWHEG+PYTHIA6 | 113.9 | 43.9 | full |
| 117838 | $m_{\text{top}}^{MC} = 167.5$ GeV | POWHEG+PYTHIA6 | 105.4 | 47.4 | full |
| 117840 | $m_{\text{top}}^{MC} = 170.0$ GeV | POWHEG+PYTHIA6 | 97.7 | 51.2 | full |
| 117842 | $m_{\text{top}}^{MC} = 175.0$ GeV | POWHEG+PYTHIA6 | 84.1 | 59.5 | full |
| 117844 | $m_{\text{top}}^{MC} = 177.5$ GeV | POWHEG+PYTHIA6 | 78.1 | 64.1 | full |
| 117846 | $m_{\text{top}}^{MC} = 180.0$ GeV | POWHEG+PYTHIA6 | 72.6 | 68.9 | full |

Table 7.7: $t\bar{t}$ datasets used in the top-quark mass measurement.

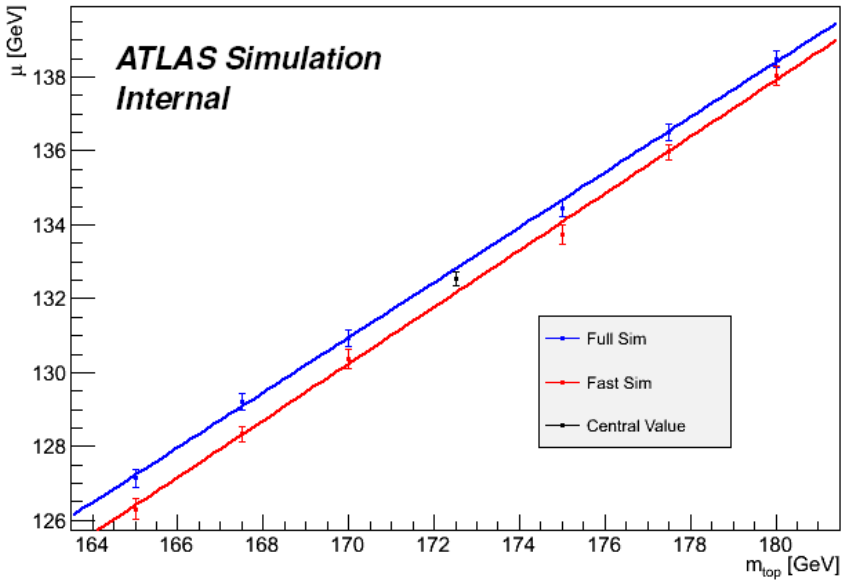


Figure 7.16: Calibration curves using the 2012 and 2013 mass variation datasets. The 2012 calibration curve uses fast simulation datasets generated with MC@NLO+Herwig, while the 2013 calibration curve uses full simulation datasets generated with Powheg+Pythia6. The central value point is obtained using the Powheg+Pythia6 $t\bar{t}$ dataset.

electron candidates is replaced by $p_{\mathrm{T}} > 25$ GeV, while the $p_{\mathrm{T}}$ threshold for muon candidates is lowered from $p_{\mathrm{T}} > 25$ GeV to $p_{\mathrm{T}} > 20$ GeV. In the $e\mu$ channel, the $E_{\mathrm{T}}^{\mathrm{miss}}$ and the $H_{\mathrm{T}}$ requirements are removed. The $b$-tagging algorithm efficiency is lowered from 85% to 70%, giving a significant reduction in the number of $b$-tagged jets that are not true $b$-jets. Furthermore, the extra $p_{\mathrm{T}}$ requirement on the leading and subleading $b$-tagged jets is removed, reducing it to the standard $p_{\mathrm{T}} > 25$ GeV requirement. The upper $m_{\mathrm{T2}}$ cut and the $\Delta\phi_{b_1 b_2}$ cuts are also removed. Additional requirements must be met by $ee$-channel and $\mu\mu$-channel events:

- The invariant mass of the leptons must be larger than 15 GeV. This requirement is used to suppress low-energy resonances.
- The invariant mass of the dilepton system is required to satisfy $|m_{\ell\ell} - m_Z| > 10$ GeV in order to suppress $Z$ + jets events.
- $E_{\mathrm{T}}^{\mathrm{miss}} > 60$ GeV.

Table 7.8 summarizes all the changes in the event selection.

### 7.4.3 Improvements to the calibration observable

The observable used so far is the $\overline{m}_{\mathrm{T2}}$, which is susceptible to changes and mismodelings in the tail of the $m_{\mathrm{T2}}$ distribution, as discussed in Section 7.3.10. This issue can be addressed by changing the definition of the observable extracted from the $m_{\mathrm{T2}}$ distribution to a fitted parameter.

The distribution is fitted assuming that the $m_{\mathrm{T2}}$ distribution is an asymmetric Gaussian given by:

$$f\left(x, \mu\left(x\right), \sigma, R_\sigma, A\right) = A \cdot \left[H\left(\mu\left(x\right) - x\right) G\left(x, \sigma\right) + H\left(x - \mu\left(x\right)\right) G\left(x, \sigma \cdot R_\sigma\right)\right], \tag{7.18}$$

| Description | 2012 selection | 2013 selection |
|---|---|---|
| Dilepton channels | Only $e\mu$ channel | All |
| Electron trigger for data periods before K | EF_e20_medium | EF_e22_medium |
| Electron energy/momentum | $E_{\mathrm{T}} > 25$ GeV | $p_{\mathrm{T}} > 25$ GeV |
| Muon $p_{\mathrm{T}}$ | $p_{\mathrm{T}} > 25$ GeV | $p_{\mathrm{T}} > 20$ GeV |
| $H_{\mathrm{T}}$ for $e\mu$ channel | $H_{\mathrm{T}} > 130$ GeV | None |
| $E_{\mathrm{T}}^{\mathrm{miss}}$ for $e\mu$ channel | $E_{\mathrm{T}}^{\mathrm{miss}} > 45$ GeV | None |
| $b$-tagging MV1 working point | 85% | 70% |
| $b$-tagged jet $p_{\mathrm{T}}$ | $p_{\mathrm{T}} > 45$ GeV | $p_{\mathrm{T}} > 25$ GeV |
| $m_{\mathrm{T2}}$ | $m_{\mathrm{T2}} < 220$ GeV | None |
| $\Delta\phi_{b_1 b_2}$ | $\Delta\phi_{b_1 b_2} > 2.2$ | None |
| $m_{\ell\ell}$ in $ee$ channel and $\mu\mu$ channel | Channels are not used | $m_{\ell\ell} > 15$ GeV |
| $\lvert m_{\ell\ell} - m_Z \rvert$ in $ee$ channel and $\mu\mu$ channel | Channels are not used | $\lvert m_{\ell\ell} - m_Z \rvert > 10$ GeV |
| $E_{\mathrm{T}}^{\mathrm{miss}}$ in $ee$ channel and $\mu\mu$ channel | Channels are not used | $E_{\mathrm{T}}^{\mathrm{miss}} > 60$ GeV |

Table 7.8: Changes in the event selection of the top-quark mass measurement.

where $H$ is the Heaviside function, $G$ is the symmetric Gaussian function, $\mu(x)$ is the mean of the asymmetric Gaussian, $\sigma$ is the standard deviation of the left tail of the asymmetric Gaussian ($\sigma_{\mathrm{L}}$), $R_\sigma = \frac{\sigma_{\mathrm{R}}}{\sigma_{\mathrm{L}}}$ is the ratio between the standard deviation of the right tail ($\sigma_{\mathrm{R}}$) and the left tail of the asymmetric Gaussian, and $A$ is the overall normalization of the distribution. The values of $A$, $\sigma$ and $\mu(x)$ are determined fitting the model to the $m_{\mathrm{T2}}$ distribution, while the value of $R_\sigma$ remains fixed to 1.25 during the whole analysis. The value of $R_\sigma$ is chosen such that the resulting fit has the lowest value of $\chi^2$.

The fit used to determine $\mu(x)$ in the previous discussion is not performed on a fixed range. Instead, a dynamic range is used based on the following iterative process:

- Fit the distribution in the active range to determine $\mu(x)$ and $\sigma$.
- Redefine the active range as the 17 bins (with 5 GeV width) range containing the value of $\mu(x)$ in the central bin.
- Repeat the procedure until the changes in $\mu(x)$ and $\sigma$ are below the tolerance ($10^{-6}$%, satisfied independently).

The starting active range is $[0, 240]$ GeV for the $m_{\mathrm{T2}}$ distribution and is considered large enough to describe the shape of the whole $m_{\mathrm{T2}}$ distribution. The convergence usually takes place within three iterations, which is the minimum number of iterations. Figure 7.17 shows the fit to the $m_{\mathrm{T2}}$ distribution for all the mass variation datasets. The values of $\mu(x) = \overline{m}_{\mathrm{T2}}$ obtained from these fits are used to build the calibration curve shown in Figure 7.18.

### 7.4.4 Alternative to the $m_{\mathrm{T2}}$ variable: the $m_{\mathrm{T2perp}}$ variable

Alternatively to the $m_{\mathrm{T2}}$ variable, the use of its perpendicular projection on the upstream momentum, $m_{\mathrm{T2perp}}$, has been explored [214, 215].

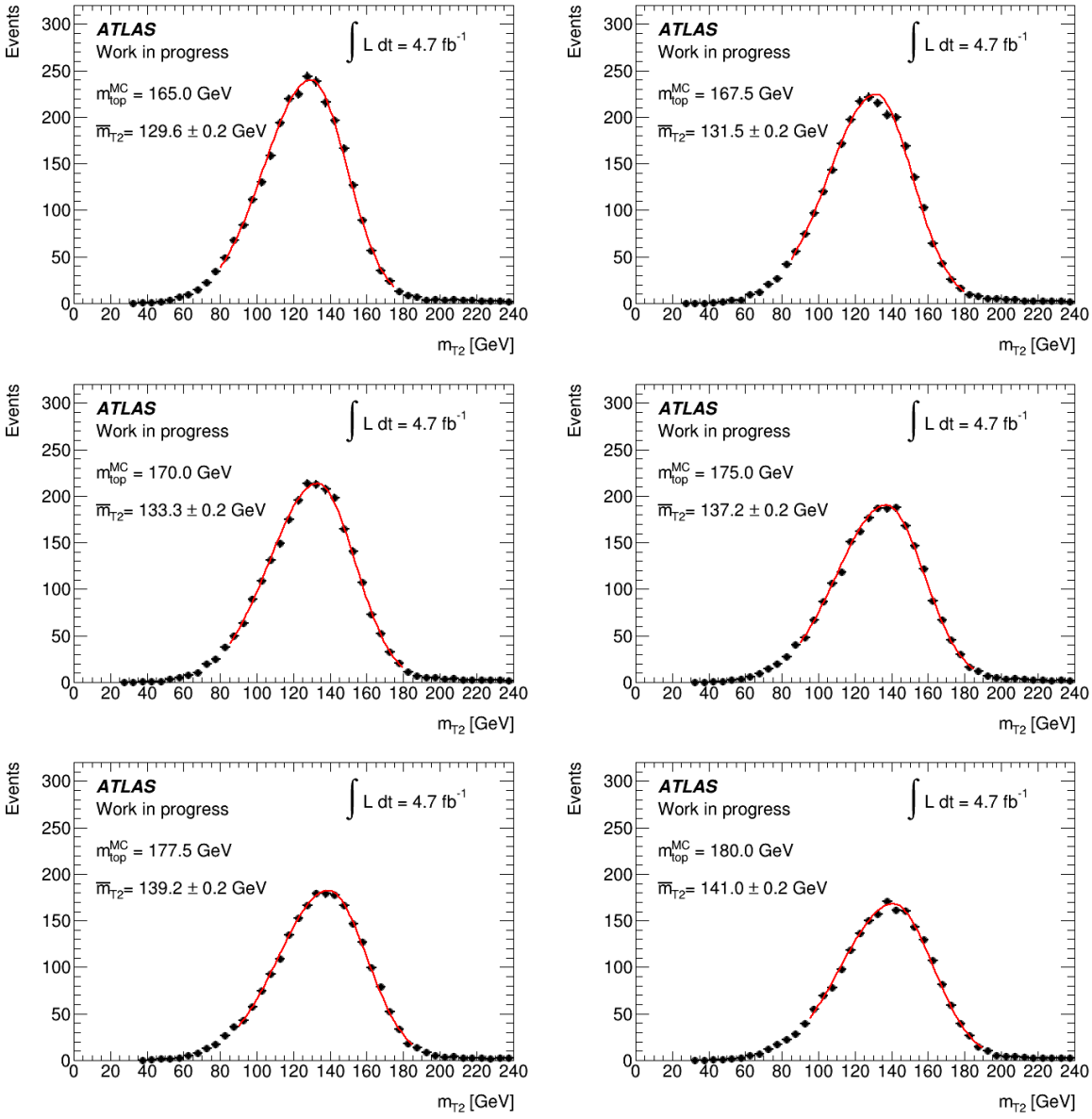


Figure 7.17: $m_{\mathrm{T2}}$ distribution for different input top-quark masses, fitted using the dynamic range fit.

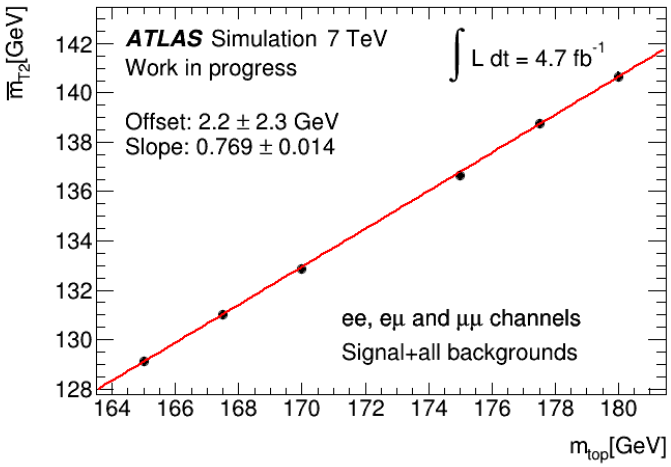


Figure 7.18: Calibration curve obtained using the dynamic range fit method with $m_{\mathrm{T2}}$.

The definition of the $m_{\mathrm{T2perp}}$ variable follows the same principles as the $m_{\mathrm{T2}}$ variable. The only difference is the use of the perpendicular projection of the particles momenta on the direction of the transverse upstream momentum. The transverse upstream momentum of an event is defined as the vectorial sum of all the particles that are not part of the hard process. In practice, momentum conservation allows for a simpler definition:

$$\vec{U}_{\mathrm{T}} = -\left( \sum_{\text{leptons}} \vec{p}_{\mathrm{T}} + \sum_{\text{jets}} \vec{p}_{\mathrm{T}} + \vec{p}_{\mathrm{T}}^{\,\mathrm{miss}} \right), \tag{7.19}$$

where only the two leptons and two jets from the dilepton decays are used.

The projection of the transverse momenta of the leptons, jets and missing transverse momentum on the upstream momentum is computed using:

$$\vec{p}_{\mathrm{Tperp}} = \frac{1}{|\vec{U}_{\mathrm{T}}|^2} \vec{U}_{\mathrm{T}} \times \left( \vec{p}_{\mathrm{T}} \times \vec{U}_{\mathrm{T}} \right). \tag{7.20}$$

Once these projections are computed, the value of $m_{\mathrm{T2perp}}$ is defined as:

$$m_{\mathrm{T2perp}}\left(m_{\mathrm{inv}}\right) = \min_{\vec{p}^{\,(1)}_{\mathrm{Tperp}}, \vec{p}^{\,(2)}_{\mathrm{Tperp}}} \left\{ \max\left[ m_{\mathrm{T}}\left(m_{\mathrm{inv}}, \vec{p}^{\,(1)}_{\mathrm{Tperp}}\right), m_{\mathrm{T}}\left(m_{\mathrm{inv}}, \vec{p}^{\,(2)}_{\mathrm{Tperp}}\right) \right] \right\}, \tag{7.21}$$

with

$$\vec{p}^{\,(1)}_{\mathrm{Tperp}} + \vec{p}^{\,(2)}_{\mathrm{Tperp}} = \vec{p}^{\,\mathrm{miss}}_{\mathrm{Tperp}}, \tag{7.22}$$

where all the variables that appear in Equation 7.21 and Equation 7.22 are the $\vec{U}_{\mathrm{T}}$-perpendicular-projection analogous of the variables in the $m_{\mathrm{T2}}$ definition shown in Equation 7.1 and Equation 7.2.

The $m_{\mathrm{T2perp}}$ variable offers an alternative observable to the $m_{\mathrm{T2}}$ variable. Its advantage is a much simpler computation, since the two-dimensional minimization needed for the $m_{\mathrm{T2}}$ computation is reduced to a one-dimensional minimization for the $m_{\mathrm{T2perp}}$ variable.

Similar to the $m_{\mathrm{T2}}$ case, the lepton-jet pairing in a $t\bar{t}$ event is unknown. Therefore, all suitable lepton-jet combinations are tried and the combination giving the smallest value of $m_{\mathrm{T2perp}}$ is taken as the correct

combination.

A calibration curve (see Figure 7.20) can be derived from the $m_{\mathrm{T2perp}}$ distributions of the mass variation datasets applying the same asymmetric Gaussian model used in the $m_{\mathrm{T2}}$ fit, but using the dynamic range fit with 9 bins to each side of the central bin, as shown in Figure 7.19.

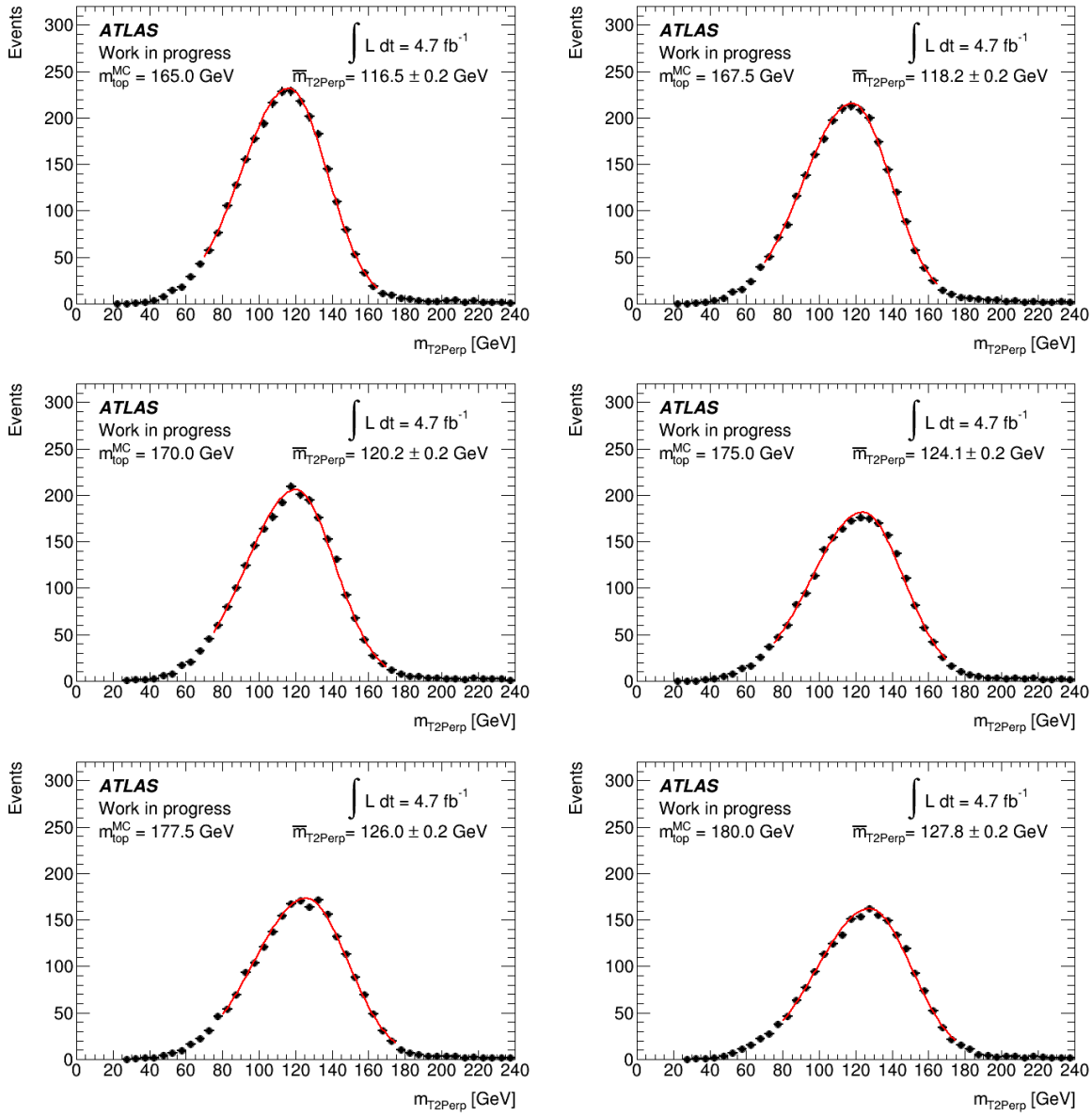


Figure 7.19: $m_{\mathrm{T2perp}}$ distribution for different input top-quark masses, fitted using the dynamic range fit.

### 7.4.5 Comparison of the top-quark mass measurement using $m_{\mathrm{T2}}$ and using $m_{\mathrm{T2perp}}$

The full systematic and statistical uncertainties are estimated for both variables and compared in Table 7.9. Overall, the systematic uncertainty is reduced by roughly 40%, 20% of which are associated to the overall improvements to the baseline systematic uncertainties, as discussed in Section 7.4.1. The statistical uncertainty is reduced by roughly 50%, mainly due to additional information obtained from the

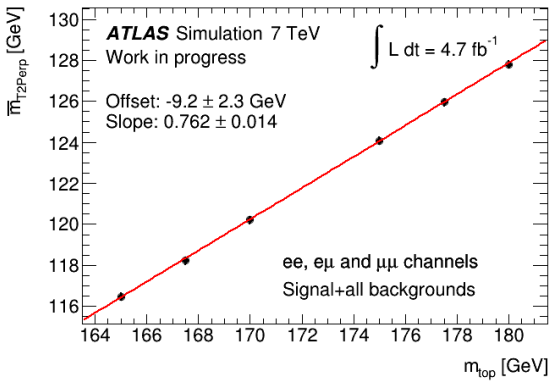


Figure 7.20: Calibration curve obtained using the dynamic range fit method with $m_{\mathrm{T2perp}}$.

fitting process and partly because of the inclusion of the *ee* channel and the $\mu\mu$ channel. The top-quark mass measurements using $m_{\mathrm{T2}}$ and $m_{\mathrm{T2perp}}$ have roughly the same uncertainty, with $m_{\mathrm{T2perp}}$ bringing an improvement of roughly 5% to the total uncertainty.

The agreement between data and simulation for the $m_{\mathrm{T2}}$ and the $m_{\mathrm{T2perp}}$ distributions is shown in Figure 7.21, where the nominal $t\bar{t}$ dataset is used. The excess in data of roughly 20% is a known issue and is taken into account in the $t\bar{t}$ normalization uncertainty. The top-quark mass measurement is barely affected by this excess, since the measurement only compares the shapes of the distributions.

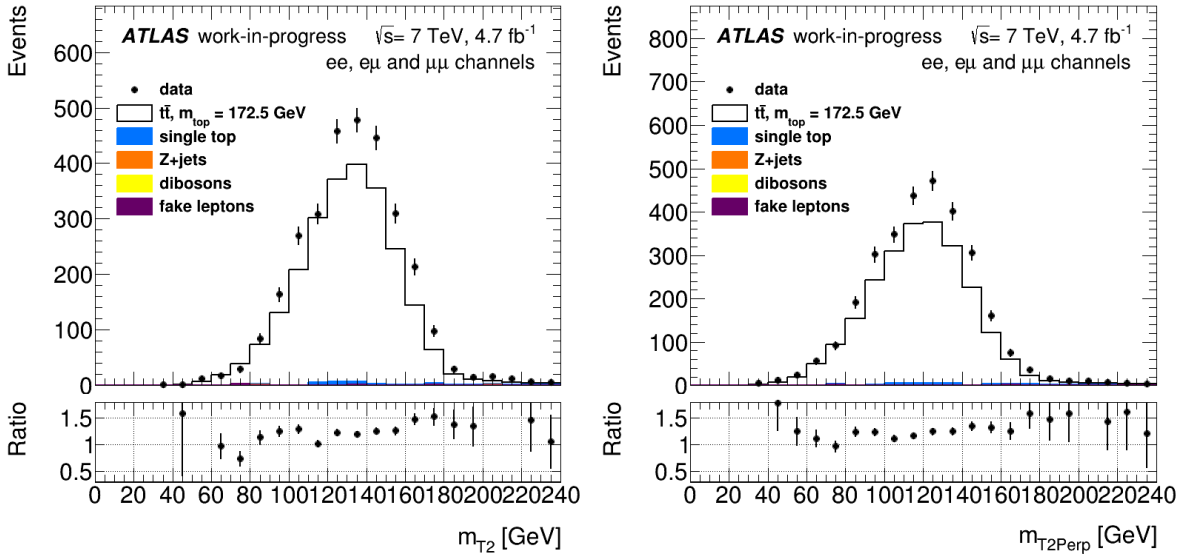


Figure 7.21: Comparison between data and simulation distributions of $m_{\mathrm{T2}}$ and $m_{\mathrm{T2perp}}$.

In summary, the top-quark mass has been measured using three methods. The nominal method, using the mean value of the $m_{\mathrm{T2}}$ distribution, gives a top-quark mass of:

$$m_{\mathrm{top}}^{\mathrm{data}} = 175.2 \pm 1.6\,(\mathrm{stat.}) \pm 3.1\,(\mathrm{syst.})\ \mathrm{GeV}. \tag{7.23}$$

The improved method, using the fitted mean of the $m_{T2}$ distribution, gives a top-quark mass of:

$$m_{top}^{data} = 173.7 \pm 0.8 \text{ (stat.)} \pm 1.8 \text{ (syst.) GeV}. \quad (7.24)$$

Finally, the top-quark mass measurement using the $m_{T2perp}$ variable yields:

$$m_{top}^{data} = 173.3 \pm 0.7 \text{ (stat.)} \pm 1.7 \text{ (syst.) GeV}. \quad (7.25)$$

| Description | Value [GeV] | | |
|---|---|---|---|
| | $m_{T2}$ (nominal, mean) | $m_{T2}$ (improved, fit) | $m_{T2perp}$ (fit) |
| MC generator | ± 1.2 | ± 0.56 | ± 0.52 |
| Fast simulation bias | ± 0.3 | ± 0.00 | ± 0.00 |
| Parton shower | ± 0.9 | ± 0.04 | ± 0.29 |
| Color reconnection | ± 1.2 | ± 0.17 | ± 0.40 |
| ISR/FSR | ± 0.5 | ± 0.68 | ± 0.68 |
| Underlying events | ± 0.4 | ± 0.02 | ± 0.02 |
| Normalization | ± 0.3 | ± 0.10 | ± 0.13 |
| Jet energy scale | ± 1.6 | ± 1.11 | ± 0.97 |
| *b*-jet energy scale | ± 1.5 | ± 0.92 | ± 0.85 |
| *b*-tagging | ± 0.4 | ± 0.34 | ± 0.33 |
| Other uncertainties | ± 0.5 | ± 0.35 | ± 0.36 |
| Total systematic uncertainty | ± 3.1 | ± 1.77 | ± 1.71 |
| Statistical uncertainty | ± 1.6 | ± 0.84 | ± 0.74 |
| Total uncertainty | ± 3.4 | ± 1.96 | ± 1.86 |

Table 7.9: Comparison of the uncertainty for the top-quark mass measurement using $m_{T2}$ (mean value and fit) and $m_{T2perp}$ (fit). All the uncertainties have been symmetrized. The uncertainties of the last two measurements are shown with two decimal places to allow a better comparison between the measurements using $m_{T2}$ and $m_{T2perp}$.

When compared to the 2012 measurement [205], the total uncertainty in the top-quark mass measurement is nearly halved in the 2013 analysis. Furthermore, the analysis has a comparable precision as the 2013 ATLAS top-quark mass measurement in the dilepton channel:

$$m_{top} = 173.1 \pm 0.6 \text{ (stat.)} \pm 1.5 \text{ (syst.) GeV}, \quad (7.26)$$

which uses a template method with the $m_{\ell b}$ variable [216].

In Ref. [217], a similar analysis using the calibration method with the $m_{T2}$ and $m_{T2perp}$ variables is presented, where the asymmetric Gaussian fit with dynamic range is replaced with a repeated Gaussian fit. The selection is optimized to give the lowest total uncertainty and uses a different *b*-tagging working point (MV1@85%) and a tighter cut on the $p_T$ of jets. The results of both analyses are compatible within their uncertainties:

- top-quark mass measurement with $m_{\mathrm{T2}}$: $m_{\mathrm{top}} = 175.1 \pm 0.9\,(\mathrm{stat.}) \pm 1.6\,(\mathrm{syst.})$ GeV.
- top-quark mass measurement with $m_{\mathrm{T2perp}}$: $m_{\mathrm{top}} = 174.1 \pm 0.8\,(\mathrm{stat.}) \pm 1.4\,(\mathrm{syst.})$ GeV.

Three years after the first ATLAS top-quark mass measurement in the dilepton channel presented in this thesis, the channel gives a significant contribution towards the precise measurement of the top-quark mass in ATLAS. The most recent ATLAS measurement (2015) is performed in the $t\bar{t}$ single-lepton and dilepton channels [218], measuring:

$$m_{\mathrm{top}}^{\text{single lepton}} = 172.33 \pm 0.75\,(\mathrm{stat.} + \mathrm{JES} + \mathrm{bJES}) \pm 1.02\,(\mathrm{syst.})\ \mathrm{GeV}, \tag{7.27}$$

and

$$m_{\mathrm{top}}^{\text{dilepton}} = 173.79 \pm 0.54\,(\mathrm{stat.}) \pm 1.30\,(\mathrm{syst.})\ \mathrm{GeV}. \tag{7.28}$$

The combination of these two results gives a top-quark mass value of

$$m_{\mathrm{top}}^{\text{combined}} = 172.99 \pm 0.48\,(\mathrm{stat.}) \pm 0.78\,(\mathrm{syst.})\ \mathrm{GeV}. \tag{7.29}$$

The measurement in the dilepton channel uses an event selection similar to the one described in Section 7.4.2, but also includes events with exactly one $b$-tagged jet. The improvement in the total systematic uncertainty with respect to the 2013 ATLAS top-quark mass measurement in the dilepton channel is mainly due to a better understanding of the jet energy scale, reducing the uncertainty associated with it.

CHAPTER 8

# $t\bar{t}Z$ cross-section measurement

## 8.1 Event selection

### 8.1.1 Definition of variables

In order to describe the event selection used in the $t\bar{t}Z$ cross-section measurement, it is useful to introduce the following definitions for events with four reconstructed leptons: the $Z1$ lepton pair, the $Z2$ lepton pair, $m_{Z1}$, $m_{Z2}$ and $p_{\mathrm{T}34}$. The leptons and jets are numbered in descending order according to the value of their transverse momentum.

- The $Z1$ lepton pair is the pair of leptons which is most likely to originate from a $Z$ boson decay. This is defined as the pair of leptons with opposite-sign (OS) and same-flavor (SF) in the event. If more than one OSSF[1] lepton combination is possible, the lepton combination with the closest invariant mass to the mass of the $Z$ boson is chosen. If no OSSF lepton pair is found, $Z1$ is undefined.
- The $Z2$ lepton pair is defined as the two leptons that do not belong to the $Z1$ pair.
- $m_{Z1}$ and $m_{Z2}$ are the invariant masses of the $Z1$ and $Z2$ lepton pairs, respectively.
- $p_{\mathrm{T}34}$ is defined as the scalar sum of the transverse momentum of the two leptons with the smallest transverse momentum.

### 8.1.2 Four lepton Standard Model backgrounds

The $t\bar{t}Z \to 4\ell$ channel has the following signature:

- four leptons, two from the $t\bar{t}$ dilepton decay and two from the $Z$ leptonic decay,
- two $b$-jets from the $t\bar{t}$ dilepton decay and
- large missing transverse momentum, due to the two neutrinos produced in the $t\bar{t}$ dilepton decay.

The most important Standard Model processes that produce four prompt leptons in their final state are: $ZZ$, $WtZ$, $t\bar{t}H$, $H \to ZZ$, $t\bar{t}t\bar{t}$, $t\bar{t}WW$ and tribosons (see Section 4.2.2).

[1] OSSF=OS+SF

- The $ZZ \to 4\ell$ decay produces two pairs of OSSF leptons, each of them with an invariant mass close to the mass of the $Z$ boson. It is the most important background in the $t\bar{t}Z$ cross-section measurement due to its large cross section, with more than 1000 $ZZ \to 4\ell$ events produced for each $t\bar{t}Z \to 4\ell$ event. This background can be suppressed using a number of observables: the number of jets and $b$-tagged jets in the event, large $E_{\mathrm{T}}^{\mathrm{miss}}$, large value of $|m_{Z2} - m_Z|$ and the flavor composition of the $Z2$ lepton pair.
- The $WtZ$ background is the $4\ell$ analogous of the single-top background in the $t\bar{t}$ dilepton channel. It is difficult to find a set of cuts that provide a good separation between the signal and this background, since their signatures only differ in the number of $b$-jets, but the contribution of this background is small due to its relatively small cross section.
- The $t\bar{t}H$, $H \to ZZ$, $t\bar{t}t\bar{t}$ and tribosons backgrounds are small backgrounds that have little impact in the overall analysis, with their combined contribution to the total expected number of events being smaller than 7% after all cuts are applied.

### 8.1.3 Events preselection

The event quality criteria used in this analysis are commonly used in the ATLAS top working group and are available in the TopRootCore framework [219]:

- Data events must pass the good run list filter, as explained in Section 4.1. Simulation events are required to be true four lepton events (i.e., they have exactly four leptons at generator level), where $\tau$ leptons only add towards the lepton count if they decay leptonically.
- At least one of the lepton triggers has fired (see Section 4.1). This trigger lepton is required to have $p_{\mathrm{T}} > 25$ GeV.
- The trigger object reconstructed must match a reconstructed lepton within $\Delta R < 0.15$.
- The event must contain at least one good primary vertex with at least five associated tracks with $p_{\mathrm{T}} > 400$ MeV.
- Events with cosmic muons are rejected.
- At least one reconstructed lepton with $p_{\mathrm{T}} > 25$ GeV.
- The events must not have bad jets, i.e., there are no LooseBadMinus jets in the AntiKt4TopoEMJets collection with $p_{\mathrm{T}} > 20$ GeV and $E > 0$ [161].
- The event is rejected if an electron and a muon share an inner detector track.

In addition to the event quality criteria, the analysis preselection also requires exactly four reconstructed leptons, as defined in Section 5.1.3 and Section 5.2.2, with a minimum transverse momentum of 7 GeV. Furthermore, it is required that $Z1$ is defined, i.e., there is at least one pair of OSSF leptons in the event. Finally, an overlap between the selected events in this analysis and the $t\bar{t}Z$ three-leptons analysis [220] is avoided by vetoing all the events that would pass the selection of the three-leptons analysis, in order to simplify the combination of the results of these analyses.

The events passing this preselection are classified in six signal regions, according to the flavor composition of the $Z2$ pair (SF or DF[2]) and the number of $b$-tagged jets, as shown in Table 8.1. The classification defined in Table 8.1 splits the events in different regions with different background conditions: the

[2] Different flavor

SF regions have a significantly higher $ZZ$ background contamination than their DF counterparts, while regions with a larger number of $b$-tagged jets have less contamination and a good purity can be achieved with only a few additional requirements.

| Regions | $Z2$ is SF | $Z2$ is DF |
|---|---|---|
| $N_{b\text{tag}} = 0$ | 0b – SF | 0b – DF |
| $N_{b\text{tag}} = 1$ | 1b – SF | 1b – DF |
| $N_{b\text{tag}} \geq 2$ | 2b – SF | 2b – DF |

Table 8.1: Classification of the events in the preselection in different regions.

The event selection for each of these regions is discussed in detail in the next subsections. It is important to notice that the 0b – SF is not used in the analysis, since the $ZZ$ contamination is so large that it is not possible to obtain a statistically significant signal-region selection.

### 8.1.4 0b – DF

The 0b – DF signal region is required to have no $b$-tagged jets and a DF $Z2$ lepton pair. In addition to the preselection and these additional requirements, the following cuts are used:

- The event must have at least two jets.
- The transverse momentum of the fourth lepton must be larger than 10 GeV.
- $p_{\text{T}34}$ must be larger than 45 GeV.

The $ZZ \to 4\ell$ process is the dominant background in this signal region due to its large cross section, even after the DF requirement on the $Z2$ lepton pair, which strongly suppresses it.

The requirement on the number of jets is used to reduce the amount of $ZZ$ background, while the requirements on the $p_{\text{T}}$ of the fourth lepton and on $p_{\text{T}34}$ reduce the amount of fake events (see Figure 8.1).

### 8.1.5 1b – DF

The 1b – DF signal region requires exactly one $b$-tagged jet and a $Z2$ lepton pair with DF.

The $b$-tagging and flavor requirements strongly suppress the $ZZ$ background. Consequently, the fake lepton events become the dominant background. The fake lepton events background is already significantly reduced due to the $b$-tagging requirements, and only the requirement $p_{\text{T}34} > 35$ GeV is added to further reduce it, as shown in Figure 8.2. Notice that the fake lepton events are expected to have a low value of $p_{\text{T}34}$, since fake leptons are usually less energetic than prompt leptons.

### 8.1.6 2b – DF

The 2b – DF signal region is composed of events with at least two $b$-tagged jets and a DF $Z2$ lepton pair. The strong $b$-tagging requirements suppress the $ZZ$ and the fake lepton events. Moreover, the $Z2$ lepton pair flavor requirement also significantly reduces the amount of $ZZ$ contamination. Therefore, no extra cuts are applied, since the signal region is already very clean, as shown in Figure 8.3.

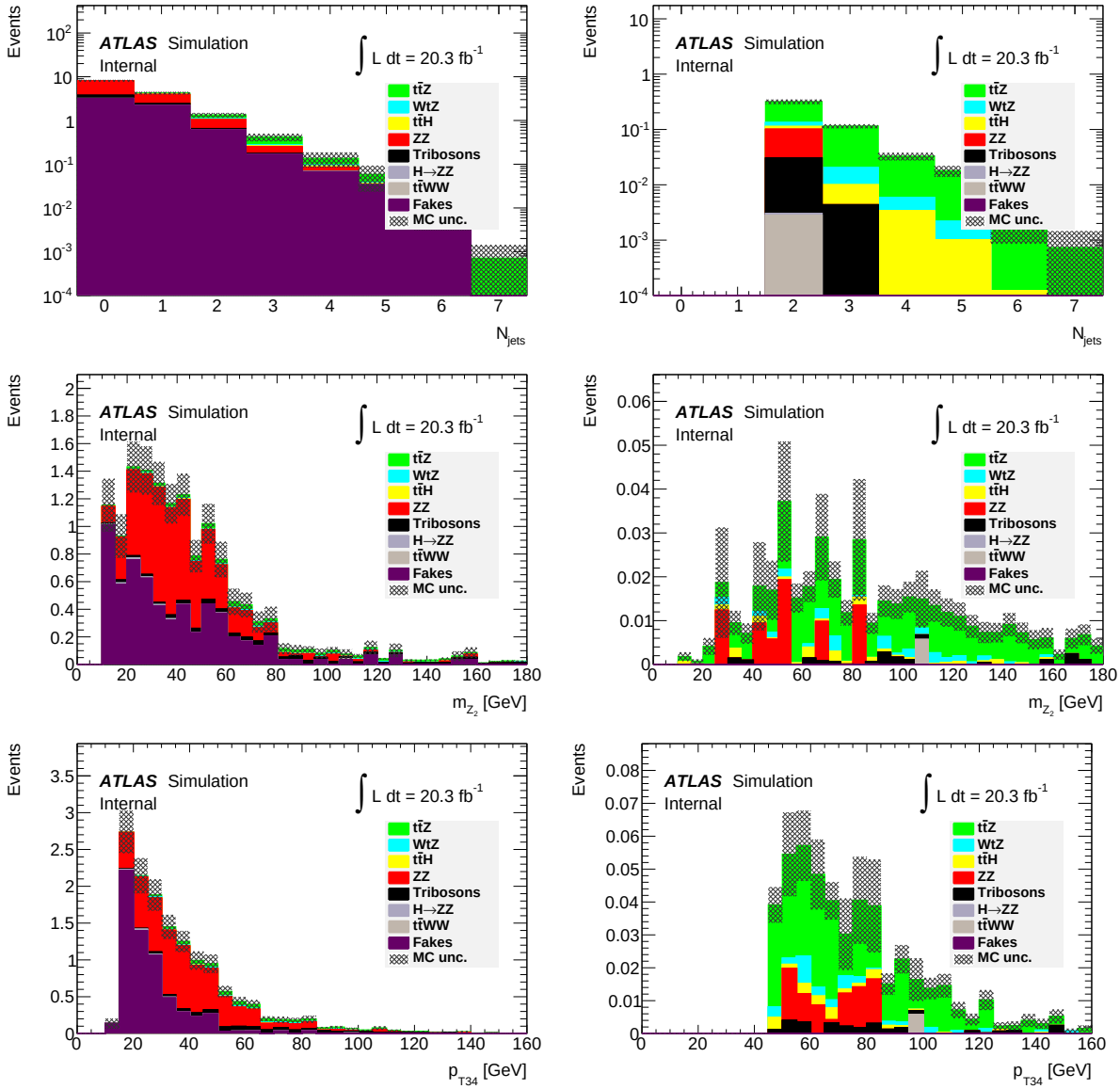


Figure 8.1: Distribution of $N_{\text{jets}}$, $m_{Z2}$ and $p_{\text{T34}}$ in the 0b – DF signal region before (left) and after (right) the additional requirements.

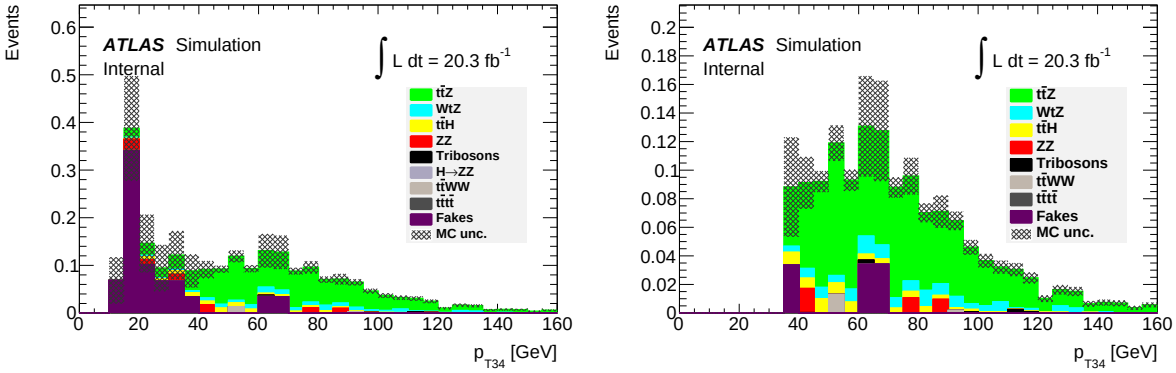


Figure 8.2: Distribution of $p_{\mathrm{T34}}$ in the 1b – DF signal region before (left) and after (right) the $p_{\mathrm{T34}}$ cut.

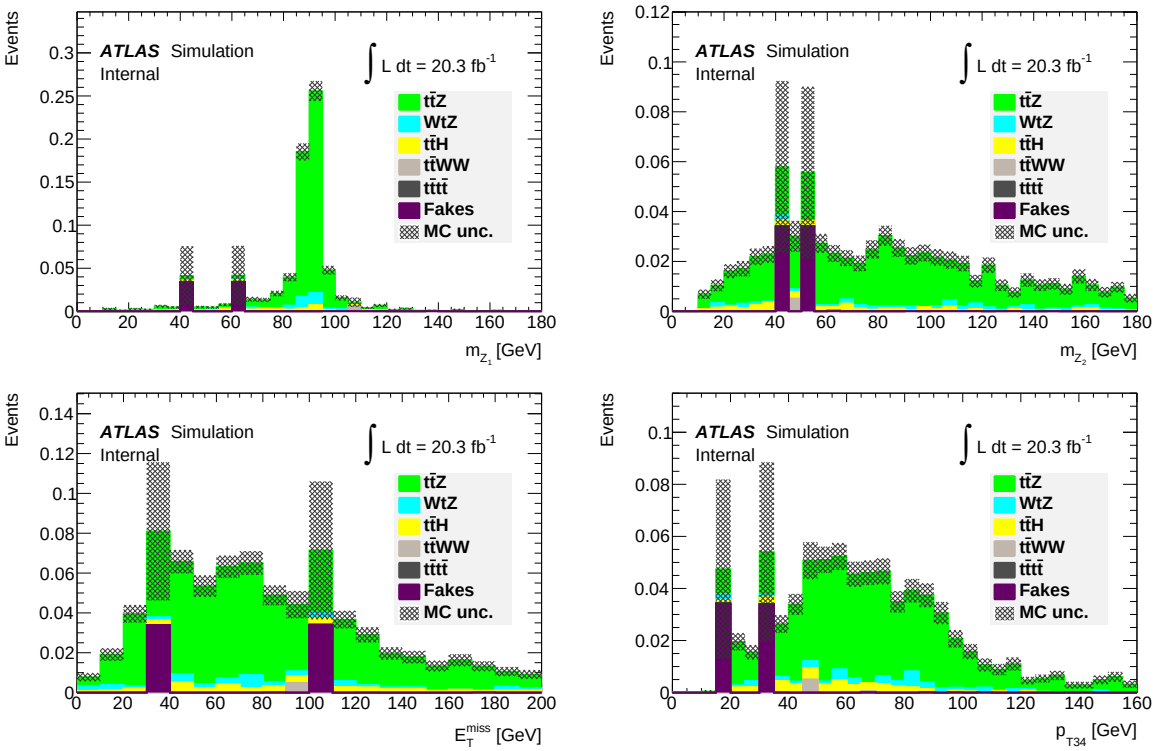


Figure 8.3: Distributions of the 2b – DF signal region. The error bands only show the statistical uncertainty.

### 8.1.7 1b – SF

In the 1b – SF signal region, exactly one $b$-tagged jet and a $Z2$ lepton pair with SF are required. Since a SF $Z2$ lepton pair is required, this signal region has an abundant amount of $ZZ$ background that needs to be suppressed in order to define a clean signal region. Moreover, since the $b$-tagging requirement by itself is not enough to reduce the contribution of fake lepton events to an acceptable level, further cuts must be imposed.

To reduce the contribution due to fake leptons and the $ZZ$ background, the following requirements are introduced:

- $p_{\mathrm{T}34} > 25$ GeV.
- $E_{\mathrm{T}}^{\mathrm{miss}} > 40$ GeV.
- $E_{\mathrm{T}}^{\mathrm{miss}} > 80$ GeV or $|m_{Z2} - m_Z| > 10$ GeV.

The cut on $p_{\mathrm{T}34}$ reduces the contribution of events with fake leptons, while the rest of the requirements are used to reduce the $ZZ$ background. The distributions before and after applying the extra cuts of all the variables involved in these cuts are shown in Figure 8.4.

### 8.1.8 2b – SF

The 2b – SF signal region includes events that have at least two $b$-tagged jets and a SF $Z2$ lepton pair. Due to the lepton flavor requirements, this region also has a significant contribution from $ZZ$ background events, although not as strong as the 1b – SF region due to the more stringent $b$-tagging requirement. Nevertheless, this background must still be reduced.

The suppression of the $ZZ$ background is done requiring that the events in this region meet at least one of the following two conditions:

- $E_{\mathrm{T}}^{\mathrm{miss}} > 40$ GeV.
- $|m_{Z2} - m_Z| > 10$ GeV.

The choice of these criteria becomes evident after examining Figure 8.5. Most of the $ZZ$ events are removed by the $E_{\mathrm{T}}^{\mathrm{miss}}$ requirement. The events that survive it are removed with the $|m_{Z2} - m_Z|$ cut. Requiring at least one of these cuts to be satisfied, instead of both, slightly increases the amount of expected $ZZ$ background. However, since the low $E_{\mathrm{T}}^{\mathrm{miss}}$ and $|m_{Z2} - m_Z|$ regions contain a fair amount of signal events, this slight increase in the background is well compensated with an increase in the number of expected signal events.

## 8.2 Event yields

Applying the cuts described in the last section to the MC simulation datasets (using the ABCD method to estimate the contribution of events with fake leptons, as described in Section 4.3.3), the expected number of events in each signal region can be estimated. These estimates are presented in Table 8.2. From this table, it can be computed that roughly five events are expected in the data with a signal-to-background ratio of 2.5, which corresponds to a purity of 72%.

A few limits are listed in Table 8.2. These limits are placed when no event is selected in the simulation datasets for a given background. In this case, the luminosity weight of the dataset, as defined in Section 6.2.1, is used as the upper limit, except for the $Z$ + jets and $W$ + jets backgrounds, which have large luminosity weights. The estimation of the limit for those cases is described in Ref. [200].

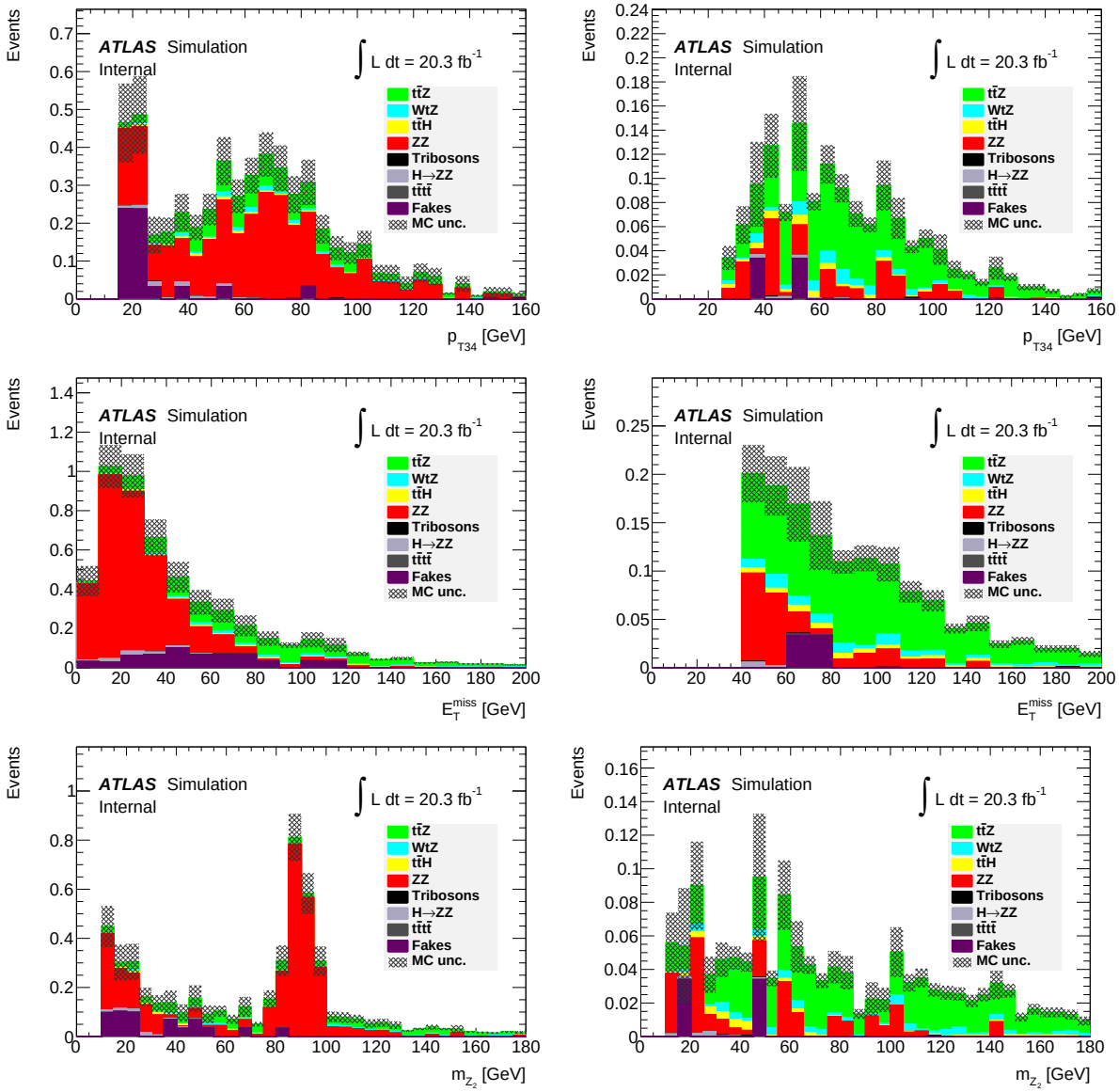


Figure 8.4: Distribution of $p_{\mathrm{T34}}$, $E_{\mathrm{T}}^{\mathrm{miss}}$ and $m_{Z2}$ in the 1b – SF signal region before (left) and after (right) the extra cuts.

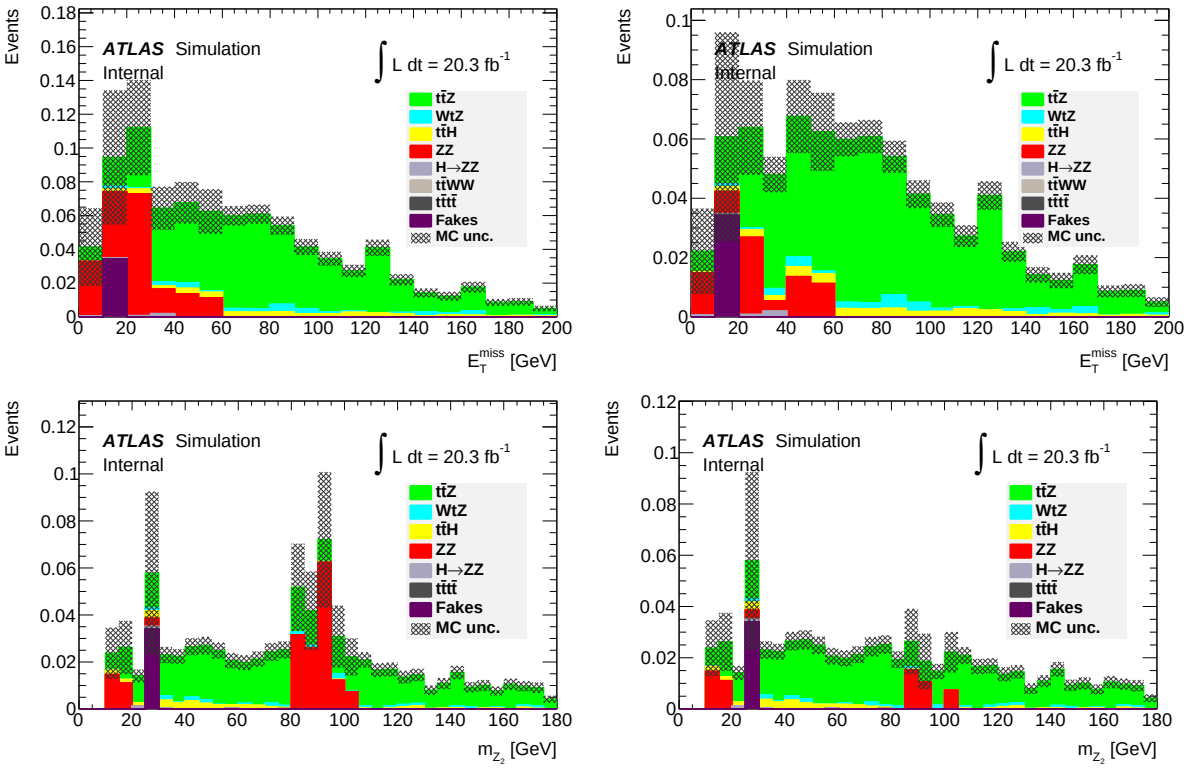


Figure 8.5: Distribution of $E_{\mathrm{T}}^{\mathrm{miss}}$ and $|m_{Z2} - m_Z|$ in the 2b – SF signal region before (left) and after (right) the additional cuts.

| Description | 0b – DF | 1b – DF | 2b – DF | 1b – SF | 2b – SF |
|---|---|---|---|---|---|
| MC exp. signal | 0.324(16) | 1.042(25) | 0.583(17) | 0.915(23) | 0.576(17) |
| MC exp. $ZZ$ | 0.070(27) | 0.037(22) | $< 0.012$ | 0.262(51) | 0.077(28) |
| MC exp. $WtZ$ | 0.034(6) | 0.126(11) | 0.042(6) | 0.104(9) | 0.031(5) |
| MC exp. $t\bar{t}H$ | 0.023(3) | 0.073(5) | 0.048(4) | 0.056(4) | 0.038(3) |
| MC exp. tribosons | 0.033(6) | 0.008(3) | $< 0.002$ | 0.004(2) | $< 0.002$ |
| MC exp. $H \to ZZ$ | $< 0.001$ | $< 0.001$ | $< 0.001$ | 0.013(3) | 0.004(2) |
| MC exp. $t\bar{t}WW$ | 0.006(6) | 0.015(10) | 0.005(5) | $< 0.004$ | $< 0.004$ |
| MC exp. $t\bar{t}t\bar{t}$ | $< 0.000$ | $< 0.000$ | 0.003(1) | $< 0.000$ | 0.002(0) |
| Exp. fake events (ABCD) | $< 0.034$ | 0.096(67) | 0.065(53) | 0.057(52) | 0.028(35) |
| Exp. fake events (MC) | 0.022(4) | 0.058(8) | 0.072(39) | 0.082(26) | 0.023(3) |
| Signal-to-background ratio | 1.95(53) | 2.94(60) | 3.6(1.2) | 1.84(28) | 3.20(81) |

Table 8.2: Expected event yields per signal and background process in the five selected signal regions. The numbers in parentheses are the uncertainties associated to the limited number of simulated events.

## 8.3 Estimation of events with fake leptons

The ATLAS $t\bar{t}Z$ cross-section measurement in the four lepton channel uses the fake factor method [200] as the nominal fake estimation technique and the ABCD method discussed in Section 4.3.3 as a crosscheck.

### 8.3.1 Estimation using the fake factor method

The main idea of the fake factor method [200] is to correct the simulation predictions of events with fake leptons using weight factors computed from data in different control regions.

A total of four fake factors are computed, corresponding to:

- fake electrons from light jets,
- fake electrons from heavy jets,
- fake muons from light jets and
- fake muons from heavy jets.

Two control regions aiming to select $Z$ + jets or $t\bar{t}$ events with at least one fake lepton are used to determine the fake factors from data. The fake leptons originating from $Z$ + jets events are assumed to come from light jets, while the ones from $t\bar{t}$ events are assumed to arise from heavy jets. These two control regions are defined as follows [200]:

- $t\bar{t}$ control region:
  - Exactly 3 leptons.
  - No OSSF lepton pair.
  - One OS lepton pair.

  - At least one jet with $p_{\mathrm{T}} > 30$ GeV.

- $Z$ + jets control region:
  - Exactly 3 leptons.
  - One OSSF lepton pair.
  - $E_{\mathrm{T}}^{\mathrm{miss}} < 30$ GeV.
  - $m_{\mathrm{T}} < 30$ GeV.

The $m_{\mathrm{T}}$ variable in the $Z$ + jets control region is used to suppress the contribution from $WZ$ events and is defined as the transverse mass of the $W$ boson. This is computed using as input the missing transverse momentum and the $p_{\mathrm{T}}$ of the lepton that does not originate from a $Z$ decay[3].

Using these two regions, the fake factors can be computed from the solution of the system of equations defined by:

$$N_{\mathrm{data}}^{X,R} - N_{\mathrm{others}}^{X,R} = \mu_{\mathrm{heavy}}^{X} \cdot N_{t\bar{t}}^{X,R} + \mu_{\mathrm{light}}^{X} \cdot N_{Z+\mathrm{jets}}^{X,R}, \tag{8.1}$$

with $X = \{e, \mu\}$ and $R = \left\{t\bar{t}, Z + \mathrm{jets}\right\}$. For a given control region $R$, $N_{\mathrm{data}}^{X,R}$ is the number of $X$-flavored lepton events measured in data and $N_{C}^{X,R}$ ($C = \left\{t\bar{t}, Z + \mathrm{jets}, \mathrm{others}\right\}$) is the number of expected $C$-process events where an $X$-flavored lepton is assumed to be a fake lepton. For the $t\bar{t}$ control region, the lepton with the lowest $p_{\mathrm{T}}$ is assumed to be fake. For the $Z$ + jets control region, the lepton that is not part of the $Z$-decay lepton pair is considered to be fake. The process classification $C$ = others is defined as the events that are neither $t\bar{t}$ or $Z$ + jets.

The event yields used to solve Equation 8.1 are shown in Table 8.3 for the $t\bar{t}$ and the $Z$ + jets control regions. Using these values, the following fake factors are obtained [200]:

- $\mu_{\mathrm{heavy}}^{e} = 1.23 \pm 0.13$ ,
- $\mu_{\mathrm{heavy}}^{\mu} = 1.25 \pm 0.09$ ,
- $\mu_{\mathrm{light}}^{e} = 1.35 \pm 0.05$ and
- $\mu_{\mathrm{light}}^{\mu} = 1.61 \pm 0.05$ .

| Process | $t\bar{t}$ control region | | $Z$ + jets control region | |
|---|---|---|---|---|
| | Fake electron | Fake muon | Fake electron | Fake muon |
| $t\bar{t}$ | 125.4 ± 6.7 | 207.7 ± 3.1 | 45.2 ± 1.1 | 59.2 ± 1.4 |
| $Z$ + jets | 9.13 ± 0.53 | 1.29 ± 0.02 | 3338 ± 79 | 3264 ± 76 |
| Others | 8.62 ± 0.35 | 7.63 ± 0.08 | 871 ± 18 | 897 ± 17 |
| Data | 185 | 273 | 5437 | 6241 |

Table 8.3: Expected yields from simulation and measured number of events in data for the different control regions. The numbers are used to compute the fake factors used in this analysis. The quoted uncertainty is the statistical uncertainty [200].

[3] The definition of the pair of leptons originating from a $Z$ decay is the same as the $Z1$ lepton pair in the four-leptons case.

### 8.3.2 Estimation using the ABCD method

In order to apply the ABCD method to estimate the contribution of events with fake leptons in this analysis (see Section 4.3.3), it is necessary to define the regions A, B, C and D. In Section 5.1 and Section 5.2, the loose and the tight lepton definitions are given. The tight definition is the nominal lepton definition used throughout the analysis, while the loose definition, which has a lower fake lepton rejection rate than its tight counterpart, is used to define two of the four regions of the ABCD method.

As discussed in Section 4.3.3, two sets of cuts are needed to define the four regions. The first set of cuts is based on the lepton definition:

- Loose events: events with exactly four reconstructed leptons, where at least one of the reconstructed leptons is loose but not tight.
- Tight events: events with exactly four reconstructed leptons, where all reconstructed leptons are tight.

The second set of cuts is defined based on two orthogonal event selections:

- Fakes selection: events with exactly four reconstructed leptons, where the $Z2$ lepton pair has same-sign (SS) leptons. This selection enhances the number of fake events.
- Signal selection: events selected using the signal region of interest (0b – DF, 1b – DF, 2b – DF, 1b – SF, 2b – SF or all of them), but not using necessarily a tight lepton definition. Since all the signal regions require that the $Z2$ lepton pair is DF, the fakes selection is orthogonal to every signal selection.

Once the two sets of cuts are given, the A, B, C and D regions are defined as the region with loose events passing the fakes selection, the region with loose events passing the signal selection, the region with tight events passing the fakes selection and the region with tight events passing the signal selection, respectively.

All four regions are constructed such that they are orthogonal to each other. It is important to notice that region D is equivalent to the signal region of interest, i.e., the region where the estimate is needed. The number of events with fake leptons in region D can be determined using a rearranged form of Equation 4.16:

$$N_{\mathrm{F}}^{\mathrm{D}} = \frac{N_{\mathrm{Data}}^{\mathrm{C}} - N_{\mathrm{R}}^{\mathrm{C}}}{N_{\mathrm{Data}}^{\mathrm{A}} - N_{\mathrm{R}}^{\mathrm{A}}} \times \left(N_{\mathrm{Data}}^{\mathrm{B}} - N_{\mathrm{R}}^{\mathrm{B}}\right), \tag{8.2}$$

where $N_{\mathrm{Data}}^{\mathrm{X}}$ is the number of events selected in data in region $X$ and $N_{\mathrm{R}}^{\mathrm{X}}$ is the number of expected events in region $X$ with four prompt leptons, as estimated from the MC simulations.

Since the fraction in Equation 8.2 only depends on the definitions of regions A and C, it does not depend on the chosen signal region. Therefore, it only needs to be measured once:

- $N_{\mathrm{Data}}^{\mathrm{A}} = 418.$
- $N_{\mathrm{R}}^{\mathrm{A}} = 14.59 \pm 0.40$ .
- $N_{\mathrm{Data}}^{\mathrm{C}} = 18.$
- $N_{\mathrm{R}}^{\mathrm{C}} = 4.15 \pm 0.21$ .
- $\frac{N_{\mathrm{Data}}^{\mathrm{C}} - N_{\mathrm{R}}^{\mathrm{C}}}{N_{\mathrm{Data}}^{\mathrm{A}} - N_{\mathrm{R}}^{\mathrm{A}}} = 0.034 \pm 0.011$ .

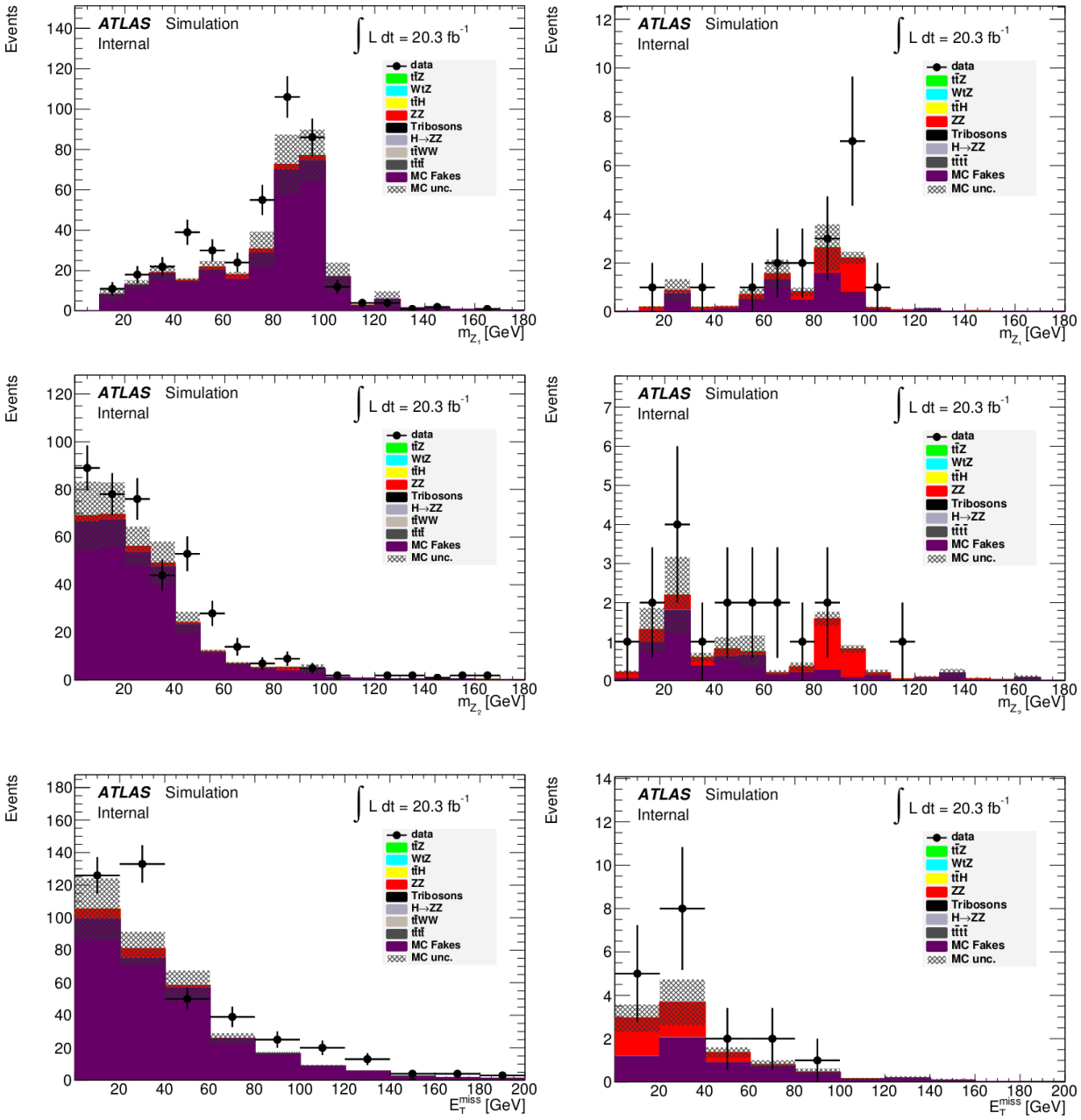


Figure 8.6: Distributions of $m_{Z1}$, $m_{Z2}$ and $E_{\mathrm{T}}^{\mathrm{miss}}$ in regions A (left) and C (right), as defined for the ABCD method.

Figure 8.6 shows the data-simulation comparison of the distribution of $m_{Z1}$, $m_{Z2}$ and $E_{\mathrm{T}}^{\mathrm{miss}}$ of regions A and C.

The ABCD estimate of the number of events with fake leptons for each signal region is given in Table 8.4. The uncertainty associated with the measurement of the quantities in the ABCD method is computed using error propagation and assuming that all the quantities are uncorrelated. The Poissonian statistical uncertainties of the values measured in data ($N_{\mathrm{Data}}^{\mathrm{A}}$, $N_{\mathrm{Data}}^{\mathrm{B}}$ and $N_{\mathrm{Data}}^{\mathrm{C}}$) are the dominant contributions to the total uncertainty, while the uncertainties of the quantities estimated with MC-simulations ($N_{\mathrm{R}}^{\mathrm{A}}$, $N_{\mathrm{R}}^{\mathrm{B}}$ and $N_{\mathrm{R}}^{\mathrm{C}}$) have a negligible impact. Notice that all the estimates are compatible, within uncertainties, with the estimation obtained from MC simulations.

| Signal region | $N_{\mathrm{Data}}^{\mathrm{B}}$ | $N_{\mathrm{R}}^{\mathrm{B}}$ | Estimated $N_{\mathrm{Data}}^{\mathrm{D}}$ | Uncertainty on $N_{\mathrm{Data}}^{\mathrm{D}}$ | Deviation from the MC estimate |
|---|---|---|---|---|---|
| 0b – DF | 0 | 0.137 ± 0.018 | -0.005 | 0.039 | 0.027 |
| 1b – DF | 3 | 0.194 ± 0.014 | 0.096 | 0.067 | 0.038 |
| 2b – DF | 2 | 0.116 ± 0.007 | 0.065 | 0.053 | 0.007 |
| 1b – SF | 2 | 0.331 ± 0.028 | 0.057 | 0.052 | 0.025 |
| 2b – SF | 1 | 0.170 ± 0.020 | 0.028 | 0.035 | 0.005 |

Table 8.4: Detailed ABCD method fake estimation for all signal regions.

The result of the estimation of the number of events with fake leptons using the ABCD method is compatible with the estimate using the fake factor method, but has a lower uncertainty. Since the ABCD method and the fake factor method are independent methods, the results obtained from the ABCD method validate the results obtained from the fake factor method [200].

## 8.4 Analysis strategy

Since the $t\bar{t}Z$ process is a rare process and it has not been yet discovered, the $t\bar{t}Z$ cross-section measurement is performed as a blinded analysis to avoid any experimental bias.

A simultaneous likelihood fit is used on the five signal regions and a $ZZ$ control region (see Section 8.4.1) used to measure the $ZZ$ normalization, as described in Ref. [200]. The technical implementation is done using the HistFactory framework [221].

The likelihood function used to fit the six regions is defined as the product of probabilities [222]:

$$\begin{aligned} L\left(n, \theta^0 | \mu_{t\bar{t}Z}, \mu_{ZZ}, \boldsymbol{\theta}\right) &= P_{\mathrm{SR}} \times P_{\mathrm{CR}} \times P_{\mathrm{syst}} \\ &= \prod_{\mathrm{SRs}} P\left(n_{\mathrm{SR}} | \lambda_{\mathrm{SR}}\left(\mu_{t\bar{t}Z}, \mu_{ZZ}, \boldsymbol{\theta}\right)\right) \times P\left(n_{ZZ} | \lambda_{ZZ}\left(\mu_{t\bar{t}Z}, \mu_{ZZ}, \boldsymbol{\theta}\right)\right) \times P_{\mathrm{syst}}\left(\boldsymbol{\theta}^0, \boldsymbol{\theta}\right), \end{aligned} \tag{8.3}$$

where the $n_{\mathrm{SR}}$ are the number of observed events in each signal region; $n_{ZZ}$, the number of observed events in the $ZZ$ control region; $\lambda_{\mathrm{SR}}$, the Poisson expectations for each signal region; and $\lambda_{ZZ}$, the Poisson expectation for the $ZZ$ control region. The term $P_{\mathrm{syst}}\left(\boldsymbol{\theta}^0, \boldsymbol{\theta}\right)$ is a probability function that includes all the systematic uncertainties, where $\boldsymbol{\theta}^0$ are the nominal values and $\boldsymbol{\theta}$ represent the varied values.

The Poisson expectations in Equation 8.3 depend on the $ZZ$ normalization factor ($\mu_{ZZ}$), the $t\bar{t}Z$ signal strength ($\mu_{t\bar{t}Z}$) and the nuisance parameters ($\boldsymbol{\theta}$) corresponding to the systematic uncertainties. All these values are determined during the maximization of the likelihood function. The $t\bar{t}Z$ signal strength

and the $ZZ$ normalization are fit unconstrained, while each of the nuisance parameters is constrained to a Gaussian with a width equal to the magnitude of the corresponding systematic uncertainty. For the uncertainties arising from the limited number of simulated events, a Poissonian constraint is used instead.

The measured value of the $t\bar{t}Z$ signal strength can be used to determine the $t\bar{t}Z$ cross section using:

$$\sigma_{t\bar{t}Z} = \mu_{t\bar{t}Z} \cdot \sigma_{t\bar{t}Z}^{\text{expected}}, \tag{8.4}$$

where $\sigma_{t\bar{t}Z}^{\text{expected}}$ is the assumed cross-section value (Standard Model prediction) used to compute the expected number of $t\bar{t}Z$ events from the simulated datasets.

### 8.4.1 *ZZ* normalization

The $ZZ$ control region is defined by the following cuts:

- Exactly four reconstructed leptons.
- The $Z2$ lepton pair is OSSF.
- $|m_{Z1} - m_Z| < 10$ GeV and $|m_{Z2} - m_Z| < 10$ GeV.
- $E_{\text{T}}^{\text{miss}} < 50$ GeV.

A preliminary normalization correction for the $ZZ$ background is obtained applying a likelihood fit only to the $ZZ$ control region, giving a value of 1.17 [200]. This correction is applied to all the $ZZ$ expectation values obtained from simulation. Since the $ZZ$ control region is the main component in the determination of the $ZZ$ normalization in the likelihood fit, no significant deviation from this value is expected from the full fit ($ZZ$ control region and signal regions).

## 8.5 Systematic uncertainties

General considerations on the estimation of the systematic uncertainties on $t\bar{t}Z$ have been already discussed in Chapter 6. Unlike the top-quark mass measurement, where the systematic uncertainties play a central role, systematic uncertainties play a minor role in the $t\bar{t}Z$ cross-section measurement, since the measurement is dominated by the statistical uncertainty. Nevertheless, the determination of some systematic uncertainties merits extra discussion, since it can affect the final measurement. These uncertainties are discussed in this section.

### 8.5.1 *ZZ* normalization extrapolation uncertainty

The $ZZ$ background is the main background in the $t\bar{t}Z$ cross-section measurement. In order to improve the accuracy of the $ZZ$ background estimation, the $ZZ$ normalization is fitted in a $ZZ$ control region, as described above. This fit is performed in an on-shell control region with low missing transverse momentum and low jet multiplicity, whereas the signal regions where the $ZZ$ background is important are off-shell, have higher missing transverse momentum and higher jet multiplicity.

Therefore, the extrapolation of the normalization scale obtained in the $ZZ$ control region to the signal regions can introduce uncertainties that need to be accounted for. In order to estimate the effect of this systematic uncertainty, an ABCD method (see Section 4.3.3) is used to compute a second estimate for a signal-region-like validation region (i.e., off shell and with large missing transverse momentum). The

difference of the estimate obtained using the ABCD method and the estimate obtained from simulation using the corrected $ZZ$ normalization provides the systematic uncertainty associated with the $ZZ$ normalization extrapolation.

Two comparisons are performed to estimate the extrapolation uncertainty. The first comparison estimates the effect of extrapolating from an on-shell region with low missing transverse momentum to an off-shell region with high missing transverse momentum.

The regions are defined in Table 8.5. For all regions, the events must have exactly 4 reconstructed leptons and the $Z2$ pair must be OSSF.

| Cuts | $E_{\mathrm{T}}^{\mathrm{miss}} < 40$ GeV | $E_{\mathrm{T}}^{\mathrm{miss}} > 40$ GeV |
|---|---|---|
| $\lvert m_{Z2} - m_Z \rvert < 10$ GeV | Region A | Region C |
| $\lvert m_{Z2} - m_Z \rvert > 10$ GeV | Region B | Region D |

Table 8.5: Definition of the ABCD regions for the $ZZ$ on-shell to off-shell and low $E_{\mathrm{T}}^{\mathrm{miss}}$ to high $E_{\mathrm{T}}^{\mathrm{miss}}$ extrapolation uncertainty estimation.

The observed and expected number of events in regions A, B and C are shown in Table 8.6, along with the ABCD and the corrected MC estimate for region D. The difference between these two results is 32%, which is assigned as the systematic uncertainty.

| Region | $N_{\mathrm{data}}$ | $N_{\mathrm{MC(No\ ZZ)}}$ | $N_{\mathrm{data}} - N_{\mathrm{MC(No\ ZZ)}}$ |
|---|---|---|---|
| A | 148 | $0.1 \pm 0.0$ | 147.9 |
| B | 149 | $12.3 \pm 1.8$ | 136.7 |
| C | 14 | $0.4 \pm 0.0$ | 13.6 |
| D (ABCD estimate) | X | X | $12.6 \pm 3.8$ |
| Corrected MC | X | X | $16.6 \pm 0.4$ |

Table 8.6: Estimation of the $ZZ$ background in region D using the ABCD method and comparison with the estimate using the normalization correction factor in simulation events.

The second comparison is analogous to the first one, with modified definitions of the A, B, C and D regions as shown in Table 8.7. For all regions, the events must have exactly 4 reconstructed leptons, $E_{\mathrm{T}}^{\mathrm{miss}} < 40$ GeV, and the $Z2$ pair must be OSSF.

| Cuts | $N_{\mathrm{jets}} = 0$ | $N_{\mathrm{jets}} > 0$ |
|---|---|---|
| $\lvert m_{Z2} - m_Z \rvert < 10$ GeV | Region A | Region C |
| $\lvert m_{Z2} - m_Z \rvert > 10$ GeV | Region B | Region D |

Table 8.7: Definition of the ABCD regions for the estimation of the $ZZ$ normalization extrapolation uncertainty from a low jet multiplicity to a high jet multiplicity region.

The observed and expected number of events are shown in Table 8.8, with the ABCD and the corrected MC estimate for region D. Both results are compatible within the 20% uncertainty from the ABCD method. Therefore, an uncertainty of 20% is quoted for this extrapolation.

Summing both uncertainties in quadrature, the total systematic uncertainty associated with the extrapolation of the $ZZ$ normalization is 38%.

| Region | $N_{\text{data}}$ | $N_{\text{MC(No ZZ)}}$ | $N_{\text{data}} - N_{\text{MC(No ZZ)}}$ |
|---|---|---|---|
| A | 102 | 0.0 ± 0.0 | 102.0 |
| B | 95 | 8.4 ± 1.8 | 86.6 |
| C | 46 | 0.1 ± 0.0 | 45.9 |
| D (ABCD estimate) | X | X | 39.0 ± 8.2 |
| Corrected MC | X | X | 35.9 ± 0.6 |

Table 8.8: Estimation of the $ZZ$ background in region D using the ABCD method and comparison with the estimate using the normalization correction factor in simulation events.

### 8.5.2 $ZZ$ heavy-flavor composition

As described in Section 4.2.2, the $ZZ$ background is simulated using Sherpa, assuming a given $ZZ$ heavy-flavor ($ZZ$+HF) composition. This description of the $ZZ$+HF composition has a limited accuracy and this uncertainty has to be propagated to the analysis.

In order to quantify the effect of this systematic uncertainty, the $ZZ$+HF composition at reconstruction level is determined comparing statistically equivalent datasets generated with Powheg with the datasets generated with Sherpa. In particular, since the $t\bar{t}Z$ signal regions are defined in regions with different $b$-tagging requirements, the selection efficiency of requiring additional $b$-tagged jets is obtained for both datasets.

The relative discrepancy between the selection efficiencies in Sherpa and Powheg provides a measure of the systematic uncertainty associated with the $ZZ$+HF composition. The discrepancy between the selection efficiencies in Sherpa and Powheg is chosen as the systematic uncertainty per each $b$-tagged jet required. The systematic uncertainty is added linearly for each additional $b$-tagged jet required.

The estimation of the $ZZ$ heavy-flavor composition uncertainty is performed in the following control region:

- The event must have exactly 4 reconstructed leptons.
- The $Z2$ lepton pair must be OSSF.
- $E_{\text{T}}^{\text{miss}} < 40$ GeV.
- $|m_{Z2} - m_Z| < 10$ GeV.

The selection efficiency of requiring an extra $b$-tagged jet can be computed using the cuts: $N_{b\text{tag}} >= 0$, $N_{b\text{tag}} >= 1$ and $N_{b\text{tag}} >= 2$, and comparing the fraction of events selected. This selection efficiency can be associated with the $ZZ$+HF content of each simulation. Comparing these efficiencies in Sherpa and Powheg, the $ZZ$+HF composition modeling uncertainty can be estimated. The results are shown in Table 8.9. The modeling difference is of the order of 20% per $b$-tagged jet, while the largest statistical uncertainty on the computation of $\frac{\epsilon_{\text{Powheg}}}{\epsilon_{\text{Sherpa}}}$ is 31%. Therefore, an uncertainty of 31% per required $b$-tagged is assigned as the systematic uncertainty associated with the MC modeling of the $ZZ$+HF composition.

| Region | $N_{\text{POWHEG}}$ | $N_{\text{SHERPA}}$ | $\epsilon_{\text{POWHEG}}$ (%) | $\epsilon_{\text{SHERPA}}$ (%) | $\frac{\epsilon_{\text{POWHEG}}}{\epsilon_{\text{SHERPA}}}$ |
|---|---|---|---|---|---|
| $N_{b\text{tag}} \geq 0$ | 144.04 ± 0.64 | 146.3 ± 1.3 | N/A | N/A | N/A |
| $N_{b\text{tag}} \geq 1$ | 1.857 ± 0.075 | 2.32 ± 0.17 | 1.289 ± 0.052 | 1.58 ± 0.12 | 0.813 ± 0.068 |
| $N_{b\text{tag}} \geq 2$ | 0.081 ± 0.015 | 0.123 ± 0.039 | 4.36 ± 0.83 | 5.3 ± 1.7 | 0.82 ± 0.31 |

Table 8.9: Selection efficiency in POWHEG and SHERPA of requiring additional $b$-tagged jets. The efficiency ($\epsilon$) is defined as the fraction of events remaining after requiring one more $b$-tagged jet.

## 8.6 Unblinding and final results

### 8.6.1 Observed events

After unblinding, 7 signal event candidates are observed in data. Table 8.10 shows a summary of the main event properties of these candidates. The distribution of these observed events in the different signal regions are shown in Figure 8.7.

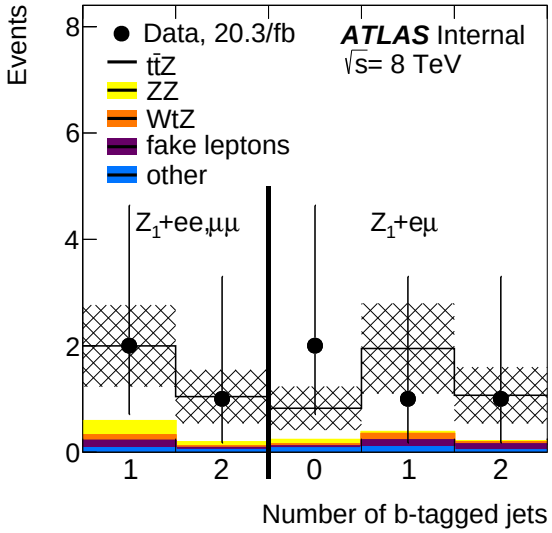


Figure 8.7: Comparison of the number of observed events and expected events after the fit in the different signal regions [200].

Figure 8.8 shows a graphical display of a signal event candidate in the 2b – DF region, corresponding to the event #6 in Table 8.10. The graphical display shows an event with three reconstructed electrons (green lines) and one reconstructed muon (red line), two reconstructed jets (white and blue cones) and missing transverse energy (gray dashed line). The two reconstructed electrons to the right are associated with a $Z$ candidate, while the rest of the reconstructed objects are related to the $t\bar{t}$ dilepton candidate, where the two jets are $b$-tagged.

### 8.6.2 Measured $t\bar{t}Z$ cross section

The $t\bar{t}Z$ signal strength and the $ZZ$ normalization are extracted from data using the likelihood fit described in Section 8.4, giving the following results [200] $\mu_{t\bar{t}Z} = 1.54^{+1.04}_{-0.72}$ and $\mu_{t\bar{t}Z} = 1.17^{+0.12}_{-0.11}$, and a

| Description | Event #1 | Event #2 | Event #3 | Event #4 | Event #5 | Event #6 | Event #7 |
|---|---|---|---|---|---|---|---|
| Run number | 207532 | 208184 | 208970 | 209787 | 212144 | 212172 | 214553 |
| Event number | 5886-7495 | 8029-0967 | 11276-0463 | 12507-2975 | 20841-9767 | 7015-4285 | 16590-0755 |
| Signal region | 1b – DF | 0b – DF | 1b – SF | 0b – DF | 1b – SF | 2b – DF | 2b – SF |
| 1st lep. flavor | $\mu^-$ (*) | $e^+$ (*) | $e^+$ | $\mu^+$ (*) | $\mu^-$ (*) | $\mu^-$ | $e^+$ (*) |
| 2nd lep. flavor | $\mu^+$ | $e^+$ | $\mu^+$ (*) | $\mu^-$ (*) | $\mu^+$ (*) | $e^+$ | $e^-$ (*) |
| 3rd lep. flavor | $\mu^+$ (*) | $e^-$ (*) | $e^-$ | $\mu^+$ | $\mu^-$ | $e^-$ (*) | $\mu^-$ |
| 4th lep. flavor | $e^-$ | $\mu^-$ | $\mu^-$ (*) | $e^-$ | $\mu^+$ | $e^+$ (*) | $\mu^+$ |
| 1st lep. $p_{\mathrm{T}}$ (GeV) | 81.89 | 81.17 | 133.18 | 91.35 | 74.54 | 87.68 | 62.43 |
| 2nd lep. $p_{\mathrm{T}}$ (GeV) | 33.92 | 52.46 | 67.20 | 63.92 | 65.40 | 71.04 | 46.11 |
| 3rd lep. $p_{\mathrm{T}}$ (GeV) | 28.23 | 41.86 | 33.96 | 58.35 | 56.73 | 69.45 | 17.32 |
| 4th lep. $p_{\mathrm{T}}$ (GeV) | 24.56 | 41.08 | 31.61 | 36.09 | 32.97 | 64.61 | 10.65 |
| $m_{4\ell}$ (GeV) | 205.76 | 257.42 | 319.97 | 486.22 | 339.09 | 406.91 | 144.66 |
| $N_{\mathrm{jets}}$ | 1 | 2 | 4 | 5 | 3 | 2 | 3 |
| $N_{b\mathrm{tag}}$ | 1 | 0 | 1 | 0 | 1 | 2 | 2 |
| $E_{\mathrm{T}}^{\mathrm{miss}}$ (GeV) | 30.32 | 105.14 | 95.49 | 42.88 | 241.38 | 57.08 | 48.71 |
| $m_{Z1}$ (GeV) | 88.55 | 86.41 | 89.64 | 99.93 | 92.35 | 93.35 | 81.94 |
| $m_{Z2}$ (GeV) | 59.81 | 100.08 | 139.05 | 85.65 | 164.45 | 252.77 | 36.09 |
| 1st jet $p_{\mathrm{T}}$ (GeV) | 35.07 (b) | 27.81 | 218.42 | 41.39 | 135.12 | 66.91 (b) | 46.42 (b) |
| 2nd jet $p_{\mathrm{T}}$ (GeV) | N/A | 26.85 | 101.72 (b) | 37.77 | 59.17 | 57.25 (b) | 34.25 |
| 3rd jet $p_{\mathrm{T}}$ (GeV) | N/A | N/A | 72.25 | 31.03 | 52.24 (b) | N/A | 29.16 (b) |
| 4th jet $p_{\mathrm{T}}$ (GeV) | N/A | N/A | 41.43 | 30.44 | N/A | N/A | N/A |
| 5th jet $p_{\mathrm{T}}$ (GeV) | N/A | N/A | N/A | 26.18 | N/A | N/A | N/A |

Table 8.10: List of data events selected. The leptons marked with an asterisk (*) form the $Z1$ lepton pair. The jets marked with (b) are $b$-tagged.

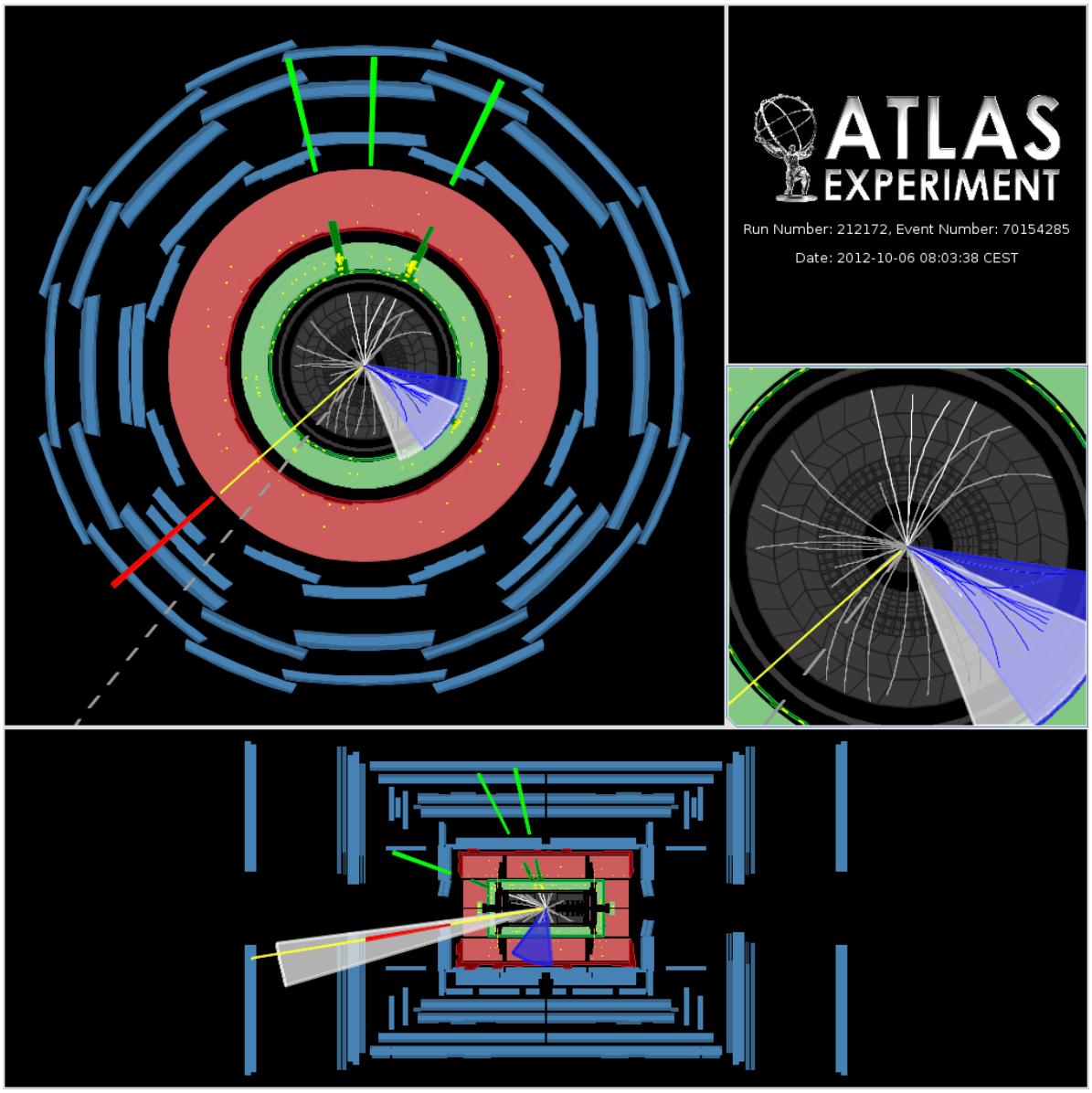


Figure 8.8: Display of the event 70154285 in run 212172. This event is one signal candidate in the 2b – DF region (Event #6 in Table 8.10). A pair of electrons (green) with an invariant mass of $m_{\ell\ell}$ = 93.4 GeV form the $Z$ candidate, while a muon (red), an additional electron, and two $b$-tagged jets (blue and white cones) are part of the $t\bar{t}$ dilepton candidate. $\vec{p}_{\mathrm{T}}^{\,\mathrm{miss}}$ is represented by the gray dashed line [200].

significance of $2.6\sigma$.

It is important to notice that the measured $ZZ$ normalization is the same as the preliminary normalization correction determined using only the $ZZ$ control region.

Applying Equation 8.4 and propagating the uncertainty, the measured $t\bar{t}Z$ cross section is:

$$\sigma_{t\bar{t}Z} = 0.32^{+0.21}_{-0.15} \text{ pb}, \tag{8.5}$$

where the total uncertainty is quoted.

In order to separate the total uncertainty in its statistical and systematic components, the fit is recomputed without considering the systematic uncertainties. The results are $\mu_{t\bar{t}Z} = 1.53^{+0.87}_{-0.67}$ and $\mu_{t\bar{t}Z} = 1.17^{+0.10}_{-0.09}$ , where only the statistical uncertainties are quoted.

Comparing the results of the two fits, the $t\bar{t}Z$ cross-section measurement can be expressed in its final form:

$$\sigma_{t\bar{t}Z} = 0.32^{+0.18}_{-0.14} \text{ (stat.)}^{+0.12}_{-0.05} \text{ (syst.) pb}. \tag{8.6}$$

This result is compatible with the $t\bar{t}Z$ Standard Model theoretical cross section (0.206(22) pb) reported in Ref. [54] within uncertainties. As expected, the measurement is dominated by the statistical uncertainty.

The $t\bar{t}Z$ cross-section measurement by the CMS Collaboration in the four-leptons channel is [223] $\sigma_{t\bar{t}Z} = 0.23^{+0.18}_{-0.13} \text{ (stat.)}^{+0.06}_{-0.03}$ (syst.) pb, which has similar uncertainties to the $t\bar{t}Z$ measurement presented in this thesis.

The preliminary $t\bar{t}Z$ cross-section measurement by the ATLAS Collaboration using the combined two-leptons and three-leptons channels is $\sigma_{t\bar{t}Z} = 0.150^{+0.055}_{-0.050}$ (stat.) $\pm$ 0.021 (syst.) pb [220]. Ongoing studies show that a combination of these measurements with the results presented in this thesis will reduce the total uncertainty on the cross section by roughly 10%, while the significance of the observed $t\bar{t}Z$ signal would increase from $3.8\sigma$ to $4.3\sigma$ [224].

CHAPTER 9

# Conclusion

The first analysis presented in this thesis describes a measurement of the top-quark mass in the $t\bar{t}$ dilepton channel. The data is collected using the ATLAS detector at the LHC and amounts to 4.6 fb$^{-1}$ of proton-proton collisions at a center-of-mass energy of 7 TeV. The measurement uses the calibration curve method to extract a dependence between the mean value of the $m_{\mathrm{T2}}$ distribution in the $t\bar{t}$ dilepton channel and the top-quark mass.

Considering all the statistical and systematic uncertainties, the value of the top-quark mass is measured to be:

$$m_{\mathrm{top}} = 175.2 \pm 1.6\,(\mathrm{stat.}) \pm 3.1\,(\mathrm{syst.})\ \mathrm{GeV}. \tag{9.1}$$

This measurement only uses events in the $e\mu$ channel and is the first top-quark mass measurement in the dilepton channel in ATLAS.

Many improvements to this measurement were explored. A reduction of the total uncertainty is achieved due to an improved understanding of the systematic uncertainty and the consequent improvement in the systematic uncertainty prescriptions, and due to changes in the event selection and the measurement method itself. The improvement of the systematic uncertainty prescriptions reduces the total systematic uncertainty by roughly 30%. Further improvements include the replacement of the mean of the distribution for the mean of the distribution obtained with an iterative asymmetric Gaussian fit, the use of the $m_{\mathrm{T2perp}}$ variable and the inclusion of the $ee$ channel and the $\mu\mu$ channel. These changes reduced the total systematic uncertainty by approximately 20% and the statistical uncertainty by roughly 50%.

Two measurements are obtained using these improvements, one corresponding to the $m_{\mathrm{T2}}$ variable and one corresponding to the $m_{\mathrm{T2perp}}$ variable. The top-quark mass measured using the $m_{\mathrm{T2}}$ variable yields:

$$m_{\mathrm{top}} = 173.7 \pm 0.8\,(\mathrm{stat.}) \pm 1.8\,(\mathrm{syst.})\ \mathrm{GeV}, \tag{9.2}$$

while the top-quark mass measured with the $m_{\mathrm{T2perp}}$ variable is:

$$m_{\mathrm{top}} = 173.3 \pm 0.7\,(\mathrm{stat.}) \pm 1.7\,(\mathrm{syst.})\ \mathrm{GeV}. \tag{9.3}$$

All these measurements are dominated by the systematic uncertainty, with the dominant contribution being from the jet energy scale. It is important to notice that all three measurements are highly correlated and a measurement combination would offer little improvement to the precision of the top-quark mass measurement.

The second analysis in this thesis presents a measurement of the $t\bar{t}Z$ cross section in the $t\bar{t}Z \to 4\ell$ channel, using 20.3 fb$^{-1}$ of proton-proton collisions at a center-of-mass of 8 TeV using the ATLAS detector. The selected events are split in five signal regions according to the flavor composition of the leptons and the number of $b$-tagged jets present in the event. An additional control region is used to determine the normalization of the main background of the analysis, i.e., the $ZZ$ background. A likelihood fit is used on these five signal regions and the $ZZ$ control region to determine simultaneously the $t\bar{t}Z$ cross section and the $ZZ$ normalization from data. A blinded analysis is used to estimate the expected number of signal and background events, the statistical and systematic uncertainties associated with the measurement and the validity of the method. After the method has been validated, the data is unblinded and the value of the measured $t\bar{t}Z$ cross section is:

$$\sigma_{t\bar{t}Z} = 0.32^{+0.18}_{-0.14}\,(\text{stat.})^{+0.12}_{-0.05}\,(\text{syst.})\ \text{pb}. \tag{9.4}$$

Since the measurement is dominated by the statistical uncertainty, a measurement with more data events would reduce the total uncertainty considerably. In particular, with the start of Run II of the LHC at a center-of-mass energy of 13 TeV, the $t\bar{t}Z$ production cross section is expected to increase roughly 4 times. Since the integrated luminosity of the data collected in 2015 is expected to be around half the integrated luminosity of the data used in the analysis presented in this thesis, approximately 2 times more $t\bar{t}Z$ events are expected in 2015. With this amount of data, a $t\bar{t}Z$ cross section measurement in the $t\bar{t}Z \to 4\ell$ channel would be improved significantly, and the systematic uncertainty will play a larger role in the precision of the measurement.

APPENDIX A

# List of acronyms

ATLAS: A Toroidal LHC ApparatuS.

BSM: (physics) beyond the Standard Model.

CDF: Collider Detector at Fermilab.

CMS: Compact Muon Solenoid.

CKM: Cabibbo-Kobayashi-Maskawa (matrix).

CR: color reconnection.

CP: charge-parity (symmetry).

DF: different flavor.

EM: electromagnetic.

ISR: initial state radiation.

FSR: final state radiation.

GRL: good run list.

HEP: high energy physics.

JER: jet energy resolution.

JES: jet energy scale.

JVF: jet vertex fraction.

LCW: local cluster weighting.

LHC: Large Hardon Collider.

LEP: Large Electron-Positron Collider.

MC: Monte Carlo (simulation).

NLO: next-to-leading order.

NNLL: next-to-next-to-leading logarithm.

NNLO: next-to-next-to-leading order.

OS: opposite signed (charge).

OSSF: opposite signed and same flavored (refering to two leptons).

PDF: parton density function.

QCD: quantum chromodynamics.

SCT: semiconductor tracker system (of the ATLAS detector).

SF: same flavor.

SHG: shower and hadronization generator.

SM: Standard Model of particle physics.

SMS: superconducting magnet system (of the ATLAS detector).

SS: same signed (charge).

TRT: transition radiation tracker (of the ATLAS detector).

UE: underlying event.

$Z1$: first lepton pair, as defined in Section 8.1.1.

$Z2$: second lepton pair, as defined in Section 8.1.1.

# Bibliography


[1] ATLAS Collaboration, *ATLAS detector and physics performance: technical design report, 1*, 1999.

[2] O. S. Bruning et al., *LHC design report*, 2004.

[3] F. Halzen and A. Martin, *Quarks and leptons*, Wiley, 1984.

[4] D. Perkins, *Introduction to high energy physics*, Addison-Wesley, 1982.

[5] D. Griffiths, *Introduction to elementary particles*, John Wiley & Sons, 1987.

[6] S. Glashow, "Partial symmetries of weak interactions", *Nucl. Phys.* 22 (1961) 579–588.

[7] S. Weinberg, "A model of leptons", *Phys. Rev. Lett.* 19 (1967) 1264–1266.

[8] A. Salam and J. C. Ward, "Gauge theory of elementary interactions", *Phys. Rev.* 136 (1964) B763–B768.

[9] F. Englert and R. Brout, "Broken symmetry and the mass of gauge vector mesons", *Phys. Rev. Lett.* 13 (1964) 321–323.

[10] P. W. Higgs, "Broken symmetries and the masses of gauge bosons", *Phys. Rev. Lett.* 13 (1964) 508–509.

[11] G. S. Guralnik, C. R. Hagen and T. W. B. Kibble, "Global conservation laws and massless particles", *Phys. Rev. Lett.* 13 (1964) 585–587.

[12] S. Raby, "Grand unified theories" (2006), arXiv:hep-ph/0608183 [hep-ph].

[13] G. B. Cleaver, "Grand unified theories from superstrings" (1996), arXiv:hep-th/9604183 [hep-th].

[14] C. Martin, "NC GUTs: a status report" (2010), arXiv:1101.4783 [hep-th].

[15] ATLAS Collaboration, "Observation of a new particle in the search for the Standard Model Higgs boson with the ATLAS detector at the LHC", *Phys. Lett.* B716 (2012) 1–29, arXiv:1207.7214 [hep-ex].

[16] CMS Collaboration, "Observation of a new boson at a mass of 125 GeV with the CMS experiment at the LHC", *Phys. Lett.* B716 (2012) 30–61, arXiv:1207.7235 [hep-ex].

[17] K. Olive et al., "Review of particle physics", *Chin. Phys. C* 38 (2014) 090001.

[18] ATLAS and CMS Collaboration, "Combined measurement of the Higgs boson mass in $pp$ collisions at $\sqrt{s} = 7$ and 8 TeV with the ATLAS and CMS experiments" (2015), arXiv:1503.07589 [hep-ex].

[19] ATLAS, CMS, CDF and DØ Collaboration,
"First combination of Tevatron and LHC measurements of the top-quark mass" (2014),
arXiv:1403.4427.

[20] A. Ali, C. Hambrock and M. J. Aslam, "A tetraquark interpretation of the BELLE data on the anomalous $\Upsilon(1S)\,\pi^+\pi^-$ and $\Upsilon(2S)\,\pi^+\pi^-$ production near the $\Upsilon(5S)$ resonance",
*Phys. Rev. Lett.* 104 (2010) 162001, arXiv:0912.5016 [hep-ph].

[21] T. Liu, Y. Mao and B.-Q. Ma, "Present status on experimental search for pentaquarks",
*Int. J. Mod. Phys.* A29 (2014) 1430020, arXiv:1403.4455.

[22] CDF Collaboration,
"Observation of top quark production in $p\overline{p}$ collisions with the Collider Detector at Fermilab",
*Phys. Rev. Lett.* 74 (1995) 2626–2631.

[23] DØ Collaboration, "Observation of the top quark", *Phys. Rev. Lett.* 74 (1995) 2632–2637,
arXiv:hep-ex/9503003 [hep-ex].

[24] W. Bernreuther, "Top quark physics at the LHC", *J. Phys.* G35 (2008) 083001,
arXiv:0805.1333 [hep-ph].

[25] L. Orr, "Decay versus hadronization for top quarks produced in hadron colliders",
*Phys. Rev. D* 44 (1991) 88–98.

[26] F. Deliot and D. Glenzinski, "Top quark physics at the Tevatron",
*Rev. Mod. Phys.* 84 (2012) 211, arXiv:1010.1202 [hep-ex].

[27] K. Agashe et al., "Working group report: top quark" (2013), arXiv:1311.2028 [hep-ph].

[28] A. Quadt, "Top quark physics at hadron colliders", *Eur. Phys. J.* C48 (2006) 835–1000.

[29] S. Willenbrock, "The Standard Model and the top quark", *NATO Sci. Ser. II* 123 (2003) 1–41,
arXiv:hep-ph/0211067 [hep-ph].

[30] M. Kobayashi and T. Maskawa,
"CP-violation in the renormalizable theory of weak interaction",
*Progr. Theo. Phys.* 49 (1973) 652–657.

[31] S. L. Glashow, J. Iliopoulos and L. Maiani, "Weak interactions with lepton-hadron symmetry",
*Phys. Rev. D* 2 (1970) 1285–1292.

[32] R. R. Wilson, "The Tevatron", *Phys. Today* 30N10 (1977) 23–30.

[33] M. Mohammadi Najafabadi, "Single top production at LHC" (2006),
arXiv:hep-ex/0605034 [hep-ex].

[34] M. Czakon, P. Fiedler and A. Mitov,
"Total top-quark pair-production cross section at hadron colliders through $O(\alpha_S^4)$",
*Phys. Rev. Lett.* 110 (2013) 252004, arXiv:1303.6254 [hep-ph].

[35] S. Moch et al., "High precision fundamental constants at the TeV scale" (2014),
arXiv:1405.4781 [hep-ph].

[36] G. Degrassi et al., "Higgs mass and vacuum stability in the Standard Model at NNLO",
*JHEP* 1208 (2012) 098, arXiv:1205.6497 [hep-ph].

[37] S. Alekhin, A. Djouadi and S. Moch,
"The top quark and Higgs boson masses and the stability of the electroweak vacuum",
*Phys. Lett.* B716 (2012) 214–219, arXiv:1207.0980 [hep-ph].

[38] CDF and DØ Collaboration, "Combination of CDF and D0 results on the mass of the top quark using up to 9.7 fb$^{-1}$ at the Tevatron" (2014), arXiv:1407.2682 [hep-ex].

[39] ATLAS Collaboration, "Measurement of the top quark mass in the $t\bar{t} \to$ lepton+jets and $t\bar{t} \to$ dilepton channels using $\sqrt{s} = 7$ TeV ATLAS data" (2015), arXiv:1503.05427 [hep-ex].

[40] CMS Collaboration,
"Combination of the CMS top-quark mass measurements from Run 1 of the LHC",
CMS-PAS-TOP-14-015 (2014).

[41] P. Z. Skands and D. Wicke, "Non-perturbative QCD effects and the top mass at the Tevatron", *Eur. Phys. J.* C52 (2007) 133–140, arXiv:hep-ph/0703081 [hep-ph].

[42] A. Hoang and I. Stewart, "Top mass measurements from jets and the Tevatron top-quark mass", *Nucl. Phys. Proc. Suppl.* 185 (2008) 220–226, arXiv:0808.0222 [hep-ph].

[43] A. Juste et al.,
"Determination of the top quark mass circa 2013: methods, subtleties, perspectives" (2013), arXiv:1310.0799 [hep-ph].

[44] M. Beneke, "Renormalons", *Phys. Rept.* 317 (1999) 1–142,
arXiv:hep-ph/9807443 [hep-ph].

[45] I. I. Bigi et al., "The pole mass of the heavy quark. Perturbation theory and beyond", *Phys. Rev.* D50 (1994) 2234–2246, arXiv:hep-ph/9402360 [hep-ph].

[46] G. 't Hooft, "Dimensional regularization and the renormalization group",
*Nucl. Phys. B* 61 (1973) 455–468.

[47] S. Weinberg, "New approach to the renormalization group", *Phys. Rev. D* 8 (1973) 3497–3509.

[48] DØ Collaboration,
"Determination of the pole and MSbar masses of the top quark from the $t\bar{t}$ cross section",
*Phys. Lett.* B703 (2011) 422–427, arXiv:1104.2887 [hep-ex].

[49] K. Melnikov and T. v. Ritbergen,
"The three loop relation between the MS-bar and the pole quark masses",
*Phys. Lett.* B482 (2000) 99–108, arXiv:hep-ph/9912391 [hep-ph].

[50] ATLAS Collaboration, "Measurement of the $t\bar{t}$ production cross-section using $e\mu$ events with $b$-tagged jets in $pp$ collisions at $\sqrt{s} = 7$ and 8 TeV with the ATLAS detector",
*Eur. Phys. J.* C74 (2014) 3109, arXiv:1406.5375 [hep-ex].

[51] CMS Collaboration, "Determination of the top-quark pole mass and strong coupling constant from the $t\bar{t}$ production cross section in $pp$ collisions at $\sqrt{s} = 7$ TeV",
*Phys. Lett.* B728 (2014) 496–517, arXiv:1307.1907 [hep-ex].

[52] R. Röntsch and M. Schulze,
"Constraining couplings of top quarks to the Z boson in $t\bar{t}$ + Z production at the LHC",
*JHEP* 1407 (2014) 091, arXiv:1404.1005 [hep-ph].

[53] F. Richard, "Present and future constraints on top EW couplings" (2014),
arXiv:1403.2893 [hep-ph].

[54] M. Garzelli et al., "$t\bar{t}W^{\pm}$ and $t\bar{t}Z$ Hadroproduction at NLO accuracy in QCD with parton shower and hadronization effects", *JHEP* 1211 (2012) 056, arXiv:1208.2665 [hep-ph].

[55] M. Schmaltz, "Physics beyond the Standard Model (theory): introducing the little Higgs",
*Nucl. Phys. Proc. Suppl.* 117 (2003) 40–49, arXiv:hep-ph/0210415 [hep-ph].

[56] J. Hubisz et al., "Electroweak precision constraints on the littlest Higgs model with T parity", *JHEP* 0601 (2006) 135, arXiv:hep-ph/0506042 [hep-ph].

[57] L. Randall and R. Sundrum, "A large mass hierarchy from a small extra dimension", *Phys. Rev. Lett.* 83 (1999) 3370–3373, arXiv:hep-ph/9905221 [hep-ph].

[58] A. Djouadi, G. Moreau and F. Richard, "Resolving the $A_{FB}^{b}$ puzzle in an extra dimensional model with an extended gauge structure", *Nucl. Phys.* B773 (2007) 43–64, arXiv:hep-ph/0610173 [hep-ph].

[59] ATLAS Collaboration, "Measurement of the top quark charge in $pp$ collisions at $\sqrt{s}$ = 7TeV with the ATLAS detector", *JHEP*, 31 (2013).

[60] DØ Collaboration, "Measurement of the electric charge of the top quark in $t\bar{t}$ events", *Phys. Rev.* D90 (2014) 051101, arXiv:1407.4837 [hep-ex].

[61] CDF Collaboration, "Exclusion of exotic top-like quarks with -4/3 electric charge using jet-charge tagging in single-lepton $t\bar{t}$ events at CDF", *Phys. Rev.* D88 (2013) 032003, arXiv:1304.4141 [hep-ex].

[62] CMS Collaboration, "Constraints on the top-quark charge from top-pair events", CMS-PAS-TOP-11-031 (2012).

[63] CMS Collaboration, "Measurement of the W boson helicity in events with a single reconstructed top quark in $pp$ collisions at $\sqrt{s}$=8 TeV" (2014), arXiv:1410.1154 [hep-ex].

[64] ATLAS Collaboration, "Measurements of the Higgs boson production and decay rates and coupling strengths using $pp$ collision data at $\sqrt{s}$ = 7 and 8 TeV in the ATLAS experiment", ATLAS-CONF-2015-007 (2015).

[65] CMS Collaboration, "Search for the associated production of the Higgs boson with a top-quark pair", *JHEP* 1409 (2014) 087, arXiv:1408.1682 [hep-ex].

[66] G. Mahlon and S. J. Parke, "Angular correlations in top quark pair production and decay at hadron colliders", *Phys. Rev.* D53 (1996) 4886–4896, arXiv:hep-ph/9512264 [hep-ph].

[67] CDF Collaboration, "Measurement of $t\bar{t}$ spin correlation in $p\bar{p}$ collisions using the CDF II detector at the Tevatron", *Phys. Rev.* D83 (2011) 031104, arXiv:1012.3093 [hep-ex].

[68] DØ Collaboration, "Evidence for spin correlation in $t\bar{t}$ production", *Phys. Rev. Lett.* 108 (2012) 032004, arXiv:1110.4194 [hep-ex].

[69] ATLAS Collaboration, "Measurements of spin correlation in top-antitop quark events from proton-proton collisions at $\sqrt{s}$ = 7 TeV using the ATLAS detector" (2014), arXiv:1407.4314 [hep-ex].

[70] CMS Collaboration, "Measurements of $t\bar{t}$ spin correlations and top-quark polarization using dilepton final states in $pp$ collisions at $\sqrt{s}$=7 TeV", *Phys. Rev. Lett.* 112 (2014) 182001, arXiv:1311.3924 [hep-ex].

[71] J. H. Kühn and G. Rodrigo, "Charge asymmetries of top quarks at hadron colliders revisited", *JHEP* 1201 (2012) 063, arXiv:1109.6830 [hep-ph].

[72] M. Czakon, P. Fiedler and A. Mitov,
"Resolving the Tevatron top quark forward-backward asymmetry puzzle" (2014),
arXiv:1411.3007 [hep-ph].

[73] CDF Collaboration, "Measurement of the top quark forward-backward production asymmetry and its dependence on event kinematic properties", *Phys. Rev.* D87 (2013) 092002,
arXiv:1211.1003 [hep-ex].

[74] DØ Collaboration, "Measurement of the forward-backward asymmetry in top quark-antiquark production in $p\overline{p}$ collisions using the lepton+jets channel", *Phys.Rev.* D90 (2014) 072011,
arXiv:1405.0421 [hep-ex].

[75] W. Bernreuther and Z. G. Si,
"Top quark and leptonic charge asymmetries for the Tevatron and LHC",
*Phys. Rev.* D86 (2012) 034026, arXiv:1205.6580 [hep-ph].

[76] ATLAS and CMS Collaboration, "Combination of ATLAS and CMS $t\bar{t}$ charge asymmetry measurements using LHC proton-proton collisions at 7 TeV", CMS-PAS-TOP-14-006 (2014).

[77] S. Myers, "The LEP collider, from design to approval and commissioning",
CERN-91-08 (1991).

[78] M. Lamont, "Status of the LHC", *J. Phys. Conf. Ser.* 455 (2013) 012001.

[79] ATLAS Collaboration, "Improved luminosity determination in $pp$ collisions at $\sqrt{s} = 7$ TeV using the ATLAS detector at the LHC", *Eur. Phys. J.* C73 (2013) 2518,
arXiv:1302.4393 [hep-ex].

[80] L. Rossi, "The Large Hadron Collider of CERN and the roadmap toward higher performance",
CERN-ACC-2014-0225 (2012).

[81] ATLAS Collaboration, "The ATLAS experiment at the CERN Large Hadron Collider",
*JINST* 3 (2008) S08003.

[82] CMS Collaboration, "The CMS experiment at the CERN LHC", *JINST* 3 (2008) S08004.

[83] ALICE Collaboration, "The ALICE experiment at the CERN LHC", *JINST* 3 (2008) S08002.

[84] LHCb Collaboration, "The LHCb detector at the LHC", *JINST* 3 (2008) S08005.

[85] LHCf Collaboration, "The LHCf detector at the CERN Large Hadron Collider",
*JINST* 3 (2008) S08006.

[86] TOTEM Collaboration, "The TOTEM experiment at the CERN Large Hadron Collider",
*JINST* 3 (2008) S08007.

[87] MoEDAL Collaboration, "The physics programme of the MoEDAL experiment at the LHC",
*Int. J. Mod. Phys.* A29 (2014) 1430050, arXiv:1405.7662 [hep-ph].

[88] J. J. Goodson, "Search for supersymmetry in states with large missing transverse momentum and three leptons including a Z-boson", PhD thesis: Stony Brook University, 2012.

[89] ATLAS Collaboration,
"Expected performance of the ATLAS experiment - detector, trigger and physics" (2009),
arXiv:0901.0512 [hep-ex].

[90] ATLAS Collaboration, "Commissioning of the ATLAS muon spectrometer with cosmic rays",
*Eur. Phys. J.* C70 (2010) 875–916, arXiv:1006.4384 [physics.ins-det].

[91] M. S. Neubauer, "A fast hardware tracker for the ATLAS trigger system" (2011), arXiv:1110.1910 [hep-ex].

[92] ATLAS Collaboration, "Improved luminosity determination in $pp$ collisions at $\sqrt{s} = 7$ TeV using the ATLAS detector at the LHC", *Eur. Phys. J.* C73 (2013) 2518, arXiv:1302.4393 [hep-ex].

[93] ATLAS internal document, "Preliminary luminosity determination in $pp$ collisions at $\sqrt{s} = 8$ teV using the ATLAS detector in 2012", ATL-COM-LUM-2012-013 (2012).

[94] ATLAS internal document, *Luminosity For Physics*, revision 11, URL: https://twiki.cern.ch/twiki/bin/view/Atlas/LuminosityForPhysics?rev=11.

[95] ATLAS internal document, *COMA period description report: data11*, URL: https://atlas-tagservices.cern.ch/tagservices/RunBrowser/runBrowserReport/rBR_Period_Report.php?fnt=data11*.

[96] ATLAS internal document, *COMA period description report: data12*, URL: https://atlas-tagservices.cern.ch/tagservices/RunBrowser/runBrowserReport/rBR_Period_Report.php?fnt=data12*.

[97] J. Adelman et al., "Technical aspects of the first top pair analyses", ATL-PHYS-INT-2010-140 (2010).

[98] M. Dobbs et al., "Les Houches guidebook to Monte Carlo generators for hadron collider physics" (2004) 411–459, arXiv:hep-ph/0403045 [hep-ph].

[99] H. L. Lai et al., "New parton distributions for collider physics", *Phys. Rev.* D82 (2010) 074024, arXiv:1007.2241 [hep-ph].

[100] J. Pumplin et al., "New generation of parton distributions with uncertainties from global QCD analysis", *JHEP* 0207 (2002) 012, arXiv:hep-ph/0201195 [hep-ph].

[101] P. M. Nadolsky et al., "Implications of CTEQ global analysis for collider observables", *Phys. Rev.* D78 (2008) 013004, arXiv:0802.0007 [hep-ph].

[102] A. Martin et al., "Parton distributions for the LHC", *Eur. Phys. J.* C63 (2009) 189–285, arXiv:0901.0002 [hep-ph].

[103] M. L. Mangano et al., "ALPGEN, a generator for hard multiparton processes in hadronic collisions", *JHEP* 0307 (2003) 001, arXiv:hep-ph/0206293 [hep-ph].

[104] B. P. Kersevan and E. Richter-Was, "The Monte Carlo event generator AcerMC versions 2.0 to 3.8 with interfaces to PYTHIA 6.4, HERWIG 6.5 and ARIADNE 4.1", *Comput. Phys. Commun.* 184 (2013) 919–985, arXiv:hep-ph/0405247 [hep-ph].

[105] T. Stelzer and W. Long, "Automatic generation of tree level helicity amplitudes", *Comput. Phys. Commun.* 81 (1994) 357–371, arXiv:hep-ph/9401258 [hep-ph].

[106] S. Frixione and B. R. Webber, "Matching NLO QCD computations and parton shower simulations", *JHEP* 0206 (2002) 029, arXiv:hep-ph/0204244 [hep-ph].

[107] P. Nason, "A new method for combining NLO QCD with shower Monte Carlo algorithms", *JHEP* 0411 (2004) 040, arXiv:hep-ph/0409146 [hep-ph].

[108] T. Gleisberg et al., "Event generation with SHERPA 1.1", *JHEP* 0902 (2009) 007, arXiv:0811.4622 [hep-ph].

[109] G. Corcella et al., "HERWIG 6: an event generator for hadron emission reactions with interfering gluons (including supersymmetric processes)", *JHEP* 0101 (2001) 010, arXiv:hep-ph/0011363 [hep-ph].

[110] ATLAS Collaboration, "First tuning of HERWIG/JIMMY to ATLAS data", ATL-PHYS-PUB-2010-014 (2010).

[111] J. Butterworth, J. R. Forshaw and M. Seymour, "Multiparton interactions in photoproduction at HERA", *Z. Phys.* C72 (1996) 637–646, arXiv:hep-ph/9601371 [hep-ph].

[112] T. Sjostrand, S. Mrenna and P. Z. Skands, "PYTHIA 6.4 physics and manual", *JHEP* 0605 (2006) 026, arXiv:hep-ph/0603175 [hep-ph].

[113] ATLAS Collaboration, "ATLAS tunes of PYTHIA 6 and PYTHIA 8 for MC11", ATL-PHYS-PUB-2011-009 (2011).

[114] P. Z. Skands, "Tuning Monte Carlo generators: the Perugia tunes", *Phys. Rev.* D82 (2010) 074018, arXiv:1005.3457 [hep-ph].

[115] T. Sjostrand, S. Mrenna and P. Z. Skands, "A brief introduction to PYTHIA 8.1", *Comput. Phys. Commun.* 178 (2008) 852–867, arXiv:0710.3820 [hep-ph].

[116] ATLAS Collaboration, "Further ATLAS tunes of PYTHIA6 and PYTHIA 8", ATL-PHYS-PUB-2011-014 (2011).

[117] S. Agostinelli et al., "GEANT4: a simulation toolkit", *Nucl. Instrum. Meth.* A506 (2003) 250–303.

[118] J. Allison et al., "Geant4 developments and applications", *IEEE Trans. Nucl. Sci.* 53 (2006) 270.

[119] W. Lukas, "Fast simulation for ATLAS: Atlfast-II and ISF", ATL-SOFT-PROC-2012-065 (2012).

[120] B. Abi et al., "Mis-identified lepton backgrounds to top quark pair production for Moriond 2011 analysis", ATL-COM-PHYS-2011-144 (2011).

[121] B. Acharya et al., "Object selection and calibration, background estimations and MC samples for the winter 2012 top quark analyses with 2011 data", ATL-COM-PHYS-2012-224 (2012).

[122] W. Lampl et al., "Calorimeter clustering algorithms: description and performance", ATL-LARG-PUB-2008-002 (2008).

[123] ATLAS internal document, *Electron reconstruction*, revision 74, URL: https://twiki.cern.ch/twiki/bin/view/AtlasProtected/ElectronReconstruction?rev=74.

[124] ATLAS Collaboration, "Expected electron performance in the ATLAS experiment", ATL-PHYS-PUB-2011-006 (2011).

[125] ATLAS internal document, *TechnicalitiesForMedium1*, revision 44, URL: https://twiki.cern.ch/twiki/bin/view/AtlasProtected/TechnicalitiesForMedium1?rev=44.

[126] ATLAS internal document, *TopCommonObjects2011*, revision 5, URL: https://twiki.cern.ch/twiki/bin/view/AtlasProtected/TopCommonObjects2011?rev=5.

[127] ATLAS internal document, *LArCleaningAndObjectQuality*, revision 34, URL: https://twiki.cern.ch/twiki/bin/view/AtlasProtected/LArCleaningAndObjectQuality?rev=34.

[128] K. Benslama and E. Ortega, "Electron Likelihood", ATL-PHYS-INT-2009-107 (2009).

[129] ATLAS internal document, *TechnicalitiesForMedium1*, revision 49, URL: https://twiki.cern.ch/twiki/bin/view/AtlasProtected/ElectronLikelihoodPID?rev=49.

[130] M. Agustoni et al., "Electromagnetic energy scale in-situ calibration and performance: supporting document for the egamma performance paper", ATL-COM-PHYS-2011-263 (2011).

[131] ATLAS Collaboration, "Electron performance measurements with the ATLAS detector using the 2010 LHC proton-proton collision data", *Eur. Phys. J.* C72 (2012) 1909, arXiv:1110.3174 [hep-ex].

[132] ATLAS internal document, *TopCommonScales2011*, revision 3, URL: https://twiki.cern.ch/twiki/bin/view/AtlasProtected/TopCommonScales2011?rev=3.

[133] ATLAS internal document, *TopCommonScales*, revision 146, URL: https://twiki.cern.ch/twiki/bin/view/AtlasProtected/TopCommonScales?rev=146.

[134] ATLAS Collaboration, "Electron performance measurements with the ATLAS detector using the 2010 LHC proton-proton collision data", *Eur. Phys. J.* C72 (2012) 1909, arXiv:1110.3174 [hep-ex].

[135] B. Acharya et al., "Object selection and calibration, background estimations and MC samples for the winter 2012 top quark analyses with 2011 data", ATL-COM-PHYS-2012-224 (2012).

[136] ATLAS Collaboration, "Muon reconstruction performance", ATLAS-CONF-2010-064 (2010).

[137] ATLAS internal document, *TopCommonObjects*, revision 265, URL: https://twiki.cern.ch/twiki/bin/view/AtlasProtected/TopCommonObjects?rev=265.

[138] ATLAS internal document, *MuidMuonCollection*, revision 7, URL: https://twiki.cern.ch/twiki/bin/view/AtlasProtected/MuidMuonCollection?rev=7.

[139] ATLAS internal document, *MCPAnalysisGuidelinesRel17MC11a*, revision 30, URL: https://twiki.cern.ch/twiki/bin/view/AtlasProtected/MCPAnalysisGuidelinesRel17MC11a?rev=30.

[140] ATLAS internal document, *JetVertexFraction*, revision 8, URL: https://twiki.cern.ch/twiki/bin/view/Main/JetVertexFraction?rev=8.

[141] ATLAS Collaboration, "Measurement of the muon reconstruction performance of the ATLAS detector using 2011 and 2012 LHC proton-proton collision data", *Eur. Phys. J.* C74 (2014) 3130, arXiv:1407.3935 [hep-ex].

[142] ATLAS Collaboration, "Muon reconstruction efficiency in reprocessed 2010 LHC proton-proton collision data recorded with the ATLAS detector", ATLAS-CONF-2011-063 (2011).

[143] L. Asquith et al., "Performance of jet algorithms in the ATLAS detector", ATL-PHYS-INT-2010-129 (2010).

[144] M. Cacciari, G. P. Salam and G. Soyez, "The anti-k(t) jet clustering algorithm", *JHEP* 0804 (2008) 063, arXiv:0802.1189 [hep-ph].

[145] C. Bertella et al., "Underlying event particle flow based on calorimeter clusters in $pp$ collisions at 7 TeV with the ATLAS detector at the LHC", ATL-COM-PHYS-2010-293 (2010).

[146] ATLAS Collaboration,
"Jet energy measurement with the ATLAS detector in proton-proton collisions at $\sqrt{s} = 7$ TeV",
*Eur. Phys. J.* C73 (2013) 2304, arXiv:1112.6426 [hep-ex].

[147] ATLAS Collaboration, "Jet energy measurement and its systematic uncertainty in proton-proton collisions at $\sqrt{s} = 7$ TeV with the ATLAS detector",
*Eur. Phys. J.* C75 (2015) 17, arXiv:1406.0076 [hep-ex].

[148] B. Acharya et al., "Object selection and calibration, background estimations and MC samples for top quark analyses using the full 2012 data set", ATL-COM-PHYS-2013-1016 (2013).

[149] ATLAS Collaboration, "Jet energy measurement and its systematic uncertainty in proton-proton collisions at $\sqrt{s} = 7$ TeV with the ATLAS detector",
*Eur. Phys. J.* C75 (2015) 17, arXiv:1406.0076 [hep-ex].

[150] S. Argyropoulos et al., "Pile-up subtraction and suppression for jets in ATLAS",
ATL-COM-PHYS-2013-251 (2013).

[151] M. Cacciari, G. P. Salam and G. Soyez, "The catchment area of jets", *JHEP* 0804 (2008) 005, arXiv:0802.1188 [hep-ph].

[152] ATLAS internal document, *Bad jets*, revision 20, URL: https://twiki.cern.ch/twiki/bin/view/AtlasProtected/HowToCleanJets2011#Bad_jets?rev=20.

[153] ATLAS Collaboration, "Jet energy resolution in proton-proton collisions at $\sqrt{s} = 7$ TeV recorded in 2010 with the ATLAS detector", *Eur. Phys. J.* C73 (2013) 2306, arXiv:1210.6210 [hep-ex].

[154] ATLAS Collaboration,
"Jet energy resolution and selection efficiency relative to track jets from in-situ techniques with the atlas detector using proton-proton collisions at a center of mass energy $\sqrt{s} = 7$ TeV",
ATLAS-CONF-2010-054 (2010).

[155] ATLAS Collaboration, "Calibration of the performance of $b$-tagging for $c$ and light-flavour jets in the 2012 ATLAS data", ATLAS-CONF-2014-046 (2014).

[156] ATLAS Collaboration, "Commissioning of the ATLAS high-performance $b$-tagging algorithms in the 7 TeV collision data", ATLAS-CONF-2011-102 (2011).

[157] G. Piacquadio and C. Weiser,
"A new inclusive secondary vertex algorithm for $b$-jet tagging in ATLAS",
*J. Phys. Conf. Ser.* 119 (2008) 032032.

[158] R. Frühwirth, "Application of Kalman filtering to track and vertex fitting",
*Nucl. Instrum. Meth.* A262 (1987) 444–450.

[159] ATLAS Collaboration,
"Calibrating the $b$-tag efficiency and mistag rate in 35 $pb^{-1}$ of data with the ATLAS detector",
ATLAS-CONF-2011-089 (2011).

[160] ATLAS Collaboration, "Measuring the $b$-tag efficiency in a top-pair sample with 4.7 $\text{fb}^{-1}$ of data from the ATLAS detector", ATLAS-CONF-2012-097 (2012).

[161] ATLAS internal document, *HowToCleanJets2012*, revision 16, URL: https://twiki.cern.ch/twiki/bin/view/AtlasProtected/HowToCleanJets2012?rev=16.

[162] ATLAS internal document, *BTaggingBenchmarks*, revision 23, URL: https://twiki.cern.ch/twiki/bin/view/AtlasProtected/BTaggingBenchmarks?rev=23.

[163] ATLAS internal document, *FlavourTagging*, revision 203, URL: https://twiki.cern.ch/twiki/bin/view/AtlasProtected/FlavourTagging?rev=203.

[164] ATLAS Collaboration, "Calibration of *b*-tagging using dileptonic top pair events in a combinatorial likelihood approach with the ATLAS experiment", ATLAS-CONF-2014-004 (2014).

[165] ATLAS Collaboration, "Calibration of the performance of *b*-tagging for *c* and light-flavour jets in the 2012 ATLAS data", ATLAS-CONF-2014-046 (2014).

[166] ATLAS Collaboration, "Performance of missing transverse momentum reconstruction in proton-proton collisions at 7 TeV with ATLAS", *Eur. Phys. J.* C72 (2012) 1844, arXiv:1108.5602 [hep-ex].

[167] ATLAS internal document, *TopElectronSFUtils-00-00-18*, URL: https://svnweb.cern.ch/trac/atlasoff/browser/PhysicsAnalysis/TopPhys/TopPhysUtils/TopElectronSFUtils/tags/TopElectronSFUtils-00-00-18/TopElectronSFUtils/electron_SF_R17.h.

[168] ATLAS internal document, *TElectronEfficiencyCorrectionTool*, revision 47, URL: https://twiki.cern.ch/twiki/bin/viewauth/AtlasProtected/TElectronEfficiencyCorrectionTool?rev=47.

[169] ATLAS internal document, *EnergyRescaler*, revision 22, URL: https://twiki.cern.ch/twiki/bin/view/AtlasProtected/EnergyRescaler?rev=22.

[170] ATLAS internal document, *egammaAnalysisUtils-00-02-81*, URL: https://svnweb.cern.ch/trac/atlasoff/browser/Reconstruction/egamma/egammaAnalysis/egammaAnalysisUtils/tags/egammaAnalysisUtils-00-02-81.

[171] ATLAS internal document, *egammaAnalysisUtils-00-04-58*, URL: https://svnweb.cern.ch/trac/atlasoff/browser/Reconstruction/egamma/egammaAnalysis/egammaAnalysisUtils/tags/egammaAnalysisUtils-00-04-58.

[172] ATLAS internal document, *TopMuonSFUtils-00-00-14*, URL: https://svnweb.cern.ch/trac/atlasoff/browser/PhysicsAnalysis/TopPhys/TopPhysUtils/TopMuonSFUtils/tags/TopMuonSFUtils-00-00-14.

[173] ATLAS internal document, *TrigMuonEfficiency*, revision 72, URL: https://twiki.cern.ch/twiki/bin/viewauth/Atlas/TrigMuonEfficiency?rev=72.

[174] ATLAS internal document, *TrigMuonEfficiency*, URL: https://svnweb.cern.ch/trac/atlasoff/browser/Trigger/TrigAnalysis/TrigMuonEfficiency/tags/TrigMuonEfficiency-00-02-42.

[175] ATLAS internal document, *TopMuonSFUtils-00-00-20*, URL: https://svnweb.cern.ch/trac/atlasoff/browser/PhysicsAnalysis/TopPhys/TopPhysUtils/TopMuonSFUtils/tags/TopMuonSFUtils-00-00-20.

[176] ATLAS internal document, *MuonEfficiencyCorrections-01-01-00*, URL: https://svnweb.cern.ch/trac/atlasoff/browser/PhysicsAnalysis/MuonID/MuonIDAnalysis/MuonEfficiencyCorrections/tags/MuonEfficiencyCorrections-01-01-00.

[177] ATLAS internal document, *MuonEfficiencyCorrections-02-01-20*, URL: https://svnweb.cern.ch/trac/atlasoff/browser/PhysicsAnalysis/MuonID/MuonIDAnalysis/MuonEfficiencyCorrections/tags/MuonEfficiencyCorrections-02-01-20.

[178] ATLAS internal document, *ApplyJetCalibration-00-02-07*, URL: https://svnweb.cern.ch/trac/atlasoff/browser/Reconstruction/Jet/ApplyJetCalibration/tags/ApplyJetCalibration-00-02-07.

[179] ATLAS internal document, *JetUncertainties2011*, revision 18, URL: https://twiki.cern.ch/twiki/bin/view/AtlasProtected/JetUncertainties2011?rev=18.

[180] ATLAS internal document, *JetUncertainties-00-08-07*, URL: https://svnweb.cern.ch/trac/atlasoff/browser/Reconstruction/Jet/JetUncertainties/tags/JetUncertainties-00-08-07.

[181] ATLAS internal document, *JetUncertainties2012*, revision 37, URL: https://twiki.cern.ch/twiki/bin/view/AtlasProtected/JetUncertainties2012?rev=37.

[182] ATLAS internal document, *JetResolution-02-00-03*, URL: https://svnweb.cern.ch/trac/atlasoff/browser/Reconstruction/Jet/JetResolution/tags/JetResolution-02-00-03.

[183] ATLAS internal document, *ApplyJetResolutionSmearing-00-01-03*, URL: https://svnweb.cern.ch/trac/atlasoff/browser/Reconstruction/Jet/JetAnalysisTools/ApplyJetResolutionSmearing/tags/ApplyJetResolutionSmearing-00-01-03.

[184] ATLAS internal document, *TopJetReconstructionEfficiency*, revision 20, URL: https://twiki.cern.ch/twiki/bin/view/AtlasProtected/TopJetReconstructionEfficiency?rev=20.

[185] ATLAS internal document, *TopSystematicUncertainties for winter 2012 (rel17) 5 fb$^{-1}$ analyses*, revision 6, URL: https://twiki.cern.ch/twiki/bin/viewauth/AtlasProtected/TopSystematicUncertainties2011?rev=6.

[186] ATLAS internal document, *TopSystematicUncertainties for 8 TeV 2012 analyses (rel17.2)*, revision 250, URL: https://twiki.cern.ch/twiki/bin/viewauth/AtlasProtected/TopSystematicUncertainties?rev=250.

[187] ATLAS internal document, *JetEffiProvider-00-00-04*, URL: https://svnweb.cern.ch/trac/atlasoff/browser/PhysicsAnalysis/TopPhys/TopPhysUtils/JetEffiProvider/tags/JetEffiProvider-00-00-04.

[188] ATLAS internal document, *JetEffiProvider-00-00-05*, URL: https://svnweb.cern.ch/trac/atlasoff/browser/PhysicsAnalysis/TopPhys/TopPhysUtils/JetEffiProvider/tags/JetEffiProvider-00-00-05.

[189] ATLAS internal document, *TopJetUtils-00-00-07*, URL: https://svnweb.cern.ch/trac/atlasoff/browser/PhysicsAnalysis/TopPhys/TopPhysUtils/TopJetUtils/tags/TopJetUtils-00-00-07.

[190] ATLAS internal document, *JVF cut*, revision 45, URL: https://twiki.cern.ch/twiki/bin/viewauth/AtlasProtected/TopJetLiaisonR17Recommendations?rev=45#JVF_cut.

[191] ATLAS internal document, *JVFUncertaintyTool-00-00-04*,
URL: https://svnweb.cern.ch/trac/atlasoff/browser/Reconstruction/Jet/JetAnalysisTools/JVFUncertaintyTool/tags/JVFUncertaintyTool-00-00-04.

[192] ATLAS internal document, *Calibration data interface*, revision 73,
URL: https://twiki.cern.ch/twiki/bin/view/AtlasProtected/BTaggingCalibrationDataInterface?rev=73.

[193] ATLAS internal document, *CalibrationDataInterface-00-01-02*,
URL: https://svnweb.cern.ch/trac/atlasoff/browser/PhysicsAnalysis/JetTagging/JetTagPerformanceCalibration/CalibrationDataInterface/tags/CalibrationDataInterface-00-01-02.

[194] ATLAS internal document, *CalibrationDataInterface-00-03-06*,
URL: https://svnweb.cern.ch/trac/atlasoff/browser/PhysicsAnalysis/JetTagging/JetTagPerformanceCalibration/CalibrationDataInterface/tags/CalibrationDataInterface-00-03-06.

[195] ATLAS internal document, *TopD3PDCorrections-12-01-74*,
URL: https://svnweb.cern.ch/trac/atlasoff/browser/PhysicsAnalysis/TopPhys/TopD3PDCorrections/tags/TopD3PDCorrections-12-01-74.

[196] ATLAS internal document, *TopETmissLiaisonMoriond12*, revision 14, URL: https://twiki.cern.ch/twiki/bin/view/AtlasProtected/TopETmissLiaisonMoriond12?rev=14.

[197] ATLAS internal document, *MissingETUtility-01-00-09*,
URL: https://svnweb.cern.ch/trac/atlasoff/browser/Reconstruction/MissingETUtility/tags/MissingETUtility-01-00-09.

[198] ATLAS internal document, *MissingETUtility-01-01-03*,
URL: https://svnweb.cern.ch/trac/atlasoff/browser/Reconstruction/MissingETUtility/tags/MissingETUtility-01-01-03.

[199] ATLAS internal document, *TopD3PDCorrections-12-01-20*,
URL: https://svnweb.cern.ch/trac/atlasoff/browser/PhysicsAnalysis/TopPhys/TopD3PDCorrections/tags/TopD3PDCorrections-12-01-20.

[200] M Cristinziani et al., "Measurement of the production cross-section $\sigma_{t\bar{t}Z}$ in final states with four leptons using 20.3/fb of $pp$ collisions at 8 TeV at the LHC",
ATL-COM-PHYS-2014-843 (2014).

[201] C. Lester and D. Summers,
"Measuring masses of semiinvisibly decaying particles pair produced at hadron colliders",
*Phys. Lett.* B463 (1999) 99–103, arXiv:hep-ph/9906349 [hep-ph].

[202] A. Barr, C. Lester and P. Stephens, "$m_{T2}$: The Truth behind the glamour",
*J. Phys.* G29 (2003) 2343–2363, arXiv:hep-ph/0304226 [hep-ph].

[203] H. C. Cheng and Z. Y. Han, "Minimal kinematic constraints and $m_{T2}$", *JHEP* 0812 (2008) 063, arXiv:0810.5178 [hep-ph].

[204] ATLAS Collaboration, "Measurement of the top quark pair production cross section in $pp$ collisions at in dilepton final states with ATLAS", *Phys. Lett. B* 707 (2012) 459–477.

[205] ATLAS Collaboration,
"Top quark mass measurement in the $e\mu$ channel using the $m_{T2}$ variable at ATLAS",
ATLAS-CONF-2012-082 (2012).

[206] ATLAS Collaboration, "Selection of jets produced in proton-proton collisions with the ATLAS detector using 2011 data", ATLAS-CONF-2012-020 (2012).

[207] K. Yau Wong, "Studies of a top quark mass measurement in the dilepton channel using the $m_{T2}$ variable at ATLAS", BONN-IB-2012-03, MA thesis: University of Bonn, 2012.

[208] J. Butterworth et al.,
"Les Houches 2013: physics at TeV colliders: Standard Model Working Group report" (2014), arXiv:1405.1067 [hep-ph].

[209] ATLAS internal document, *Top group's MC11(a,b,c) samples for 2011 data analyses*, revision 126,
URL: https://twiki.cern.ch/twiki/bin/view/AtlasProtected/TopMC11?rev=126.

[210] R. D. Ball et al.,
"A first unbiased global NLO determination of parton distributions and their uncertainties", *Nucl. Phys.* B838 (2010) 136–206, arXiv:1002.4407 [hep-ph].

[211] A. Ortiz Velasquez et al., "Color reconnection and flowlike patterns in $pp$ collisions", *Phys. Rev. Lett.* 111 (2013) 042001, arXiv:1303.6326 [hep-ph].

[212] R. Field, "Min-bias and the underlying event at the LHC" (2012), arXiv:1202.0901 [hep-ph].

[213] A. Buckley et al., "Systematic event generator tuning for the LHC", *Eur. Phys. J.* C65 (2010) 331–357, arXiv:0907.2973 [hep-ph].

[214] P. Konar et al., "Superpartner mass measurement technique using 1D orthogonal Decompositions of the Cambridge transverse mass variable $M_{T2}$", *Phys. Rev. Lett.* 105 (2010) 051802, arXiv:0910.3679 [hep-ph].

[215] M. Burns et al., "Using subsystem MT2 for complete mass determinations in decay chains with missing energy at hadron colliders", *JHEP* 0903 (2009) 143, arXiv:0810.5576 [hep-ph].

[216] ATLAS Collaboration, "Measurement of the top quark mass in dileptonic top quark pair decays with $\sqrt{s}$ = 7 TeV ATLAS data", ATLAS-CONF-2013-077 (2013).

[217] T. H. N. Phan, "Measurement of the top quark mass in the $t\bar{t} \to$ dilepton decay channel using the $m_{T2}, m_{T2\perp}$ and $m_{lb}$ variables with ATLAS data", BONN-IB-2013-02,
MA thesis: University of Bonn, 2013.

[218] ATLAS Collaboration, "Measurement of the top quark mass in the $t\bar{t} \to$ lepton + jets and $t\bar{t} \to$ dilepton channels using $\sqrt{s}$ = 7 TeV ATLAS data" (2015), arXiv:1503.05427 [hep-ex].

[219] ATLAS internal document, *TopRootCoreRelease*, revision 169, URL: https://twiki.cern.ch/twiki/bin/viewauth/AtlasProtected/TopRootCoreRelease?rev=169.

[220] ATLAS Collaboration, "Evidence for the associated production of a vector boson (W, Z) and top quark pair in the dilepton and trilepton channels in $pp$ collision data at $\sqrt{s}$ = 8 TeV collected by the ATLAS detector at the LHC", ATLAS-CONF-2014-038 (2014).

[221] K. Cranmer et al.,
"HistFactory: A tool for creating statistical models for use with RooFit and RooStats", CERN-OPEN-2012-016 (2012).

[222] R. Bruneliere et al., "Setting exclusion limits in ATLAS supersymmetry searches with a likelihood ratio based method", ATL-PHYS-INT-2011-032 (2011).

[223] CMS Collaboration, "Measurement of top quark-antiquark pair production in association with a W or Z boson in $pp$ collisions at $\sqrt{s} = 8$ TeV", *Eur. Phys. J.* C74 (2014) 3060, arXiv:1406.7830 [hep-ex].

[224] T. Vázquez, *Towards the $t\bar{t}V$ combination: first test*, URL: https://indico.cern.ch/event/377905/contribution/2/material/slides/0.pdf.

# List of Figures

# List of Tables